Asymptotically Accurate Analytical Studies of Elastic Couplings in Anisotropic Beams

A Thesis Submitted

in Partial Fulfilment of the Requirements

for the Degree of

DOCTOR OF PHILOSOPHY

by

Nishant Kumar Shakya

(2016MEZ0008)

DEPARTMENT OF MECHANICAL ENGINEERING

INDIAN INSTITUTE OF TECHNOLOGY ROPAR

Apr,2024

Dedicated to my Family and Teachers

Declaration of Originality

I hereby declare that the work which is being presented in the thesis entitled **Asymptotically Accurate Analytical Studies of Elastic Couplings in Anisotropic Beams** has been solely authored by me. It presents the result of my own independent investigation/research conducted during the time period from July, 2016 to Apr,2024 under the supervision of **Dr. Srikant Sekhar Padhee**, Assistant Professor, Indian Institute of Technology Ropar. To the best of my knowledge, it is an original work, both in terms of research content and narrative, and has not been submitted or accepted elsewhere, in part or in full, for the award of any degree, diploma, fellowship, associateship, or similar title of any university or institution. Further, due credit has been attributed to the relevant state-of-the-art with appropriate citations and acknowledgments, in line with established ethical norms and practices. I also declare that any idea/data/fact/source stated in my thesis has not been fabricated/ falsified/ misrepresented. All the principles of academic honesty and integrity have been followed. I fully understand that if the thesis is found to be unoriginal, fabricated, or plagiarized, the Institute reserves the right to withdraw the thesis from its archive and revoke the associated Degree conferred. Additionally, the Institute also reserves the right to appraise all concerned sections of society of the matter for their information and necessary action (if any). If accepted, I hereby consent for my thesis to be available online in the Institute's Open Access repository, inter-library loan, and the title & abstract to be made available to outside organizations.

Signature

Name: Nishant Kumar Shakya
Entry Number: 2016MEZ0008
Program: PhD
Department: Mechanical Engineering
Indian Institute of Technology Ropar
Rupnagar, Punjab 140001

Date: Apr,2024

Acknowledgement

I extend my heartfelt gratitude to my supervisor, Dr. Srikant Sekhar Padhee, whose guidance, support, and mentorship were invaluable throughout my doctoral journey. His expertise and encouragement were crucial in shaping this research, inspiring me to tackle challenging problems in the field of applied mechanics. Beyond being an excellent mentor, Dr. Padhee's positive attitude, cheerful demeanor, calmness, and helpfulness have set a profound example for me. I hold immense respect for him and consider it a privilege to have worked with such a kind-hearted individual who encourages a life filled with joy and happiness.

I am deeply indebted to my doctoral committee members, Dr. Navin Kumar, Dr. Rakesh Kumar Maurya, Dr. Anupam Agrawal, and Dr. Pushpendra P. Singh, for their insightful feedback and constructive criticism, which significantly contributed to the refinement of this thesis. Special thanks to Dr. Prabhat Agnihotri, the Head of the Department, for his continuous support and encouragement. I am grateful to the other faculty members of the Department of Mechanical Engineering for their valuable suggestions. I also thank the staff members of the Department for their kindness and help with administrative formalities.

I would like to acknowledge IIT Ropar for providing financial support throughout my PhD, including assistance for attending conferences and workshops. This support not only alleviated the financial burden of my research but also enabled me to participate in academic events both nationally and internationally, enriching my research experience and fostering professional connections.

I thank my lab mates, Ajinkya (Bhau), Amandeep, Shivanshu, Pathak ji, and Dinesh, whose friendship made the research environment both stimulating and enjoyable. Heartfelt gratitude also goes to my friends Binod, Rahul, Rakesh, Jitendra, Anubhav, Hreetabh, Sohaib, Mukesh, and Varinder, whose unwavering support and camaraderie during challenging times were invaluable. Their encouragement not only eased the academic burden but also enhanced the journey with enjoyable and memorable moments. I would like to thank all the souls of IIT Ropar who have crossed my path and cheered me up at all times.

My deepest gratitude extends to my family, whose support and love have been pivotal to my journey. To my parents, Shri Khushi Ram Shakya and Smt. Sarla Devi, thank you for your immeasurable support, blessings, and love. To my wife, Aradhana Shakya, your unwavering belief in me, along with your steadfast support, sacrifices, patience, and deep understanding, have been my sanctuary. My brothers, Ankit and Nitin, and my sister, Vidhyotma, along with my brother-in-law, Rajesh Shakya, your encouragement and emotional backing have been invaluable. Finally, to my adorable son, Anant, your smiles and innocence have been my constant motivation. Each of you has been a pillar of strength for me, and I am eternally grateful. All my accomplishments are owed to these individuals who dedicated their efforts, making this daunting task achievable for me.

Nishant Kumar Shakya

Certificate

This is to certify that the thesis entitled **Asymptotically Accurate Analytical Studies of Elastic Couplings in Anisotropic Beams**, submitted by **Nishant Kumar Shakya (2016MEZ0008)** for the award of the degree of **Doctor of Philosophy** of Indian Institute of Technology Ropar, is a record of bonafide research work carried out under my (our) guidance and supervision. To the best of my knowledge and belief, the work presented in this thesis is original and has not been submitted, either in part or full, for the award of any other degree, diploma, fellowship, associateship or similar title of any university or institution.

In my (our) opinion, the thesis has reached the standard fulfilling the requirements of the regulations relating to the Degree.

Dr. Srikant Sekhar Padhee
Department of Mechanical Engineering
Indian Institute of Technology Ropar
Rupnagar, Punjab 140001
Date:

Graphical Abstract

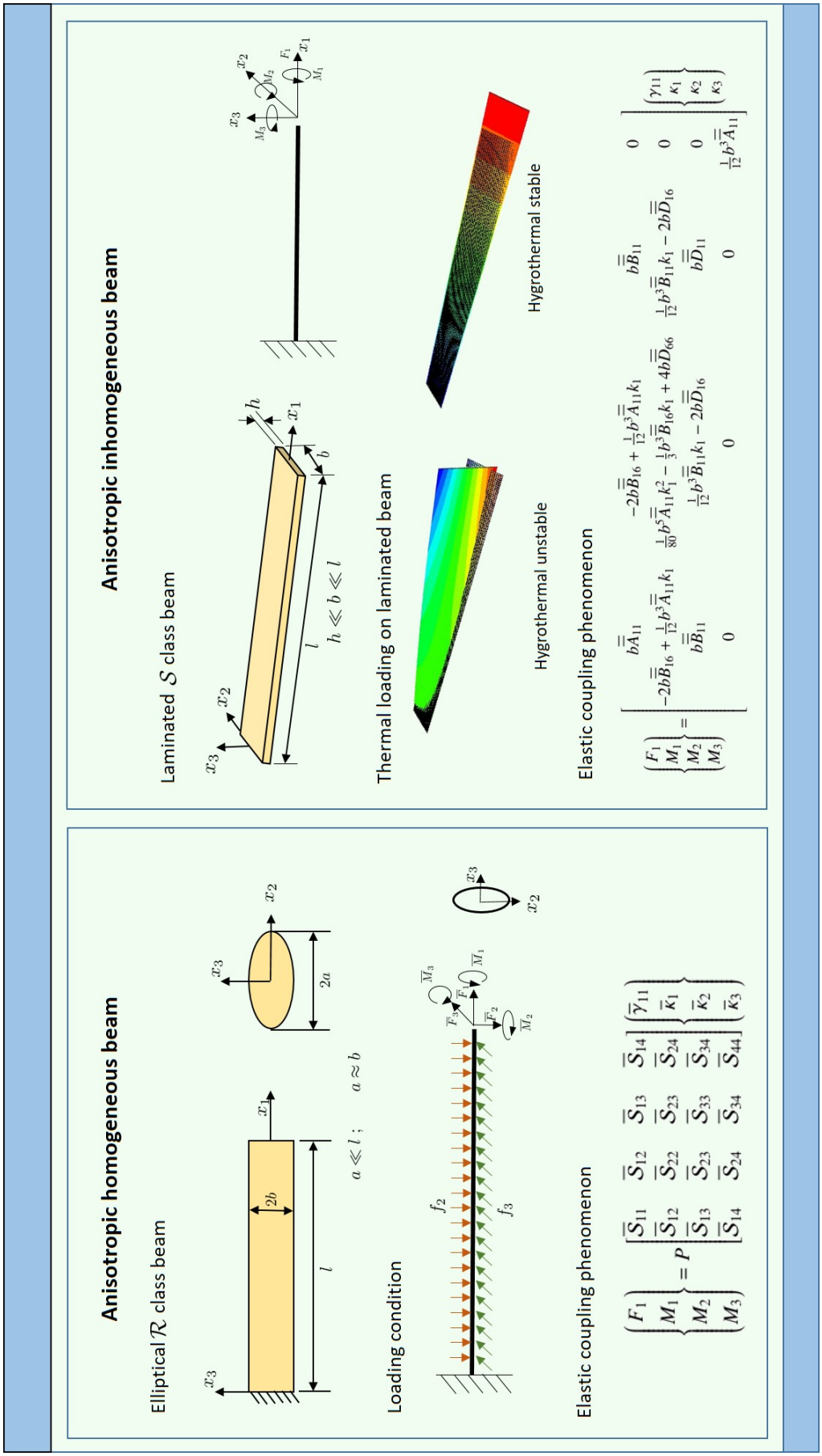

Abstract

Elastic coupling is a unique phenomenon exhibited by anisotropic beams. Due to this elastic coupling, different modes of beam deformation, such as extension, bending, and twisting, interact with each other. Modern structures are utilizing this elastic coupling to control them passively. The rotor blade of a wind turbine is one of the most well-known examples, where the bend-twist coupling is being implemented to passively control the angle of attack according to the wind load. This phenomenon of elastic coupling is mainly studied in laminated composite beams, which are generally anisotropic and inhomogeneous. There is a lack of research on elastic coupling in anisotropic-homogeneous beams. In addition, the work that is currently available is based on specific assumptions or has been solved for simplified loading cases.

This thesis work investigates the elastic coupling within both anisotropic-homogeneous and anisotropic-inhomogeneous beams. The Variational Asymptotic Method (VAM) has been employed as a mathematical tool, facilitating the simplification of the beam problem. It systematically decomposes the 3D elasticity beam problem into a 2D linear cross-sectional analysis and a 1D non-linear analysis along the beam length. VAM employs the small parameters associated with the beam problem to perform this decomposition, avoiding ad-hoc assumptions. These small parameters are utilized to order the strain energy terms. The procedure begins by considering the dominant terms first, then systematically includes lesser dominant terms in higher-order solutions.

The analysis of anisotropic-homogeneous beams has been carried out by considering a prismatic beam with solid elliptical cross-section. The study is divided into two parts based on solution characteristics. The first part addresses orthotropic beams, offering solutions for both the Classical and Timoshenko-like beam models. The second part extends the analysis to monoclinic and complete anisotropic beams, providing solutions exclusively for the Classical beam model. For both cases, closed-form expressions for 1D strain measures and displacement fields have been derived, facilitating the recovery of 3D displacement, stress, and strain fields. Notably, it is observed that beams with material anisotropy up to orthotropy do not exhibit elastic coupling phenomena; this phenomenon is first observed in monoclinic material beams and subsequently in complete anisotropic material beams. Furthermore, it is noted that even in complete anisotropic-homogeneous material beams, a fully elastically coupled system is not achieved; instead, only bend-twist coupling is observed. Additionally, the analysis reveals a violation of the plane stress condition in all coupled cases. To validate the results, comparisons have been made with Finite Element Analysis (FEA) and existing literature results, demonstrating a high level of agreement.

The analysis of anisotropic-inhomogeneous beam has been carried out using a laminated composite strip-like beam. These laminated composite structures provide the most feasible way to model this type of beam. This analysis is divided into two parts. The first part deals with the hygrothermal instabilities of these structures. Hygrothermal stability conditions have been derived using Classical Laminated Plate Theory (CLPT).

These conditions have been used to propose the generalized hygrothermally stable stacking sequences with different modes of elastic coupling. Furthermore, these stacking sequences have been optimized to achieve maximum coupling response. The optimized results are compared with conventional numerically optimized results. Additionally, both results are checked for robustness against small perturbations in the optimized results. The comparison shows that the proposed hygrothermally stable stacking sequence provides better results as the number of plies increases. Both stacking sequences show almost similar error distribution in the sensitivity analysis. The second part involves a mathematical analysis of these beams using VAM. Here, nonlinear kinematics for the strip-like beam are presented. The 2D shell membrane and curvature terms are derived from the 3D strain field, enabling the expression of 2D shell parameters in terms of 1D beam parameters. These newly defined 2D shell parameters are utilized to compute the 2D strain energy density functional. The zeroth-order approximate solution is obtained by minimizing the strain energy corrected up to $O(E\varepsilon^2)$ through the variational principle. This process ultimately yields the linear constitutive relation governing the linear coupling behavior of these beams. To capture nonlinear coupling behavior, the first-order approximate solution is employed. The hygrothermal stability of these structures is verified through FE simulations, using previously optimized hygrothermally stable stacking sequences. The simulation results confirm hygrothermal stability and comparison with FEA results shows a close agreement in the coupling results.

Keywords: VAM; Beam; Elastic-coupling; Elliptic cross-section; Hygrothermal stability; Laminate composite;

List of Publications

1. **Shakya NK**, Padhee SS. Asymptotic Analysis of Elastic Coupling in Anisotropic-Homogeneous Beam. Journal of Applied Mechanics. 2023 Apr 1;90(4):044501.
   https://doi.org/10.1115/1.4056458

2. **Shakya NK**, Padhee SS. Hygrothermally stable stacking sequence for tailoring of extension-twist coupling in composite structures. Composite Structures. 2023 Jan 18:116706.
   https://doi.org/10.1016/j.compstruct.2023.116706

3. **Shakya NK**, Padhee SS. Computationally efficient optimal design of hygrothermally stable laminate with bend-twist coupling by analytical and numerical strategy. Composites Part A: Applied Science and Manufacturing 2023; 170:107546.
   https://doi.org/10.1016/j.compositesa.2023.107546

4. **Shakya NK**,Padhee SS. Asymptotic analysis of Timoshenko-like Orthotropic beam with elliptical cross-section. European Journal of Mechanics-A/Solids. 2023 Jul 31:105100.
   https://doi.org/10.1016/j.euromechsol.2023.105100

5. **Shakya NK**,Padhee SS. Asymptotic Analysis of Anisotropic Beam with Elliptical Cross-Section. Acta Mechanica. (To be submitted)

Contents

List of Figures

List of Tables

Chapter 1

Introduction

Beam analysis is one of the important problems of structure design, as most of the structural members fall under the beam category. It is a slender structural member in which one of its dimensions is much larger than the other two. Because of this characteristic, it is generally analyzed by considering it as a 1D structural member. For this purpose, 1D beam theories are developed by the researchers. These 1D beam theories require pre-determined cross-sectional stiffness/rigidity constants. These theories are exhaustively investigated for the isotropic homogeneous beam. When it comes to anisotropic homogeneous beams, there is limited work available. Moreover, very few of these works included the analysis of the elastic coupling aspect.
The elastic coupling aspect is mostly investigated in laminated composite structures, which are generally anisotropic and inhomogeneous. The Classical Laminate Theory (CLT) has been used for the purpose which providing constitutive law relating force and moment resultants with mid-plane strains and curvatures. These structures provide freedom to tailor the desired elastic coupling behavior by wisely choosing the fiber orientation in its constituent plies. This choice of fiber orientation is limited by the phenomenon called hygrothermal instability. Because of this phenomenon, laminated structures deform due to temperature and moisture changes. These hygrothermal instabilities should be removed to maintain the functionality of these structures in environmental working conditions. This can be achieved by properly selecting fiber angles in its constituent plies governed by hygrothermal stability conditions.

1.1 Motivation

The interaction among the three modes of beam deformation (extension, bending and twisting) is known as elastic coupling. This elastic coupling permits the designing of passively controlled structures. Extension-twist coupling is extensively exploited in rotating beam-like structures such as the wings of tilt-rotor aircraft. Here, the centrifugal force regulates the angle of attack. Similarly, the bend-twist coupling is employed in wind turbines and forward-swept aircraft. Here the aerodynamic bending load controls the angle of attack in the wind turbine, while in forward-swept aircraft, it provides additional torsional rigidity without adding the stiffeners hence, without increasing the aircraft's weight. This elastic coupling can be implemented to mimic the coupled wing motion of flying insects or birds for the bio-inspired flapping wing micro bio-inspired air vehicles. Successful implementation of this elastic coupling in the abovementioned applications

requires a deep understanding of elastic coupling in anisotropic beam-like structures and factors affecting this elastic coupling. This becomes the motivation of the present work providing the analysis of elastic coupling in anisotropic beam-like structures.

1.2 Objective

The primary objective of this study is to investigate the elastic coupling behavior of anisotropic beams. The study also aims to determine closed-form expressions for 3D displacement, stress/strain fields, and 1D beam parameters ($\overline{\gamma}_{11}(x_1)$, $\overline{\kappa}_i(x_1)$, and $\overline{u}_i(x_1)$). Additionally, the study seeks to determine cross-sectional stiffness constants without relying on ad-hoc assumptions. Furthermore, the research aims to provide generalized stacking sequence schemes for anisotropic-inhomogeneous (laminate composite) beams with different modes of elastic coupling that are hygrothermally stable. The study is broadly divided into two parts based on the spatial characteristics of the beam material, homogeneous or inhomogeneous. The first part focuses on the analysis of anisotropic-homogeneous beams, while the second part is dedicated to the analysis of anisotropic-inhomogeneous (laminated composite) strip-like beams.

An elliptical cross-section beam has been considered to investigate the elastic coupling and to obtain beam field variables of the anisotropic-homogeneous beam. The complete analysis is divided into two parts based on the available elastic coupling and the nature of the solution. The first part provides the generalized analytical solution for the orthotropic beam. The 1D constitutive relation suggests that the orthotropic beam does not have elastic coupling characteristics. This solution can be reduced to the transverse-isotropic and isotropic beam by applying the appropriate elastic symmetry. Therefore, all homogeneous material beams with the level of anisotropy of orthotropy remain elastically uncoupled. The second part covers the analysis of three cases of monoclinic material and a complete anisotropic beam. It has been found that beams with material anisotropy higher than orthotropy exhibit elastic coupling.

An anisotropic-inhomogeneous beam is investigated using a strip-like structure to model the laminated beam. Laminated structures provide the most feasible way to model anisotropic-inhomogeneous beams. The 2D strain measures are derived from the 3D strain measures of the beam and expressed in terms of 1D beam parameters. Afterward, Classical Laminate Plate Theory (CLPT) is employed to analyze the beam. As composite structures exhibit hygrothermal instabilities, hygrothermal analysis is conducted to determine stability conditions using CLPT. Using these conditions, generalized hygrothermal stable stacking sequences are proposed for three types of coupling, namely extension-twist, bend-twist, and extension-bend.

1.3 Literature Survey

In order to achieve the objectives of this thesis, it is crucial to have a comprehensive understanding of the previous as well as recent advancements and developments in the field of beam theory. The history of beam theory can be traced back to the 16th century. This historical aspect can be found in the book [3] by Timoshenko. The purpose of this section is not to provide an exhaustive literature survey of previous beam theories; rather, it provides work on beams that is more relevant and important to the present work.

1.3.1 Beam Theories

Beams are slender structures in which one dimension is much larger than the other two. This structural characteristic makes them most suitable to be analyzed as 1D structures. Euler-Bernoulli beam model [4, 5, 6] is the most popular and well-known model. It relies on the assumption that the beam cross-sectional plane acts as a rigid body that remains normal to the beam axis before and after the deformation in bending. The beam theory formulated using these assumptions incorporates the deformations of the beam arising from both extension and bending. To include the deformation due to torsion, the rigidity assumption of the cross-section is relaxed for out-of-plane deformation, i.e., deformation is allowed in the normal direction of the cross-sectional plane [7, 8, 9, 10, 11]. The beam theories that account for deformation due to extension, bending and twisting are termed as classical beam theories. For the higher accuracy of the results, further refinement of the classical beam model is required. Timoshenko [12] suggests that though the cross-section of the beam will act as a rigid body, it will not remain normal to the axis of the beam due to the transverse shear.

The plane elasticity assumption is often made to solve beam problems having a thickness very small compared to its width. For this class of beam problems, the load is assumed to be in the plane of the beam and uniform along the thickness direction. These problems are also called plane stress problems since the stress components corresponding to the thickness coordinate index are zero. In contrast, the non-zero stress components solely depend on the plane coordinates. These problems are solved by using Airy stress functions. These functions identically satisfy the equilibrium equations and when put in only survived compatibility equation, result in a bi-harmonic equation for zero body force. Hence this problem can be solved by finding the appropriate Airy stress function, which satisfies the loading boundary conditions and bi-harmonics equations. The detailed discussion can be found in any standard test book on the theory of elasticity [10, 11, 13]. Hashin [14] used this approach to solve the plane anisotropic beam problem. However, the compatibility condition is not obtained in the form of a bi-harmonic equation due to normal-shear coupling compliance coefficients. The problem is solved for cantilever beam configuration with end concentration load and simply supported beam configuration with uniformly distributed load. Murakami and Yamakawa [15] plane anisotropic cantilever problem by using Hashin's solution approach to solve for the Airy stress function, Timoshenko-like

beam model and Euler-Bernoulli beam model. Ding et al. [16] presented the analysis of a planer functionally graded beam. They also used the Airy stress function method to solve this problem. The work presented by Sullivan and Oene [17], Schoeftner and Gahleitner [18], Karttunen and Hertzen [19] are also in the same line.

The 1D beam theories require cross-sectional stiffness constants; hence the accuracy of these theories depends on the accurate determination of the cross-sectional stiffness constants. These stiffness constants carry the information of material and cross-section geometry. These stiffness constants provided information about the coupling among 1D beam parameters. Mansfield and Sobey [20] derived the cross-sectional stiffness properties for Fiber-Reinforce Composite (FRC) tube loaded with extension, bending and torsion. Rehfield et al. [21] discussed the non-classical restrained torsional warping and bending-shear coupling in thin-walled composite beams having close-cross-section. Kosmatka and Friedmann [22] presented an analytical model for composite turbo-fan to determine its vibration characteristics and cross-sectional stiffness constants were found using the 2D FE model. Worndle [23] provides a finite element-based method to calculate the cross-sectional properties, shear stress distribution and location of the shear center, etc. Giavotto et al. [24] proposed FE-based cross-section analysis to obtain cross-sectional stiffness and stress for anisotropic-inhomogeneous rotor blades. Kosmatka and Dong [25] introduced an analytical beam model to obtain global cross-sectional properties of anisotropic-homogeneous beams.

Carrera et al. proposed the Carrera Unified Formulation (CUF), a hierarchical formulation that can be used to unify the reduction of 3D problems to 2D or 1D. Originally, it was presented to derive a class of 2D plate theories [26], later it was used to derive the higher-order beam theories. Carrera and Giunta [27] presented a CUF-based approach to derive higher-order 1D beam models. Subsequently, different 1D beam models were developed using CUF in various studies [28, 29, 30, 31, 32], which were utilized for analyzing static and dynamic beams. The Generalized Unified Formulation (GUF) is a generalized version of CUF, which allows for the treatment of each unknown of the problem independently. This technique is advantageous in FEA discretization.

The Variational Asymptotic Method (VAM) provides a systematic way to analyze beam-like structures. It splits the 3D elasticity problem of the beam into 2D linear cross-sectional analysis and 1D nonlinear analysis along the axis of the beam. This decomposition greatly simplifies the beam analysis. Here it should be noted that VAM does not take any *ad-hoc* assumptions regarding the deformation field of the beam for this decomposition; instead, it takes the small parameters involved in the problem under consideration. The linear cross-section analysis provides the cross-sectional stiffness constant and 2D warping functions in terms of 1D strain measures and strain recovery relations. The cross-sectional stiffness constants are supplied for the 1D nonlinear analysis, which provides the 1D stain measures and 1D displacements. These 1D stain measures, 1D displacements, 2D warping functions and strain recovery relations are used in 3D recovery relations, which provide the 3D stress, strain and displacement field. This whole procedure

can be found in the book by Hodges [36] on Nonlinear Composite Beam Theory.

The VAM was proposed by Berdichevsky for the development of the shell theory [37] and for elastic rods [38, 39]. His work on shell vibrations [40] and analysis of thin-walled beam [41] also uses the VAM. He introduces the transverse shear in rod analysis in his further work [42]. Danielson and Hodges [43] derived the kinematic relations by using the decomposition of the rotation tensor. This decomposition allows the 3D strain to be expressed in the local Cartesian coordinate system, greatly simplifying the beam analysis. This kinematic description of the beam along with VAM, has been used to extend the previous work on beams, which provides a simplified but mathematically rigorous workable and practical solution. Atilgan and Hodges [44] used this approach to analyze the anisotropic-inhomogeneous beam subjected to large small strain, large global rotation and small local rotation. The resultant set of equations obtained from the 2D cross-sectional analysis is identical to that given by Giavotto et al. [24]. Fulton and Hodges further extended this work [45, 46] for the analysis of the aeroelastic stability of rotor-blades. They used computer code to calculate the cross-sectional stiffness based on Giavotto et al. [24].

A new concept of employing asymptotic methods for the development of finite-element-based beam cross-section analysis was introduced by Hodges et al. [47]. Further work of Cesnik et al. [48, 49, 50, 51, 52], Hodges et al.[53] and Yu et al. [54] improved this methodology. This approach facilitates the analysis of the irregular or complicated cross-section, for which analytical solution is not possible.

Transverse shear is a crucial factor of beam analysis under flexural loading. It is ignored in the classical beam models. Popescu and Hodges [55] introduced the transverse shear to classical beam theories involving extension, bending and torsion using VAM. They suggested that in the general case, there is no asymptotically correct Timoshenko-like beam exists. They proposed a method that can capture the transverse shear in prismatic composite beams. They used the least square minimization method to obtain the most accurate solution. Popescu et al. [56] relaxed the constraint that the cross-section should be normal and suggested that any reference cross-section can be chosen without affecting the interior solution. Yu and Hodges [57] used VAM to find the expression of shear stiffness constants for homogeneous-isotropic beams with elliptical and rectangular cross-sections. Rajagopal [58] obtained it for isotropic circular tubes. Renton [59] extracted the shear stiffness for isotropic and homogeneous bars having simple cross-sections. Dong et al. [60] and Pai and Schulz [61] calculated the shear-correction factors for isotropic beams. Ho [62] and Tolf [63] derived the expression of shear stiffness for orthotropic beams having elliptic cross-section.

Thin-walled beam-like structures exhibit non-classical Brazier effects, Trapeze effect and Vlasov effect. These effects cannot be captured through the linear cross-sectional analysis. Volovoi [64] was the first who investigate the thin-walled open cross-section anisotropic prismatic beam for the end effects. However, the linearity of cross-section analysis prevents it from capturing non-classical effects. Harursampath and Hodges [65] investigated the

tubular beam using VAM and presented a nonlinear cross-sectional analysis to capture the non-classical Brazier effect.

The trapeze effect is basically a nonlinear coupling between extension and twisting. This effect is observable in the structures, which are soft in torsion and bending in one direction. Hence, these structures may show large bending stiffness in one direction. A long slender structure with one cross-sectional dimension significantly smaller than the other shows this characteristic. Helicopter rotor blades and wings of aircraft fall under this category. Buckley [66] considered the isotropic beam composed of several longitudinal fibers to explain the trapeze effect. Wagner [67] used this approach to analyze torsion buckling in beams. Biot [68] investigated the prismatic bar to calculate the increment in torsional stiffness due to pre-applied axial tension using the second-order rotation effect. Hodges [69] suggested that the trapeze effect arises due to the nonlinear strain field. Borri and Merlini [70] presented a cross-sectional analysis and derived geometric stiffness terms required to model the trapeze effect. Armanios et al. [71] presented the asymptotic analysis of laminated composite strip and derived nonlinear extension-twist coupling in anti-symmetric laminate. Popescu [72] treated the trapeze effect numerically using VAM and geometric nonlinear theory. Hodges et al. [73] provided the analytical solution for this problem; however, this solution is derived for the strip-like beam only. Popescu and Hodges [74] presented numerical cross-sectional analysis to treat such nonlinear effects.

1.3.2 Elastic Coupling in Anisotropic Beams

Elastic coupling is a unique characteristic of anisotropic beams due to which different modes of beam deformation (extension, bending, twisting) interact with each other. This elastic coupling assists in passive control in beam-like structures. It provides passive control of pitch angle in wind turbine rotor blades, aeroelastic stability of helicopter rotor blades. It is exploited as the control mechanism of forward-swept wing aircraft such as X-29A.

This elastic coupling characteristic is generally analyzed in composite structures that are not only anisotropic but also generally inhomogeneous. As per the author's best knowledge, very limited works are available on elastic coupling in anisotropic-homogeneous beams. Hong and Chopra [75, 76] developed a composite beam model to analyze the aerodynamic stability of bearingless rotor blades. Mansfield and Sobey [77] studied the coupling behavior of fiber composite tubes to mimic the helicopter blade and derived the expression for extensional, flexural, and torsional stiffness. Chandra and Chopra [78] investigated the composite I beam with bend-twist coupling and studied the effect of bend-twist coupling and constrained warping of the torsional stiffness. Badir et al. [79] and Volovoi et al. [80] used VAM to analyze the thin-walled open cross-section composite beams and derived the closed-form expressions of coupling stiffness constants. Yu et al. [81] provided the cross-sectional analysis using VABS. They showed that the location of the shear center varies due to the bend-twist coupling. Rehfield et al. [21] investigated the non-classical extension-twist coupling in thin-walled composite beam with

closed cross-section. Armanios et al. [71] and Hodges et al. [73] presented the non-linear extension-twist coupling in the strip-like beam.

Researchers investigate the effects of the ply angles on the coupling parameters and other dependent parameters such as aeroelastic stability. Bagherpour et al. [82] and Goeij et al. [83] implemented bend-twist coupling in composite wind turbine blades by modifying plies angles. Shams et al. [84] developed a model to investigate the effect of ply angles on nonlinear aeroelastic stability parameters. Authors found that bend-twist and bend-bend coupling stiffness significantly influence the aeroelastic stability. Hayat et al. [85] investigated the fatigue loading in the wind turbine rotor blade and suggested that this fatigue load can be mitigated by using different types of unbalance (i.e., ply-material, ply-angle, and ply-thickness unbalances) in the laminate of composites which ultimately regulates the bend-twist coupling.

Kosmatka and Dong [25] presented the analysis of anisotropic-homogeneous prismatic beam with a general cross-section and determined the displacement and stress distribution and also investigated the elastic coupling. IE and Kosmatka [86] extended this work for the anisotropic-homogeneous prismatic beam with elliptical cross-section. Ho [87] also investigated the anisotropic-homogeneous prismatic beam with elliptical cross-section; however, he provided the results in 1D form. He extracted the extensional, torsion, and other coupling constants. He further extended this work for the orthotropic materials [62].

1.3.3 Orthotropic Beam Analysis

Anisotropic material with three orthogonal planes of elastic symmetry reduces it to orthotropic material. Orthotropic beams have been investigated mostly for simplified cases. Tolf [63] presented the analysis of orthotropic beam with flexural loading, which is a plane stress problem. The author obtained the solution for elliptical and rectangular cross-sections using Saint-Venant's semi-inverse method. Yang et al. [88] solved the bending problem of the 2D orthotropic beam by introducing the Hamiltonian system. Sullivan and Oene [89] presented the solution of the 2D orthotropic beam problem using the Airy stress function method for plane stress conditions. Schoeftner and Gahleitner [90] derived analytical expressions of horizontal and vertical deflection for orthotropic rectangular strips using extended Castigliano's theorem. Lim and Han [91] proposed a higher-order deformation theory for 2D orthotropic beams to account for the deformation due to impact loading. Santoro [92] presented the solution of Saint-Venant's torsion problem. Gaspari and Aristodemo [93] provided the solution for Saint-Venant's coupled torsion-flexure problem for orthotropic beam. Jimmy C. Ho [62] extracted the expression of extensional, torsional and coupling stiffness constants for prismatic homogeneous orthotropic beam. Omri Rand [94] developed a successive iterative method to solve the orthotropic beam problem.

1.3.4 Hygrothermal Stability Analysis of Anisotropic-Inhomogeneous Beams

Anisotropic structures are generally modeled as laminated composite structures, as discussed above. These composite materials can be tailored to achieve specific elastic properties according to the application. If we talk about the elastic coupling aspect, it can be tuned by altering the fiber angles in its constituent plies. However, these laminated composite materials are sensitive to moisture and temperature changes. Whenever these two factors change, these structures get deformed. This deformation caused by the change in temperature and moisture is called "hygrothermal instability". The composite structures immune to this temperature and moisture change are called "hygrothermally stable". Composite structures should be hygrothermally stable to maintain the functionality in the working conditions.

The hygrothermal stability condition can be achieved when the fiber orientation of constituent plies satisfies certain conditions known as hygrothermal stability conditions. Cross et al. [95] derived necessary and sufficient conditions for the hygrothermal stability and proved that no asymmetric hygrothermal stable laminate is possible for 1 to 4-ply stacking sequence. Further, they derived the family of hygrothermal stable laminates for the 5, 6, 7, and 8-ply laminate. Chen [96] introduced the necessary and sufficient conditions for hygrothermal isotropic laminate and proved that any laminate composed of hygrothermal isotropic sub-laminates is also hygrothermally isotropic. Numerical optimization has also been carried out to maximize the extension-twist coupling for 16-ply laminate. Cross et al. [97] and Haynes et al. [98, 99] have investigated extension-twist coupling and provided optimized hygrothermally stable stacking sequence using Sequential Quadratic Programming (SQP). Aditya et al. [100] presented optimized results for bend-twist coupled hygrothermally stable laminate using ant colony optimization technique to obtain the globally optimized result. Optimization of multi-coupled laminates with hygrothermal stability conditions has been done by Li et al. [101], Haynes and Armanios [102, 2]. Optimization of hygrothermally stable laminate multi-objective function has been done by Li and Li [103]. A Hygro-Thermally Curvature stable Coupling laminate (HTCC) with 8-ply $[\theta, (\theta+90)_2, \theta, -\theta, (-\theta+90)_2, -\theta]_T$ was proposed by Winckler [104] for Extension-twist coupling. However, this solution lagged optimality conditions.

1.4 Outline of Thesis

This thesis is divided into five chapters which are based on the objective of the thesis. From the literature survey, it is found that the elastic coupling phenomenon of anisotropic beams is generally investigated in laminated composite thin-walled structures. The laminated composite materials are generally anisotropic and inhomogeneous. Very limited work is available which investigates the elastic coupling in anisotropic-homogeneous beams. The work, whichever is available, is solved either for the planer anisotropy or simple loading conditions. These shortcomings are addressed in chapter 2 and chapter 3. In

chapter 2, analysis of orthotropic-homogeneous beam having solid elliptical cross-section has been provided using VAM. It includes the analytical closed-form solution for the Classical beam model as well as the Timoshenko-like beam model. The cross-section analysis provides the cross-section stiffness constants and 1D constitutive law. The 1D analysis provides the closed-form expression of 1D stain measure and 1D displacement and rotation, which ultimately provides closed form solution for 3D stress/strain and displacement field. The obtained results are compared with FEA results. Chapter 3 deals with similar beams but having monoclinic and complete anisotropic material. Due to the increased complexity, this chapter only provides results for the Classical beam model only with a slightly change methodology. In this chapter semi-analytical approach has been used. In this approach, the stiffness constants are pre-assigned with numerical values rather than keeping them symbolically. The constitutive law provides the elastic coupling behavior. The 1D displacement, rotation and strain measures are obtained and also provided 3D displacement, stress and strain field. The obtained results are compared with FEA results in this chapter also.

As already discussed, the anisotropic beams are generally being modeled as composite structures and composite structures show hygrothermal instabilities, which should be eliminated to maintain the functionality of these structures in working conditions. The literature survey reveals that this hygrothermal instability problem is handled using numerical optimization techniques. Though this technique provides the hygrothermally stable stacking sequence, there are two major issues (i) The number of resultant hygrothermally stable fiber angles may be as high as the number of plies in laminate, (ii) obtained ply angles may not be in whole numbers. These two issues make manufacturing a very difficult task. Chapter 4 deals with this issue and provides generalized hygrothermally stable stacking sequences for extension-twist, bend-twist and extension-bend. In the resultant hygrothermally stable laminates will have total $4i$ $(i = 2, 3, 4...)$ plies and independent fiber angles are $i/2$ in the case when i is an even number and $(i-1)/2$ in the case when i odd number. Hence, the proposed hygrothermally stable laminate can have a theoretically infinite number of plies, it reduces independent fiber angles to a great extent and any arbitrary value of independent fiber angles will result in a hygrothermally stable stacking sequence. Moreover, it reduces computational time when used with numerical techniques as the number of independent fiber angles is much less and need not be checked for hygrothermal stability. These proposed stacking sequences are optimized for each coupling case results are compared with those obtained from conventional numerical optimization and also checked with sensitivity towards small perturbations in optimized results. In the next section, a nonlinear analysis of strip-like composite beams has been provided. The previously obtained results are used in this formulation. FEA simulation has been carried out to check the hygrothermal stability of these structures with these optimized results. This confirms the hygrothermal stability of these beams with proposed optimized results. Chapter 5 concludes the thesis with the key observations and the future aspects of the current study. In summary, the thesis is organized as follows:

Chapter 1 Introduction

Chapter 2 Orthotropic Homogeneous Beam Analysis

Chapter 3 Anisotropic and Monoclinic Homogeneous Beam Analysis

Chapter 4 Anisotropic Inhomogeneous Beam Analysis

Chapter 5 Conclusion and Future Scope

Chapter 2

Orthotropic Homogeneous Beam Analysis

This chapter discusses the analysis of the orthotropic homogeneous beam problem. It provides the essential beam kinematics, cross-sectional beam analysis, 1D beam analysis, results and discussion with special cases and numerical validation. The cross-sectional analysis provides the cross-sectional stiffness constants which are supplied to the 1D beam analysis. Basically, the cross-sectional analysis is the foundation of 1D beam analysis and the accuracy of the solution depends on the accurate determination of these cross-sectional stiffness constants. The cross-sectional solution corrected up to the second order corresponds to the Classical beam model and this solution corrected up to the third order corresponds to the Timoshenko-like beam model. 1D strain energy and, ultimately, 1D constitutive law is obtained using cross-sectional analysis. The 1D constitutive law relates the 1D strain measures and curvature terms to forces and moments, respectively. The 1D beam analysis provides the 1D displacement field $\overline{u}_i$ and rotation $\overline{\phi}_1$. Finally, the obtained solution is verified with literature by reducing it for the isotropic case and also validated with FEA results.

2.1 Beam Kinematics

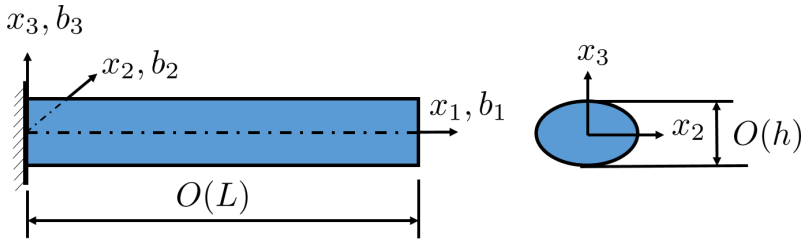

Figure 2.1: A schematic

In the beam-type structure, cross-sectional dimensions $O(h)$ are much smaller than the length dimension $O(L)$. The ratio of cross-sectional dimension to length dimension, $O(h/L)$ is a small parameter, which is exploited by VAM. For $\mathcal{R}$ class beam [36], This is the only small parameter for beam having solid cross-section with dimensions of the same order. It serves the purpose of obtaining asymptotically correct solutions for beam problems. The schematic of the beam is shown in Fig. 2.1. The fixed Cartesian coordinate system b_i is also shown in this figure with i =1, 2 and 3. (From here and onward, the

Latin index takes the values 1 to 3 while the Greek index takes the values 2 and 3). The position vector of any arbitrary material point of the un-deform beam in the fixed Cartesian coordinate system b_i is given as

$$\hat{r} = x_1 b_1 + x_2 b_2 + x_3 b_3 = x_i b_i \tag{2.1}$$

Now let this beam deform and every material point takes a new position in the deform configuration. Let $u(x_1, x_2, x_3) = u_i b_i$ be the 3D displacement field due to which every material point takes the position. The position vector $\hat{R}$ of the previously taken material point in the deformed configuration is

$$\hat{R} = (x_1 + u_1)b_1 + (x_2 + u_1)b_2 + (x_3 + u_3)b_3 = (x_i + u_i)b_i \tag{2.2}$$

The covariant base vectors in the undeformed state are

$$g_i = \frac{\partial \hat{r}}{\partial x_i} \tag{2.3}$$

and the contravariant base vectors in the undeformed state are

$$g^i = \frac{1}{2\sqrt{\mathbf{g}}} e_{ijk}\ g_j \times g_k \tag{2.4}$$

here $\mathbf{g} = det(g_i\ .\ g_j)$ Similarly, covariant base vector G_i in the deformed state of the beam can be obtained as

$$G_i = \frac{\partial \hat{R}}{\partial x_i} \tag{2.5}$$

The deformation gradient tensor $\underline{\chi}$, defined by Ogden [105] is

$$\underline{\chi} = G_i g^i \tag{2.6}$$

For the beam under consideration, the influence of the local rotations is negligible. In addition, the warping is small and the warping gradient in the cross-sectional plane is also of the same order. The strain in this case given as

$$\Gamma = \frac{\chi + \chi^T}{2} - I = \begin{bmatrix} u_1' & \frac{1}{2}(u_{1,2} + u_2') & \frac{1}{2}(u_{1,3} + u_3') \\ \frac{1}{2}(u_{1,2} + u_2') & u_{2,2} & \frac{1}{2}(u_{2,3} + u_{3,2}) \\ \frac{1}{2}(u_{1,3} + u_3') & \frac{1}{2}(u_{2,3} + u_{3,2}) & u_{3,3} \end{bmatrix} \tag{2.7}$$

Here $(\bullet)' = \frac{\partial}{\partial x_1}$ and $(\bullet)_{,\alpha} = \frac{\partial}{\partial x_\alpha}$. Eq. (2.7) gives the general definition of the strain for $\mathcal{R}$ class beam with small local rotations. In the upcoming section, it can be seen that the deformation of the beam is dictated by both material properties and cross-sectional geometry. The purpose of this work is to understand these effects and to provide a generalized framework for the deformation of anisotropic beams in terms of 1D variables without making any a-prior *ad hoc* assumptions on displacement and/or stress fields. For

the most general anisotropic materials, there are 21 independent elastic coefficients in the stiffness matrix C. This stiffness matrix is symmetric with size 6×6 and represented as

$$C = \begin{bmatrix} C_{11} & C_{12} & C_{13} & C_{14} & C_{15} & C_{16} \\ & C_{22} & C_{23} & C_{24} & C_{25} & C_{26} \\ & & C_{33} & C_{34} & C_{35} & C_{36} \\ & & & C_{44} & C_{45} & C_{46} \\ & \text{sym.} & & & C_{55} & C_{56} \\ & & & & & C_{66} \end{bmatrix} \tag{2.8}$$

The strain energy density (strain energy per unit volume) for a general anisotropic beam is

$$\mathcal{U}_{3D} = \frac{1}{2}\, \Gamma^T : C : \Gamma \tag{2.9}$$

The total potential energy of the beam is given by the following equation.

$$\Pi = \int_0^L \langle \mathcal{U}_{3D} \rangle \, dx_1 - W \tag{2.10}$$

where $\langle \bullet \rangle = \int\int (\bullet)\, dx_2 dx_3$. In Eq. (2.10), W is work done by the external loads and $\langle \mathcal{U}_{3D} \rangle$ is 1D strain energy. In order to carry out this integration, $\mathcal{U}_{3D}$ should be known as a function of x_2 and x_3. This is done by minimizing the strain energy functional $\mathcal{U}_{1D} = \langle \mathcal{U}_{3D} \rangle$. VAM facilitates this minimization over the cross-section independently. Eq. (2.10) forms the basis of 1D beam theory and minimization of this total potential energy establishes the relation between 1D quantities and external loads.

2.2 Cross-sectional Analysis

In this section, we have provided the cross-section analysis of the beam. It analysis can be divided into two parts (i) asymptotically correct cross-section analysis that provides 1D strain energy which includes energy contribution by extension, bending and torsion, forms Classical beam model, and (ii) refined cross-section analysis which adds energy contribution due to transverse shear into the Classical beam model forms Timoshenko-like beam model. These two beam models are discussed below.

Classical Beam Model

2.2.1 Zeroth-Order Approximation

The zeroth-order approximation considers strain energy which is corrected up to $O(\mu\varepsilon^2)$, where μ represents the order of the material constants and is assumed to be of the same order [36]. Minimization of this energy functional using variational principle provides the stationary point of this strain energy functional. The functions that minimize this strain energy functional are governed by the following Euler-Lagrange equations,

$$C_{66}u_{1,22} + 2C_{56}u_{1,23} + C_{55}u_{1,33} + C_{26}u_{2,22} + \big(C_{25} + C_{46}\big)u_{2,23} + C_{45}u_{2,33} + C_{46}u_{3,22} + (C_{36} + C_{45})\,u_{3,23} + C_{35}u_{3,33} = 0 \quad (2.11)$$

$$C_{26}u_{1,22} + (C_{25} + C_{46})\,u_{1,23} + C_{45}u_{1,33} + C_{22}u_{2,22} + 2C_{24}u_{2,23} + C_{44}u_{2,33} + C_{24}u_{3,22} + (C_{23} + C_{44})\,u_{3,23} + C_{34}u_{3,33} = 0 \quad (2.12)$$

$$C_{46}u_{1,22} + (C_{36} + C_{45})\,u_{1,23} + C_{35}u_{1,33} + C_{24}u_{2,22} + (C_{23} + C_{44})\,u_{2,23} + C_{34}u_{2,33} + C_{44}u_{3,22} + 2C_{34}u_{3,23} + C_{33}u_{3,33} = 0 \quad (2.13)$$

with associated boundary conditions

$$n_2\big(C_{66}u_{1,2} + C_{56}u_{1,3} + C_{26}u_{2,2} + C_{46}u_{2,3} + C_{46}u_{3,2} + C_{36}u_{3,3}\big) + n_3\big(C_{56}u_{1,2} + C_{55}u_{1,3} + C_{25}u_{2,2} + C_{45}u_{2,3} + C_{45}u_{3,2} + C_{35}u_{3,3}\big) = 0 \quad (2.14)$$

$$n_2\big(C_{26}u_{1,2} + C_{25}u_{1,3} + C_{22}u_{2,2} + C_{24}u_{2,3} + C_{24}u_{3,2} + C_{23}u_{3,3}\big) + n_3\big(C_{46}u_{1,2} + C_{45}u_{1,3} + C_{24}u_{2,2} + C_{44}u_{2,3} + C_{44}u_{3,2} + C_{34}u_{3,3}\big) = 0 \quad (2.15)$$

$$n_2\big(C_{46}u_{1,2} + C_{45}u_{1,3} + C_{24}u_{2,2} + C_{44}u_{2,3} + C_{44}u_{3,2} + C_{34}u_{3,3}\big) + n_3\big(C_{36}u_{1,2} + C_{35}u_{1,3} + C_{23}u_{2,2} + C_{34}u_{2,3} + C_{34}u_{3,2} + C_{33}u_{3,3}\big) = 0 \quad (2.16)$$

Here n_α are direction cosines of the outward normal with respect to x_α. For simplicity, the cross-section of the beam is taken as the elliptical. The solution which satisfy these Euler-Lagrange equations (2.11-2.13) and boundary conditions (2.14-2.16) are

$$u_1^0 = \overline{u}_1(x_1) \quad (2.17)$$

$$u_2^0 = \overline{u}_2(x_1) - x_3\overline{\phi}_1(x_1) \quad (2.18)$$

$$u_3^0 = \overline{u}_3(x_1) + x_2\overline{\phi}_1(x_1) \quad (2.19)$$

In Eqs. (2.17-2.19), $\overline{u}_i(x_1)$ and $\overline{\phi}_1(x_1)$ are arbitrary 1D function of x_1. The expression for these unknown functions will be found using 1D constitutive relations. These terms represent rigid body-like deformations. $\overline{u}_i(x_1)$ represents the rigid body-like translations, while $x_\alpha\overline{\phi}_1$ gives the rigid body-like rotation of the cross-section plane during deformation. It is to be noted that this cross-sectional solution neither depends on the material properties nor the cross-sectional geometry. So this solution represents the generic deformation of the homogeneous beam.

Beyond the zeroth order approximation, the solution becomes material-dependent. As this chapter focused on the beam analysis of orthotropic material; hence, for further development, the stiffness matrix (2.8) is reduced for the orthotropic material case. Beam with material anisotropy higher than orthotropy will be treated separately using a semi-analytical approach in the chapter 3.

2.2.2 First Order Approximation

Orthotropic materials are defined by 9 independent engineering elastic constant ($E_{ii}, \nu_{ij},$ and G_{ij}). Here summation convention will not be followed for i. The expression for coefficient of stiffness matrix (C_{ij}) in terms of engineering elastic constants is well established and can be found in literature [94, 106].
In order to find the first-order solution, the strain energy considered should be corrected up to order $O\left(\mu\varepsilon^2(h/L)^2\right)$. To obtain this energy, it is required to perturb the zeroth order solution, which is given as

$$u_i^I = u_i^0 + v_i(x_1, x_2, x_3) \tag{2.20}$$

where $v_i(x_1, x_2, x_3)$ are asymptotically smaller than u_i^0 and. For the definiteness of the solution, we have to apply four constraints on $v_i(x_1, x_2, x_3)$. These constraints define the 1D functions $\left(\overline{u}_i(x_1)\right.$ and $\left.\overline{\phi}_1(x_1)\right)$ in term of the 3D displacement field. The constraints chosen are

$$\langle v_i \rangle = 0 \qquad \langle v_{3,2} - v_{2,3} \rangle = 0 \tag{2.21}$$

By applying these constraints to Eq. (2.20) and using Eqs. (2.17-2.19), following relations between the 1D function and 3D displacement field have been obtained.

$$\begin{aligned} \mathcal{A}\,\overline{u}_i(x_1) &= \langle\, u_i^I \,\rangle \\ \mathcal{A}\,\overline{\phi}_1(x_1) &= \frac{1}{2}\langle\, u_{3,2}^I - u_{2,3}^I \,\rangle \end{aligned} \tag{2.22}$$

Here $\mathcal{A}$ is the cross-sectional area. The Eq. (2.22) shows that the 1D displacement variable represents the average of 3D displacement over the cross-section of the beam. After using the perturbed displacement field (2.20), the new modified strains field are

$$\begin{aligned} \Gamma_{11}^I &= \overline{u}_1\,(x_1)' + v_1' \\ \Gamma_{22}^I &= v_{2,2} \\ \Gamma_{33}^I &= v_{3,3} \\ \Gamma_{23}^I &= v_{2,3} + v_{3,2} \\ \Gamma_{13}^I &= \overline{u}_3\,(x_1)' + x_2\overline{\phi}_1\,(x_1)' + v_{1,3} + v_3' \\ \Gamma_{12}^I &= \overline{u}_2\,(x_1)' - x_3\overline{\phi}_1\,(x_1)' + v_{1,2} + v_2' \end{aligned} \tag{2.23}$$

The strain energy is calculated using the strain field (2.23). Minimization of this first-order approximate strain energy using variational method provides the following Euler-Lagrange equations

$$C_{55}v_{1,33} + C_{66}v_{1,22} = 0 \tag{2.24}$$

$$C_{23}v_{3,23} + C_{44}\left(v_{2,33} + v_{3,23}\right) + C_{22}v_{2,22} = 0 \tag{2.25}$$

$$C_{33}v_{3,33} + C_{44}\left(v_{2,23} + v_{3,22}\right) + C_{23}v_{2,23} = 0 \tag{2.26}$$

and associated boundary conditions

$$n_2 C_{66}\left[\overline{u}_2\left(x_1\right)' - x_3\overline{\phi}_1\left(x_1\right)' + v_{1,2}\right] + n_3 C_{55}\left[\overline{u}_3\left(x_1\right)' + x_2\overline{\phi}_1\left(x_1\right)' + v_{1,3}\right] = 0 \tag{2.27}$$

$$n_2\left[C_{12}\overline{u}_1\left(x_1\right)' + C_{23}v_{3,3} + C_{22}v_{2,2}\right] + n_3 C_{44}\left[v_{2,3} + v_{3,2}\right] = 0 \tag{2.28}$$

$$n_3\left[C_{13}\overline{u}_1\left(x_1\right)' + C_{33}v_{3,3} + C_{23}v_{2,2}\right] + n_2 C_{44}\left[v_{2,3} + v_{3,2}\right] = 0 \tag{2.29}$$

The displacement functions v_i which satisfy the Eqs. (2.24-2.26), boundary conditions (2.27-2.29) and constraints (2.21) are given in following equations by underbraces terms.

$$u_1^I = u_1^0(x_1,x_2,x_3) - \underbrace{x_2\overline{u}_2(x_1)' - x_3\overline{u}_3(x_1)'} + \underbrace{\psi_{ort}(x_2,x_3)\ \overline{\phi}_1(x_1)'}_{v_1(x_1,x_2,x_3)} \tag{2.30}$$

$$u_2^I = u_2^0(x_1,x_2,x_3) - \underbrace{\nu_{12}\ x_2\ \overline{u}_1(x_1)'}_{v_2(x_1,x_2,x_3)} \tag{2.31}$$

$$u_3^I = u_3^0(x_1,x_2,x_3) - \underbrace{\nu_{13}\ x_3\ \overline{u}_1(x_1)'}_{v_3(x_1,x_2,x_3)} \tag{2.32}$$

where,

$$\psi_{ort} = \frac{(b^2\ G_{12} - a^2\ G_{13})x_2x_3}{a^2\ G_{13} + b^2\ G_{12}}$$

The displacement components (2.30-2.32) are approximate up to first order. The terms $x_2\overline{u}_2(x_1)'$ and $x_3\overline{u}_3(x_1)'$ in Eq. (2.30) represent the rigid body like displacement of the cross-sectional plane due to bending of the beam. Except for these terms, all the underbraces terms are due to the deformation of the plane. $\psi_{ort}(x_2,x_3)\ \overline{\phi}_1(x_1)'$ represents the out-of-plane deformation due to torsion while $\nu_{12}\ x_2\ \overline{u}_1(x_1)'$ and $\nu_{13}\ x_3\ \overline{u}_1(x_1)'$ in-plane deformations due to poisson effect. The warping function $\psi_{ort}(x_1,x_2)$ is not only the function of cross-sectional coordinates (x_1,x_2) but also depends on the material properties (G_{12} and G_{13}) [94, 107]. For specific cases when $G_{12} = G_{13}$, it is reduced to the well-known Saint-Venant's warping function. Moreover, this warping function vanished when

$$\frac{G_{12}}{G_{13}} = \frac{a^2}{b^2} \tag{2.33}$$

hence, if this condition prevails, even though the cross-section is elliptical, no out-of-plane warping will be observed.

2.2.3 Second Order Approximation

The first-order solution can further be improved asymptotically by including the second-order solution term to it. For this purpose, the strain energy corrected up to order $O\left(\mu\varepsilon^2(h/L)^4\right)$ is considered. To obtain this required strain energy functional, we have to modify the displacement field $\overline{u}_i^I$ of Eqs. (2.30-2.32) by adding asymptotically small term $w_i(x_1,x_2,x_3)$ to it. This modified displacement field after perturbation of the

first-order displacement field is

$$u_i^{II}(x_1, x_2, x_3) = u_i^I + w_i(x_1, x_2, x_3) \tag{2.34}$$

These w_i are subjected to the same constraints as applicable for v_i, given by Eq. (2.21) due to the same reason. The corresponding modified strain field is

$$\begin{aligned}
\Gamma_{11}^{II} &= \overline{u}_1\,(x_1)' - x_2\overline{u}_2\,(x_1)'' - x_3\overline{u}_3\,(x_1)'' + \psi_{ort}\;\overline{\phi}_1\,(x_1)'' + w_1' \\
\Gamma_{22}^{II} &= -\nu_{12}\overline{u}_1\,(x_1)' + w_{2,2} \\
\Gamma_{33}^{II} &= -\nu_{13}\overline{u}_1\,(x_1)' + w_{3,3} \\
\Gamma_{23}^{II} &= w_{2,3} + w_{3,2} \\
\Gamma_{13}^{II} &= -\nu_{13}x_3\overline{u}_1\,(x_1)'' + (\psi_{ort,3} + x_2)\,\overline{\phi}_1\,(x_1)' + w_{1,3} + w_3' \\
\Gamma_{12}^{II} &= -\nu_{12}x_2\overline{u}_1\,(x_1)'' + (\psi_{ort,2} - x_3)\,\overline{\phi}_1\,(x_1)' + w_{1,2} + w_2'
\end{aligned} \tag{2.35}$$

Strain energy, corrected up to second order is calculated using equation (2.9) and strain field (2.35). Minimization of this strain energy provides the following Euler–Lagrange equations

$$\mathbb{K}_{11}\overline{u}_1\,(x_1)'' + C_{55}w_{1,33} + C_{66}w_{1,22} = 0 \tag{2.36}$$

$$\mathbb{K}_{12}x_3\overline{\phi}_1\,(x_1)'' + C_{12}\overline{u}_2\,(x_1)'' - C_{23}w_{3,23} - C_{44}\,(w_{2,33} + w_{3,23}) - C_{22}w_{2,22} = 0 \tag{2.37}$$

$$\mathbb{K}_{13}x_2\overline{\phi}_1\,(x_1)'' + C_{13}\overline{u}_3\,(x_1)'' - C_{33}w_{3,33} - C_{44}\,(w_{2,23} + w_{3,22}) - C_{23}w_{2,23} = 0 \tag{2.38}$$

and associated boundary conditions

$$\begin{aligned}
&n_3C_{55}\big[\mathbb{K}_{14}x_2\overline{\phi}_1\,(x_1)' - \mathbb{K}_{15}x_3\overline{u}_1\,(x_1)'' + w_{1,3}\big] \\
&\qquad - n_2C_{66}\big[\mathbb{K}_{16}x_3\overline{\phi}_1\,(x_1)' - \mathbb{K}_{17}x_2\overline{u}_1\,(x_1)'' - w_{1,2}\big] = 0
\end{aligned} \tag{2.39}$$

$$\begin{aligned}
&n_2\big[C_{12}\left(x_2\overline{u}_2\,(x_1)'' + x_3\overline{u}_3\,(x_1)'' - \psi_{ort}\overline{\phi}_1\,(x_1)''\right) - C_{23}w_{3,3} - C_{22}w_{2,2}\big] \\
&\qquad - n_3C_{44}\,[w_{2,3} + w_{3,2}] = 0
\end{aligned} \tag{2.40}$$

$$\begin{aligned}
&n_3\big[C_{13}\left(x_2\overline{u}_2\,(x_1)'' + x_3\overline{u}_3\,(x_1)'' - \psi_{ort}\overline{\phi}_1\,(x_1)''\right) - C_{33}w_{3,3} - C_{23}w_{2,2}\big] \\
&\qquad - n_2C_{44}\,[w_{2,3} + w_{3,2}] = 0
\end{aligned} \tag{2.41}$$

where,

$$\begin{aligned}
\mathbb{K}_{11} =& \frac{1}{C_{23}^2 - C_{22}C_{33}}\big(C_{33}C_{12}^2 - 2C_{13}C_{23}C_{12} - C_{23}C_{55}C_{12} + C_{33}C_{66}C_{12} + C_{11}C_{23}^2 \\
&+ C_{13}^2C_{22} - C_{11}C_{22}C_{33} + C_{13}C_{22}C_{55} - C_{13}C_{23}C_{66}\big); \\
\mathbb{K}_{12} =& \frac{a^2C_{12}C_{55} + 2a^2C_{55}C_{66} - b^2C_{12}C_{66}}{a^2C_{55} + b^2C_{66}}; \qquad \mathbb{K}_{13} = \frac{a^2C_{13}C_{55} - 2b^2C_{55}C_{66} - b^2C_{13}C_{66}}{a^2C_{55} + b^2C_{66}}; \\
\mathbb{K}_{15} =& \frac{C_{13}C_{22} - C_{12}C_{23}}{C_{22}C_{33} - C_{23}^2}; \quad \mathbb{K}_{16} = \frac{2a^2C_{55}}{a^2C_{55} + b^2C_{66}}; \mathbb{K}_{17} = \frac{C_{13}C_{23} - C_{12}C_{33}}{C_{22}C_{33} - C_{23}^2}
\end{aligned}$$

The unknown functions w_i are obtained by solving the Euler equations (2.36-2.38) and

boundary conditions (2.39-2.41) along with (2.21) like constraints. While solving these equations the terms $\overline{u}_1(x_1)''$ and $\overline{\phi}_1(x_1)''$ have to be dropped as these terms do not contributes in this energy [57]. The 3D displacement field corrected up to the second order is obtained as

$$u_1^{II} = u_1^I(x_1, x_2, x_3) \tag{2.42}$$

$$u_2^{II} = u_2^I(x_1, x_2, x_3) + \overbrace{\nu_{12} x_2 x_3 \overline{u}_3(x_1)''}^{w_2(x_1,x_2,x_3)} + \overbrace{\frac{\left[\nu_{12}\left(\mathcal{A}x_2^2 - \mathcal{I}_3\right) + \nu_{13}\left(\mathcal{I}_2 - \mathcal{A}x_3^2\right)\right]\overline{u}_2(x_1)''}{2\mathcal{A}}}^{w_2(x_1,x_2,x_3)} \tag{2.43}$$

$$u_3^{II} = u_3^I(x_1, x_2, x_3) + \overbrace{\nu_{13} x_2 x_3 \overline{u}_2(x_1)''}^{w_3(x_1,x_2,x_3)} - \overbrace{\frac{\left[\nu_{12}\left(\mathcal{A}x_2^2 - \mathcal{I}_3\right) + \nu_{13}\left(\mathcal{I}_2 - \mathcal{A}x_3^2\right)\right]\overline{u}_3(x_1)''}{2\mathcal{A}}}^{w_3(x_1,x_2,x_3)} \tag{2.44}$$

with

$$\mathcal{A} = \langle 1 \rangle \qquad \mathcal{I}_2 = \langle x_3^2 \rangle \qquad \mathcal{I}_3 = \langle x_2^2 \rangle$$

The overbrace terms $w_2(x_1, x_2, x_3)$ and $w_3(x_1, x_2, x_3)$, in Eqs. (2.43-2.44), are second-order terms. These terms provide the dependency of the 3D displacement field on the geometry of the cross-section and the curvature of the beam. This second-order solution only improves u_α^{II}. It is noted that ν_{23} does not influence the cross-sectional solution. The resultant 1D strain energy corrected up to order $O\left(\mu\varepsilon^2(h/L)^4\right)$ is

$$2\mathcal{U}_{1D} = E_{11}\left(\mathcal{A}\overline{u}_1(x_1)'^2 + \mathcal{I}_3\overline{u}_2(x_1)''^2 + \mathcal{I}_2\overline{u}_3(x_1)''^2\right) + \frac{\pi a^3 b^3 G_{12} G_{13}}{a^2 G_{13} + b^2 G_{12}}\overline{\phi}_1(x_1)'^2 \tag{2.45}$$

The mathematical formulation till now represents the classical model of the beam. The displacement field given by equation (2.42-2.44) is the superposition of extension, torsion, and pure bending in two directions. Arbitrary unknown ($\overline{u}_i$ & $\overline{\phi}_1$ and their derivatives) involved in these equations can be obtained by using the 1D constitutive law of the 1D boundary conditions.

Timoshenko-like Beam Model

The classical beam model does not incorporate transverse shear while solving flexure problems. The generalized Timoshenko model provided by the VABS [57] incorporates both bending and transverse shear. The most approximate one-dimensional strain energy provided by this model is

$$2\mathcal{U}_{1D} = \overline{\epsilon}^T \mathcal{K}\overline{\epsilon} + 2\overline{\epsilon}^T \mathcal{M}\overline{\epsilon}' + \overline{\epsilon}'^T \mathcal{N}\overline{\epsilon}' + 2\overline{\epsilon}^T \mathcal{P}\overline{\epsilon}'' \tag{2.46}$$

where $\mathcal{K}$, $\mathcal{M}$, $\mathcal{N}$, and $\mathcal{P}$ are matrices that contain the material and geometrical information of the beam cross-section and $\overline{\epsilon} = [\overline{\gamma}_{11} \quad \overline{\kappa}_1 \quad \overline{\kappa}_2 \quad \overline{\kappa}_3]^T$. Elements of $\overline{\epsilon}$ are 1D strain measures used in the classical beam model. A generalized Timoshenko model is extracted from energy Eq. (2.46) as

$$2\mathcal{U}_t = \epsilon^T X \epsilon + 2\epsilon^T F \gamma_s + \gamma_s^T G \gamma_s \tag{2.47}$$

where $\epsilon = [\gamma_{11} \;\; \kappa_1 \;\; \kappa_2 \;\; \kappa_3]^T$. Elements of ϵ are classical 1D strain measures defined in the generalized Timoshenko beam model framework, and $\gamma_s = [2\gamma_{12} \;\; 2\gamma_{13}]^T$ and the elements of this vector are transverse shear strain. The relation between $\bar{\epsilon}$, ϵ and γ is

$$\bar{\epsilon} = \epsilon + Q\gamma_s' \tag{2.48}$$

where

$$Q = \begin{bmatrix} 0 & 0 & 0 & 1 \\ 0 & 0 & -1 & 0 \end{bmatrix}^T$$

$X,\ F,$ and G are obtained as

$$\begin{aligned} G &= (Q^T\mathcal{K}^{-1}\mathcal{N}\mathcal{K}^{-1}Q)^{-1} \\ F &= \mathcal{M}^T\mathcal{K}^{-1}QG \\ X &= \mathcal{K} + FG^{-1}F^T \end{aligned} \tag{2.49}$$

It is known that 1D strain measures are related to the derivatives of 1D displacement & rotation measures as

$$\overline{\phi}_1(x_1)' = \overline{\kappa}_1(x_1) \quad \overline{u}_1(x_1)' = \overline{\gamma}_{11}(x_1) \quad \overline{u}_2(x_1)'' = \overline{\kappa}_3(x_1) \quad \overline{u}_3(x_1)'' = -\overline{\kappa}_2(x_1) \tag{2.50}$$

It is clear from the relations (2.50) and Eq. (2.46) that strain energy (2.45) is not adequate to extract generalized Timoshenko beam model from it. Hence, need to improve it further by proceeding for third-order solution.

2.2.4 Third Order Approximation

To proceed for third order solution, the second order solution $u_i^{II}(x_1, x_2, x_3)$ has to be perturbed by adding asymptotically small term $\mathcal{W}_i(x_1, x_2, x_3)$ to it, and (2.21) like constraints will be applied on these new variables also. The only difference is that the strain energy considered this time will be corrected up to order $O\left(\mu\varepsilon^2(h/L)^6\right)$. The resultant strain field will be

$$\begin{aligned}
\Gamma_{11}^{III} =& \overline{u}_1(x_1)' - x_2\overline{u}_2(x_1)'' - x_3\overline{u}_3(x_1)'' + \mathcal{W}_1' \\
\Gamma_{22}^{III} =& \nu_{12}\left(x_2\overline{u}_2(x_1)'' + x_3\overline{u}_3(x_1)'' - \overline{u}_1(x_1)'\right) + \mathcal{W}_{2,2} \\
\Gamma_{33}^{III} =& \nu_{13}\left(x_2\overline{u}_2(x_1)'' + x_3\overline{u}_3(x_1)'' - \overline{u}_1(x_1)'\right) + \mathcal{W}_{3,3} \\
\Gamma_{23}^{III} =& \mathcal{W}_{2,3} + \mathcal{W}_{3,2} \\
\Gamma_{13}^{III} =& \frac{1}{8}\left[\nu_{12}\left(a^2 - 4x_2^2\right) + \nu_{13}\left(4x_3^2 - b^2\right)\right]\overline{u}_3(x_1)^{(3)} \nu_{13}x_2x_3\overline{u}_2(x_1)^{(3)} \\
&+ (\psi_{ort,3} + x_2)\,\overline{\phi}_1(x_1)' + \mathcal{W}_{1,3} + \mathcal{W}_3' \\
\Gamma_{12}^{III} =& -\frac{1}{8}\left[\nu_{12}\left(a^2 - 4x_2^2\right) + \nu_{13}\left(4x_3^2 - b^2\right)\right]\overline{u}_2(x_1)^{(3)} + \nu_{12}x_2x_3\overline{u}_3(x_1)^{(3)} \\
&+ (\psi_{ort,2} - x_3)\,\overline{\phi}_1(x_1)' + \mathcal{W}_{1,2} + \mathcal{W}_2'
\end{aligned} \tag{2.51}$$

In this case Euler-Lagrange equations

$$\mathbb{K}_{11}\left[x_2\overline{u}_2\left(x_1\right)^{(3)}+x_3\overline{u}_3\left(x_1\right)^{(3)}\right]-C_{55}\mathcal{W}_{1,33}-C_{66}\mathcal{W}_{1,22}=0 \tag{2.52}$$

$$C_{23}\mathcal{W}_{3,23}+C_{44}\left(\mathcal{W}_{2,33}+\mathcal{W}_{3,23}\right)+C_{22}\mathcal{W}_{2,22}=0 \tag{2.53}$$

$$C_{33}\mathcal{W}_{3,33}+C_{44}\left(\mathcal{W}_{2,23}+\mathcal{W}_{3,22}\right)+C_{23}\mathcal{W}_{2,23}=0 \tag{2.54}$$

and associated boundary conditions are

$$\begin{aligned}n_3\Bigg[&C_{55}\left(\psi_{ort,3}\left(x_2,x_3\right)+x_2\right)\overline{\phi}_1\left(x_1\right)'-\frac{1}{8}C_{55}\left(\mathbb{K}_{17}(a^2-4x_2^2)+\mathbb{K}_{15}(b^2-4x_3^2)\right)\overline{u}_3\left(x_1\right)^{(3)}\\&+\mathbb{K}_{15}C_{55}x_2x_3\overline{u}_2\left(x_1\right)^{(3)}+C_{55}\mathcal{W}_{1,3}\Bigg]+n_2\Bigg[C_{66}\mathcal{W}_{1,2}+C_{66}\left(\psi_{ort,2}\left(x_2,x_3\right)-x_3\right)\overline{\phi}_1\left(x_1\right)'\\&+\frac{1}{8}C_{66}\left(\mathbb{K}_{17}(a^2-4x_2^2)+\mathbb{K}_{15}(b^2-4x_3^2)\right)\overline{u}_2\left(x_1\right)^{(3)}-\mathbb{K}_{17}C_{66}x_2x_3\overline{u}_3\left(x_1\right)^{(3)}\Bigg]=0\end{aligned} \tag{2.55}$$

$$n_2\Big[C_{23}\mathcal{W}_{3,3}+C_{22}\mathcal{W}_{2,2}\Big]+n_3C_{44}\Big[\mathcal{W}_{2,3}+\mathcal{W}_{3,2}\Big]=0 \tag{2.56}$$

$$n_3\Big[C_{33}\mathcal{W}_{3,3}+C_{23}\mathcal{W}_{2,2}\Big]+n_2C_{44}\Big[\mathcal{W}_{2,3}+\mathcal{W}_{3,2}\Big]=0 \tag{2.57}$$

Solution of these Eqs. (2.52-2.54) and boundary conditions (2.55-2.57) along with constraints will provides the unknown functions $\mathcal{W}_i$. The displacement components corrected up to the third order are the following

$$u_1^{III}=u_1^{II}(x_1,x_2,x_3)+\overbrace{\mathcal{F}_1(x_2,x_3)\ \overline{u}_2(x_1)^{(3)}+\mathcal{F}_2(x_2,x_3)\ \overline{u}_3(x_1)^{(3)}}^{\mathcal{W}_1(x_1,x_2,x_3)} \tag{2.58}$$

$$u_2^{III}=u_2^{II}(x_1,x_2,x_3)+\overbrace{0}^{\mathcal{W}_2(x_1,x_2,x_3)} \tag{2.59}$$

$$u_3^{III}=u_3^{II}(x_1,x_2,x_3)+\overbrace{0}^{\mathcal{W}_3(x_1,x_2,x_3)} \tag{2.60}$$

The expression of $\mathcal{F}_1(x_2,x_3)$ and $\mathcal{F}_2(x_2,x_3)$ is given in Appendix A.1. The third order solution improves only $u_1^{III}(x_1,x_2,x_3)$ and shown by overbrace term $\mathcal{W}_1(x_1,x_2,x_3)$ in Eq. (2.58). The 1D strain energy corrected up to third order is

$$\begin{aligned}2\mathcal{U}_{1D}=&E_{11}\left(\mathcal{A}\overline{u}_1\left(x_1\right)'^{\,2}+\mathcal{I}_3\overline{u}_2\left(x_1\right)''^{\,2}+\mathcal{I}_2\overline{u}_3\left(x_1\right)''^{\,2}\right)+\frac{\pi a^3b^3G_{12}G_{13}}{a^2G_{13}+b^2G_{12}}\overline{\phi}_1\left(x_1\right)'^{\,2}\\&+\overline{\mathcal{S}}_3\overline{u}_2\left(x_1\right)'''^2+\overline{\mathcal{S}}_2\overline{u}_3\left(x_1\right)'''^2\end{aligned} \tag{2.61}$$

where,

$$\overline{\mathcal{S}}_2=\frac{\pi ab^3\left(G_{12}\left(4a^4G_{13}^2\nu_{12}^2+5b^4E_{11}^2\right)+2a^2b^2E_{11}^2G_{13}\right)}{24G_{13}\left(a^2G_{13}+3b^2G_{12}\right)};\quad \overline{\mathcal{S}}_3=\frac{\pi a^3b\left(5a^4E_{11}^2G_{13}+2a^2b^2E_{11}^2G_{12}+4b^4G_{12}^2G_{13}\nu_{13}^2\right)}{24G_{12}\left(3a^2G_{13}+b^2G_{12}\right)}$$

This third-order strain energy can be written in terms of classical 1D strain measures as

$$2\mathcal{U}_{1D}=\overline{\epsilon}^T\mathcal{K}\ \overline{\epsilon}+\overline{\epsilon}'^T\mathcal{N}\ \overline{\epsilon}' \tag{2.62}$$

where,

$$\mathcal{K} = \begin{bmatrix} \mathcal{A}E_{11} & 0 & 0 & 0 \\ 0 & \frac{\pi a^3 b^3 G_{12} G_{13}}{a^2 G_{13} + b^2 G_{12}} & 0 & 0 \\ 0 & 0 & \mathcal{I}_2 E_{11} & 0 \\ 0 & 0 & 0 & \mathcal{I}_3 E_{11} \end{bmatrix}; \; \mathcal{N} = \begin{bmatrix} 0 & 0 & 0 & 0 \\ 0 & 0 & 0 & 0 \\ 0 & 0 & \overline{\mathcal{S}}_2 & 0 \\ 0 & 0 & 0 & \overline{\mathcal{S}}_3 \end{bmatrix}$$

Now by comparing the expressions of this third order strain energy given by Eq. (2.46) and Eq.(2.62), matrices $\mathcal{K}$, $\mathcal{M}$, $\mathcal{N}$, and $\mathcal{P}$ can be extracted. Further, using these matrices and Eq. (2.49), matrices G, F, and X can be extracted. By using Eq. (2.47) the Timoshenko beam model for orthotropic beam can be written as

$$2\mathcal{U}_t = \begin{Bmatrix} \gamma_{11} \\ \kappa_1 \\ \kappa_2 \\ \kappa_3 \end{Bmatrix}^T \begin{bmatrix} \mathcal{A}E_{11} & 0 & 0 & 0 \\ 0 & J_{ort} G_{eq} & 0 & 0 \\ 0 & 0 & \mathcal{I}_2 E_{11} & 0 \\ 0 & 0 & 0 & \mathcal{I}_3 E_{11} \end{bmatrix} \begin{Bmatrix} \gamma_{11} \\ \kappa_1 \\ \kappa_2 \\ \kappa_3 \end{Bmatrix} + \begin{Bmatrix} 2\gamma_{12} \\ 2\gamma_{13} \end{Bmatrix}^T \begin{bmatrix} \mathcal{S}_2 & 0 \\ 0 & \mathcal{S}_3 \end{bmatrix} \begin{Bmatrix} 2\gamma_{12} \\ 2\gamma_{13} \end{Bmatrix} \tag{2.63}$$

with,

$$X = \mathcal{K}; \; F = [0]; \; G = \begin{bmatrix} \mathcal{S}_2 & 0 \\ 0 & \mathcal{S}_3 \end{bmatrix}; \; \mathcal{S}_2 = \frac{3\pi a^3 b E_{11}^2 G_{12} \left(3a^2 G_{13} + b^2 G_{12}\right)}{10a^4 E_{11}^2 G_{13} + 4a^2 b^2 E_{11}^2 G_{12} + 8b^4 G_{12}^2 G_{13} \nu_{13}^2};$$

$$\mathcal{S}_3 = \frac{3\pi a b^3 E_{11}^2 G_{13} \left(a^2 G_{13} + 3b^2 G_{12}\right)}{2G_{12}\left(4a^4 G_{13}^2 \nu_{12}^2 + 5b^4 E_{11}^2\right) + 4a^2 b^2 E_{11}^2 G_{13}}$$

J_{ort} and G_{eq} will be defined in the upcoming section corresponding one-dimensional constitutive law is

$$\begin{Bmatrix} F_1 \\ F_2 \\ F_3 \\ M_1 \\ M_2 \\ M_3 \end{Bmatrix} = \begin{bmatrix} \mathcal{A}E_{11} & 0 & 0 & 0 & 0 & 0 \\ 0 & \mathcal{S}_2 & 0 & 0 & 0 & 0 \\ 0 & 0 & \mathcal{S}_3 & 0 & 0 & 0 \\ 0 & 0 & 0 & J_{ort} G_{eq} & 0 & 0 \\ 0 & 0 & 0 & 0 & \mathcal{I}_2 E_{11} & 0 \\ 0 & 0 & 0 & 0 & 0 & \mathcal{I}_3 E_{11} \end{bmatrix} \begin{Bmatrix} \gamma_{11} \\ 2\gamma_{12} \\ 2\gamma_{13} \\ \kappa_1 \\ \kappa_2 \\ \kappa_3 \end{Bmatrix} \tag{2.64}$$

2.3 One-Dimensional Beam Equation

The linear one-dimensional static equilibrium equations are given as [81]

$$F' + \widetilde{k}F + f = 0 \tag{2.65}$$

$$M' + \widetilde{k}M + \widetilde{e}_1 F + m = 0 \tag{2.66}$$

Where $\widetilde{(\bullet)}_{ij} = -e_{pqr}(\bullet)_r$; $e_1 = [1 \quad 0 \quad 0]^T$ and $k = [k_1 \quad k_2 \quad k_3]^T$, k_1 represents the initial twist along x_1 and k_α represents initial curvature about x_α in undeformed basis, F and M represent the column matrix of force and moment respectively, f and m are represents the column of uniformly distributed force and moment respectively over the cantilever beam. The solution of equations (2.65) and (2.66) for prismatic beam ($k_i = 0$) is obtained by applying the boundary conditions. They are, (a) at $x_1 = 0$, rotation and displacements are zero. (b) at $x_1 = L$, concentrated force and moments i.e. $F = \overline{F}$ and $M = \overline{M}$ are applied.

$$F = \overline{F} + f(L - x_1) \tag{2.67}$$

$$M = \overline{M} + \tilde{e}_1[F(L - x_1) + \frac{f}{2}(L - x_1)^2] + m(L - x_1) \tag{2.68}$$

To calculate the 1D quantities ($\overline{u}_i,\ \overline{\phi}_1$), first of all, it is required to calculate the 1D force and moment in term of strain measures ($\overline{\gamma}_{11}, \overline{\kappa}_i$), using Eqs. (2.48, 2.64, 2.67 and 2.68). After that, by using relations (2.50) and suitable boundary conditions on the displacement field and rotations, the following expression of one-dimensional quantities are obtained

$$\overline{u}_1(x_1) = \frac{\overline{F}_1}{\pi a b E_{11}} x_1 \tag{2.69}$$

$$\overline{u}_2(x_1) = \frac{2\overline{F}_2\,(3L - x_1)\,x_1^2}{3\pi a^3 b E_{11}} + \frac{f_2\left(6L^2 - 4Lx_1 + x_1^2\right)x_1^2}{6\pi a^3 b E_{11}} + \frac{2\overline{M}_3}{\pi a^3 b E_{11}} x_1^2 + \underbrace{K_2[2\overline{F}_2 + f_2\ (2L - x_1)]x_1} \tag{2.70}$$

$$\overline{u}_3(x_1) = \frac{2\overline{F}_3\,(3L - x_1)\,x_1^2}{3\pi a b^3 E_{11}} + \frac{f_3\left(6L^2 - 4Lx_1 + x_1^2\right)x_1^2}{6\pi a b^3 E_{11}} - \frac{2\overline{M}_2}{\pi a b^3 E_{11}} x_1^2 + \underbrace{K_3[2\overline{F}_3 + f_3\ (2L - x_1)]x_1} \tag{2.71}$$

$$\overline{\phi}_1\,(x_1) = \frac{\overline{M}_1\left(a^2 G_{13} + b^2 G_{12}\right)\ x_1}{\pi a^3 b^3 G_{12} G_{13}} \tag{2.72}$$

where, $K_2 = 1/2\mathcal{S}_2$ and $K_3 = 1/2\mathcal{S}_3$

2.4 Result and Discussion

In the current work, the solution corrected up to the second order provides the 1D strain energy (Eq. (2.45)), which coincides with the classical beam theory. As it is already discussed about the rigid body like deformation terms in previous sections. By citing these

terms, the whole second-order 3D displacement field (Eqs.(2.42-2.44)) can be divided into two parts (1) rigid body-like deformation where the cross-section acts like it is rigid in its plane (2) elastic deformation where cross-section deforms elastically.

$$u_1^{II} = \underline{\overline{u}_1(x_1) - \ x_2\overline{u}_2(x_1)' - x_3\overline{u}_3(x_1)'} + \underline{\underline{\psi_{ort}(x_2,x_3)\ \overline{\phi}_1(x_1)'}} \tag{2.73}$$

$$u_2^{II} = \underline{\overline{u}_2(x_1) - x_3\overline{\phi}_1(x_1)} - \underline{\underline{\nu_{12}\ x_2\ \overline{u}_1(x_1)' + \nu_{12}x_2x_3\overline{u}_3(x_1)''}} + \underline{\underline{\frac{1}{2\mathcal{A}}\left[\nu_{12}\left(\mathcal{A}x_2^2 - \mathcal{I}_3\right) + \nu_{13}\left(\mathcal{I}_2 - \mathcal{A}x_3^2\right)\right]\overline{u}_2(x_1)''}} \tag{2.74}$$

$$u_3^{II} = \underline{\overline{u}_3(x_1) + x_2\overline{\phi}_1(x_1)} - \underline{\underline{\nu_{13}\ x_3\ \overline{u}_1(x_1)' + \nu_{13}x_2x_3\overline{u}_2(x_1)''}} - \underline{\underline{\frac{1}{2\mathcal{A}}\left[\nu_{12}\left(\mathcal{A}x_2^2 - \mathcal{I}_3\right) + \nu_{13}\left(\mathcal{I}_2 - \mathcal{A}x_3^2\right)\right]\overline{u}_3(x_1)''}} \tag{2.75}$$

the once underlined terms belong to the rigid body like deformation ($\nu_{ij} = 0$) and twice-underlined terms represent the elastic deformation of the cross-sectional plane. The 1D quantities ($\overline{u}_i$ and $\overline{\phi}_1$) are given in Eqs. (2.69-2.72). The terms except under-braces ones represent classical 1D beam model solutions for extension, bending, and torsion. The under braces terms are due to the transverse shear. The Eq. (2.72) can be written as well well-known form of classical beam solution as

$$\overline{\phi}_1(x_1) = \frac{\overline{M}_1\ x_1}{J_{ort}\ G_{eq}} \tag{2.76}$$

where J_{ort} is the Saint-Venant torsion constant which is given as

$$J_{ort} = \langle x_2^2 + x_3^2 + x_2\psi_{ort,3} - x_3\psi_{ort,2}\rangle \tag{2.77}$$

$$J_{ort} = \frac{\pi a^3 b^3 (G_{12} + G_{13})}{2(a^2 G_{13} + b^2 G_{12})} \tag{2.78}$$

The expression for the G_{eq} can be obtained by comparing the equations (2.72 and 2.76) and using expression of J_{ort} from equation (2.78) and given as

$$G_{eq} = \frac{2G_{12}G_{13}}{G_{12} + G_{13}} \tag{2.79}$$

which is nothing but the harmonic mean of the G_{12} and G_{13}, which is given as

$$\frac{2}{G_{eq}} = \frac{1}{G_{12}} + \frac{1}{G_{13}} \tag{2.80}$$

2.4.1 Special Cases

All the formulations given in the previous sections are for the generic orthotropic homogeneous beam. This formulation is equally valid for the sub-classes of the orthotropic materials (i.e. transverse- isotropic and isotropic). By applying the elastic symmetry this complete formulation can be reduced for sub-classes also. For example, let us take ψ_{ort}, to reduce this for an isotropic case, one has to replace G_{12} and G_{13} with G. The resultant

expression is given by equation (2.81), which is nothing but well well-known Saint-Venant warping function for the isotropic beam with elliptical cross-section.

$$\psi_{iso} = \frac{(b^2 - a^2)x_2x_3}{a^2 + b^2} \tag{2.81}$$

Likewise, the 3D displacement field corrected up to the second order (2.73-2.75) can be reduced for the isotropic beam. For this purpose, material symmetry has to be used (i.e. $\nu_{12} = \nu_{13} = \nu_{23} = \nu,\ G_{13} = G_{12} = G_{23} = G,\ E_{11} = E_{22} = E_{33} = E$). By applying these material symmetries and taking $\overline{F}_2 = \overline{F}_3 = f_2 = f_3 = 0$ in Eqs. (2.69-2.72) and putting final expression back to Eqs.(2.73-2.75), the following 3D displacement field for isotropic material is obtained.

$$u_1^{II} = \frac{\overline{F}_1}{E\mathcal{A}}x_1 - \frac{\overline{M}_3}{E\mathcal{I}_3}x_1x_2 + \frac{\overline{M}_2}{E\mathcal{I}_2}x_1x_3 + \psi_{iso}\,\frac{\overline{M}_1}{GJ} \tag{2.82}$$

$$u_2^{II} = -\nu x_2\frac{\overline{F}_1}{E\mathcal{A}} - x_1x_3\frac{\overline{M}_1}{GJ} - \nu x_2x_3\frac{\overline{M}_2}{E\mathcal{I}_2} + \frac{\overline{M}_3x_1^2}{2E\mathcal{I}_3} + \frac{\nu\overline{M}_3}{2E\mathcal{I}_3}\left(x_2^2 - x_3^2 + \frac{\mathcal{I}_2 - \mathcal{I}_3}{\mathcal{A}}\right) \tag{2.83}$$

$$u_3^{II} = -\nu x_3\frac{\overline{F}_1}{E\mathcal{A}} + x_1x_2\frac{\overline{M}_1}{GJ} + \nu x_2x_3\frac{\overline{M}_3}{E\mathcal{I}_3} - \frac{\overline{M}_2x_1^2}{2E\mathcal{I}_2} + \frac{\nu\overline{M}_2}{2E\mathcal{I}_2}\left(x_2^2 - x_3^2 + \frac{\mathcal{I}_2 - \mathcal{I}_3}{\mathcal{A}}\right) \tag{2.84}$$

This expression of the 3D displacement field is exactly the same as given in [36] for the isotropic homogeneous beam with elliptical cross-section. In a similar manner, the generalized Timoshenko model can be obtained for isotropic-homogeneous from (2.63) and given below. This expression is also exactly the same as given in[57].

$$2\mathcal{U}_t = \begin{Bmatrix}\gamma_{11}\\ \kappa_1\\ \kappa_2\\ \kappa_3\end{Bmatrix}^T \begin{bmatrix} E\mathcal{A} & 0 & 0 & 0\\ 0 & GJ & 0 & 0\\ 0 & 0 & E\mathcal{I}_2 & 0\\ 0 & 0 & 0 & E\mathcal{I}_3\end{bmatrix} \begin{Bmatrix}\gamma_{11}\\ \kappa_1\\ \kappa_2\\ \kappa_3\end{Bmatrix} + \begin{Bmatrix}2\gamma_{12}\\ 2\gamma_{13}\end{Bmatrix}^T \begin{bmatrix}\mathcal{S}_2 & 0\\ 0 & \mathcal{S}_3\end{bmatrix} \begin{Bmatrix}2\gamma_{12}\\ 2\gamma_{13}\end{Bmatrix} \tag{2.85}$$

with

$$\mathcal{S}_2 = \frac{3a^2\left(3a^2 + b^2\right)(1+\nu)^2G\mathcal{A}}{2\left[b^4\nu^2 + 5a^4(1+\nu)^2 + 2a^2b^2(1+\nu)^2\right]};\quad \mathcal{S}_3 = \frac{3b^2\left(a^2 + 3b^2\right)(1+\nu)^2G\mathcal{A}}{2\left[a^4\nu^2 + 5b^4(1+\nu)^2 + 2a^2b^2(1+\nu)^2\right]}$$

It is important here to note that due to the dependency of the mathematical formulation for orthotropic beam on the cross-sectional elastic constants (i.e $\nu_{12}, \nu_{13}, G_{13}, G_{12}, E_{11}$), only one sub-case is possible. This is when cross-sectional elastic constants are equal (i.e $\nu_{12} = \nu_{13} = \nu,\ G_{13} = G_{12} = G,\ E_{11} = E$) which means the cross-section is isotropic. Because of this fact, for the two sub-classes of the transverse-isotropic material beam, the complete formulation will remain the same as the orthotropic beam, while for one sub-class, it will be the same as of isotropic beam.

So this complete mathematical formulation for the generic orthotropic beam is equally valid for isotropic and transverse-isotropic beams also. Moreover, this study conveys that orthotropic as well as its sub-classes material beam, does not provide any elastic coupling.

This can be verified from 1D constitutive law (2.64), where all the one-dimensional strain measures (γ_{11}, κ_i) terms are decoupled from each other.
In the next section, results will be validated by comparing them with numerical results. As it has already been discussed these results are equally valid for sub-classes of orthotropic material, so this validation automatically validates the rest of the cases.

2.4.2 Numerical Validation

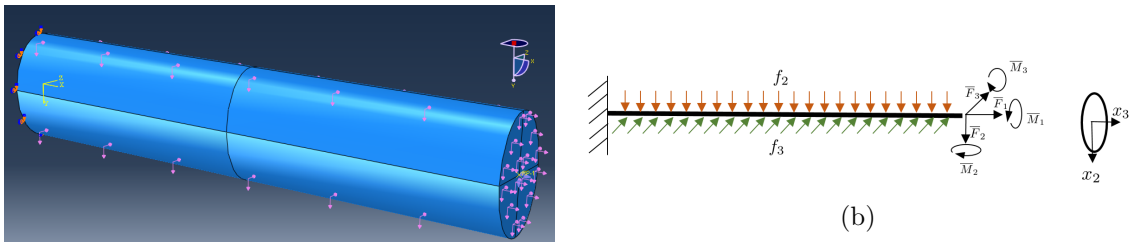

(a) (b)

Figure 2.2: (a) Abaqus model with loading and boundary conditions (b) Schematic of the beam with loading and boundary conditions

The analytical results are validated with the results of the commercially available FEM solver Abaqus. A model of a Beam of the elliptical cross-section has been developed with length $L = 1$ m, semi-major axis $a = 10$ cm, and semi-minor axis $b = 7$ cm minor axis of the beam respectively. This beam is fixed at one end while free at the other end. The origin of the coordinate system is located on the centroid of the beam at the fixed end. The coordinate axis x_1 is aligned along the centroidal axis of the beam, while the coordinate axes x_2 and x_3 are aligned along with the major and the minor axis of the beam, respectively. A twisting moment $(\overline{M}_1)$ and bending moments $(\overline{M}_2$ & $\overline{M}_3)$ are applied at the free end with the magnitude of $5 \times 10^4\ N - m$. The distributed moment (m) is taken as zero. Axial surface traction $(\widehat{F}_1\ )$ of magnitude $2.27364 \times 10^9\ N/m^2$ and tangential traction $(\widehat{F}_2$ & $\widehat{F}_3)$ of magnitude $2.27364 \times 10^7\ N/m^2$ in the direction of x_2 and x_3 respectively, has been applied at the free end cross-section. On the lateral surface of the beam, surface traction $(\widehat{f}_2$ & $\widehat{f}_3)$ of magnitude 929023 N/m^2 has been applied in the x_2 and x_3 direction respectively. The Abaqus beam model, featuring all the discussed applied loads, is depicted in Fig. 2.2a. Here, it should be noted that the $x - y - z$ coordinates of Abaqus correspond to $x_1 - x_2 - x_3$. The relation between $\widehat{F}_i$ and $\overline{F}_i$, between $\widehat{f}_\alpha$ and f_α

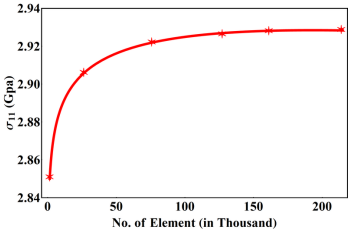

Figure 2.3: Convergence plot of FEA simulaion

is given as

$$\overline{F}_i = \langle \widehat{F}_i \rangle \qquad f_\alpha = \oint_{\partial\Omega} \widehat{f}_\alpha \, ds \tag{2.86}$$

Here $\partial\Omega$ represents the lateral surface of the beam. Using relation (2.86) $\overline{F}_1 \approx 5 \times 10^7$ N, $\overline{F}_\alpha \approx 5 \times 10^5$ N and $f_\alpha \approx 5 \times 10^5$ N/m. The schematic of 1D beam with all applied 1D loads is depicted in Fig. 2.2b. The meshing has been done using 8-node linear brick, reduced integration, hourglass control (C3D8R) element.

The convergence plot of FEA results is provided in Fig. 2.3. Here σ_{11} is plotted against the number of elements in the meshed beam model. In the present case, the mesh size is taken 5 mm, which corresponds to the 214000 elements in the meshed beam model. From Fig. 2.3, it can be observed for this mesh size, the FEA solution has converged. For the comparison of analytical and FEA solutions, absolute and relative error plots have been used. These error terms are defined as

$$\text{Absolute Error} = |\text{FEM result} - \text{Present result}| \tag{2.87}$$

$$\text{Relative Error} = \left| \frac{\text{FEM result} - \text{Present result}}{\text{FEM result}} \right| \tag{2.88}$$

The material properties used for the orthotropic beam have been provided in table (2.1)

Before further discussion, it should be noted that to obtain error surface plots, the

Table 2.1: Material properties of the orthotropic beam

E_{11} (GPa)	E_{22} (GPa)	E_{33} (GPa)	G_{12} (GPa)	G_{13} (GPa)	G_{23} (GPa)	ν_{12}	ν_{13}	ν_{23}
181	133	103	7.17	7	3	0.28	0.28	0.6

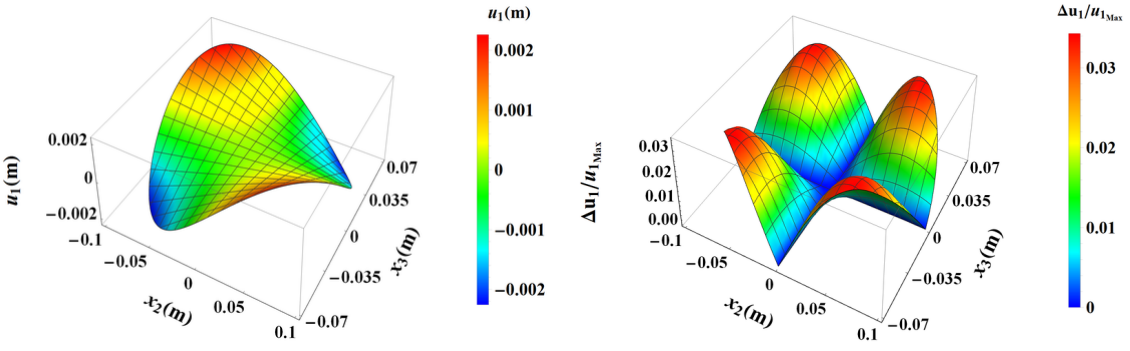

(a) (b)

Figure 2.4: Surface plot for out-of-plane warping obtained analytically and absolute error between analytical and FEM results (a) analytical result plot (b) absolute error plot

analytical results are calculated at the nodes obtained from the FEA model. In Fig. 2.4 surface plot for out-of-plane warping is given. To obtain these plots, only twisting moment ($\overline{M}_1$) is considered while all other loading is taken zero in Eq. (2.58). This

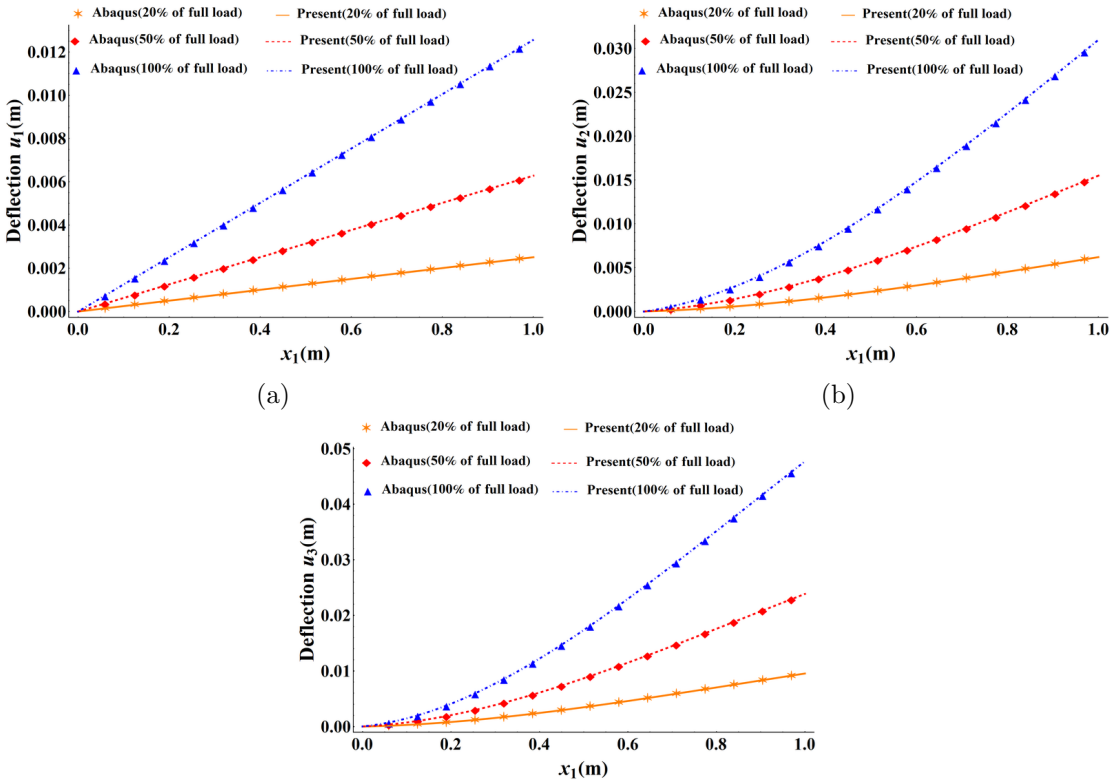

Figure 2.5: Deflection of the beam along the centroidal axis for three different loads (a) axial stretch (b) deflection in x_2 direction (c) deflection in x_3 direction

surface plot is taken for the mid-cross-sectional plane of the beam. Fig. 2.4a is due to the analytical result of the current study and Fig. 2.4b is the surface plot for the normalized absolute error between analytical and FEM results. We have used the maximum value of out-of-plane warping obtained from FE analysis to normalize the error. It can be seen from this normalized error plot 2.4b that the magnitude of absolute error is less than 3% of maximum out-of-plane warping value. This signifies that the difference between FEA and current study results is very small.

In Fig. 2.5, curves showing the beam axis deflection in three coordinate directions have been plotted. Each sub-figure contains three curves corresponding to three loading conditions. These conditions are when the loads depicted in Fig. 2.2b are at 20%, 50%, and 100% of their maximum magnitudes. The maximum value of each applied load is provided earlier. Upon observing these plots, it can be inferred that the analytical results of the current study are in excellent agreement with the FEA results.

The 3D displacement field over the mid-cross-sectional plane of the beam is shown in Fig. 2.6. In this, surface plots 2.6a, 2.6c, and 2.6e are from the analytical results while surface plots 2.6b, 2.6d, and 2.6f are due to relative error. The displacement field plotted in this figure is corrected up to the third order and given by Eqs. (2.58-2.60) and the 1D quantities (2.69-2.72). All loading conditions discussed earlier have been applied for these surface plots. It can be seen from the error surface plots that the maximum relative error is 0.4% for u_1 and 1% for u_2 and u_3.

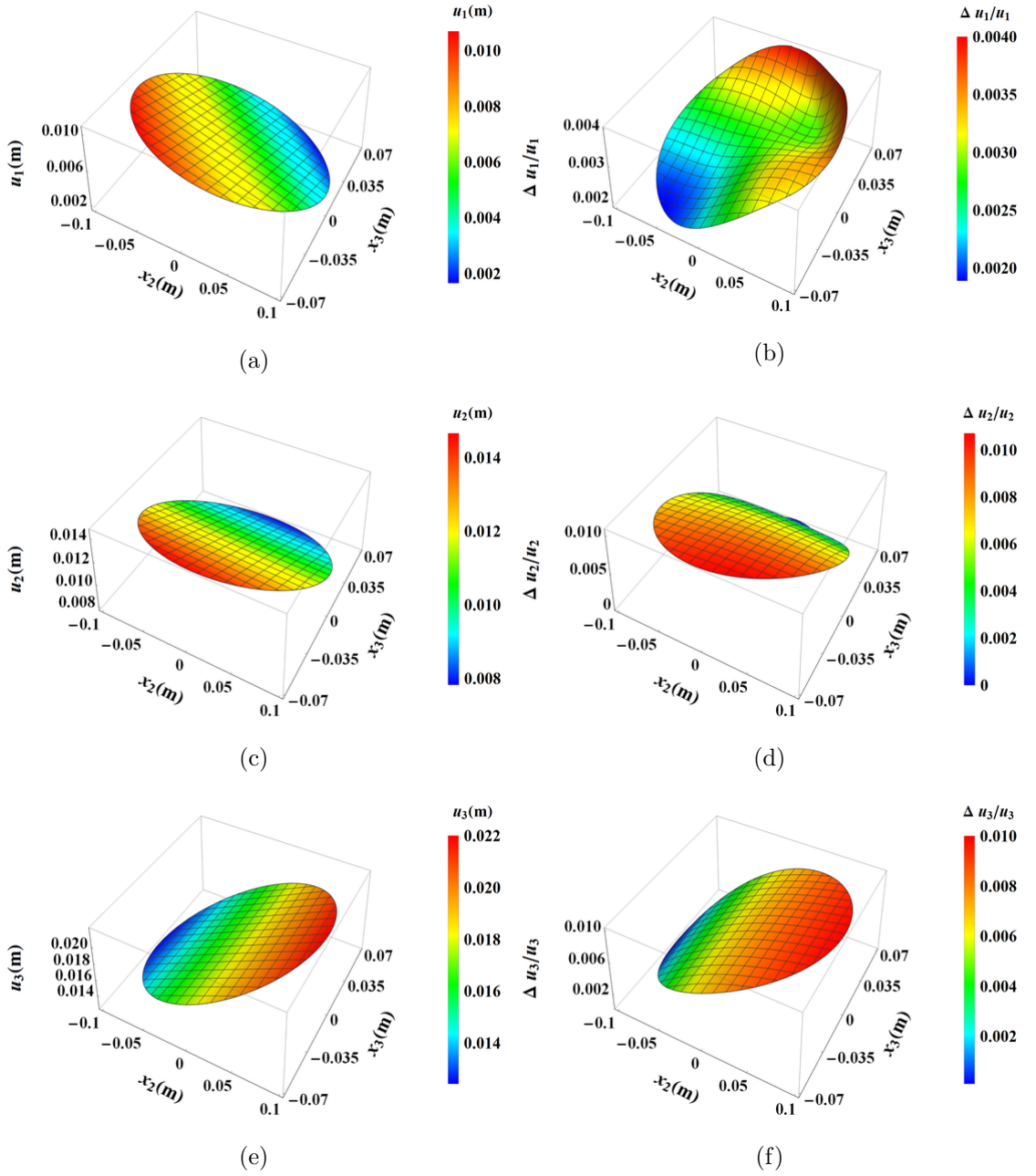

Figure 2.6: Surface plot of the displacement field and relative error w.r.t. FEM results (a, c, e) displacement along x_1, x_2 and x_3 coordinate axis due to analytical result, (b, d, f) relative error respectively

The surface plot of the 3D stress field corrected up to the third order is given in Fig. 2.7. Analytical results of this stress field are shown in surface plots 2.7a, 2.7c, and 2.7e while their corresponding absolute relative error plot is given in surface plots 2.7b, 2.7d, and 2.7f. Here plot for only three stress components (σ_{11}, σ_{12} and σ_{13}) are shown as other three stress components (σ_{22}, σ_{33} and σ_{23}) are obtained as zero which corresponds to the assumption of classical beam model.

Surface plot 2.7b suggests that the analytical result for the stress component (σ_{11}) of the current work is in very close agreement with FEM results. The maximum relative error

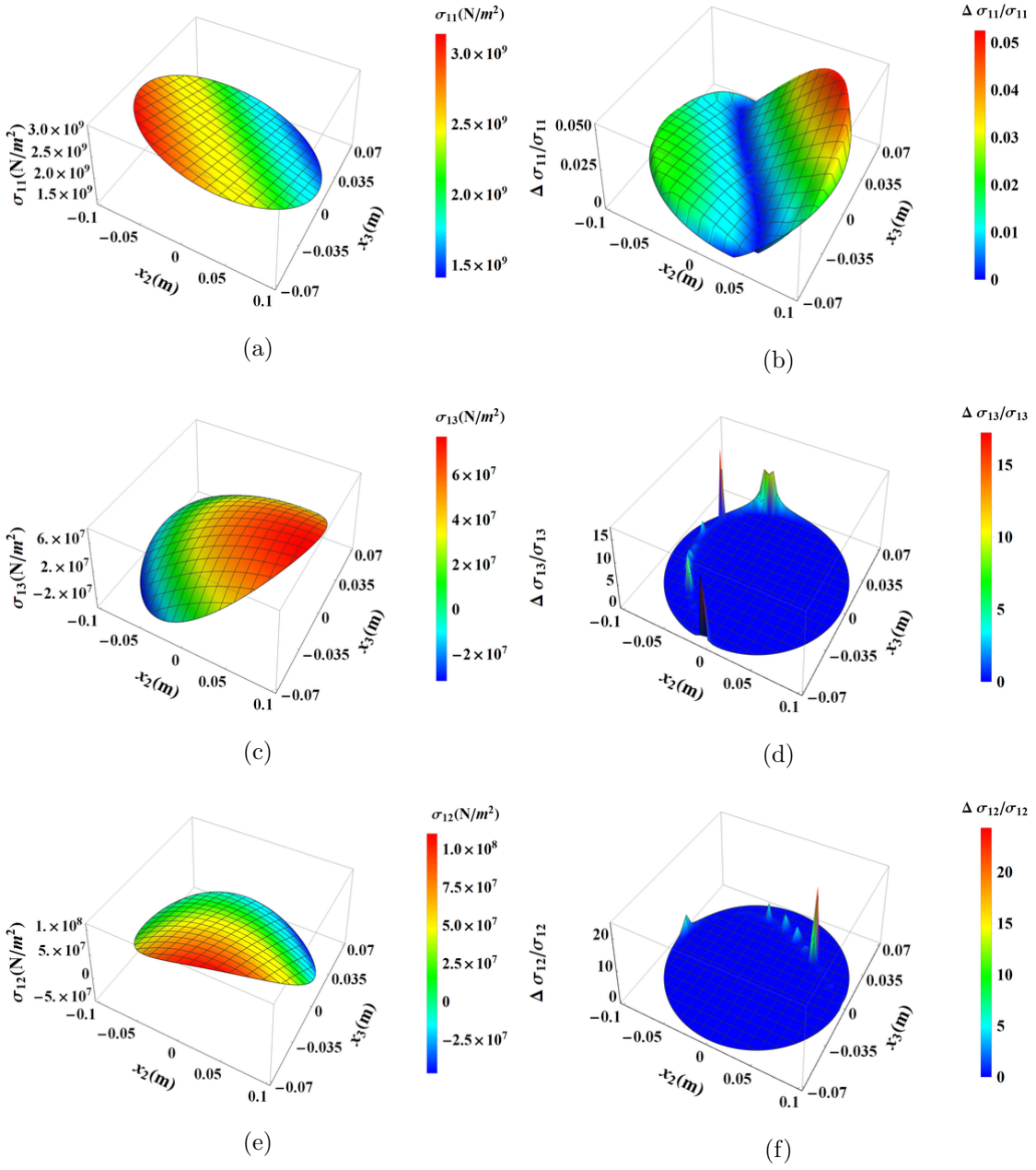

Figure 2.7: Surface plot of stress field and relative error w.r.t. FEM result (a, c, e) analytical plot of σ_{11}, σ_{13} and σ_{12} , (b, d, f) relative error plot respectively

for this stress component obtained 0.05, while for other stress components (σ_{13} and σ_{12}) this error seems to be very large, as can be seen from the surface plots 2.7f and 2.7d. However, this is not true for the whole domain as this is a localized phenomenon and occurs at some nodes of the domain. If we exclude the peak region, the relative error is within 10% and this can be confirmed from surface plots 2.7d and 2.7f. By inspecting these figures, it is observed that the peaks occur along a curve. Careful observation of surface plots 2.7c and 2.7e suggests that the magnitude of the stress components (σ_{13} and σ_{12}) is zero along or in the vicinity of this curve. The accuracy of stress components (σ_{13} and σ_{12}) compared to FEA results are assessed through normalized absolute error

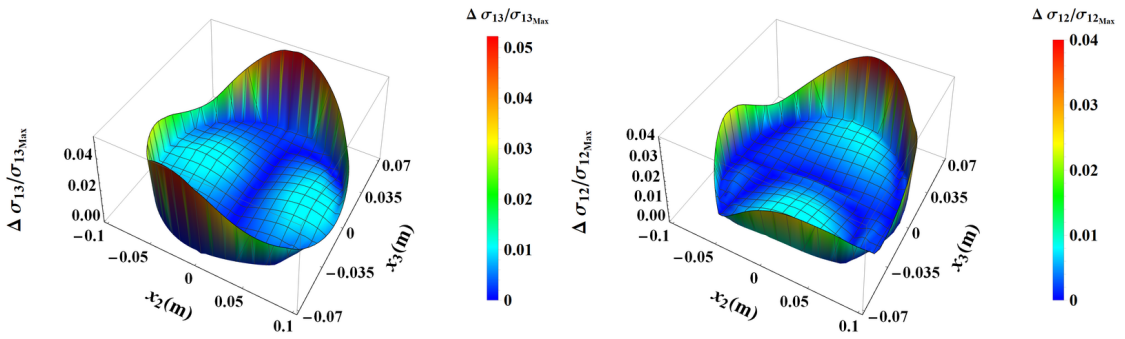

(a) (b)

Figure 2.8: Normalized absolute error of (a) σ_{13} (b) σ_{12}

plots, as shown in Fig. 2.8. The maximum values of the corresponding stress components obtained from the FE analysis are used for normalization. Upon examining these plots, it is evident that the maximum absolute error between the current results and FEA results is approximately 5% of $\sigma_{13_{Max}}$ for σ_{13} and about 4% of $\sigma_{12_{Max}}$ for σ_{12}. This value lies along the boundary curve of the cross-section, except at the boundary curve this error is less than 1% of the corresponding maximum stress.

Now we will discuss the reason behind the peaks that appeared in these plots. The

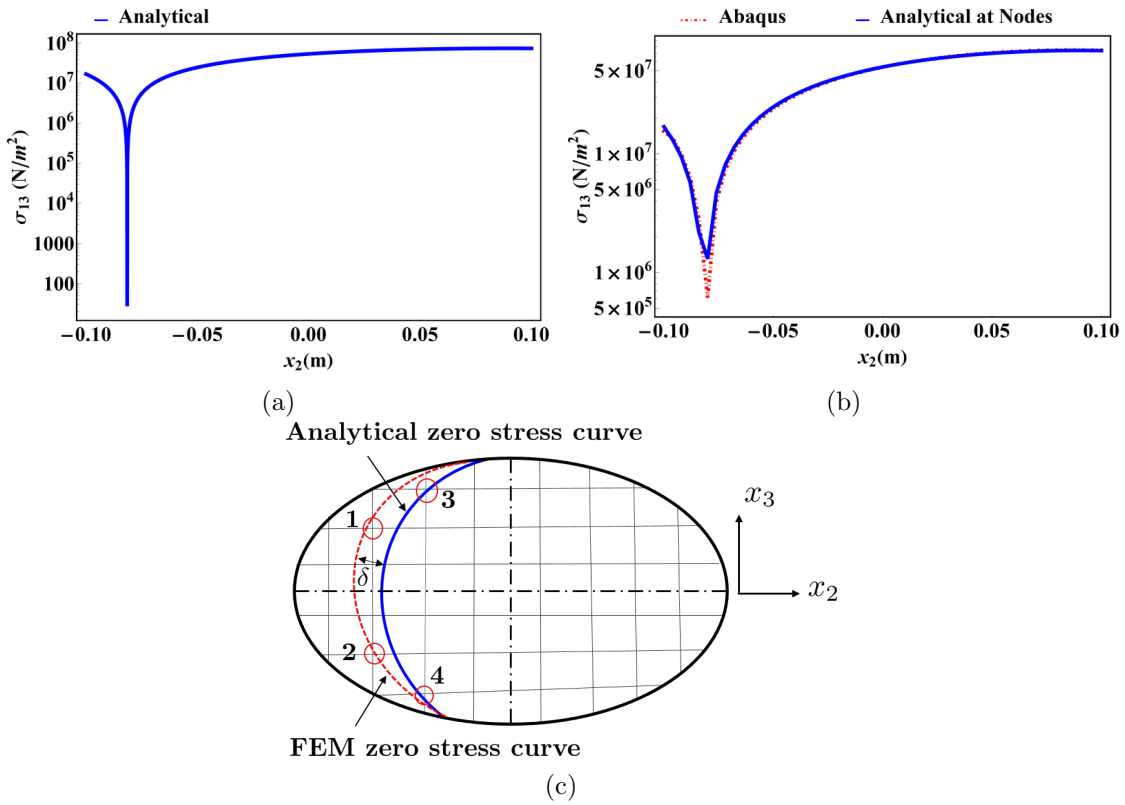

(a) (b)

(c)

Figure 2.9: (a) Linear-Log plot of stress (σ_{13}) plot along the major axis of cross-section obtained analytically, (b) Linear-Log plot of stress (σ_{13}) plot along the major axis of the cross-section obtained from FEM and analytically on the same nodes (c) schematic of the meshed cross-section with zero value curves

occurrence of the peaks can be understood by Fig. 2.9. In Figs. 2.9a and 2.9b Log-Linear plot of the absolute magnitude of stress component σ_{13} along the major axis of the cross-section is plotted. The first is plotted using the current analytical expression, while the second is from the FEA result and analytical result at the same FEA nodes. From analytical plot 2.9a, it can be observed that the stress value suddenly drops to zero within a very narrow region. Due to the small error between the results obtained from the two approaches, the zero stress curve will be different for these two approaches as shown in schematic Fig. 2.9c. Hence in this narrow region, the absolute error will be significant or very large depending on the position of nodes w.r.t. zero stress curves as shown in Fig. 2.9b. It should also be remembered that FEA results are available for the nodes, and these nodes may or may not lie on this zero-stress curve. Depending on the position of nodes w.r.t the analytical and FEA zero stress curves, different types of peaks are possible, and the formation of these peaks can be understood by relative error Eq.(2.88). Whenever a node occurs in the vicinity of the FEA zero stress curve, the absolute error between FEA and analytical results will be significant, as discussed above, and the FEA result value will approach zero. In this case, the calculated relative error will be very high; in fact, this relative error can be as high as infinity, depending on the closeness of the node to the FEA zero stress curve. In schematic Fig. 2.9c, nodes 1 and 2 represent such nodes. Similarly, whenever a node occurs in the vicinity of the analytical zero stress curve, the absolute error for such nodes will also have a significant value. However, in

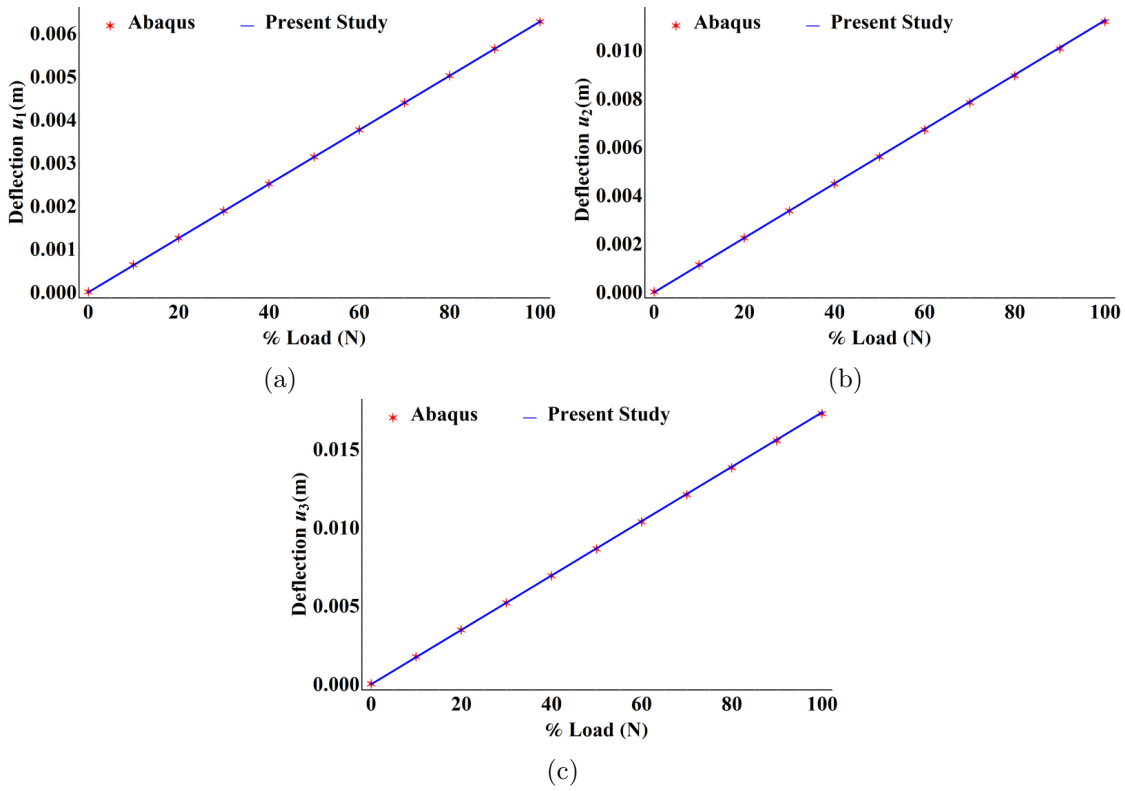

Figure 2.10: Deflection of mid-node vs% Load plot for all load condition (a) deflection in x_1 direction (b) deflection in x_2 direction and (c) deflection in x_3 direction

this case, the analytical value will approach zero, while FEA results will have a significant value. For such nodes, the relative error will be unity. Nodes 3 and 4 shown in schematic Fig. 2.9c represent such nodes.
In Fig. 2.10 the 3D displacement field for mid node ($x_1 = 0.5$ m and $x_2 = x_3 = 0$) of the beam is plotted w.r.t. loads. In this case, all loads are applied, which are discussed earlier. These figures suggest the FEA and the analytical results are in great agreement with each other. This also confirms the linear dependency of the displacement field on applied loads, which is already established in the analytical formulation.

The numerical validation of the current 3D displacement and stress field has

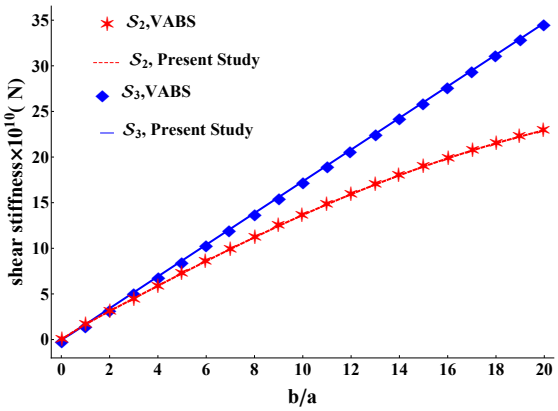

(a)

Figure 2.11: Variation of shear stiffness $\mathcal{S}_2$ and $\mathcal{S}_3$ w.r.t. ratio of cross-section dimension (b/a) with a=1

been presented in the above discussion, which shows that current and FEA results are in great agreement. Although the presented 3D displacement and strain field is corrected up to the third order that includes transverse shear deformation, assessing the improvement over the classical beam model after shear deformation is included becomes important. For this purpose, the closed-form expression of shear stiffness constants ($\mathcal{S}_2$ and $\mathcal{S}_3$) has been verified by comparing it with the VABS results [62]. Material properties use for this particular result are $E_{11} = 141.96$ GPa, $E_{22} = E_{33} = 9.7901$ GPa, $G_{12} = G_{13} = 6.1360$ GPa, $G_{23} = 5.5155$ GPa, $\nu_{12} = \nu_{13} = 0.42$ and $\nu_{23} = 0.54$. Shear stiffness constants $\mathcal{S}_2$ and $\mathcal{S}_3$ have been plotted w.r.t. b/a with $a = 1$ m. The corresponding plot is given in Fig. 2.11. This figure shows that the numerical values of shear stiffness constants ($\mathcal{S}_2$ and $\mathcal{S}_3$) obtained from the presented closed-form solution and VABS are in very close agreement. Hence, it validates the current close-form solution.

The expression of shear stiffness constants reveals that these are the function of cross-sectional dimensions (a and b) and material properties (E_{11}, G_{12}, G_{13}, ν_{12} and ν_{13}). The variation of shear stiffness constants w.r.t. these geometric and material parameters have been studied and corresponding surface plots are provided in Fig. 2.12 and Fig. 2.13. In the Fig 2.12, $\mathcal{S}_2$ and $\mathcal{S}_3$ are plotted against G_{12} and G_{13} for three different values of b/a ratio with $a = 1$ m. It can be observed that as the value b/a ratio increased, the

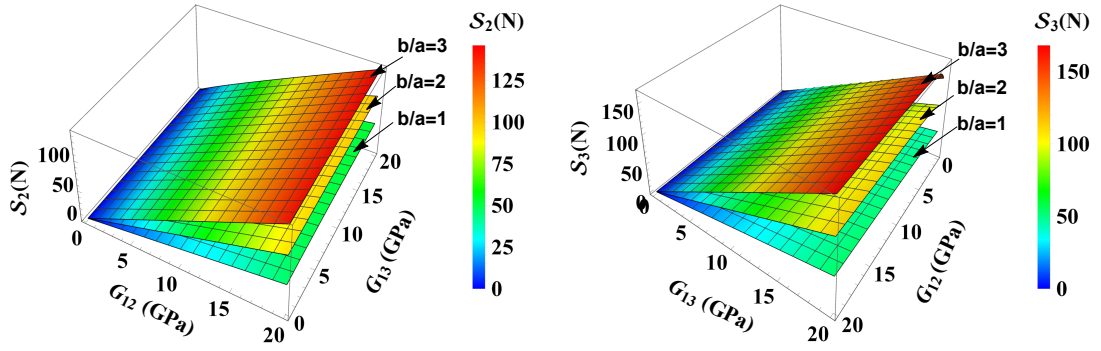

(a) (b)

Figure 2.12: Variation of shear stiffness $\mathcal{S}_2$ and $\mathcal{S}_3$ w.r.t. shear modulus for different b/a for $a = 1$ m

value of both the stiffness constants also increased for fixed G_{12} and G_{13}. From Fig. 2.12a, it can be seen that for given b/a ratio $\mathcal{S}_2$ linearly varies with G_{12} while it does not change significantly with G_{13}. Hence, apparently $\mathcal{S}_2$ does not depends on the G_{13}. From Fig. 2.12b, similar observation can be made for $\mathcal{S}_3$, in this case $\mathcal{S}_3$ linearly varies with G_{13} and does not change significantly with G_{12}. Hence, it can be concluded that $\mathcal{S}_3$ apparently does not depend on the G_{12}. One more observation can be made from Fig. 2.12b that shear stiffness constant $\mathcal{S}_3$ varies slightly for smaller value of G_{12} at a higher value of b/a ratio, which gets saturated as G_{12} increases. A similar trend is observed for $\mathcal{S}_2$ for smaller G_{13} when the b/a ratio is less than unity.

Fig. 2.13, both the shear stiffness constants have been plotted against E_{11} for three

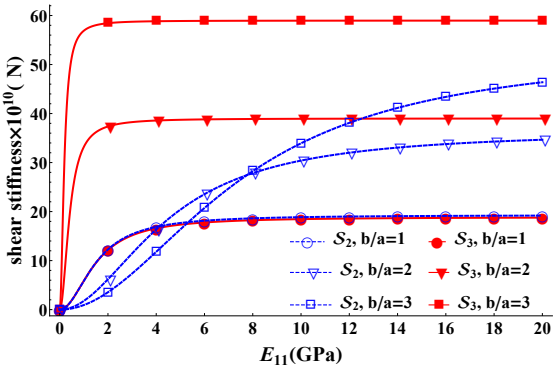

(a)

Figure 2.13: Variation of shear stiffness $\mathcal{S}_2$ and $\mathcal{S}_3$ w.r.t. young modulus for different b/a for $a = 1$ m

different values of b/a ratio. Here, from this figure, it can be observed that the value of both the shear stiffness constants increased with the increment in the b/a ratio. However, this change is different for both the shear stiffness constants. $\mathcal{S}_3$ increases linearly while $\mathcal{S}_2$ shows non-linear trend. It can also be confirmed from Fig. 2.11. For a fixed b/a ratio, both the stiffness constants increase with E_{11} and get saturated after a specific value of E_{11}. It can be observed that the saturation point of $\mathcal{S}_2$ shifts towards a higher value of

E_{11} as the b/a ratio increases. Contrary to this observation, for $\mathcal{S}_3$, saturation points shift towards lower E_{11} as the b/a ratio increases. It is important to note here that saturation of $\mathcal{S}_3$ is achieved at a very small value of E_{11} while $\mathcal{S}_2$ saturates at a very high value of E_{11} for b/a greater than unity. This trend reverses if plots are taken w.r.t. a/b with $b = 1$. It happens because of the symmetry i.e. $\mathcal{S}_3$ can be obtained from $\mathcal{S}_2$ if G_{12}, ν_{12} and a are interchanged with G_{13}, ν_{13} and b respectively.

The effect of transverse shear stiffness constants ultimately reflects on the deflection

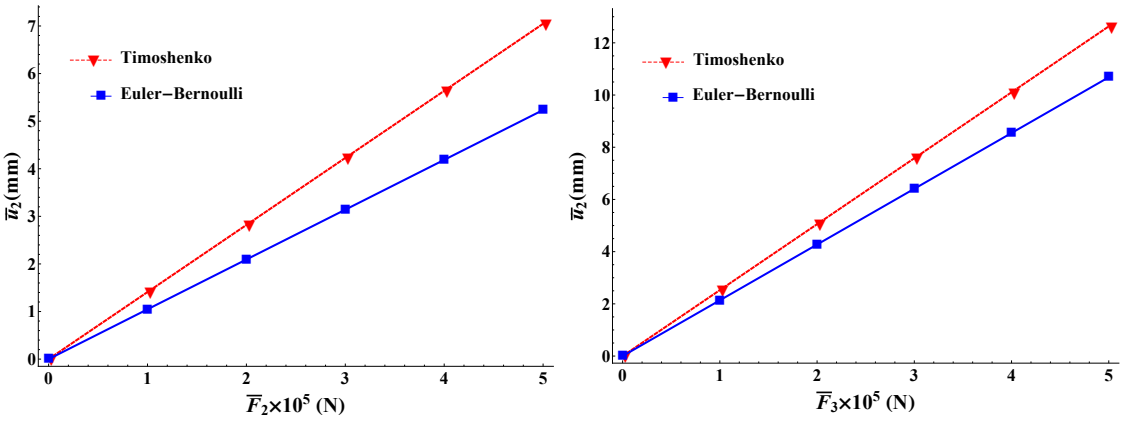

Figure 2.14: 1D displacement predicted from Classical and Timoshenko beam model

in the transverse direction. 1D deflection ($\overline{u}_2$ and $\overline{u}_3$) of the beam obtained from Euler-Bernoulli and Timoshenko beam model is plotted against transverse shear load ($\overline{F}_2$ and $\overline{F}_3$) and these plots are provided in Fig. 2.14. The Eqs. (2.70 and 2.71) have been used to get these plots. It has already been discussed that the underbrace terms in these equations are due to the transverse shear. These terms can be divided into two parts (i) constant multiple K_α ($\alpha = 2, 3$) having unit N^{-1} (ii) term related to force and axial coordinate x_1. In fact K_α is function of $\mathcal{S}_\alpha$ and related as $K_\alpha = (2\mathcal{S}_\alpha)^{-1}$. Hence, the value of K_α depends on the cross-sectional geometry and material properties of the beam. Fundamentally, the value of K_α governs the difference in deflection of the beam obtained from the Euler-Bernoulli and Timoshenko Beam model. From Fig. 2.14, it can be seen that the deflection predicted by the Timoshenko beam model is more than the deflection predicted by the Euler-Bernoulli beam model. This observation suggests that the Euler-Bernoulli beam model is stiffer than the Timoshenko beam model. From Eqs. (2.70 and 2.71) it can be observed that for $K_\alpha = 0$ Timoshenko beam model will reduce to Euler-bernoulli beam model. This condition corresponds to infinite transverse shear stiffness ($\mathcal{S}_\alpha = \infty$); in other words, the Euler–Bernoulli beam model is infinitely stiff in transverse shear.

2.5 Concluding Remarks

In this chapter, we have provided an analysis of a homogeneous-orthotropic beam with an elliptical cross-section. Solutions have been presented for both the Classical and

Timoshenko-like beam models. Closed-form analytical expressions for the 3D displacement field, stress/strain field, and 1D field variables have been derived. While these solutions are specific to homogeneous-orthotropic materials, they can be adapted for transversely isotropic and homogeneous cases by applying elastic symmetry conditions. The 1D constitutive law suggests that these material beams lack elastic coupling characteristics. Furthermore, a comparison of these analytical results with FEA results demonstrates a close agreement between the results of the two approaches.

Chapter 3

Anisotropic and Monoclinic Homogeneous Beam Analysis

In the previous chapter 2, analysis was provided for orthotropic material beam, which is also valid for beams having material anisotropy levels lower than orthotropy. This chapter focuses on the analysis of the beam made of materials having anisotropy level higher than orthotropy, i.e., complete anisotropic and monoclinic materials. The solution methodology will remain the same as provided in the chapter 2. The only difference is that in this chapter semi-analytical approach will be used because of the increased complexity. Besides, this chapter provides the analysis for the Classical beam model only. The main objective of this chapter is to explore the elastic coupling in beam-like structures made of these materials. However, other field variables have also been obtained. The analysis in the previous chapter 2 showed that no elastic coupling is available for orthotropic material beams. This chapter first provides the analysis of complete anisotropic material beams, followed by the analysis of monoclinic material beams. Numerical validation of current results is provided for each case under consideration.

3.1 Anisotropic Homogeneous Beam Analysis

Anisotropic materials are defined by 21 independent elastic constants. Hence, the stiffness matrix for these materials is a fully populated 6×6 matrix given by Eq. (2.8). This makes the coupled Euler-Lagrange equations and associated boundary conditions obtained after the application of VAM very complex and lengthy, which cannot be solved analytically with the currently available resources. Hence, these are solved by taking a semi-analytical approach. In this approach, the elastic constants are replaced by their numerical value instead of keeping them in symbolic form. (This semi-analytical approach will be applied from first-order approximation onward. Zeroth order solution is obtained through analytical approach.) Though the solution obtained using this approach will not provide information about the effect of elastic constants on the results, it provides information about the elastic coupling in the anisotropic beams. Moreover, the closed-form solution for the 3D displacement/stress/strain field can be obtained, equivalent to the analytical solution for that particular anisotropic material.

In this semi-analytical approach, the elastic constants of the stiffness matrix (2.8) are replaced by numerical values and the resultant stiffness matrix for this case is given by Eq. (3.1). In this equation, P is a scalar multiplier and has a value of 10^9. The elastic

constants of this stiffness matrix are arbitrarily chosen in such a way that this matrix remains positive definite.

$$C = \begin{bmatrix} 220 & 58 & 50 & 32 & 22 & 38 \\ & 200 & 52 & 30 & 26 & 20 \\ & & 190 & 22 & 28 & 26 \\ & & & 110 & 34 & 36 \\ & \text{sym.} & & & 100 & 28 \\ & & & & & 90 \end{bmatrix} \times P \tag{3.1}$$

3.1.1 Cross-sectional Analysis

As mentioned above, zeroth order approximate solution is obtained analytically. The Euler-Lagrange equations and boundary conditions for this case are given by Eqs. (2.11-2.13) and Eqs.(2.11-2.13) respectively. The zeroth order approximate solution is given by Eqs. (2.17-2.19). As already discussed in chapter 2, this solution represents rigid body-like deformation of the beam cross-section and depends on the axial coordinate (x_1) only. The first-order and second-order solutions are obtained by using a semi-analytical approach. A detailed discussion is provided in the following sub-sections.

First order approximation

In order to obtain the first-order approximate results using VAM, it is required to consider the strain energy corrected up to order $O\left(\mu\varepsilon^2(h/L)^2\right)$. This required energy is obtained by perturbing the zeroth order solution and it is given as

$$u_i^I = u_i^0 + v_i(x_1, x_2, x_3) \tag{3.2}$$

where $v_i(x_1, x_2, x_3)$ are asymptotically smaller than u_i^0. For the definiteness of the solution, $v_i(x_1, x_2, x_3)$ is subjected to four constraints. These constraints provides the interpretation of 1D unknown functions $\left(\overline{u}_i(x_1) \text{ and } \overline{\phi}_1(x_1)\right)$. These constraints are chosen as

$$\langle v_i \rangle = 0 \qquad \langle v_{3,2} - v_{2,3} \rangle = 0 \tag{3.3}$$

application of these constraints to Eq. (2.20) and using Eqs. (2.17-2.19), provides the relation between 1D unknown functions and 3D displacement fields and is given as follows

$$\begin{aligned} \mathcal{A}\ \overline{u}_i(x_1) &= \langle\ u_i^I\ \rangle \\ \mathcal{A}\ \overline{\phi}_1(x_1) &= \frac{1}{2}\langle\ u_{3,2}^I - u_{2,3}^I\ \rangle \end{aligned} \tag{3.4}$$

Here $\mathcal{A}$ is the cross-sectional area. The Eq. (3.4) suggests that the 1D displacement and rotation are the average of 3D displacement and rotation over the cross-section. The

perturbed displacement field (3.2), provides following modified strain field

$$\begin{aligned}
\Gamma^I_{11} &= \overline{u}_1\,(x_1)' + v_1' \\
\Gamma^I_{22} &= v_{2,2} \\
\Gamma^I_{33} &= v_{3,3} \\
\Gamma^I_{23} &= v_{2,3} + v_{3,2} \\
\Gamma^I_{13} &= \overline{u}_3\,(x_1)' + x_2\overline{\phi}_1\,(x_1)' + v_{1,3} + v_3' \\
\Gamma^I_{12} &= \overline{u}_2\,(x_1)' - x_3\overline{\phi}_1\,(x_1)' + v_{1,2} + v_2'
\end{aligned} \tag{3.5}$$

This modified strain field (3.5) provides the required first-order strain energy. This strain energy is minimized using the variational principle to give the following Euler-Lagrange equations.

$$\begin{aligned}
&45v_{1,22} + 28v_{1,23} + 50v_{1,33} + 10v_{2,22} + 31v_{2,23} + 17v_{2,33} \\
&\qquad + 18v_{3,22} + 30v_{3,23} + 14v_{3,33} = 0
\end{aligned} \tag{3.6}$$

$$\begin{aligned}
&5\overline{\phi}_1\,(x_1)' - 10v_{1,22} - 31v_{1,23} - 17v_{1,33} - 100v_{2,22} - 30v_{2,23} \\
&\qquad - 55v_{2,33} - 15v_{3,22} - 81v_{3,23} - 11v_{3,33} = 0
\end{aligned} \tag{3.7}$$

$$\begin{aligned}
&4\overline{\phi}_1\,(x_1)' + 18v_{1,22} + 30v_{1,23} + 14v_{1,33} + 15v_{2,22} + 81v_{2,23} \\
&\qquad + 11v_{2,33} + 55v_{3,22} + 22v_{3,23} + 95v_{3,33} = 0
\end{aligned} \tag{3.8}$$

with associated boundary conditions

$$\begin{aligned}
&n_2\Big[19\overline{u}_1\,(x_1)' + 45\overline{u}_2\,(x_1)' + 14\overline{u}_3\,(x_1)' + (14x_2 - 45x_3)\,\overline{\phi}_1(x_1)' \\
&\quad + 45v_{1,2} + 14v_{1,3} + 10v_{2,2} + 18v_{2,3} + 18v_{3,2} + 13v_{3,3}\Big] \\
&+ n_3\Big[11\overline{u}_1\,(x_1)' + 14\overline{u}_2\,(x_1)' + 50\overline{u}_3\,(x_1)' + 2\,(25x_2 - 7x_3)\,\overline{\phi}_1(x_1)' \\
&\quad + 14v_{1,2} + 50v_{1,3} + 13v_{2,2} + 17v_{2,3} + 17v_{3,2} + 14v_{3,3}\Big] = 0
\end{aligned} \tag{3.9}$$

$$\begin{aligned}
&n_2\Big[29\overline{u}_1\,(x_1)' + 10\overline{u}_2\,(x_1)' + 13\overline{u}_3\,(x_1)' + (13x_2 - 10x_3)\,\overline{\phi}_1(x_1)' \\
&\quad + 10v_{1,2} + 13v_{1,3} + 100v_{2,2} + 15v_{2,3} + 15v_{3,2} + 26v_{3,3}\Big] \\
&+ n_3\Big[16\overline{u}_1\,(x_1)' + 18\overline{u}_2\,(x_1)' + 17\overline{u}_3\,(x_1)' + (17x_2 - 18x_3)\,\overline{\phi}_1(x_1)' \\
&\quad + 18v_{1,2} + 17v_{1,3} + 15v_{2,2} + 55v_{2,3} + 55v_{3,2} + 11v_{3,3}\Big] = 0
\end{aligned} \tag{3.10}$$

$$\begin{aligned}
&n_2\Big[16\overline{u}_1\,(x_1)' + 18\overline{u}_2\,(x_1)' + 17\overline{u}_3\,(x_1)' + (17x_2 - 18x_3)\,\overline{\phi}_1(x_1)' \\
&\quad + 18v_{1,2} + 17v_{1,3} + 15v_{2,2} + 55v_{2,3} + 55v_{3,2} + 11v_{3,3}\Big] \\
&+ n_3\Big[25\overline{u}_1\,(x_1)' + 13\overline{u}_2\,(x_1)' + 14\overline{u}_3\,(x_1)' + (14x_2 - 13x_3)\,\overline{\phi}_1(x_1)' \\
&\quad + 13v_{1,2} + 14v_{1,3} + 26v_{2,2} + 11v_{2,3} + 11v_{3,2} + 95v_{3,3}\Big] = 0
\end{aligned} \tag{3.11}$$

solution of Eqs. (3.6-3.8) satisfying boundary conditions (3.9-3.11) and constraints (3.3) provides the first order approximate solution v_i. The displacement field corrected up to the first order is given in the following equations.

$$u_1^I = \overline{u}_1(x_1) \underbrace{- x_2\overline{u}_2(x_1)' - x_3\overline{u}_3(x_1)' + \psi_{aniso}(x_2,x_3)\ \overline{\phi}_1(x_1)' + \mathcal{F}_1^1(x_2,x_3)\ \overline{u}_1(x_1)'}_{v_1(x_1,x_2,x_3)} \quad (3.12)$$

$$u_2^I = \overline{u}_2(x_1) - x_3\overline{\phi}_1(x_1) \underbrace{+\mathcal{F}_1^2(x_2,x_3)\ \overline{u}_1\,(x_1)' + \mathcal{F}_2^2(x_2,x_3)\overline{\phi}_1(x_1)'}_{v_2(x_1,x_2,x_3)} \quad (3.13)$$

$$u_3^I = \overline{u}_3(x_1) + x_2\overline{\phi}_1(x_1) \underbrace{+\mathcal{F}_1^3(x_2,x_3)\ \overline{u}_1\,(x_1)' + \mathcal{F}_2^3(x_2,x_3)\overline{\phi}_1(x_1)'}_{v_3(x_1,x_2,x_3)} \quad (3.14)$$

In the above Eqs. (3.12-3.14), underbraces terms represent the first-order approximate results (v_i). The 2D functions used in the underbraces terms are provided in Appendix B.1.1. The terms $x_2\overline{u}_2(x_1)'$ and $x_3\overline{u}_3(x_1)'$ in Eq. (3.12) represent the displacement due to the rigid body like rotation of cross-sectional plane about x_3 and x_2 axis respectively resultant from the bending of the beam. The other terms of the first-order approximation (v_i) represent the displacement due to the deformation of the cross-sectional plane. The term $\psi_{aniso}\overline{\phi}_1(x_1)'$ represents the out-of-plane deformation due to the rotation and ψ_{aniso} is the Saint-Venant-like warping function for anisotropic beam. Similarly, $\mathcal{F}_1^2\ \overline{u}_1\,(x_1)'$ and $\mathcal{F}_1^3\ \overline{u}_1\,(x_1)'$ represents the in-plane deformation of the cross-sectional plane due to Poisson effect. Here it can be observed that $\mathcal{F}_1^1\ \overline{u}_1(x_1)'$, $\mathcal{F}_2^2\ \overline{\phi}_1(x_1)'$ and $\mathcal{F}_2^3\ \overline{\phi}_1(x_1)'$ are additional terms in classical beam model solution for anisotropic beam compared to isotropic beam [36].

This first-order solution does not capture the complete strain energy corresponding to the classical beam model. It provides strain energy component corresponding to extension and twisting only. It does not involve energy corresponding to the flexural deformation. Hence this first-order solution needs to be improved by adding the second-order solution.

Second order Approximation

The procedure to obtain the second-order approximate solution is similar to that used for the first-order solution. The modified strain energy required for the second order approximate solution is corrected up to order $O\left(\mu\varepsilon^2(h/L)^4\right)$. The asymptotically small term used to obtain perturbed first-order solution is $w_i(x_1,x_2,x_3)$ and the resultant perturbed first-order displacement field is

$$u_i^{II}(x_1,x_2,x_3) = u_i^I + w_i(x_1,x_2,x_3) \quad (3.15)$$

The w_i are also subjected to the same constraints used for the v_i, given by Eq. (3.3). These constraints are given as

$$\langle w_i \rangle = 0 \qquad \langle w_{3,2} - w_{2,3} \rangle = 0 \quad (3.16)$$

The perturbed first order displacement field (3.15) provides the following modified strain field

$$\begin{aligned}
\Gamma_{11}^{II} &= \overline{u}_1(x_1)' - x_2\overline{u}_2(x_1)'' - x_3\overline{u}_3(x_1)'' + \psi_{aniso}\,\overline{\phi}_1(x_1)'' + \mathcal{F}_1^1\overline{u}_1(x_1)'' + w_1' \\
\Gamma_{22}^{II} &= \mathcal{F}_{1,2}^2\overline{u}_1(x_1)' + \mathcal{F}_{2,2}^2\overline{\phi}_1(x_1)' + w_{2,2} \\
\Gamma_{33}^{II} &= \mathcal{F}_{1,3}^3\overline{u}_1(x_1)' + \mathcal{F}_{2,3}^3\overline{\phi}_1(x_1)' + w_{3,3} \\
\Gamma_{23}^{II} &= \left(\mathcal{F}_{1,3}^2 + \mathcal{F}_{1,2}^3\right)\overline{u}_1(x_1)' + \left(\mathcal{F}_{2,3}^2 + \mathcal{F}_{2,2}^3\right)\overline{\phi}_1(x_1)' + w_{2,3} + w_{3,2} \\
\Gamma_{13}^{II} &= \mathcal{F}_{1,3}^1\overline{u}_1(x_1)' + \mathcal{F}_1^3\overline{u}_1(x_1)'' + \mathcal{F}_2^3\overline{\phi}_1(x_1)'' + (\psi_{aniso,3} + x_2)\,\overline{\phi}_1(x_1)' + w_{1,3} + w_3' \\
\Gamma_{12}^{II} &= \mathcal{F}_{1,2}^1\overline{u}_1(x_1)' + \mathcal{F}_1^2\overline{u}_1(x_1)'' + \mathcal{F}_2^2\overline{\phi}_1(x_1)'' + (\psi_{aniso,2} - x_3)\,\overline{\phi}_1(x_1)' + w_{1,2} + w_2'
\end{aligned} \tag{3.17}$$

The required second-order strain energy is calculated using this modified strain field. Minimizing this second-order strain energy using the variational principle gives the following Euler-Lagrange equations.

$$\begin{aligned}
&19\overline{u}_2(x_1)'' + 11\overline{u}_3(x_1)'' - \chi_1^1\,\overline{\phi}_1(x_1)' - \chi_2^1\,\overline{u}_1(x_1)' - \chi_3^1\,\overline{u}_1(x_1)'' \\
&- \chi_4^1\,\overline{\phi}_1(x_1)'' - 45w_{1,22} - 28w_{1,23} - 50w_{1,33} - 10w_{2,22} - 31w_{2,23} \\
&- 17w_{2,33} - 18w_{3,22} - 30w_{3,23} - 14w_{3,33} = 0
\end{aligned} \tag{3.18}$$

$$\begin{aligned}
&29\overline{u}_2(x_1)'' + 16\overline{u}_3(x_1)'' + \chi_1^2\,\overline{\phi}_1(x_1)' + \chi_2^2\,\overline{u}_1(x_1)' - \chi_3^2\,\overline{u}_1(x_1)'' \\
&+ \chi_4^2\,\overline{\phi}_1(x_1)'' - 10w_{1,22} - 31w_{1,23} - 17w_{1,33} - 100w_{2,22} - 30w_{2,23} \\
&- 55w_{2,33} - 15w_{3,22} - 81w_{3,23} - 11w_{3,33} = 0
\end{aligned} \tag{3.19}$$

$$\begin{aligned}
&16\overline{u}_2(x_1)'' + 25\overline{u}_3(x_1)'' - \chi_1^3\,\overline{\phi}_1(x_1)' - \chi_2^3\,\overline{u}_1(x_1)' - \chi_3^3\,\overline{u}_1(x_1)'' \\
&- \chi_4^3\,\overline{\phi}_1(x_1)'' - 18w_{1,22} - 30w_{1,23} - 14w_{1,33} - 15w_{2,22} - 81w_{2,23} \\
&- 11w_{2,33} - 55w_{3,22} - 22w_{3,23} - 95w_{3,33} = 0
\end{aligned} \tag{3.20}$$

with the following associated boundary conditions

$$\begin{aligned}
&n_2\Big[-19x_2\overline{u}_2(x_1)'' - 19x_3\overline{u}_3(x_1)'' + \mathcal{B}_1^1\overline{u}_1(x_1)' + \mathcal{B}_2^1\overline{\phi}_1(x_1)' + \mathcal{B}_3^1\overline{u}_1(x_1)'' \\
&\quad + \mathcal{B}_4^1\overline{\phi}_1(x_1)'' + 45w_{1,2} + 14w_{1,3} + 10w_{2,2} + 18w_{2,3} + 18w_{3,2} + 13w_{3,3}\Big] \\
&+ n_3\Big[-11x_2\overline{u}_2(x_1)'' - 11x_3\overline{u}_3(x_1)'' + \mathcal{B}_5^1\overline{u}_1(x_1)' + \mathcal{B}_6^1\overline{\phi}_1(x_1)' + \mathcal{B}_7^1\overline{u}_1(x_1)'' \\
&\quad + \mathcal{B}_8^1\overline{\phi}_1(x_1)'' + 14w_{1,2} + 50w_{1,3} + 13w_{2,2} + 17w_{2,3} + 17w_{3,2} + 14w_{3,3}\Big] = 0
\end{aligned} \tag{3.21}$$

$$\begin{aligned}
&n_2\Big[-29x_2\overline{u}_2(x_1)'' - 29x_3\overline{u}_3(x_1)'' + \mathcal{B}_1^2\overline{u}_1(x_1)' + \mathcal{B}_2^2\overline{\phi}_1(x_1)' + \mathcal{B}_3^2\overline{u}_1(x_1)'' \\
&\quad + \mathcal{B}_4^2\overline{\phi}_1(x_1)'' + 10w_{1,2} + 13w_{1,3} + 100w_{2,2} + 15w_{2,3} + 15w_{3,2} + 26w_{3,3}\Big] \\
&+ n_3\Big[-16x_2\overline{u}_2(x_1)'' - 16x_3\overline{u}_3(x_1)'' + \mathcal{B}_5^2\overline{u}_1(x_1)' + \mathcal{B}_6^2\overline{\phi}_1(x_1)' + \mathcal{B}_7^2\overline{u}_1(x_1)'' \\
&\quad + \mathcal{B}_8^2\overline{\phi}_1(x_1)'' + 18w_{1,2} + 17w_{1,3} + 15w_{2,2} + 55w_{2,3} + 55w_{3,2} + 11w_{3,3}\Big] = 0
\end{aligned} \tag{3.22}$$

$$\begin{aligned}
&n_2\Big[-16x_2\overline{u}_2(x_1)'' - 16x_3\overline{u}_3(x_1)'' + \mathcal{B}_1^3\overline{u}_1(x_1)' + \mathcal{B}_2^3\overline{\phi}_1(x_1)' + \mathcal{B}_3^3\overline{u}_1(x_1)'' \\
&\quad + \mathcal{B}_4^3\overline{\phi}_1(x_1)'' + 18w_{1,2} + 17w_{1,3} + 15w_{2,2} + 55w_{2,3} + 55w_{3,2} + 11w_{3,3}\Big]
\end{aligned}$$

$$+ n_3\Big[-25x_2\overline{u}_2\,(x_1)'' - 25x_3\overline{u}_3\,(x_1)'' + \mathcal{B}_5^3\overline{u}_1\,(x_1)' + \mathcal{B}_6^3\overline{\phi}_1(x_1)' + \mathcal{B}_7^3\overline{u}_1\,(x_1)''$$
$$+ \mathcal{B}_8^3\overline{\phi}_1(x_1)'' + 13w_{1,2} + 14w_{1,3} + 26w_{2,2} + 11w_{2,3} + 11w_{3,2} + 95w_{3,3}\Big] = 0 \tag{3.23}$$

The solution of Euler-Lagrange equations (3.18-3.20) satisfying boundary conditions (3.21-3.23) and constraints (3.16) provides the unknown warping function $w_i(x_1, x_2, x_3)$ of anisotropic beam. The terms $\overline{u}_1(x_1)''$ and $\overline{\phi}_1\,(x_1)''$ do not contribute to the classical beam model energy [57] hence these terms has to be dropped while solving these equations. The 3D displacement field corrected up to the second order is given as

$$u_1^{II} = \overline{u}_1(x_1) - \; x_2\overline{u}_2(x_1)' - x_3\overline{u}_3(x_1)' + \psi_{aniso}(x_2, x_3)\;\overline{\phi}_1(x_1)' + \mathcal{F}_1^1\;\overline{u}_1(x_1)'$$
$$\underbrace{+\mathcal{F}_2^1(x_2, x_3)\;\overline{u}_2(x_1)'' + \mathcal{F}_3^1(x_2, x_3)\;\overline{u}_3(x_1)''}_{w_1(x_1,x_2,x_3)} \tag{3.24}$$

$$u_2^{II} = \overline{u}_2(x_1) - x_3\overline{\phi}_1(x_1) + \mathcal{F}_1^2(x_2, x_3)\;\overline{u}_1\,(x_1)' + \mathcal{F}_2^2(x_2, x_3)\overline{\phi}_1(x_1)'$$
$$+ \underbrace{\mathcal{F}_3^2(x_2, x_3)\;\overline{u}_2(x_1)'' + \mathcal{F}_4^2(x_2, x_3)\;\overline{u}_3(x_1)''}_{w_2(x_1,x_2,x_3)} \tag{3.25}$$

$$u_3^{II} = \overline{u}_3(x_1) + x_2\overline{\phi}_1(x_1) + \mathcal{F}_1^3(x_2, x_3)\;\overline{u}_1\,(x_1)' + \mathcal{F}_2^3(x_2, x_3)\overline{\phi}_1(x_1)'$$
$$\underbrace{+\mathcal{F}_3^3(x_2, x_3)\;\overline{u}_2(x_1)'' + \mathcal{F}_4^3(x_2, x_3)\;\overline{u}_3(x_1)''}_{w_3(x_1,x_2,x_3)} \tag{3.26}$$

The expressions of 2D functions used here are given in Appendix B.1.1. The underbraces terms in Eqs. (3.24-3.26) are the second order terms $w_i(x_1, x_2, x_3)$. Here it can be noted that the underbraces terms in Eq. (3.24) are new additional terms in the classical beam model solution for axial displacement of the anisotropic beam compared to the isotropic beam. By using the following identity relations

$$\begin{aligned} \overline{\phi}_1(x_1)' &= \overline{\kappa}_1\,(x_1) \quad & \overline{u}_1(x_1)' &= \overline{\gamma}_{11}\,(x_1) \\ \overline{u}_2(x_1)'' &= \overline{\kappa}_3\,(x_1) \quad & \overline{u}_3(x_1)'' &= -\overline{\kappa}_2\,(x_1) \end{aligned} \tag{3.27}$$

the resultant 1D strain energy corrected up to order $O\left(\mu\varepsilon^2(h/L)^4\right)$ is given as

$$2\mathcal{U}_{1D} = \mathcal{S}_{11}\overline{\gamma}_{11}^2 + \mathcal{S}_{22}\overline{\kappa}_1^2 + \mathcal{S}_{23}\overline{\kappa}_1\overline{\kappa}_2 + \mathcal{S}_{24}\overline{\kappa}_1\overline{\kappa}_3 + \mathcal{S}_{33}\overline{\kappa}_2^2 + \mathcal{S}_{34}\overline{\kappa}_2\overline{\kappa}_3 + \mathcal{S}_{44}\overline{\kappa}_3^2 \tag{3.28}$$

The terms $\mathcal{S}_{ij}$ $(i, j = 1, 2, 3, 4)$ are the cross-sectional stiffness constants. Expressions of these stiffness constants are given in Appendix B.1.1. The second-order strain energy (3.28) completely captures the classical beam model energy. From this energy, 1D inverse constitutive law can be extracted and given as

$$\begin{Bmatrix} \overline{\gamma}_{11} \\ \overline{\kappa}_1 \\ \overline{\kappa}_2 \\ \overline{\kappa}_3 \end{Bmatrix} = \frac{1}{P}\begin{bmatrix} \overline{\Phi}_{11} & 0 & 0 & 0 \\ 0 & \overline{\Phi}_{22} & \overline{\Phi}_{23} & \overline{\Phi}_{24} \\ 0 & \overline{\Phi}_{23} & \overline{\Phi}_{33} & 0 \\ 0 & \overline{\Phi}_{24} & 0 & \overline{\Phi}_{44} \end{bmatrix}\begin{Bmatrix} F_1 \\ M_1 \\ M_2 \\ M_3 \end{Bmatrix} \tag{3.29}$$

In the above equation, terms $\overline{\Phi}_{ij}$ $(i,j=1,2,3,4)$ are cross-sectional flexibility constants. Expressions of these constants are given in Appendix B.1.1. This 1D inverse constitutive law (3.29) suggests that axial strain ($\overline{\gamma}_{11}$) remains uncoupled from the curvature terms $\overline{\kappa}_i$. Similarly, $\overline{\kappa}_2$ and $\overline{\kappa}_3$ remain uncoupled from each other while both of these are coupled to the $\overline{\kappa}_1$ term. Hence, the anisotropic-homogeneous beam will not show extension-bend, extension-twist and bend-bend coupling. It will show bend-twist coupling only. It is the highest possible level of elastic coupling in the anisotropic-homogeneous beam.

3.1.2 One-Dimensinal Beam Equation

The 1D intrinsic equations for linear geometrically exact classical beam theory for static equilibrium [81] are given by the Eqs. (2.65 and 2.66) and the solution of these equations for prismatic beam ($k_i=0$) with the boundary conditions, at $x=L$, $F=\overline{F}$ and $M=\overline{M}$ is given by the Eqs. (2.67 and 2.68).

The 1D strain measures ($\overline{\gamma}_{11}$, $\overline{\kappa}_i$) are obtained in terms of applied forces and moments using Eqs. (2.67, 2.68 and 3.29). As these strain measures are functions of 1D displacement ($\overline{u}_i$) and rotation ($\overline{\phi}_1$) defined by the relations given in Eq. (3.27) hence, integration of these strain measures followed by 1D boundary conditions provides the expressions of $\overline{u}_i$ and $\overline{\phi}_1$. The boundary conditions used here are

at $x_1=0$

$$\overline{u}_2'=0; \quad \overline{u}_3'=0; \quad \overline{u}_1=0; \quad \overline{u}_2=0; \quad \overline{u}_3=0; \quad \overline{\phi}_1=0; \tag{3.30}$$

The resultant 1D displacements and rotation terms are given below

$$\overline{u}_1(x_1) = \frac{732963519\ \overline{F}_1}{136276798454\ \pi ab\ P}x_1 \tag{3.31}$$

$$\begin{aligned}\overline{u}_2(x_1) =& \frac{244321173\,(3L-x_1)\,x_1^2\ \overline{F}_2}{68138399227\ \pi a^3 b\ P} + \frac{244321173\left(6L^2-4Lx_1+x_1^2\right)x_1^2\ f_2}{272553596908\pi a^3 bP} \\ &+ \frac{732963519x_1^2\ \overline{M}_3}{68138399227\ \pi a^3 b\ P} + \frac{4753211x_1^2\ \overline{M}_1}{136276798454\ \pi a^3 b\ P}\end{aligned} \tag{3.32}$$

$$\begin{aligned}\overline{u}_3(x_1) =& \frac{244321173\,(3L-x_1)\,x_1^2\ \overline{F}_3}{68138399227\ \pi ab^3\ P} + \frac{244321173\left(6L^2-4Lx_1+x_1^2\right)x_1^2\ f_3}{272553596908\ \pi ab^3\ P} \\ &- \frac{732963519x_1^2\ \overline{M}_2}{68138399227\ \pi ab^3\ P} - \frac{210232453x_1^2\ \overline{M}_1}{136276798454\ \pi ab^3\ P}\end{aligned} \tag{3.33}$$

$$\begin{aligned}\overline{\phi}_1(x_1) =& \frac{\left(1908076279a^2+1629623061b^2\right)x_1\ \overline{M}_1}{136276798454\ \pi a^3 b^3\ P} + \frac{4753211\,(2L-x_1)\,x_1\ \overline{F}_2}{136276798454\ \pi a^3 b\ P} \\ &- \frac{210232453\,(2L-x_1)\,x_1\ \overline{F}_3}{136276798454\ \pi ab^3\ P} + \frac{4753211\left(3L^2-3Lx_1+x_1^2\right)x_1\ f_2}{408830395362\ \pi a^3 b\ P} \\ &- \frac{210232453\left(3L^2-3Lx_1+x_1^2\right)x_1\ f_3}{408830395362\ \pi ab^3\ P} + \frac{210232453x_1\ \overline{M}_2}{68138399227\ \pi ab^3\ P} \\ &+ \frac{4753211x_1\ \overline{M}_3}{68138399227\pi a^3 bP}\end{aligned} \tag{3.34}$$

The 3D displacement field corresponds to classical beam model u_i^{II} for anisotropic beam can be obtained by putting these 1D displacement and rotation terms in Eqs (3.24-3.26).

3.1.3 Numerical Validation

The presented results are validated by comparing them with FEA results obtained from Abaqus. The FEA model and the loading condition are the same as those used to validate orthotropic material beam results provided in section 2.4.2. Everything is similar except for material properties.

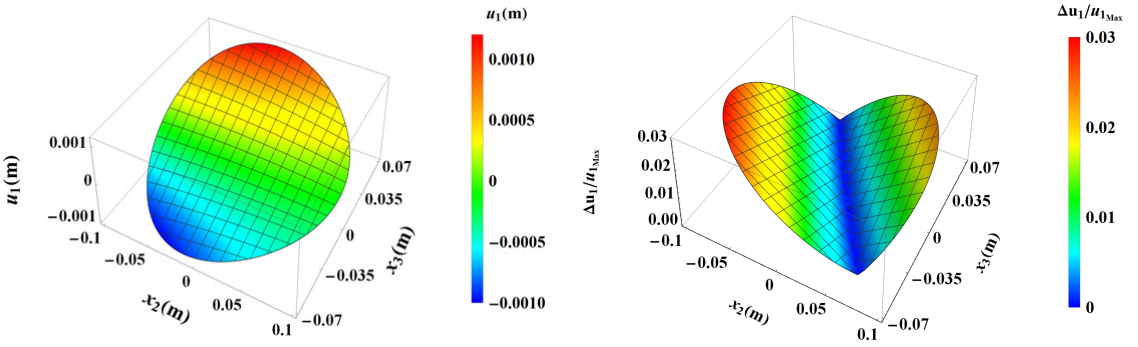

(a) (b)

Figure 3.1: Surface plot for out-of-plane warping obtained analytically and normalized error between analytical and FEM results (a) analytical result plot (b) absolute error plot

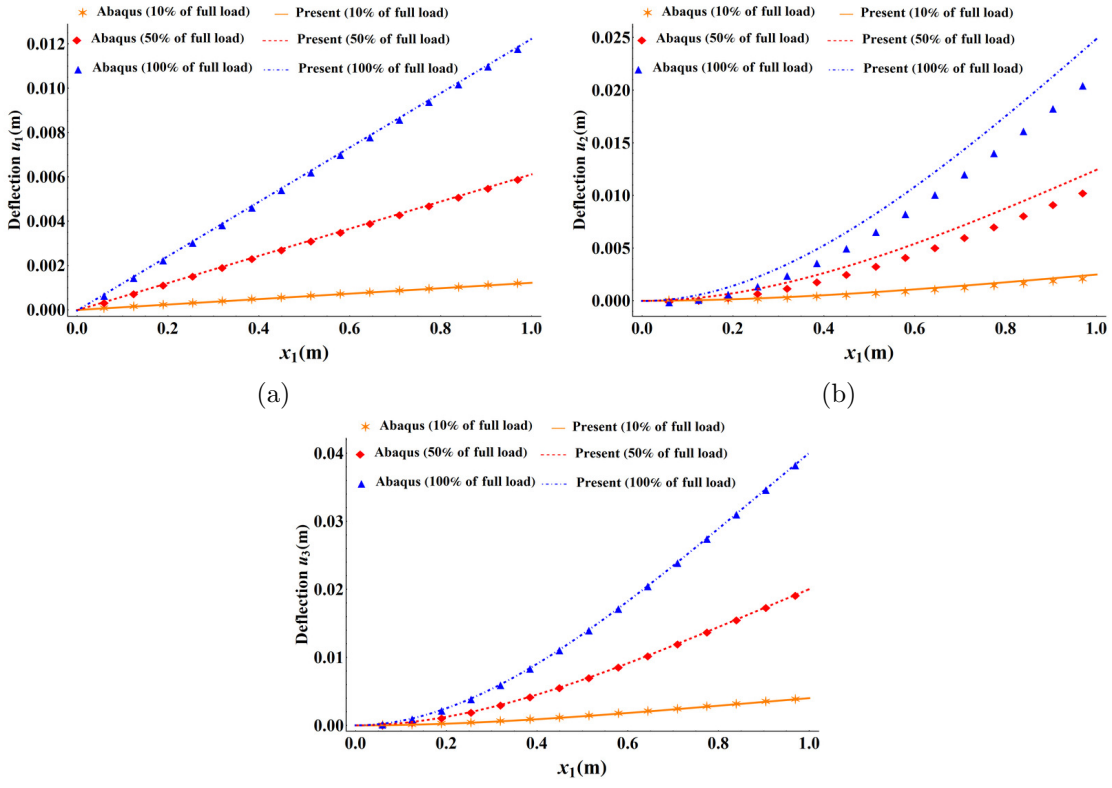

(a) (b)

(c)

Figure 3.2: Deflection of the beam along beam axis with three different loading conditions (a) deflection along x_1 coordinate direction (b) deflection along x_2 coordinate direction (c) deflection along x_3 coordinate direction

In Fig. 3.1, validation of the out-of-plane warping deformation due to twisting has been presented. Fig. 3.1a shows the out-of-plane warping obtained from the analytical result and Fig. 3.1b shows the normalized error between the current analytical results and the FEA results. The normalization is based on the maximum out-of-plane warping value. The error plot reveals that the maximum discrepancy between the current analytical and FEA results is 3% of the maximum out-of-plane warping. This indicates that the analytical results effectively capture the deformation of the beam under twisting loads. Here, one more important thing should be noted that the deformation of the beam's cross-section

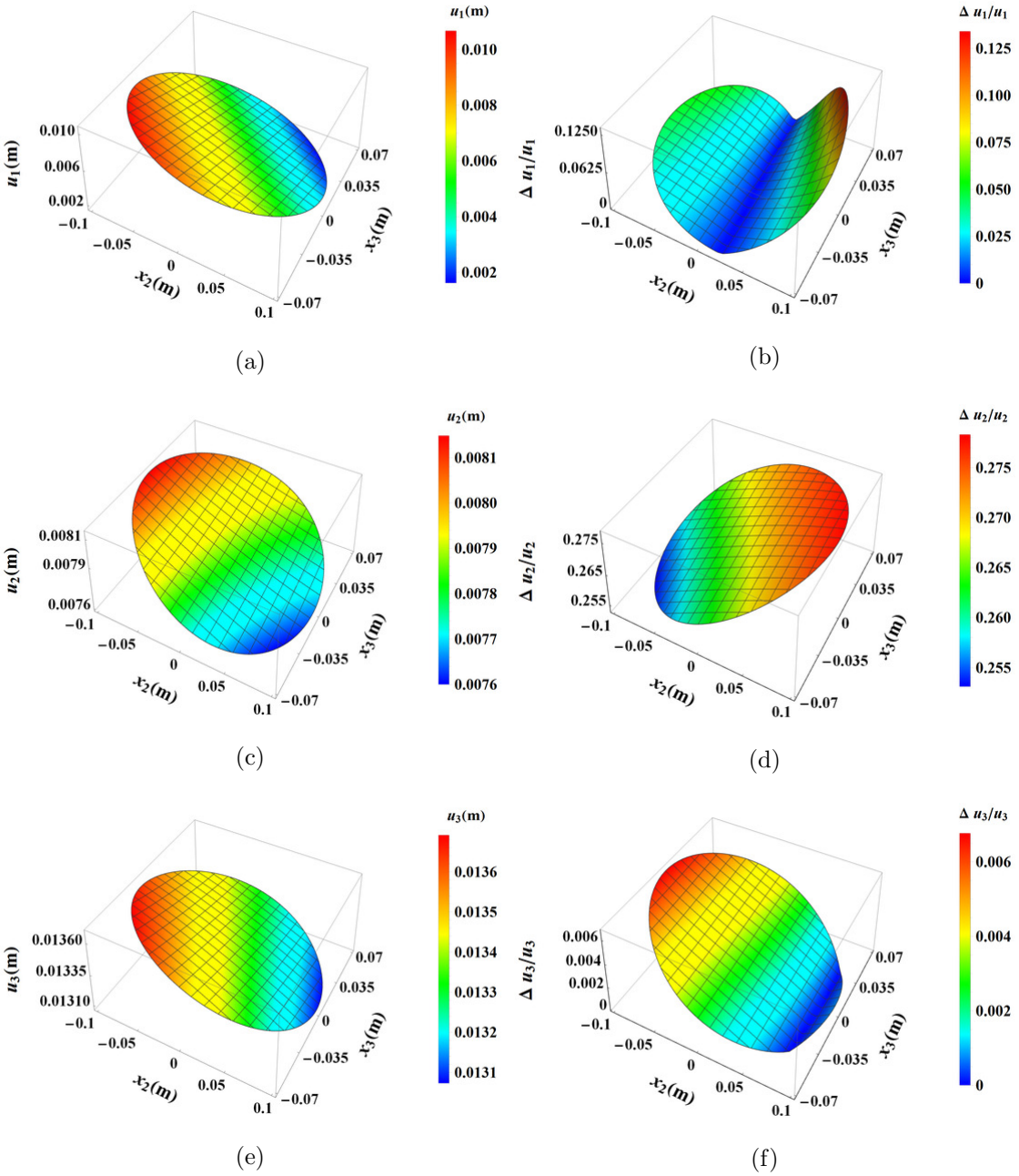

Figure 3.3: Surface plot of the displacement field and relative error w.r.t. FEA results (a,c,e) displacement along x_1, x_2 and x_3 coordinate axis due to analytical result, (b,d,f) relative error respectively

due to twisting has two components (i) Saint-Venant-like deformation and (ii) deflection due to bending. It can be confirmed from Fig. 3.1. The deflection part is coming due to the elastic coupling among the κ_1, κ_2 and κ_3 provided by Eq. (3.29).

In Figure 3.2, the plots of three displacement components u_i along the centroidal axis of the beam are presented. All the loads mentioned earlier and depicted in Fig. 2.2b are applied to the beam to generate these plots. Each plot features three curves corresponding to the three loading conditions, as indicated in the figures. Notably, the results for the displacement components u_1 and u_3 exhibit excellent agreement between the current analytical results and FEA results. However, there is an observable inconsistency

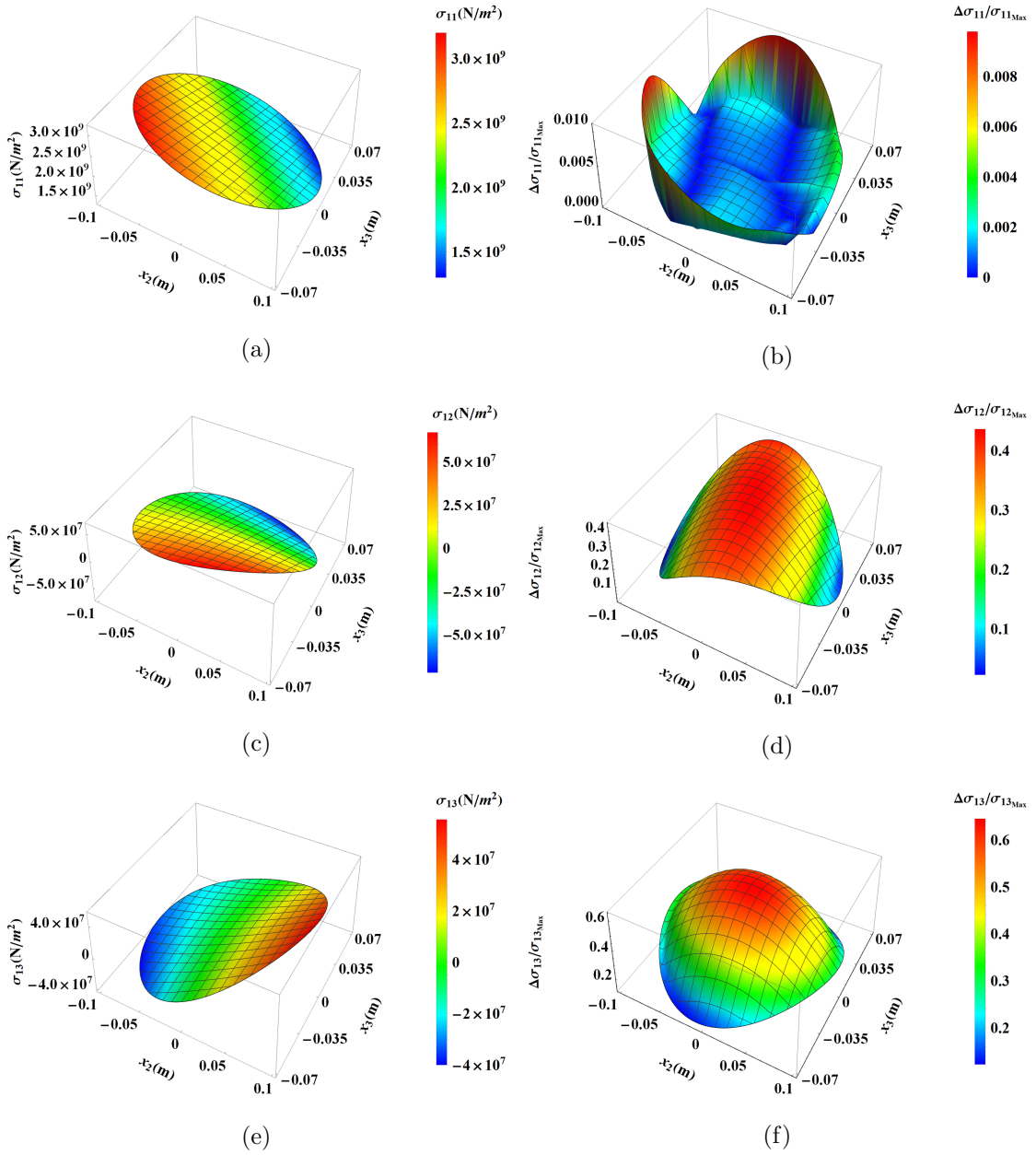

Figure 3.4: Surface plot of stress field and normalized error w.r.t. FEA result (a,c,e) analytical plot of σ_{11}, σ_{12} and σ_{13}, (b,d,f) normalized error plot respectively

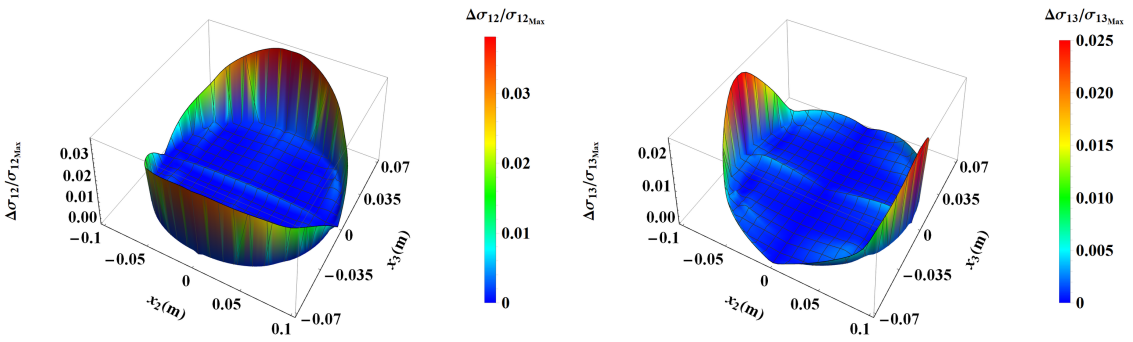

(a) (b)

Figure 3.5: Normalized error plots in the absence of transverse loading (a) σ_{12} (b) σ_{13}

in the displacement component u_2, and this deviation becomes more pronounced as the applied loads increase. It is observed that this discrepancy occurs in cases involving the material, imparting coupling to the beam, as will be demonstrated in the upcoming sections. However, further investigation is required to determine the factors responsible for this deviation, which falls outside the scope of this study.

The surface plots illustrating the 3D displacement field are presented in Fig. 3.3. To mitigate end effects, these surface plots are captured at the mid-surface of the beam. All previously discussed loads are applied at their full magnitude in this case. The relative error surface plots reveal that the maximum relative error for u_1, u_2, and u_3 is 12.5%, 27.5%, and 0.6%, respectively. The substantial error in u_2 aligns with earlier results (depicted in Fig. 3.2). The notable error in u_1 is attributed to the axial displacement error in the x_2 direction, as illustrated in the preceding Fig. 3.2. This axial displacement error leads to an error in the cross-sectional rotation about the x_3 axis. Given that this rotation contributes to one component of the 3D u_1 (as evident from Eq. 3.24), the error in u_2 propagates to u_1. This is shown by the relative error plot (Fig. 3.3b), indicating that the error is most pronounced at the boundary of the cross-section, while at the midsection, it is negligible.

The stress components σ_{11}, σ_{12}, and σ_{13}, along with their corresponding normalized error plots, are presented in Fig. 3.4. Similar to previous cases, error normalization has been performed by considering the respective maximum stress values. Analysis of Fig. 3.4b reveals that the maximum error between the current analytical results and FEA results for σ_{11} is approximately 1% of the maximum σ_{11}, demonstrating the effective capture of the stress component σ_{11} by the analytical solution under the applied loads shown in Fig. 2.2b.

However, the error for σ_{12} and σ_{13} is notably higher, reaching up to 40% and 60% of their respective maximum values. This significant discrepancy can be attributed to two main reasons. Firstly, it stems from errors in the 3D displacement fields u_1 and u_2, as discussed earlier and illustrated in Fig. 3.3b and Fig. 3.3d since stress is a function of the displacement field. Secondly, the analysis presented here provides a solution for the

classical beam model only, failing to capture transverse shear. The plots are generated for the loading conditions depicted in Fig. 2.2b, which involve transverse loads. These loads result in transverse shear stress, adequately captured by 3D FEA but not accounted for in the current analytic solution, leading to the observed substantial errors.

To support this argument, error plots for σ_{12} and σ_{13} are provided in Fig. 3.5 under the absence of transverse loads. In this case, the maximum errors for σ_{12} and σ_{13} are reduced to 3% and 2.5% of their maximum values, respectively.

In this case, the stress components σ_{22}, σ_{33}, and σ_{23} are determined to be non-zero, contrary to the plain stress condition stipulated by beam theory. Surface plots illustrating these stress components, derived from both current analytic results and FEA analyses,

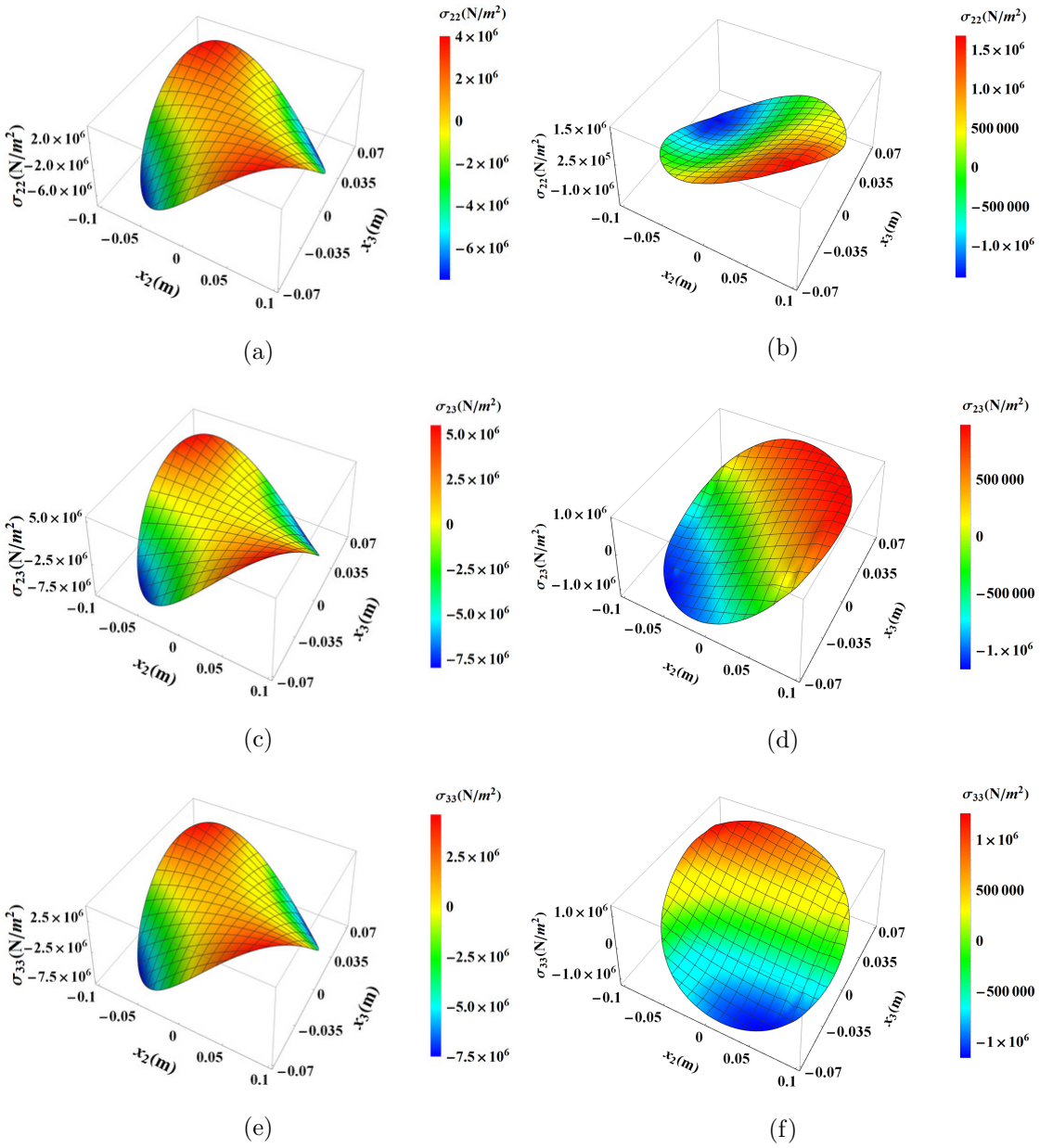

Figure 3.6: Surface plot of stress components σ_{22}, σ_{23} and σ_{33} obtained from (a,c,e) analytical results, (b,d,f) FEA analysis

are presented in Fig. 3.6. Notably, the magnitudes of the results obtained through the two approaches are of the order of MPa, but they exhibit substantial differences. Furthermore, the stress distribution markedly differs between the two approaches. It is important to note that our concern lies not in the magnitudes or distribution of these stress components, but rather in their non-zero states as confirmed by both analytic and FEA approaches. However, the observed difference in stress distribution could be due to the omission of certain higher-order terms in the expressions of these stress components. Additional investigation is needed to validate this potential explanation.

Fig. 3.7 provides surface plots depicting the influence of direct (M_1) and coupling (M_2 and M_3) action on the twisting curvature (κ_1). It can be seen from this figure that for the present anisotropic material (present stiffness matrix) beam, the effect of direct action on the twisting curvature is about 10 times that of the coupling action. In Fig. 3.8,

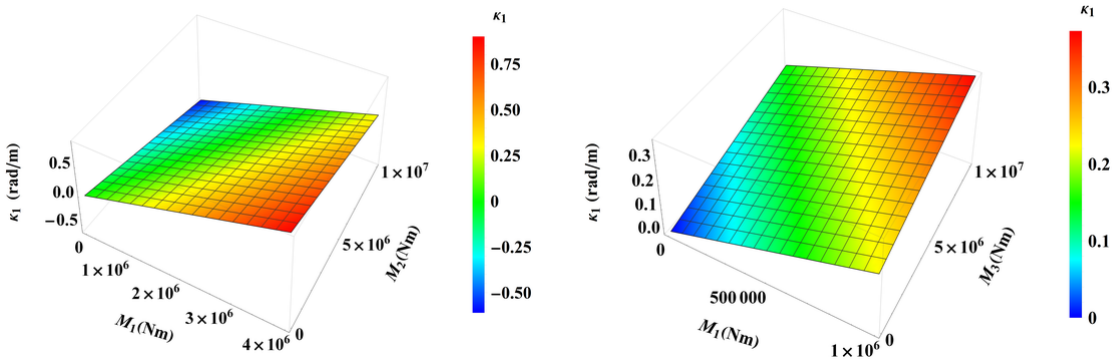

(a) (b)

Figure 3.7: Twisting curvature κ_1 due to twisting moment M_1, bending moments M_2 and M_3 (a) with $M_3 = 0$ (b) with $M_2 = 0$

bend-twist coupling plots are provided. Here, Figs. 3.8a and 3.8b corresponds to current work while Figs. 3.8c and 3.8d are because of the stiffness matrix used in article [1]. It can be seen that for the current work, one of the bend-twist coupling (Fig. 3.8a) results is in close agreement with the FEA result, while the second bend-twist coupling (Fig. 3.8b) result deviates from the FEA result. However, both the bend-twist coupling results provided in Figs. 3.8c and 3.8d shows close agreement between current analytical and FEA results.

The observations pertaining to the axial deflection of the beam, the 3D displacement field, the 3D stress field, and coupling plots collectively indicate the potential absence of certain terms in the expressions of these quantities, likely associated with the next higher-order solution. Subsequent sections will delve into the fact that these discrepancies manifest exclusively in coupled beam cases, implying that these terms may either be negligible or zero in uncoupled scenarios but become pronounced in coupled beam situations. However, further investigation is required to substantiate this assertion.

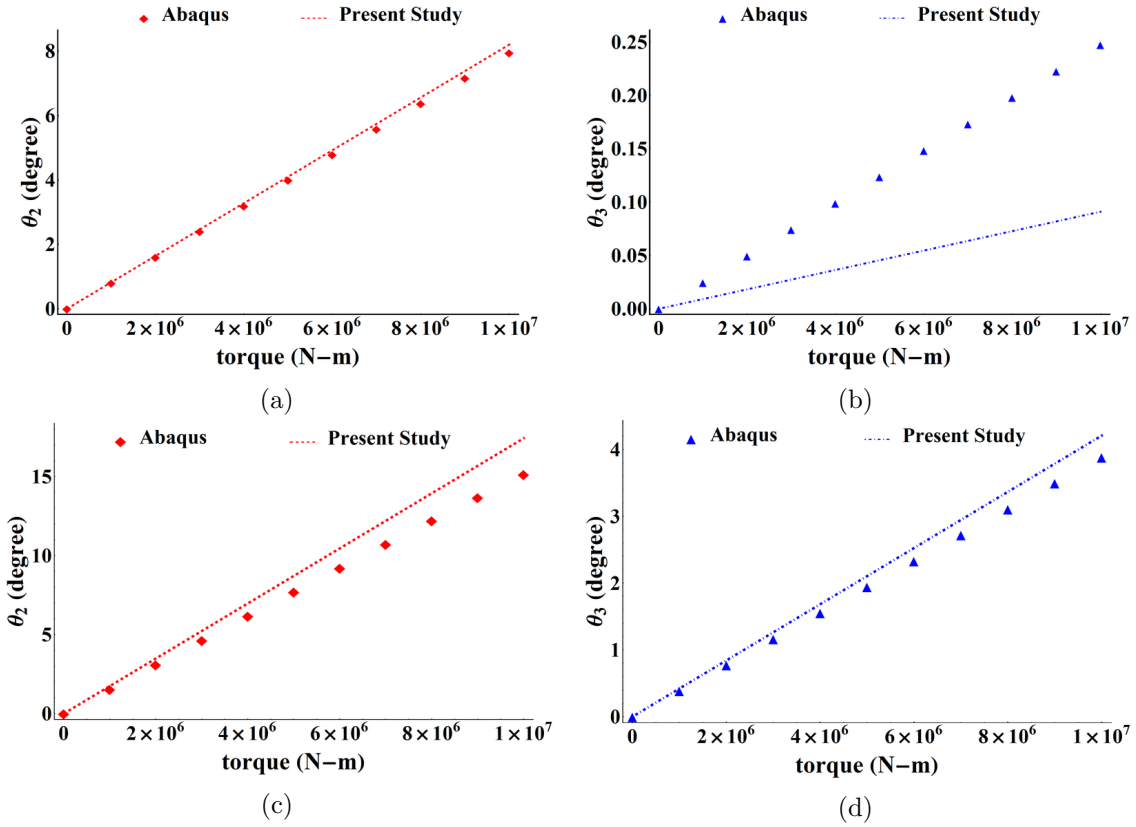

Figure 3.8: Bend-twist coupling for the stiffness matrix used in (a,b) current work (c,d) reference [1]

3.2 Monoclinic Homogeneous Beam Analysis

Monoclinic materials have one plane of elastic symmetry and are defined by 13 independent elastic moduli. Depending on the plane of elastic symmetry, these materials are further divided into three sub-classes. Results for each of these sub-classes beam are presented in subsequent sub-sections. The corresponding stiffness matrix can be obtained from Eq. (3.1) by making elastic moduli zero according to the plane of elastic symmetry.
The procedure to obtain the solution for these monoclinic material beams is the same as provided for anisotropic material beams in the preceding section (3.1). Hence, the direct results are provided instead of repeating the same process in the following sections.

3.2.1 Monoclinic With $x_2 - x_3$ Plane of Elastic Symmetry

For monoclinic materials with plane $x_2 - x_3$ as elastic symmetry $C_{15} = C_{16} = C_{25} = C_{26} = C_{35} = C_{36} = C_{45} = C_{46} = 0$. Hence, the stiffness matrix (3.1) reduces accordingly for this case. For these material beams, inverse constitutive law is given by Eq. (3.35). This relation suggests that all the 1D quantities will remain uncoupled from each other. The expressions of these flexibility constants Φ_{ij} $(i, j = 1, 2, 3, 4)$ are given in Appendix B.2.1.

$$\begin{Bmatrix} \overline{\gamma}_{11} \\ \overline{\kappa}_1 \\ \overline{\kappa}_2 \\ \overline{\kappa}_3 \end{Bmatrix} = \frac{1}{P} \begin{bmatrix} \overline{\Phi}_{11} & 0 & 0 & 0 \\ 0 & \overline{\Phi}_{22} & 0 & 0 \\ 0 & 0 & \overline{\Phi}_{33} & 0 \\ 0 & 0 & 0 & \overline{\Phi}_{44} \end{bmatrix} \begin{Bmatrix} F_1 \\ M_1 \\ M_2 \\ M_3 \end{Bmatrix} \tag{3.35}$$

The 3D displacement field is given in Eqs. (3.36-3.38). The two-dimensional functions used in these equations are provided in Appendix B.2.2.

$$u_1(x_1,x_2,x_3) = \overline{u}_1(x_1) - x_2\overline{u}_2(x_1)' - x_3\overline{u}_3(x_1)' + \psi_{mx_1}(x_2,x_3)\ \overline{\phi}_1(x_1)' \tag{3.36}$$

$$u_2(x_1,x_2,x_3) = \overline{u}_2(x_1) - x_3\overline{\phi}_1(x_1) + \mathcal{F}_1^2(x_2,x_3)\ \overline{u}_1(x_1)' + \mathcal{F}_2^2(x_2,x_3)\ \overline{u}_2(x_1)'' + \mathcal{F}_3^2(x_2,x_3)\ \overline{u}_3(x_1)'' \tag{3.37}$$

$$u_3(x_1,x_2,x_3) = \overline{u}_3(x_1) + x_2\overline{\phi}_1(x_1) + \mathcal{F}_1^3(x_2,x_3)\ \overline{u}_1(x_1)' + \mathcal{F}_2^3(x_2,x_3)\ \overline{u}_2(x_1)'' + \mathcal{F}_3^3(x_2,x_3)\ \overline{u}_3(x_1)'' \tag{3.38}$$

The 1D quantities of this formulation are given by the following Eqs. (3.39-3.42). Here $\overline{F}_i$, $\overline{M}_i$ $(i = 1,2,3)$ are concentrated forces and moments respectively applied at the free end of the beam. f_α $(\alpha = 2,3)$ are distributed transverse load along the length of the beam.

$$\overline{u}_1(x_1) = \frac{460425\ \overline{F}_1}{88515418\ \pi ab\ P} x_1 \tag{3.39}$$

$$\overline{u}_2(x_1) = \frac{153475\,(3l - x_1)\,x_1^2\ \overline{F}_2}{44257709\ \pi a^3 b\ P} + \frac{153475\left(6l^2 - 4lx_1 + x_1^2\right)x_1^2\ f_2}{177030836\ \pi a^3 b\ P} + \frac{460425 x_1^2\ \overline{M}_3}{44257709\ \pi a^3 b\ P} \tag{3.40}$$

$$\overline{u}_3(x_1) = \frac{153475\,(3l - x_1)\,x_1^2\ \overline{F}_3}{44257709\ \pi a^3 b\ P} + \frac{153475\left(6l^2 - 4lx_1 + x_1^2\right)x_1^2\ f_3}{177030836\ \pi a^3 b\ P} - \frac{460425 x_1^2\ \overline{M}_2}{44257709\ \pi a^3 b\ P} \tag{3.41}$$

$$\overline{\phi}_1(x_1) = \frac{5\left(10a^2 + 9b^2\right)x_1\ \overline{M}_1}{4108\ \pi a^3 b^3\ P} \tag{3.42}$$

Numerical Validation

The present analytical results are validated by comparing them with FEA results. Here plots are provided for the displacement along the centroidal axis of the beam, surface plots for the 3D displacement field, and out-of-plane warping at the mid-plane of the beam. The precise determination of the displacement field also ensures the preciseness of the strain and stress field, as these are the functions of the displacement field. For the surface plots of out-of-plane warping, only twisting moment $\overline{M}_1$ is applied, and for the remaining plots, all the loads discussed in the section 2.4.2 are applied on the beam.

The surface plot depicting the out-of-plane warping obtained from analytical results, along

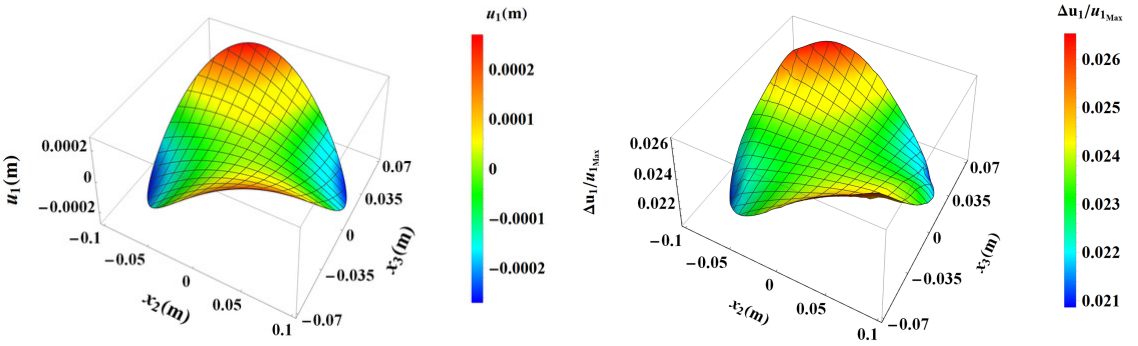

(a) (b)

Figure 3.9: Surface plot for out-of-plane warping (a) analytical expression (b) normalized error

with its normalized error, is presented in Fig. 3.9. This out-of-plane warping plot consists of saint-Venant like deformation only; hence confirms the uncoupled behavior for the current material beam as determined by the Eq. 3.35. The normalized error plot in Fig. 3.9b illustrates that the maximum error between the current analytical results and the FEA results is approximately 2.6% of the maximum out-of-plane warping value. Consequently, the analytical results demonstrate good agreement with the FEA results.

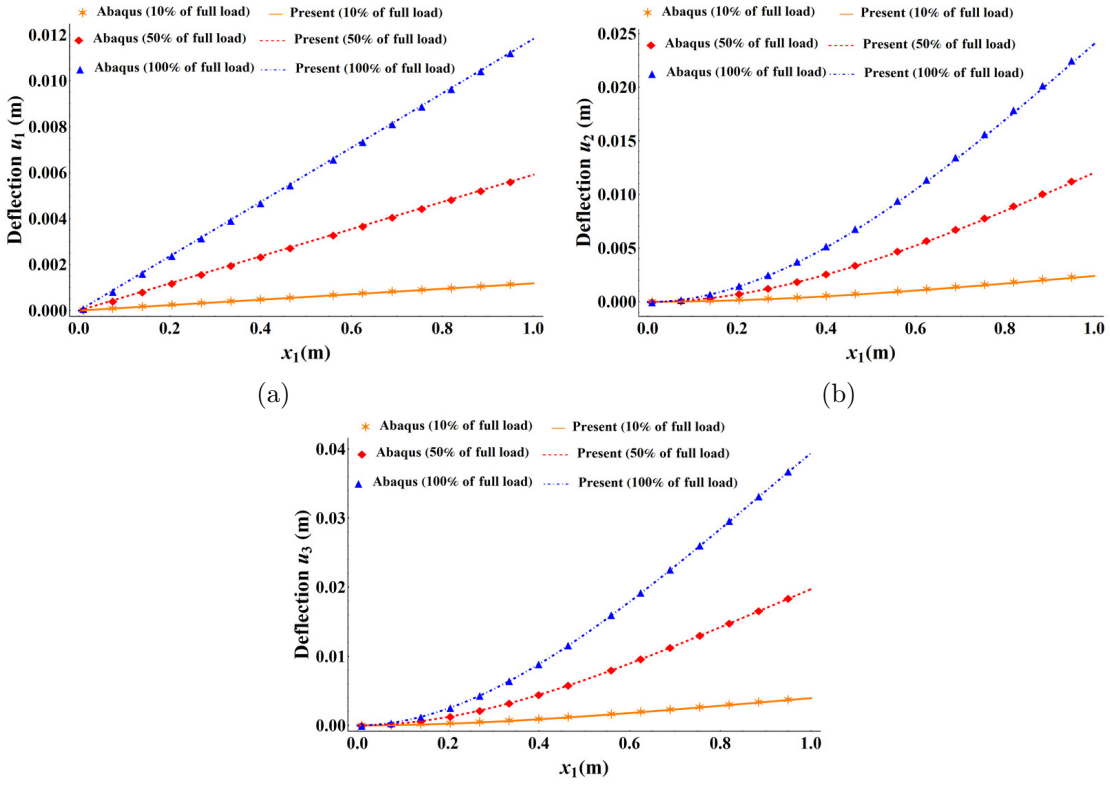

(a) (b)

(c)

Figure 3.10: Deflection of the beam along the centroidal axis for three different loading conditions (a) deflection along x_1 coordinate direction (b) deflection along x_2 coordinate direction (c) deflection along x_3 coordinate direction

In Fig. 3.10, plots of displacement along the centroidal axis of the beam are given. Each figure has three curves corresponding to three different loading conditions, which are 10%, 50%, and 100% of the maximum applied loads. In this figure, 3 different types of lines are due to the analytical solution, while three types of markers represent the results of FEA solutions. From these plots, it can be seen that the present results have almost overlapped with the FEA results.

The surface plot of the 3D displacement field is given in Fig. 3.11. These surface plots are taken at the mid-cross-sectional plane of the beam to avoid the end effects. All loads

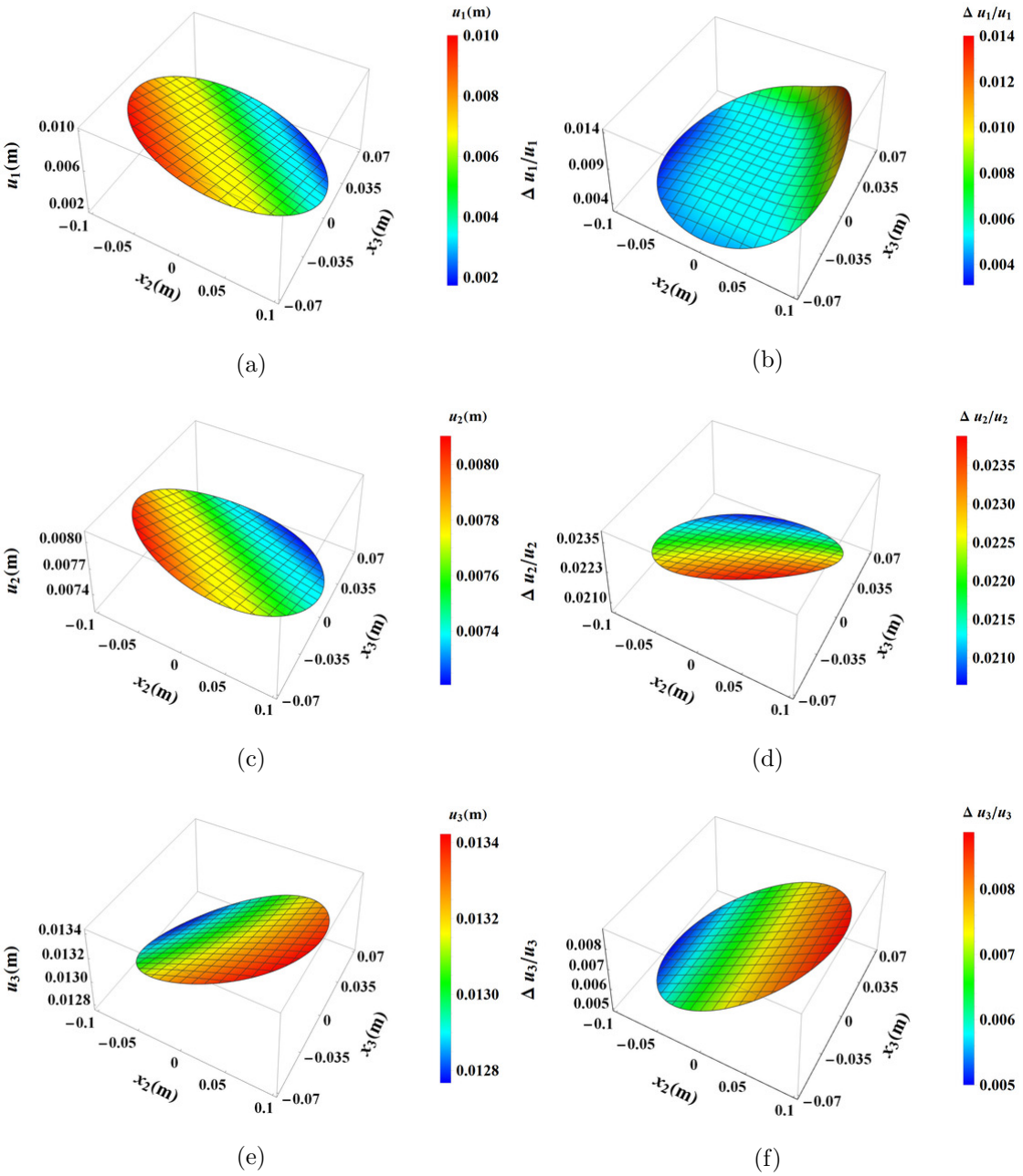

Figure 3.11: Surface plot of the displacement field and relative error w.r.t. FEA results (a,c,e) displacement along x_1, x_2 and x_3 coordinate axis due to analytical result, (d,b,f) relative error respectively

with their maximum magnitude are considered for this case. From the relative error plots (Figs. 3.11b, 3.11d and 3.11f), it can be observed that the error between analytical and FEA results is very small. The maximum relative error for u_1 is 1.4%; for u_2 it is 2.35%; for u_3 it is obtained about 0.8%. All the error plots provided suggest that the analytical results are in very close agreement with FEA results for present monoclinic materials. In Fig. 3.12, surface plots illustrating the three non-zero stress components

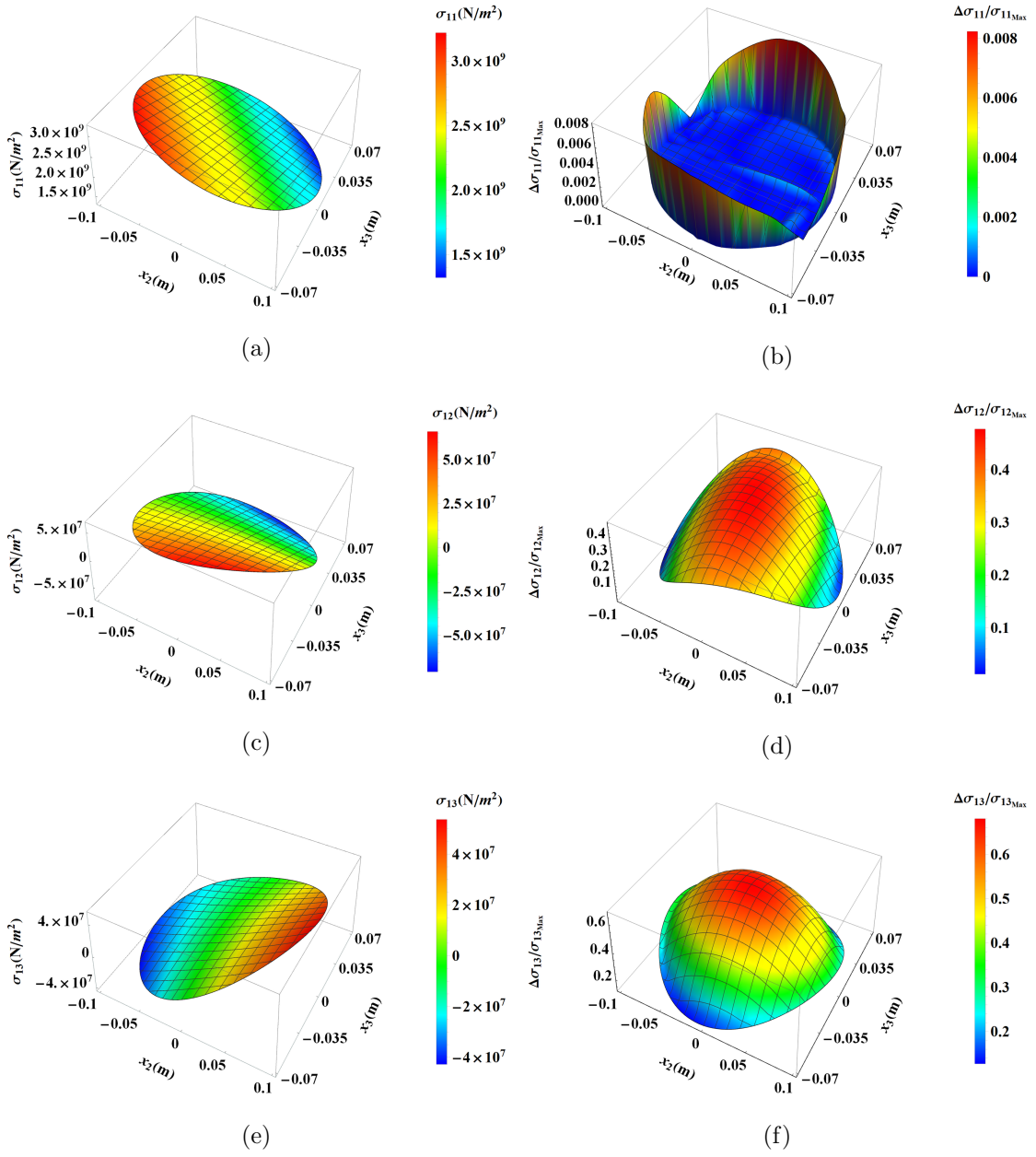

Figure 3.12: Surface plot of stress field and normalized error of σ_{11}, σ_{12} and σ_{13} (a,c,e) analytical result plots, (d,b,f) normalized error plots

(σ_{11}, σ_{12}, and σ_{13}) are presented, along with their normalized errors between analytical results and FEA results. The remaining three stress components (σ_{22}, σ_{33}, and σ_{23}) are determined to be zero for this class of monoclinic materials, thereby validating the plain

stress condition for this case as well. The error plots reveal that the maximum error for σ_{11} is 0.8% of its maximum value, while for σ_{12} and σ_{13}, it is approximately 40% and 60% of their respective maximum values. This substantial error arises due to the presence of transverse shear stress, which is not captured by the classical beam model solution, as discussed previously for the anisotropic beam case.

3.2.2 Monoclinic With $x_1 - x_3$ Plane of Elastic Symmetry

For this class of monoclinic material $C_{14} = C_{16} = C_{24} = C_{26} = C_{34} = C_{36} = C_{45} = C_{56} = 0$. The stiffness matrix for this case can be obtained by putting these zero-value elastic moduli in the stiffness matrix (3.1). VAM analysis provides the inverse constitutive relation given by Eq. (3.43). This relation suggests that for this type of material beam $\overline{\kappa}_1$ and $\overline{\kappa}_3$ are coupled i.e the twisting moment $\overline{M}_1$ can influence $\overline{u}_2$ similarly bending moment $\overline{M}_3$, concentrated force $\overline{F}_2$ and distributed loadf_2 can influence $\overline{\phi}_1$. The flexibility coefficient Φ_{24} provides this coupling behavior. Expressions of these flexibility coefficients are provided in Appendix B.3.1.

$$\begin{Bmatrix} \overline{\gamma}_{11} \\ \overline{\kappa}_1 \\ \overline{\kappa}_2 \\ \overline{\kappa}_3 \end{Bmatrix} = \frac{1}{P} \begin{bmatrix} \overline{\Phi}_{11} & 0 & 0 & 0 \\ 0 & \overline{\Phi}_{22} & 0 & \overline{\Phi}_{24} \\ 0 & 0 & \overline{\Phi}_{33} & 0 \\ 0 & \overline{\Phi}_{24} & 0 & \overline{\Phi}_{44} \end{bmatrix} \begin{Bmatrix} F_1 \\ M_1 \\ M_2 \\ M_3 \end{Bmatrix} \tag{3.43}$$

The 3D displacement field for this case is given by Eqs. (3.44-3.46). The expressions of the 2D functions used in these equations are given in Appendix B.3.2.

$$\begin{aligned} u_1(x_1,x_2,x_3) =& \overline{u}_1(x_1) - x_2\overline{u}_2(x_1)' - x_3\overline{u}_3(x_1)' + \psi_{mx_2}(x_2,x_3)\ \overline{\phi}_1(x_1)' \\ &+ \mathcal{F}_1^1(x_2,x_3)\ \overline{u}_2(x_1)'' + \mathcal{F}_2^1(x_2,x_3)\ \overline{u}_3(x_1)'' + \mathcal{F}_3^1\ \overline{u}_1(x_1)' \end{aligned} \tag{3.44}$$

$$\begin{aligned} u_2(x_1,x_2,x_3) =& \overline{u}_2(x_1) - x_3\overline{\phi}_1(x_1) + \mathcal{F}_1^2(x_2,x_3)\ \overline{u}_1(x_1)' + \mathcal{F}_2^2(x_2,x_3)\ \overline{u}_2(x_1)'' \\ &+ \mathcal{F}_3^2(x_2,x_3)\ \overline{u}_3(x_1)'' + \mathcal{F}_4^2(x_2,x_3)\overline{\phi}_1(x_1)' \end{aligned} \tag{3.45}$$

$$\begin{aligned} u_3(x_1,x_2,x_3) =& \overline{u}_3(x_1) + x_2\overline{\phi}_1(x_1) + \mathcal{F}_1^3(x_2,x_3)\ \overline{u}_1(x_1)' + \mathcal{F}_2^3(x_2,x_3)\ \overline{u}_2(x_1)'' \\ &+ \mathcal{F}_3^3(x_2,x_3)\ \overline{u}_3(x_1)'' + \mathcal{F}_4^3(x_2,x_3)\overline{\phi}_1(x_1)' \end{aligned} \tag{3.46}$$

The 1D quantities for this case are given in Eqs (3.47-3.50). By inspecting Eq. (3.48) and Eq.(3.50), the coupling behavior of these beams can be observed.

$$\overline{u}_1(x_1) = \frac{59287\overline{F}_1}{11569970\ \pi ab\ P}x_1 \tag{3.47}$$

$$\begin{aligned} \overline{u}_2(x_1) =& \frac{59287\,(3l - x_1)\,x_1^2\ \overline{F}_2}{17354955\ \pi a^3 b\ P} + \frac{59287\left(6l^2 - 4lx_1 + x_1^2\right)x_1^2\ f_2}{69419820\ \pi a^3 b\ P} + \frac{59287x_1^2\ \overline{M}_3}{5784985\ \pi a^3 b\ P} \\ &+ \frac{1293x_1^2\ \overline{M}_1}{2313994\ \pi a^3 b\ P} \end{aligned} \tag{3.48}$$

$$\overline{u}_3(x_1) = \frac{59287\,(3l - x_1)\,x_1^2\,\overline{F}_3}{17354955\,\pi ab^3\,P} + \frac{59287\left(6l^2 - 4lx_1 + x_1^2\right)x_1^2\,f_3}{69419820\,\pi ab^3\,P} - \frac{59287x_1^2\,\overline{M}_2}{5784985\,\pi ab^3\,P} \tag{3.49}$$

$$\begin{aligned}\overline{\phi}_1(x_1) = &\frac{\left(445443845a^2 + 3725295396^2\right)x_1\,\overline{M}_1}{34841807658\,\pi a^3b^3\,P} + \frac{1293\,(2l - x_1)\,x_1\,\overline{F}_2}{2313994\,\pi a^3b\,P} \\ &+ \frac{431\left(3l^2 - 3lx_1 + x_1^2\right)x_1\,f_2}{2313994\,\pi a^3b\,P} + \frac{1293x_1\,\overline{M}_3}{1156997\,\pi a^3b\,P}\end{aligned} \tag{3.50}$$

Numerical Validation

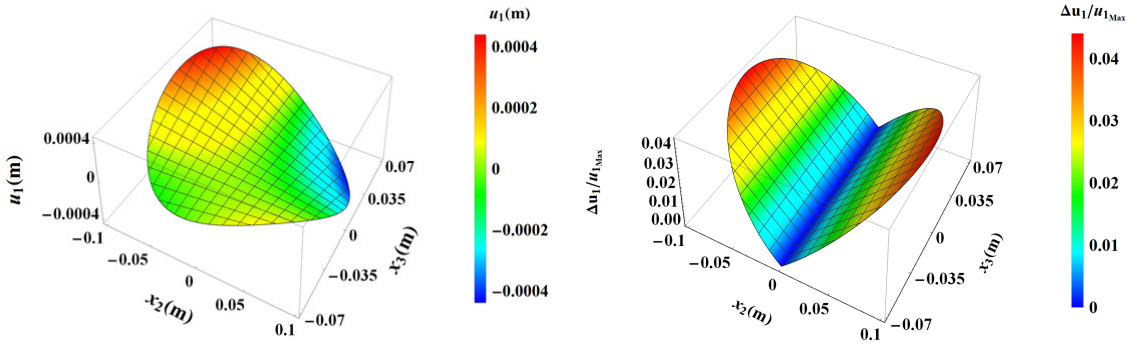

(a) (b)

Figure 3.13: Surface plot for out-of-plane warping (a) analytical expression (b) normalized error

In this section, analytical results have been validated by comparing them with FEA results. In addition to deflection along centroidal axis plots, surface plots of out-of-plane warping and 3D displacement field, stress plots are provided. Here, surface plots of stress components σ_{22}, σ_{33} and σ_{23} are provided as these are found to be non-zero mathematically unlike uncoupled cases.

Surface plots of out-of-plane warping and its normalized error are presented in Fig. 3.13. Analogous to prior cases, normalization has been done using the maximum out-of-plane warping These plots are generated by applying the twisting moment only. The magnitude of this twisting moment is the same as described in section 2.4.2. A careful examination of Fig. 3.13a discloses that akin to the anisotropic case, the deformation of the cross-section manifests in two components: (i) Saint-Venant warping deformation and (ii) bending deformation induced by bend-twist coupling. It can be seen from the normalized error plot 3.13b that the error between current analytical and FEA results is zero in the vicinity of the minor axis of the cross-section and the maximum error is approximately 4% of maximum out-of-plane warping. This error plot implies a close concurrence between the current analytical results and those derived from the FEA.

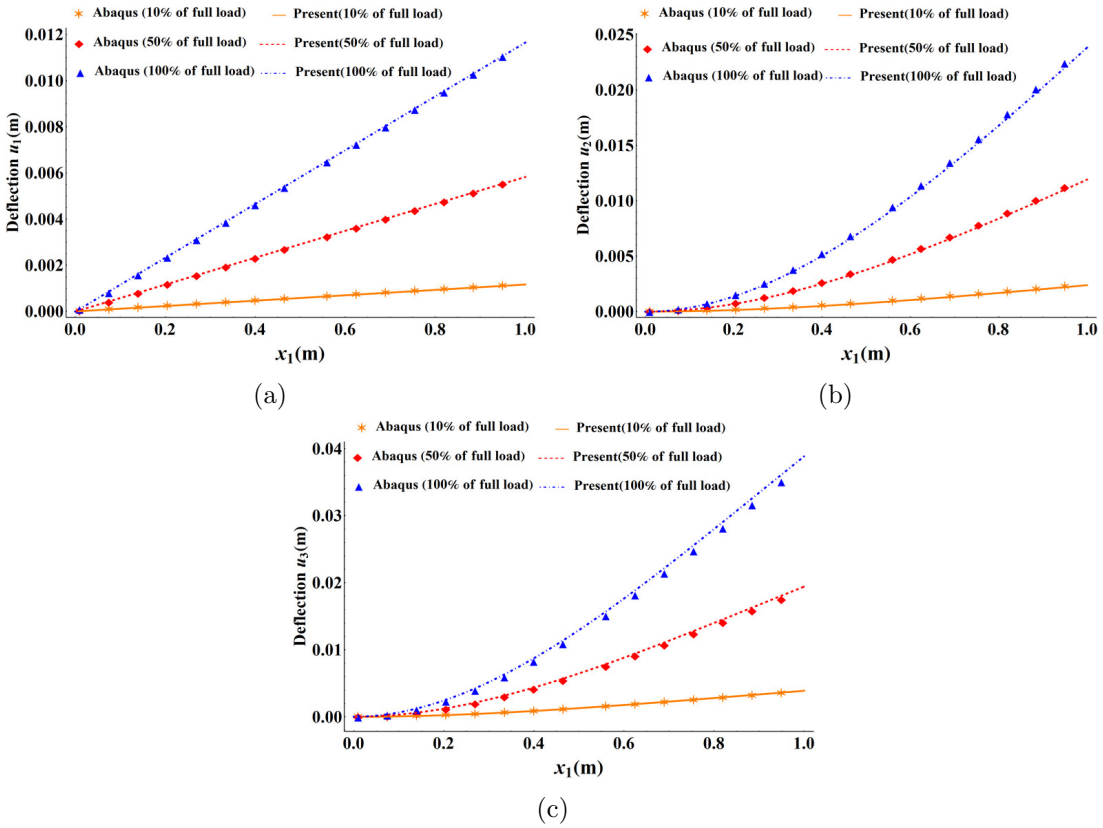

Figure 3.14: Deflection of the beam along beam axis with three different loading conditions (a) deflection along x_1 coordinate direction (b) deflection along x_2 coordinate direction (c) deflection along x_3 coordinate direction

The plots of the 3D displacement field along the centroidal axis of the beam are provided in Fig. 3.14. The description of these figures is similar to that of Fig. 3.10. It can be seen from Fig. 3.14 that analytical and FEA results are very close and it is difficult to distinguish them.

Surface plots of the 3D displacement field have been provided in Fig. 3.15. The loading conditions and description of the figure remain similar as described for Fig. 3.11. It can be seen from Figs. 3.15b, 3.15d and 3.15f that for this case maximum relative error for u_1 is 3%, for u_2 is 3.3% and for u_3 it is 4.7%. Here it should be noted that though in this case coupling is observed, the centroidal displacement and 3D displacement results obtained from current analysis and FEA analysis are in very close agreement. This result further can be improved by using the next higher-order solution incorporating the transverse shear effect.

Surface plots of stress components σ_{11}, σ_{12}, σ_{13} and corresponding normalized error plots are provided in Fig. 3.16. From normalized error plot 3.16b, it can be seen that out of three stress components given here the normalized error of stress component σ_{11} is negligible. The maximum error of this component is approximately 0.8% of the maximum value. However, this normalized error for stress components σ_{12} and σ_{13} is very large and approximately 40% and 60% of the corresponding maximum value respectively. The reason for this large error is the transverse shear stress which is not captured in the

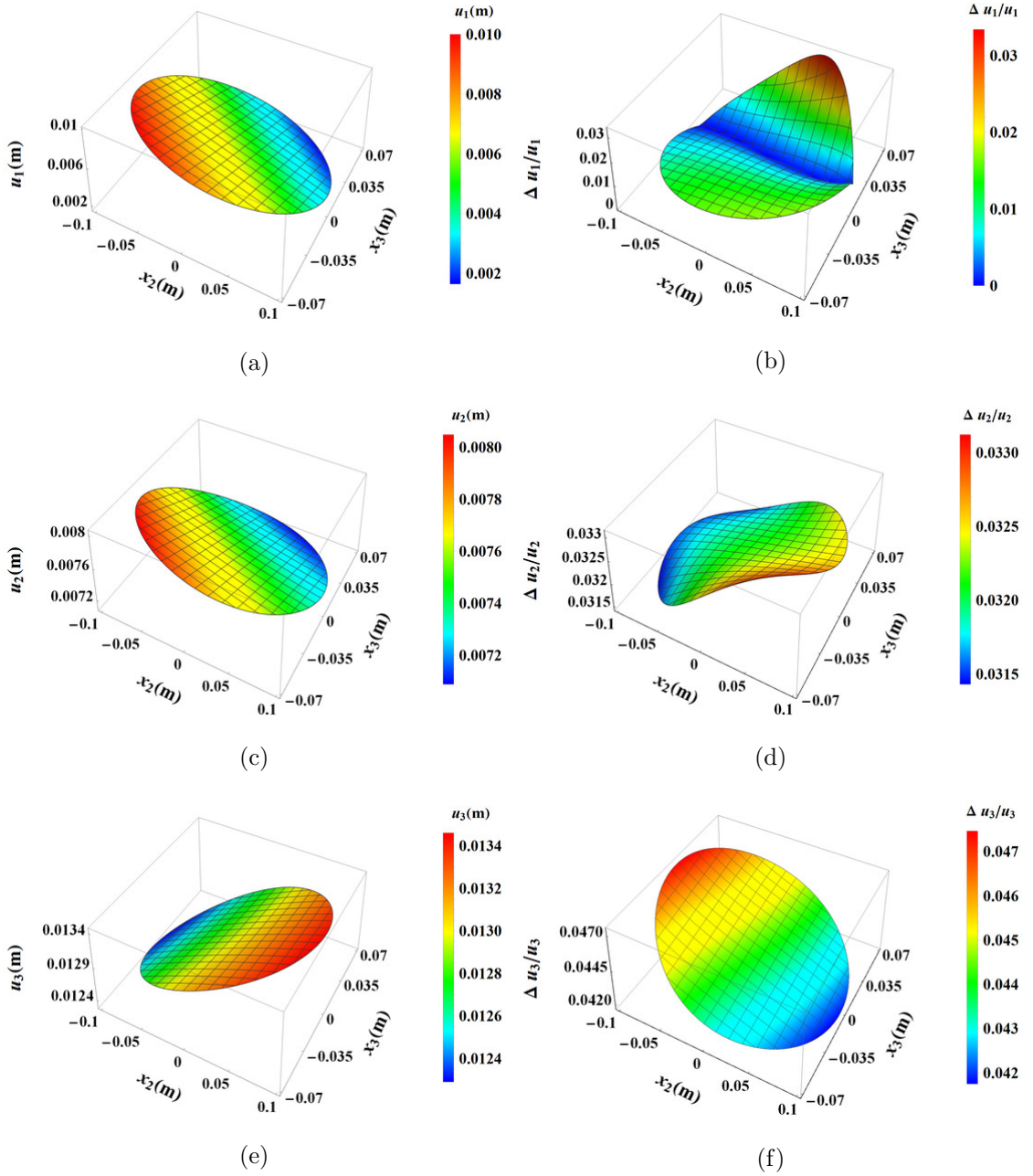

Figure 3.15: Surface plot of the displacement field and relative error w.r.t. FEA results (a,c,e) displacement along x_1, x_2 and x_3 coordinate axis due to analytical result, (b,d,f) relative error respectively

current solution but in the FEA result. The detailed explanation and justification are already provided in the complete anisotropy case.

The stress components σ_{22}, σ_{33}, and σ_{23} are depicted in Fig. 3.17. As discussed previously, the surface plots (Fig. 3.17) of these stress components are presented here because they are found to be non-zero mathematically, which contradicts the plane stress assumption of the beam theory. These stress components have been computed utilizing the 3D displacement field (3.44-3.46) and the corresponding stiffness matrix. These plots confirm the violation of the plane stress condition, as indicated by both the current

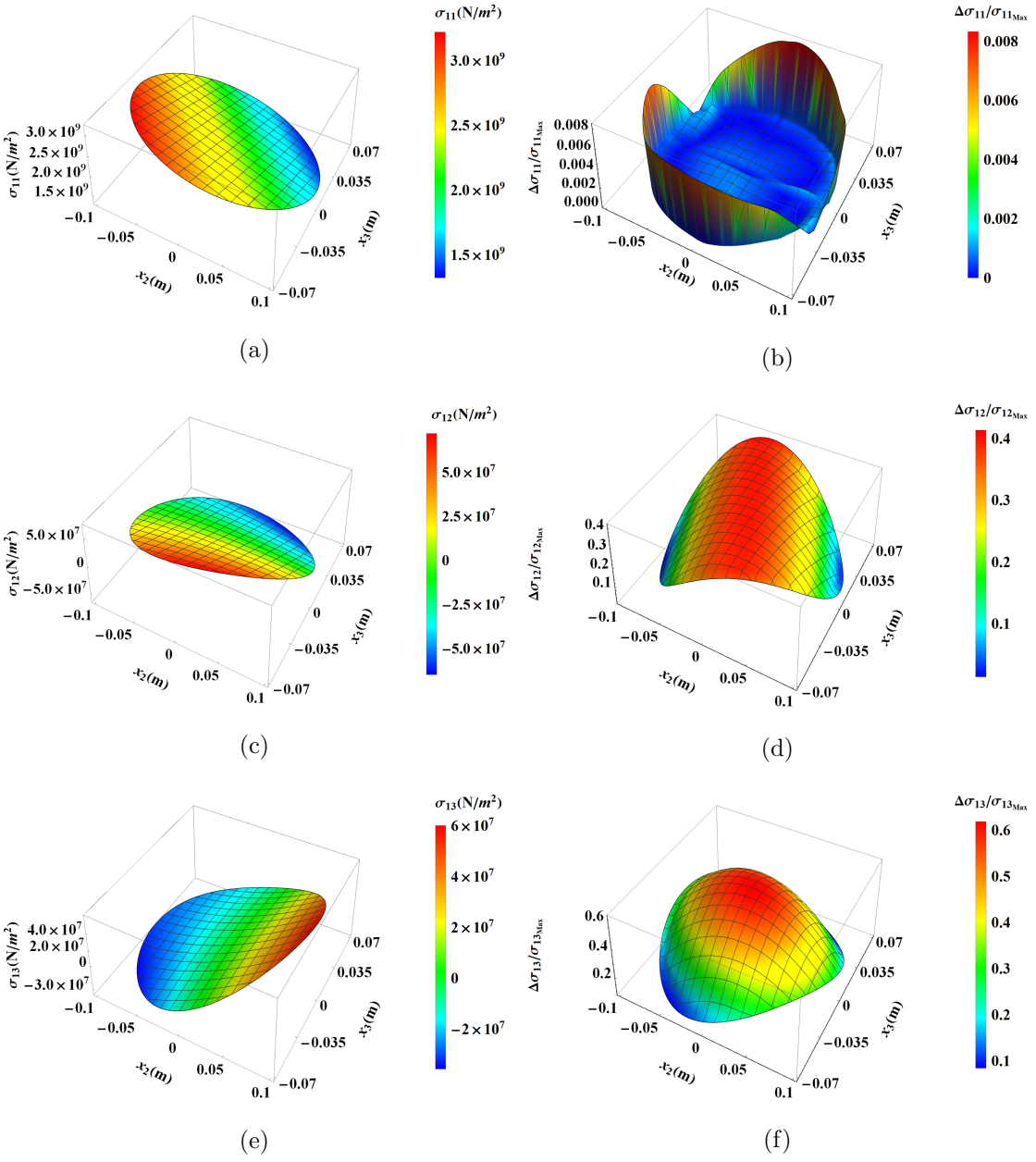

Figure 3.16: Surface plot of stress field and normalized error w.r.t. FEA result (a,c,e) analytical plot of σ_{11}, σ_{12} and σ_{13}, (b,d,f) relative error plot respectively

analytic solution and the FEA solution. However, there are differences in the stress distribution between the two approaches. The potential reason behind this disparity could be the presence of higher-order terms, which are absent in the current second-order solution. Since our focus lies solely on verifying the violation of the plane stress condition, the specific distribution is of less significance here.

Similar to the anisotropic case, a surface plot depicting the influence of direct (M_1) and coupling (M_3) action on the twisting curvature (κ_1) is provided in Fig. 3.18. By comparing this figure with Fig. 3.7, it can be observed that the coupling action for the current monoclinic material beam is weaker compared to the anisotropic material beam

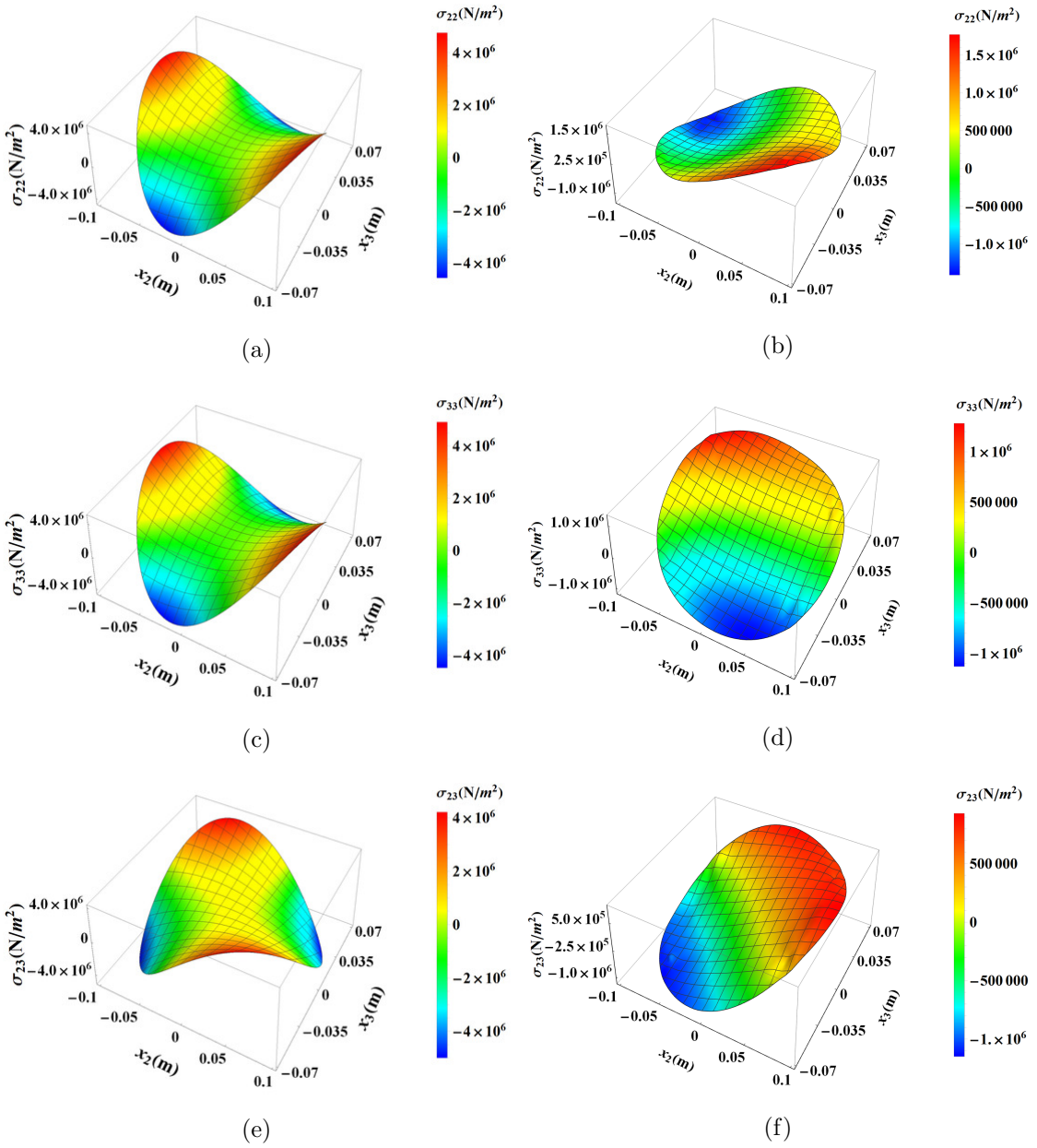

Figure 3.17: Surface plot of stress components σ_{22}, σ_{33} and σ_{23} obtained from (a,c,e) analytical results, (b,d,f) FEA analysis

used in this study. However, it can be modified by adjusting the elastic constants of the stiffness matrix.

The bend-twist coupling plot is provided in Fig. 3.19. Here, Fig. 3.19a corresponds to the current stiffness matrix of monoclinic material while Fig. 3.19b corresponds to the material used in article [1]. It can be observed here that the current and FEA coupling results are close to each other but for the presented monoclinic material properties; however, these results deviate from each other for the material properties of article [1]. Similar to the anisotropic case, in this case also, this deviation depends on the stiffness matrix. As mentioned previously, the potential cause of this discrepancy might be the absence of higher-order terms in the current solution. However, further investigation is

required to confirm this claim, which falls beyond the scope of the current study.

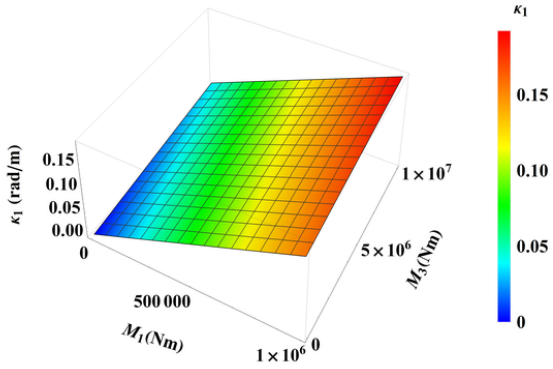

(a)

Figure 3.18: Twisting curvature (κ_1) due to twisting moment (M_1) and bending moment (M_3)

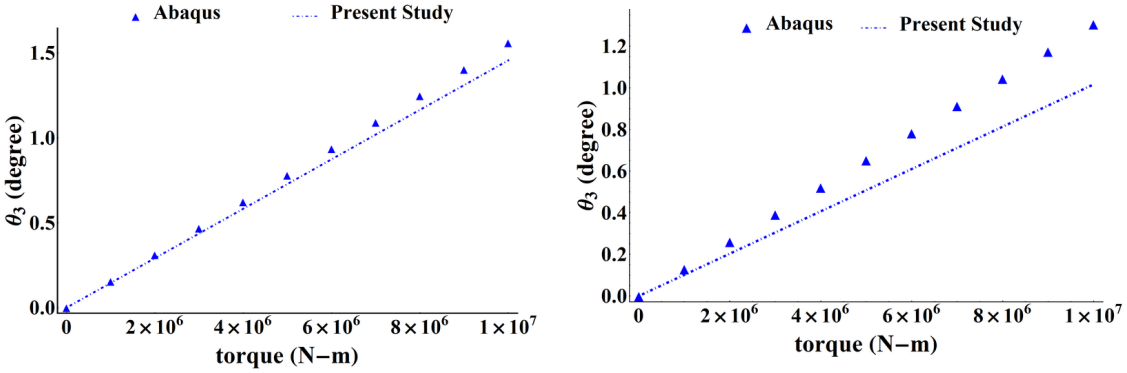

(a) (b)

Figure 3.19: Couling plots for two different stiffness matrix

3.2.3 Monoclinic With $x_1 - x_2$ Plane of Elastic Symmetry

For this case $C_{14} = C_{15} = C_{24} = C_{25} = C_{34} = C_{35} = C_{46} = C_{56} = 0$. Substitution of these elastic moduli in the stiffness matrix (3.1) produces stiffness matrix for this case. The cross-sectional analysis of the beam using VAM provides the cross-sectional rigidity constant matrix and constitutive relation. Hence, inverse-constitutive relation (3.51) can be obtained. This inverse-constitutive relation suggests that $\overline{\kappa}_1$ and $\overline{\kappa}_2$ are coupled for this case. So for this case $\overline{M}_1$ will influence $\overline{u}_3$ and similarly $\overline{M}_2$, $\overline{F}_3$ and f_3 will influence $\overline{\phi}_1$. The expressions of cross-sectional flexibility constants are provided in Appendix B.4.1.

$$\begin{Bmatrix} \overline{\gamma}_{11} \\ \overline{\kappa}_1 \\ \overline{\kappa}_2 \\ \overline{\kappa}_3 \end{Bmatrix} = \frac{1}{P} \begin{bmatrix} \overline{\Phi}_{11} & 0 & 0 & 0 \\ 0 & \overline{\Phi}_{22} & \overline{\Phi}_{23} & 0 \\ 0 & \overline{\Phi}_{23} & \overline{\Phi}_{33} & 0 \\ 0 & 0 & 0 & \overline{\Phi}_{44} \end{bmatrix} \begin{Bmatrix} F_1 \\ M_1 \\ M_2 \\ M_3 \end{Bmatrix} \tag{3.51}$$

The 3D displacement field for this case is given by Eqs. (3.52-3.54). The expressions of the 2D functions are provided in Appendix B.4.2.

$$\begin{aligned} u_1(x_1,x_2,x_3) =& \overline{u}_1(x_1) - x_2\overline{u}_2(x_1)' - x_3\overline{u}_3(x_1)' + \psi_{mx_3}(x_2,x_3)\ \overline{\phi}_1(x_1)' \\ &+ \mathcal{F}_1^1(x_2,x_3)\ \overline{u}_2(x_1)'' + \mathcal{F}_2^1(x_2,x_3)\ \overline{u}_3(x_1)'' + \mathcal{F}_3^1(x_2,x_3)\ \overline{u}_1(x_1)' \end{aligned} \tag{3.52}$$

$$\begin{aligned} u_2(x_1,x_2,x_3) =& \overline{u}_2(x_1) - x_3\overline{\phi}_1(x_1) + \mathcal{F}_1^2(x_2,x_3)\ \overline{u}_1(x_1)' + \mathcal{F}_2^2(x_2,x_3)\ \overline{u}_2(x_1)'' \\ &+ \mathcal{F}_3^2(x_2,x_3)\ \overline{u}_3(x_1)'' + \mathcal{F}_4^2(x_2,x_3)\overline{\phi}_1(x_1)' \end{aligned} \tag{3.53}$$

$$\begin{aligned} u_3(x_1,x_2,x_3) =& \overline{u}_3(x_1) + x_2\overline{\phi}_1(x_1) + \mathcal{F}_1^3(x_2,x_3)\ \overline{u}_1(x_1)' + \mathcal{F}_2^3(x_2,x_3)\ \overline{u}_2(x_1)'' \\ &+ \mathcal{F}_3^3(x_2,x_3)\ \overline{u}_3(x_1)'' + \mathcal{F}_4^3(x_2,x_3)\overline{\phi}_1(x_1)' \end{aligned} \tag{3.54}$$

The 1D quantities for this case are given by the Eqs. (3.55-3.58). These equations also confirm the coupling in these material beams.

$$\overline{u}_1(x_1) = \frac{94360\ \overline{F}_1}{17650107\ \pi ab\ P} x_1 \tag{3.55}$$

$$\begin{aligned} \overline{u}_2(x_1) =& \frac{188720\,(3L-x_1)\,x_1^2\ \overline{F}_2}{52950321\ \pi a^3 b\ P} + \frac{47180\left(6L^2-4Lx_1+x_1^2\right)x_1^2\ f_2}{52950321\ \pi a^3 b\ P} \\ &+ \frac{188720 x_1^2\ \overline{M}_3}{17650107\ \pi a^3 b\ P} \end{aligned} \tag{3.56}$$

$$\begin{aligned} \overline{u}_3(x_1) =& \frac{188720\,(3L-x_1)\,x_1^2\ \overline{F}_3}{52950321\ \pi ab^3\ P} + \frac{47180\left(6L^2-4Lx_1+x_1^2\right)x_1^2\ f_3}{52950321\pi ab^3 P} \\ &- \frac{188720 x_1^2\ \overline{M}_2}{17650107\ \pi ab^3\ P} - \frac{30977 x_1^2\ \overline{M}_1}{17650107\ \pi ab^3\ P} \end{aligned} \tag{3.57}$$

$$\begin{aligned} \overline{\phi}_1(x_1) =& \frac{5\left(426218129a^2+388302354b^2\right)x_1\ \overline{M}_1}{173747653308\ \pi a^3b^3\ P} - \frac{30977\,(2L-x_1)\,x_1\ \overline{F}_3}{17650107\ \pi ab^3\ P} \\ &- \frac{30977\left(3L^2-3Lx_1+x_1^2\right)x_1\ f_3}{52950321\ \pi ab^3\ P} \frac{61954 x_1\ \overline{M}_2}{17650107\ \pi ab^3\ P} \end{aligned} \tag{3.58}$$

Numerical Validation

This section provides the validation of all the current results by providing a comparison with FEA results. Here, surface plots of out-of-plane warping and normalized error are shown in Fig. 3.20. Similar to the previous cases, this out-of-plane warping plot has been obtained by applying the twisting moment only. The magnitude of this applied twisting moment is the same as used in previous cases. Here, in this case, also, this out-of-plane deformation due to the twisting of the cross-section has two parts (i) Saint-Venant warping deformation and (ii) bending deformation due to bend-twist coupling. The normalized error plot 3.20b reveals that the maximum error between the current analytical and

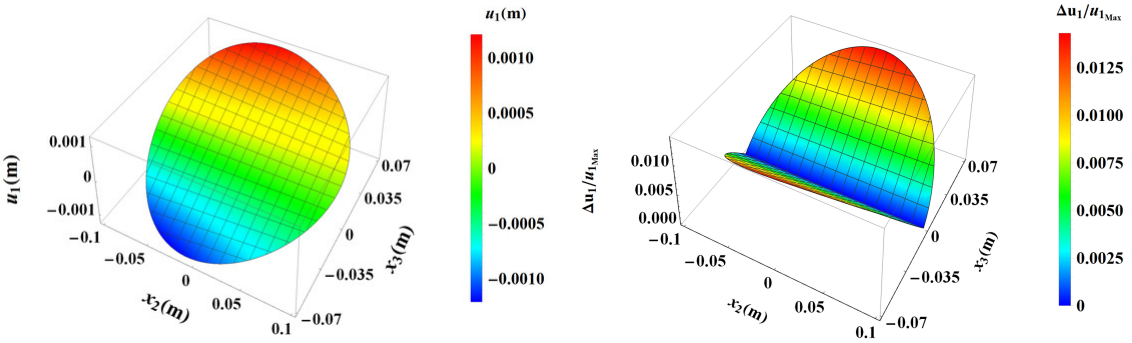

(a) (b)

Figure 3.20: Surface plot for out-of-plane warping (a) analytical expression (b) normalized error

FEA result is approximately 1.25% of maximum out-of-plane warping displacement. The normalized error plot indicates that the present analytical result has effectively captured the twisting deformation. Besides, it confirms the elastic coupling in these material beams. The plots of 3D displacement along the centroidal axis of the beam are provided in Fig. 3.21. The displacement components u_1 and u_3 obtained from both analytical and FEA are in close agreement for all three loading conditions. However, for u_2, both the results

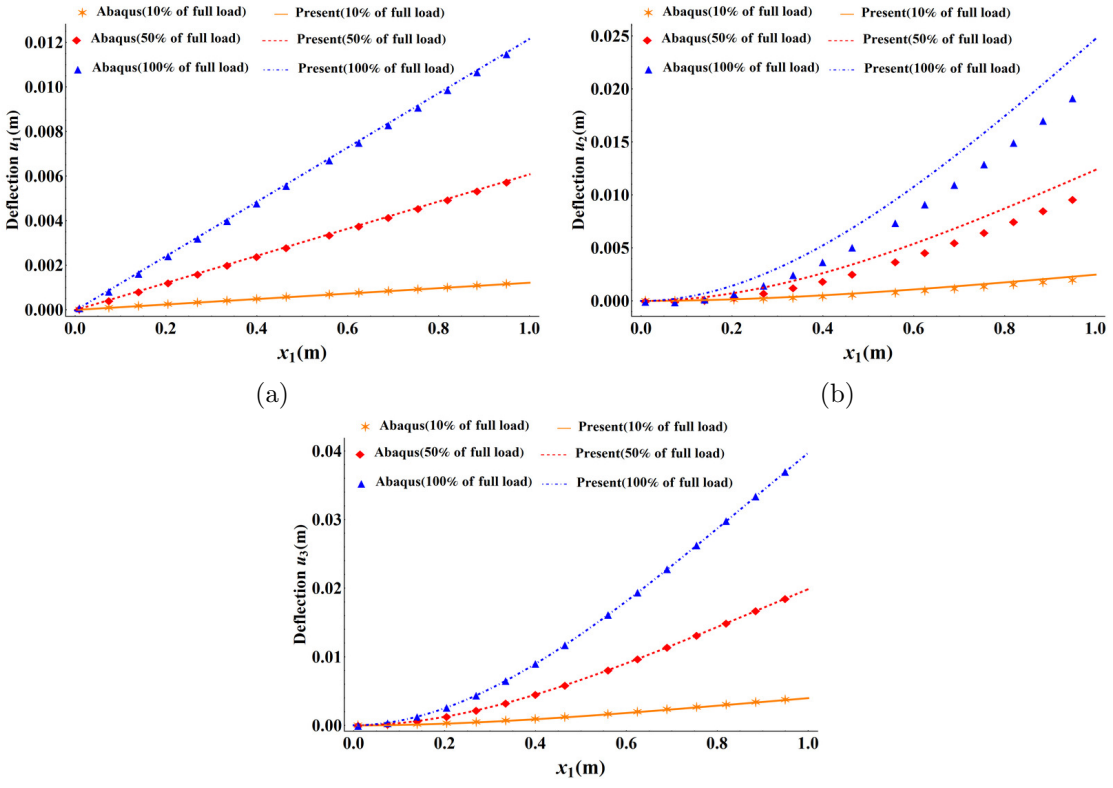

(a) (b)

(c)

Figure 3.21: Deflection of the beam along beam axis with three different loading conditions (a) deflection along x_1 coordinate direction (b) deflection along x_2 coordinate direction (c) deflection along x_3 coordinate direction

are agreed closely for lower loads, but as load increases, the analytical result starts to deviate from the FEA result. Notably, this deviation is prominent in the direction of the major semi-axis, indicating the possibility of the effect of omission of higher-order terms as discussed earlier. Further mathematical analysis is essential to ascertain this claim.

The surface plot of the 3D displacement field for this case has been provided in Fig. 3.22. The loading conditions remain the same as discussed earlier, except for the material of the beam. For this case, the relative error for u_1 and u_2 increased significantly to 15% and 34% and can be seen from the Fig. 3.22b and 3.22d respectively. The relative error for

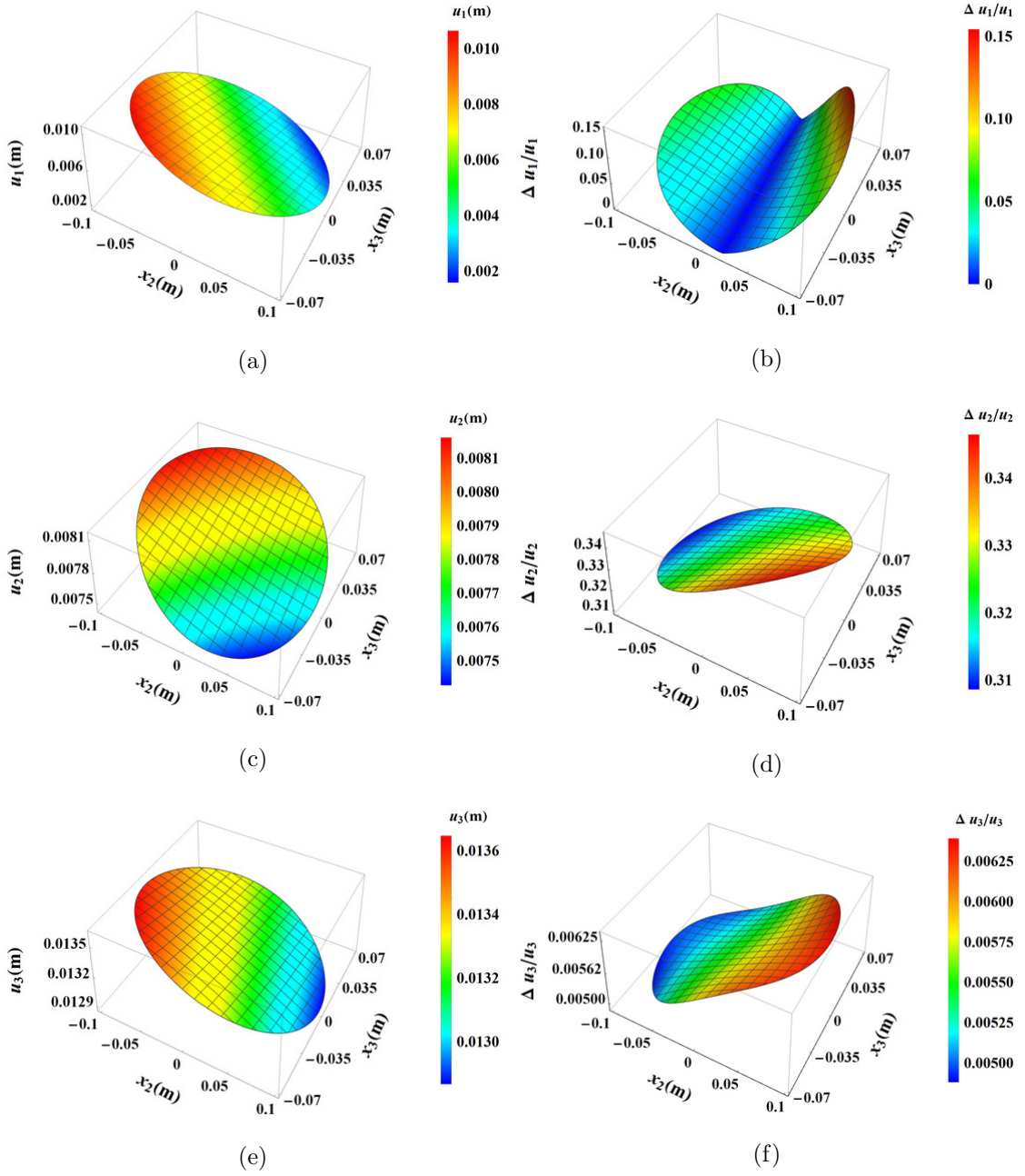

Figure 3.22: Surface plot of the displacement field and relative error w.r.t. FEA results (a,c,e) displacement along x_1, x_2 and x_3 coordinate axis due to analytical result, (b,d,f) relative error respectively

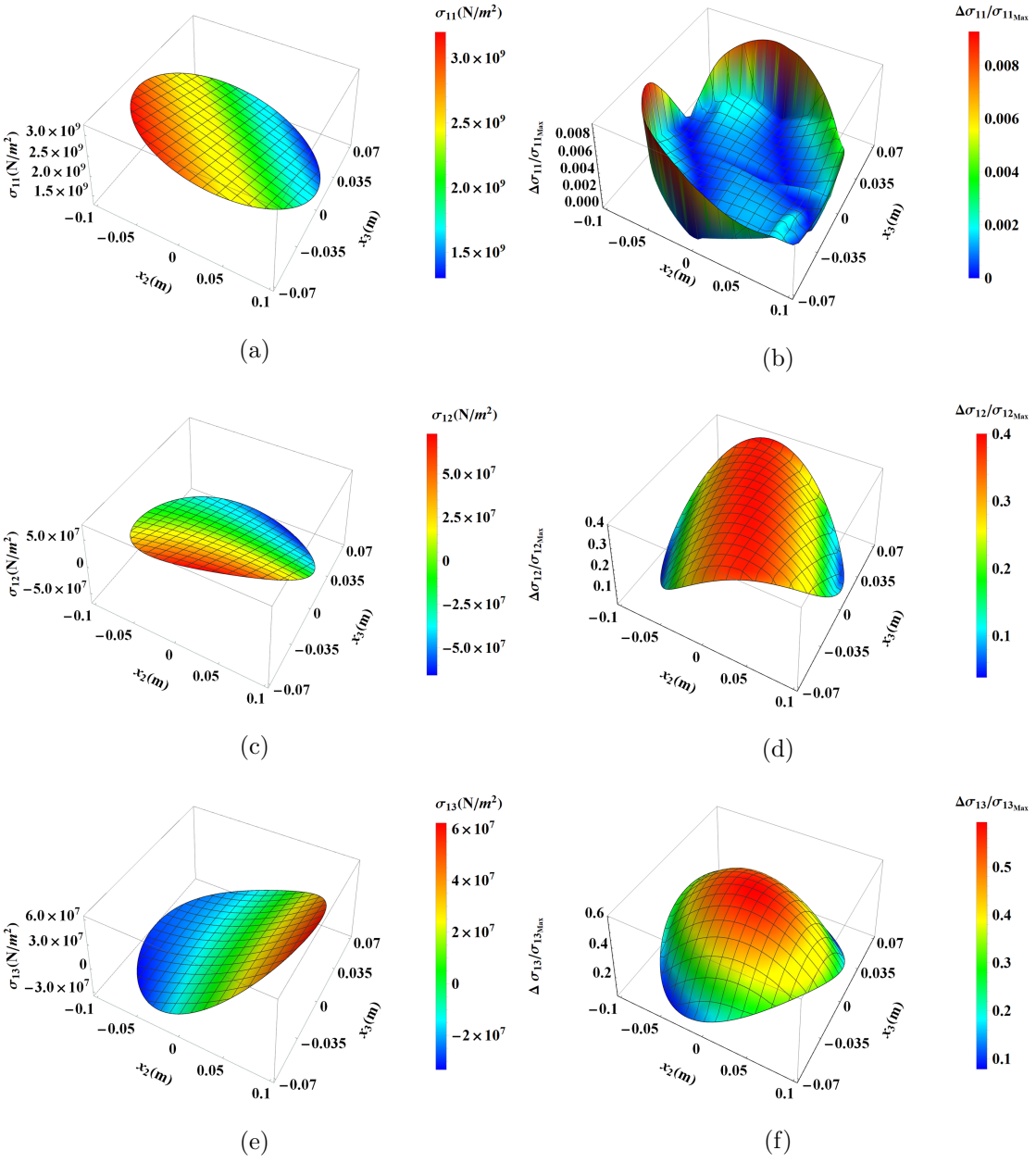

Figure 3.23: Surface plot of stress field and normalized error w.r.t. FEA result (a,c,e) analytical plot of σ_{11}, σ_{12} and σ_{13}, (b,d,f) relative error plot respectively

u_3 is still very small (0.6%); this can be seen from Fig. 3.22f. This significant error in 3D field variables u_1 and u_2 is rooted from the error in the 1D field variable $\overline{u}_2$ as both the u_1 and u_2 are function of $\overline{u}_2$.

The surface plots of stress components σ_{11}, σ_{12}, and σ_{13}, along with their corresponding normalized errors, are provided in Fig. 3.23. Similar to previous cases, normalization has been performed using the corresponding maximum value. In this case, the stress component σ_{11} is effectively captured, as shown by the normalized error plot in Fig. 3.23b. However, the other stress components σ_{12} and σ_{13} exhibit large errors compared to FEA results due to the omission of shear stress effects, as explained in previous cases.

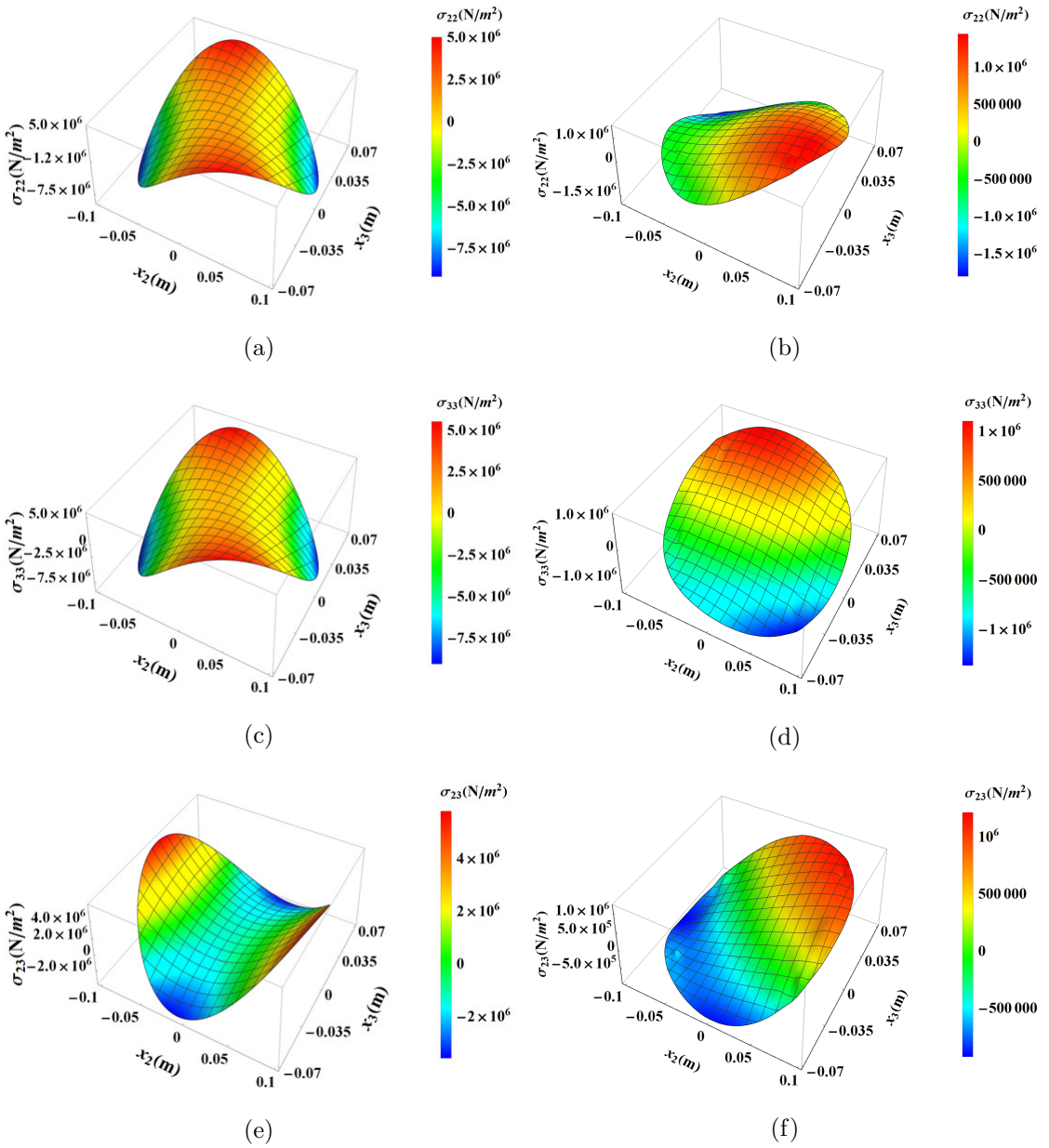

Figure 3.24: Surface plot of stress components σ_{22}, σ_{33} and σ_{23} obtained from (a,c,e) analytical results, (b,d,f) FEA analysis

In this case, the stress components σ_{22}, σ_{33}, and σ_{23} are found to be non-zero. Therefore, these stress components obtained from the current analytical results and FEA have been plotted and are presented in Fig. 3.24. Similarly, in this case, the stress distribution obtained from the two approaches differs but remains of the same order. As discussed earlier, the possible reason might be the absence of higher-order terms; hence, this result can be improved by using a higher-order solution. However, this is beyond the scope of the current study, as we are primarily interested in the characteristic behavior of the anisotropic beam.

The surface plot showing the influence of direct (M_1) and coupling (M_2) action on the

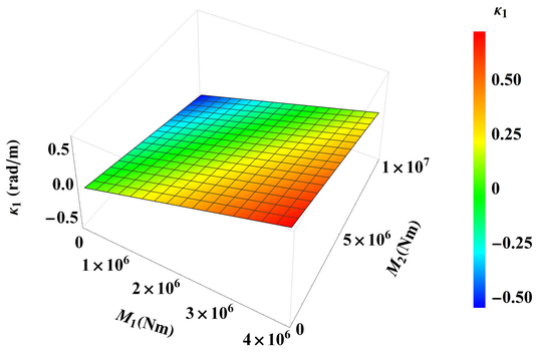

(a)

Figure 3.25: Twisting curvature (κ_1) due to twisting moment (M_1) and bending moment (M_2)

twisting curvature (κ_1)is provided in Fig. 3.25. By comparing this figure with Fig. 3.7, it can be observed that the coupling action for the current monoclinic material beam is of the same order as that of the anisotropic material beam used in this study.

In Fig. 3.26, bend-twist coupling plots are provided. Similar to the previous case

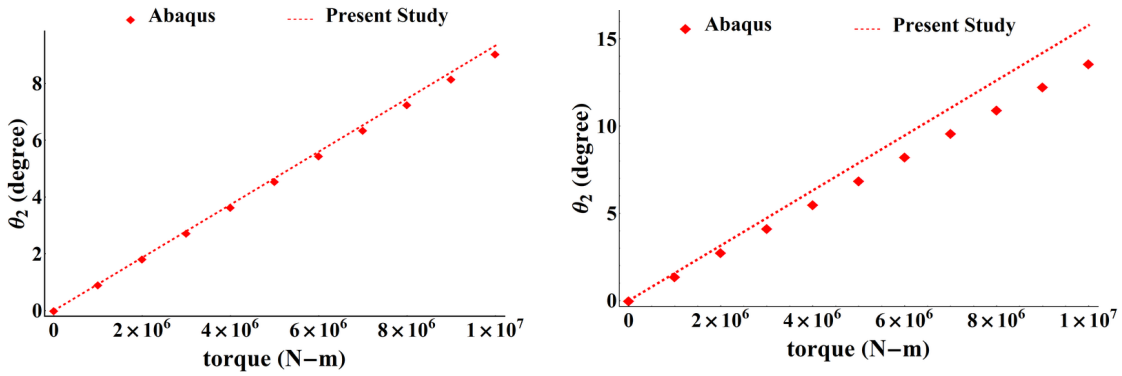

(a) (b)

Figure 3.26: Couling plots for two different stiffness matrix

of monoclinic material, Fig. 3.26a corresponds to the current stiffness matrix of the monoclinic material beam, and Fig. 3.26b corresponds to the stiffness matrix provided in the article [1]. Similar to the previous case of monoclinic material beam here in this case also it can be observed here that the current and FEA coupling results are close to each other for the presented monoclinic material properties; however, these two results deviate from each other for the material properties of article [1].

From all the discussion, it can be observed that the discrepancy between current and FEA results is only found in cases involving coupling. For all uncoupled cases, the results obtained from the two approaches are in great agreement. One possible reason for this discrepancy might be the presence of certain terms due to coupling, which highly depends on the order of material constants. These terms are not captured in the current solution as these terms might be migrated to higher-order solutions since we consider

material constants of the same order. Therefore, improving the solution may entail either incorporating a higher-order solution or considering the material order. There might be other reasons as well; however, further investigation is needed to reach a solid conclusion, which is beyond the scope of the current study.

3.3 Concluding Remarks

This chapter presented the analysis of the homogeneous material beams having material anisotropy level higher than orthotropy, i.e., monoclinic material and complete anisotropic material. The analysis is semi-analytical, as stiffness constants are assigned with numerical values at the beginning of the procedure. This chapter and the previous chapter 2 presented a comprehensive analysis providing elastic coupling behavior in anisotropic beams. This analysis suggests that beams with material anisotropy level up to orthotropy exhibit no elastic coupling. The elastic coupling is first observed in monoclinic material beams with one exception. Monoclinic material beams having the cross-sectional plane as the plane of elastic symmetry also do not show elastic coupling. The results suggest that beams do not provide a completely coupled system, even for the complete anisotropic but homogeneous material. The extensional strain γ_{11} remains uncoupled from all the twisting curvature κ_1 and bending curvatures κ_α. One more important observation of this study is that the plane stress assumption is violated for all the coupled cases, which is the basis of many anisotropic material beam models.

Chapter 4

Anisotropic Inhomogeneous Beam Analysis

This chapter presents the analysis of anisotropic but inhomogeneous beams. The laminate composite provides the most feasible way to model these types of beams. However, these structures tend to deform whenever there is a change in temperature and moisture. These deformations are collectively termed hygrothermal instabilities. In real-life applications, these structures are exposed to atmospheric conditions, hence are subjected to temperature and moisture change. Therefore, to maintain these structures' functionality under atmospheric conditions, it becomes necessary to eliminate these hygrothermal instabilities. To achieve the hygrothermal stability of laminated composite beams, conditions of hygrothermal stability have been derived. A laminated structure satisfying these hygrothermal stability conditions does not show in-plane shear and out-of-plane bending and twisting deformation due to temperature and moisture change. In this work, hygrothermally stable stacking sequences have been provided for three modes of elastic coupling, i.e., extension-twist, bend-twist, and extension-bend. These proposed stacking sequences have been optimized analytically and optimized results have been compared with the optimized result obtained from the conventional numerical approach. The optimized stacking sequences obtained from two approaches have been examined for the robustness towards small perturbation in optimized fiber angles, using sensitivity analysis. At last, a mathematical formulation of strip-like composite beam has been provided. It provides the kinematic equivalence between 1D beam parameters and 2D plate parameters. Classical Laminate Plate Theory (CLPT) has been employed along with the kinematic equivalence relation to obtained the deformation field of this strip-like beam.

4.1 Derivation of Necessary and Sufficient Conditions for Hygrothermal Stability

In the current work, Classical Laminate Theory (CLT) has been used to derive the necessary and sufficient conditions for hygrothermal stability. CLT provides the constitutive law, which relates the force and moment resultant to mid-plane strains and curvatures of laminate. It should be kept in mind that the current work provides the study of thermal effects only for convenience. However, the term "hygrothermal stability" has been used to underline the fact that the mathematical formulation of the hygral effect is

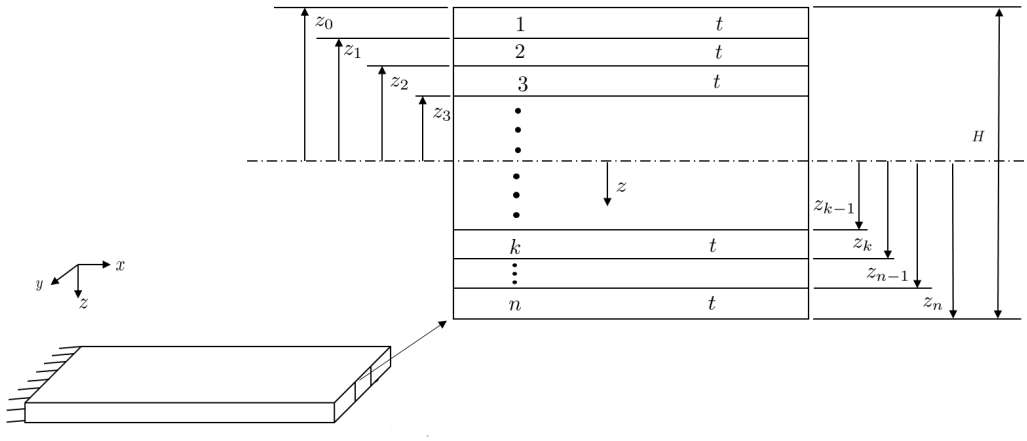

Figure 4.1: Schematic of Laminate

similar to that of the thermal effect. Hence, the presented mathematical formulation of the thermal effect can easily be extended to the hygral effect. The constitutive relation in the presence of mechanical loading along with thermal loading is given as [109].

$$\begin{Bmatrix} N_x + N_x^T \\ N_y + N_y^T \\ N_{xy} + N_{xy}^T \\ M_x + M_x^T \\ M_y + M_y^T \\ M_{xy} + M_{xy}^T \end{Bmatrix} = \begin{bmatrix} A_{11} & A_{12} & A_{16} & B_{11} & B_{12} & B_{16} \\ A_{12} & A_{22} & A_{26} & B_{12} & B_{22} & B_{26} \\ A_{16} & A_{26} & A_{66} & B_{16} & B_{26} & B_{66} \\ B_{11} & B_{12} & B_{16} & D_{11} & D_{12} & D_{16} \\ B_{12} & B_{22} & B_{26} & D_{12} & D_{22} & D_{26} \\ B_{16} & B_{26} & B_{66} & D_{16} & D_{26} & D_{66} \end{bmatrix} \begin{Bmatrix} \varepsilon_x^o \\ \varepsilon_y^o \\ \gamma_{xy}^o \\ \kappa_x \\ \kappa_y \\ \kappa_{xy} \end{Bmatrix} \tag{4.1}$$

where ε_x^o, ε_y^o and γ_{xy}^o represents mid-plane strains while κ_x, κ_y and κ_{xy} represents mid-plane curvature of the laminate. A_{pq} and D_{pq} are extensional and bending stiffnesses, respectively. B_{pq} are extension-bending coupling stiffnesses. These three types of stiffnesses are defined as,

$$A_{pq} = \sum_{k=1}^{n} \overline{Q}_{pq(k)}(z_k - z_{k-1}) \tag{4.2}$$

$$B_{pq} = \frac{1}{2}\sum_{k=1}^{n} \overline{Q}_{pq(k)}(z_k^2 - z_{k-1}^2) \tag{4.3}$$

$$D_{pq} = \frac{1}{3}\sum_{k=1}^{n} \overline{Q}_{pq(k)}(z_k^3 - z_{k-1}^3) \tag{4.4}$$

where n is the total number of plies in laminate, z_i (positive in downward direction) distance of from the mid-plane of the laminate and t is the thickness of the ply as shown in Fig. 4.1. Besides, in this Fig. 4.1, H represents the total thickness of the laminate. In Eq. (4.1) N_x, N_y and N_{xy} are force resultant and M_x, M_y and M_{xy} are moment resultant due to mechanical loading. The superscripted terms represent the quantity due to thermal

loading. The thermal force and moment caused by temperature ΔT [109] are:

$$\begin{Bmatrix} N_x^T \\ N_y^T \\ N_{xy}^T \end{Bmatrix} = \Delta T \sum_{k=1}^{n} \left[\overline{Q}\right]_k \left\{\overline{\alpha}\right\}_k (z_k - z_{k-1}) \tag{4.5}$$

$$\begin{Bmatrix} M_x^T \\ M_y^T \\ M_{xy}^T \end{Bmatrix} = \frac{1}{2}\Delta T \sum_{k=1}^{n} \left[\overline{Q}\right]_k \left\{\overline{\alpha}\right\}_k (z_k^2 - z_{k-1}^2) \tag{4.6}$$

In equations (4.2 - 4.6), $\overline{Q}_{pq(k)}$ and $\{\overline{\alpha}\}_k$ represents reduced stiffness coefficient in transformed coordinate system, and transformed thermal expansion coefficient for the k_{th} laminae respectively. Transformation of stiffness and thermal coefficient from material coordinate to the laminate coordinate system for specially orthotropic lamina is given as

$$\left[\overline{Q}\right] = \left[T\right]^{-1} \left[Q\right] \left[T\right]^{-T} \tag{4.7}$$

$$\left\{\overline{\alpha}\right\} = \begin{Bmatrix} \overline{\alpha}_x \\ \overline{\alpha}_y \\ \overline{\alpha}_{xy} \end{Bmatrix} = \left[T\right]^T \begin{Bmatrix} \alpha_1 \\ \alpha_2 \\ 0 \end{Bmatrix} \tag{4.8}$$

where,

$$\left[Q\right] = \begin{bmatrix} Q_{11} & Q_{12} & 0 \\ Q_{12} & Q_{22} & 0 \\ 0 & 0 & Q_{66} \end{bmatrix} \quad \text{and} \quad \left[T\right] = \begin{bmatrix} \cos^2\theta & \sin^2\theta & 2\ \cos\theta\ \sin\theta \\ \sin^2\theta & \cos^2\theta & -2\ \cos\theta\ \sin\theta \\ -\cos\theta\ \sin\theta & \cos\theta\ \sin\theta & \cos^2\theta - \sin^2\theta \end{bmatrix}$$

For the convenience and simplicity of the expressions, the transformed coefficients of stiffness $\overline{Q}_{pq}$ are written in the invariant form given by Tsai[110].

$$\begin{aligned} \overline{Q}_{11} &= U_1 + U_2 \cos 2\theta + U_3 \cos 4\theta \\ \overline{Q}_{22} &= U_1 - U_2 \cos 2\theta + U_3 \cos 4\theta \\ \overline{Q}_{66} &= -U_3 \cos 4\theta + U_5 \\ \overline{Q}_{12} &= -U_3 \cos 4\theta + U_4 \\ \overline{Q}_{16} &= \frac{1}{2} U_2 \sin 2\theta + U_3 \sin 4\theta \\ \overline{Q}_{26} &= \frac{1}{2} U_2 \sin 2\theta - U_3 \sin 4\theta \end{aligned} \tag{4.9}$$

where,

$$\begin{aligned}
U_1 =& \frac{1}{8}\left(3Q_{11} + 2Q_{12} + 3Q_{22} + 4Q_{66}\right) \\
U_2 =& \frac{1}{2}\left(Q_{11} - Q_{22}\right) \\
U_3 =& \frac{1}{8}\left(Q_{11} - 2Q_{12} + Q_{22} - 4Q_{66}\right) \\
U_4 =& \frac{1}{8}\left(Q_{11} + 6Q_{12} + Q_{22} - 4Q_{66}\right) \\
U_5 =& \frac{1}{8}\left(Q_{11} - 2Q_{12} + Q_{22} + 4Q_{66}\right)
\end{aligned} \tag{4.10}$$

In the above equations U_r $(r = 1, 2, 3, 4, 5)$ are invariant coefficients of laminates. By using relations (4.2 - 4.4), (4.9) and (4.10), the stiffness coefficients can be calculated and given as follow

$$\begin{Bmatrix} A_{11} \\ A_{12} \\ A_{22} \\ A_{66} \\ A_{16} \\ A_{26} \end{Bmatrix} = H \begin{bmatrix} 1 & \zeta_1 & \zeta_2 & 0 & 0 \\ 0 & 0 & -\zeta_2 & 1 & 0 \\ 1 & -\zeta_1 & \zeta_2 & 0 & 0 \\ 0 & 0 & -\zeta_2 & 0 & 1 \\ 0 & \frac{\zeta_3}{2} & \zeta_4 & 0 & 0 \\ 0 & \frac{\zeta_3}{2} & -\zeta_4 & 0 & 0 \end{bmatrix} \begin{Bmatrix} U_1 \\ U_2 \\ U_3 \\ U_4 \\ U_5 \end{Bmatrix} \tag{4.11}$$

$$\begin{Bmatrix} B_{11} \\ B_{12} \\ B_{22} \\ B_{66} \\ B_{16} \\ B_{26} \end{Bmatrix} = \frac{H^2}{2} \begin{bmatrix} 0 & \zeta_5 & \zeta_6 & 0 & 0 \\ 0 & 0 & -\zeta_6 & 0 & 0 \\ 0 & -\zeta_5 & \zeta_6 & 0 & 0 \\ 0 & 0 & -\zeta_6 & 0 & 0 \\ 0 & \frac{\zeta_7}{2} & \zeta_8 & 0 & 0 \\ 0 & \frac{\zeta_7}{2} & -\zeta_8 & 0 & 0 \end{bmatrix} \begin{Bmatrix} U_1 \\ U_2 \\ U_3 \\ U_4 \\ U_5 \end{Bmatrix} \tag{4.12}$$

$$\begin{Bmatrix} D_{11} \\ D_{12} \\ D_{22} \\ D_{66} \\ D_{16} \\ D_{26} \end{Bmatrix} = \frac{H^3}{12} \begin{bmatrix} 1 & \zeta_9 & \zeta_{10} & 0 & 0 \\ 0 & 0 & -\zeta_{10} & 1 & 0 \\ 1 & -\zeta_9 & \zeta_{10} & 0 & 0 \\ 0 & 0 & -\zeta_{10} & 0 & 1 \\ 0 & \frac{\zeta_{11}}{2} & \zeta_{12} & 0 & 0 \\ 0 & \frac{\zeta_{11}}{2} & -\zeta_{12} & 0 & 0 \end{bmatrix} \begin{Bmatrix} U_1 \\ U_2 \\ U_3 \\ U_4 \\ U_5 \end{Bmatrix} \tag{4.13}$$

where,

$$
\begin{aligned}
&H = n\ t \qquad z_k = kt - \frac{nt}{2} \\
&(\zeta_1, \zeta_2, \zeta_3, \zeta_4) = \sum_{k=1}^{n} \frac{1}{n}(\cos 2\theta_k, \cos 4\theta_k, \sin 2\theta_k, \sin 4\theta_k) \\
&(\zeta_5, \zeta_6, \zeta_7, \zeta_8) = \sum_{k=1}^{n} \left(\frac{2k-n-1}{n^2}\right)(\cos 2\theta_k, \cos 4\theta_k, \sin 2\theta_k, \sin 4\theta_k) \\
&(\zeta_9, \zeta_{10}, \zeta_{11}, \zeta_{12}) = \sum_{k=1}^{n} \left[\frac{12k^2 - 12k(n+1) + 3n^2 + 6n + 4}{n^3}\right](\cos 2\theta_k, \cos 4\theta_k, \sin 2\theta_k, \sin 4\theta_k)
\end{aligned}
\tag{4.14}
$$

Here, ζs are lamination parameter. It should be noted that the thickness (t) of each ply in the laminate is assumed to be the same. In a similar fashion thermal force (Eq.4.5) and moment (Eq. 4.6) can be rewritten in the invariant form, using Eqs. (4.8), (4.9) and (4.14) are:

$$
\begin{Bmatrix} N_x^T \\ N_y^T \\ N_{xy}^T \end{Bmatrix} = \frac{1}{2} H\ \Delta T \begin{Bmatrix} U_1^T + U_2^T\ \zeta_1 \\ U_1^T - U_2^T\ \zeta_1 \\ U_2^T\ \zeta_3 \end{Bmatrix} \tag{4.15}
$$

$$
\begin{Bmatrix} M_x^T \\ M_y^T \\ M_{xy}^T \end{Bmatrix} = \frac{1}{4} H^2\ U_2^T\ \Delta T \begin{Bmatrix} \zeta_5 \\ -\zeta_5 \\ \zeta_7 \end{Bmatrix} \tag{4.16}
$$

where U_1^T and U_2^T are another invariant terms due to thermal loading and given as

$$
\begin{aligned}
U_1^T &= \alpha_1 U_1 + \alpha_1 U_2 + \alpha_1 U_4 + \alpha_2 U_1 - \alpha_2 U_2 + \alpha_2 U_4 \\
U_2^T &= \alpha_1 U_1 + \alpha_1 U_2 + 2\alpha_1 U_3 - \alpha_1 U_4 - \alpha_2 U_1 + \alpha_2 U_2 - 2\alpha_2 U_3 + \alpha_2 U_4
\end{aligned}
$$

Two types of distortions are present in the laminates due to the temperature and moisture change. First, in-plane distortion due to the shear strain and out-of-plane distortion due to bending and twisting. These hygrothermal distortions can be eliminated by nullifying thermal shear (γ_{xy}^T) and thermal curvatures ($\kappa_x^T, \kappa_y^T, \kappa_{xy}^T$). Richard et al. [95] shows that the necessary and sufficient conditions for the curvature stable laminates can be achieved by satisfying any one of the following two conditions

$$
[B] = 0 \tag{4.17}
$$

or

$$
\begin{aligned}
&N_x^T = N_y^T \\
&N_{xy}^T = M_x^T = M_y^T = M_{xy}^T = 0
\end{aligned}
\tag{4.18}
$$

From Eq. (4.12), it is clear that the first condition i.e. $[B] = 0$ is satisfied when $\zeta_5 = \zeta_6 = \zeta_7 = \zeta_8 = 0$. It can also be observed from Eq. (4.16) that for these conditions thermal moment resultants ($M_x^T = M_y^T = M_{xy}^T$) are also zero. This condition ultimately leads to zero thermal curvature and can be verified from Eq. (4.1) in the absence of mechanical loading.

Now, by examining the Eqs. (4.15) and (4.16), it is clear that for $\zeta_1 = \zeta_3 = \zeta_5 = \zeta_7 = 0$, the second set of necessary and sufficient conditions for hygrothermal stability (Eq. 4.18) is satisfied. The in-plane strains and curvature terms in the absence of mechanical loading can be calculated using Eq. (4.1) and obtained as

$$\begin{aligned} \varepsilon_x^T = \varepsilon_y^T &= \frac{U_1^T}{2(U_1 + U_2)} \Delta T \\ \varepsilon_{xy}^T = \kappa_x^T = \kappa_y^T = \kappa_{xy}^T &= 0 \end{aligned} \tag{4.19}$$

The laminate having the above state of strain refers as the hygrothermal isotropic laminate. It can be concluded that $\zeta_1 = \zeta_3 = \zeta_5 = \zeta_7 = 0$ is one of the two conditions for hygrothermal isotropic laminate. The second condition is proven by Chen [96] which states that if principle coefficients of thermal expansion (or contraction) are equal i.e. $\alpha_1 = \alpha_2$ then these do not change with the direction.

The hygrothermal stability condition (Eq. 4.17) eliminates out-of-plane deformation due to hygrothermal bending and twisting only; it does not eliminate in-plane deformation due to hygrothermal shear. The hygrothermal stability condition (Eq. 4.18) eliminates both the in-plane and out-of-plane hygrothermal deformations. This work uses the second set of hygrothermal stability conditions (Eq. 4.18) to achieve hygrothermal stability in the proposed stacking sequences. The procedure to obtain these hygrothermally stable stacking sequences, their optimization, and sensitivity analysis have been provided in the following sections.

4.2 Extention-Twist Coupling with Hygrothermal Stable Stacking

Hygrothermal stable laminate with extension-twist coupling should have a ply layup that provides non-zero coupling coefficients B_{16} and B_{26} as well as satisfies the hygrothermal stability conditions discussed in the previous section 4.1. Winckler, in his work [104], suggested that the two laminates, each with hygrothermal isotropy but anti-symmetric to each other when combined together, formed hygrothermal stable laminate with extension-twisting coupling. The author presented a 8-ply laminate $[\theta, (\theta{+}90)_2, \theta, -\theta, (-\theta{+}90)_2, -\theta]_T$ which fulfills all these conditions. This work extends the Winckler-like stacking sequence to a generalized case for laminate having $4i$ (i = 2,3,4...), i.e., the total number of plies $n = 4i$. Here i does not start with 1 because, in this case, the laminate will have a total of 4 plies, and no hygrothermal stable asymmetric laminate is possible, as proved by Cross et al. [95]. Depending on whether i is even or odd, the

proposed stacking sequence can be divided into cases and sub-cases. This classification is given in Fig. 4.2b and discussed in the following subsections.

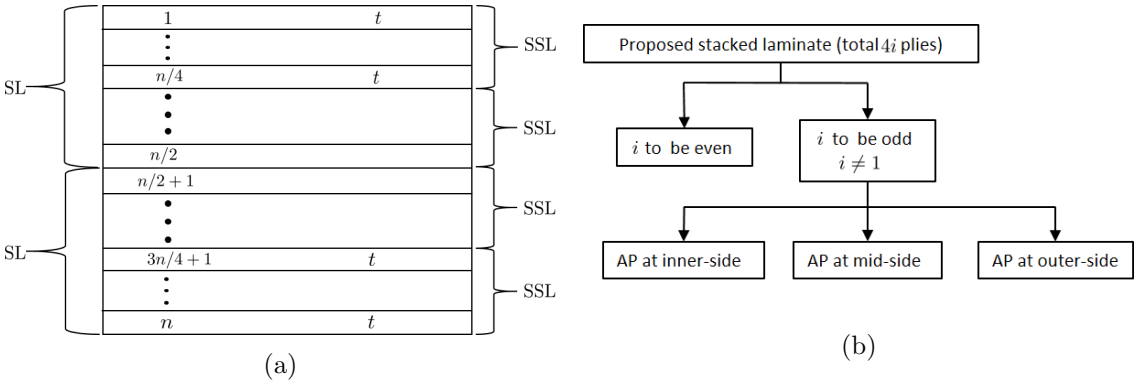

Figure 4.2: (a) division and Sub-division of Laminate (b) Case and sub-cases involved in proposed stacking sequence based on i

4.2.1 When i to be an even number

In this case, the generalized stacking sequence for hygrothermal stable laminate with extension-twist coupling is achieved by following the steps given below

(a) Apply anti-symmetric condition about the mid-plane of the laminate. This will reduce total independent fiber angles from $4i$ to $2i$. This step results in two Sub-Laminate (SL) as shown in figure (4.2a).

(b) Apply symmetric condition in one of the SLs about its own mid-plane. Due to the first step, the fiber angles of the other SL will change accordingly. This step further reduces the independent fiber angles from $2i$ to i and also produces four Sub-Sub-Laminate (SSL).

(c) In the final step half of independent fiber angles $\left(\frac{i}{2}\right)$ can be taken randomly let say ϕ_k ($k = 1, 2, 3...\frac{i}{2}$) but the remaining $\frac{i}{2}$ fiber angles has to be taken in the form $(90° + \phi_k)$. This step reduces total independent fiber angles to $\frac{i}{2}$. These total fiber angles (ϕ_k and $90° + \phi_k$) can be arranged in any random order in SSL or in factorial (i) ways.

By following these steps, for given i the resultant hygrothermal laminate can be obtained in factorial (i) ways and each laminate will have total $\frac{i}{2}$ independent fiber angles. The schematic of laminate with SSLs and SLs is shown in the figure (4.2a). The laminate with stacking sequence obtained by following the above steps will always satisfy the second set of hygrothermal stability conditions (4.18) and show extension-twist coupling.
For better understanding, let's take an example with $i = 4$. For hygrothermal stability $\zeta_1, \zeta_3, \zeta_5$ and ζ_7 has to be made zero. As discussed above, after the application of anti-symmetric and symmetric conditions, there will be only 4 independent fiber angles in

SSL, and the resultant $\zeta_1, \zeta_3, \zeta_5$ and ζ_7 terms will be of the following form

$$(\zeta_1, \zeta_3, \zeta_5, \zeta_7) = \left(\tfrac{1}{4}\left(\cos 2\theta_1 + \cos 2\theta_2 + \cos 2\theta_3 + \cos 2\theta_4\right), 0, 0, \right. \\ \left. \tfrac{1}{8}\left(-\sin 2\theta_1 - \sin 2\theta_2 - \sin 2\theta_3 - \sin 2\theta_4\right) \right) \tag{4.20}$$

Here it can be seen that ζ_3 and ζ_5 are zero. Now to make ζ_1 and ζ_7 zero, two fiber angles out of four independent fiber angles (θ_1, θ_2, θ_3 and θ_4) can be taken randomly as ϕ_1 and ϕ_2 and remaining two fiber angles has to be made randomly $(90^\circ + \phi_1)$ and $(90^\circ + \phi_2)$. This selection of fiber angles makes ζ_1 and ζ_7 also zero and can be verified by putting these angles in Eq. 4.20. Hence, the hygrothermal stability condition has been satisfied. This choice of stacking sequence also makes ζ_4, ζ_6, ζ_{11} and ζ_{12} zero. In this case, for any allowed even value of i, the generalized expression for the coefficients of $[A]$ and $[B]$ are given as

$$\begin{aligned} (A_{11} = A_{22},\ A_{12},\ A_{66},\ A_{16},\ A_{26}) &= \frac{2}{i} H \left(\frac{i}{2} U_1 + U_3 S_c,\ \frac{i}{2} U_4 - U_3 S_c,\ \frac{i}{2} U_5 - U_3 S_c,\ 0,\ 0 \right) \\ (B_{11},\ B_{12},\ B_{22},\ B_{66},\ B_{16},\ B_{26}) &= \frac{H^2}{2i} (0,\ 0,\ 0,\ 0,\ -U_3 S_s,\ U_3 S_s) \end{aligned} \tag{4.21}$$

where $S_c = \sum_{k=1}^{\frac{i}{2}} \cos 4\phi_k$ and $S_s = \sum_{k=1}^{\frac{i}{2}} \sin 4\phi_k$. In the above equation, coefficients of the $[D]$ matrix are not given because these depend on the stacking sequence and do not have invariant expressions. Here it should be noted that whenever $\frac{i}{2}$ is a even number, the S_c and S_s can be made zero by taking $\frac{i}{4}$ angles as ψ and the remaining $\frac{i}{4}$ angles as $(45^\circ + \psi)$. This ultimately makes the B matrix zero.

To consider a specific case, when all independent fiber angles (ϕ_k) are taken as equal, the term S_c and S_s will reduce to $\frac{i}{2}\cos 4\phi$ and $\frac{i}{2}\sin 4\phi$ respectively. The coefficient of $[A]$ and $[B]$ matrices will be rewritten as

$$\begin{aligned} (A_{11} = A_{22},\ A_{12},\ A_{66},\ A_{16},\ A_{26}) &= H\left(U_1 + U_3 \cos 4\phi,\ U_4 - U_3 \cos 4\phi,\ U_5 - U_3 \cos 4\phi,\ 0,\ 0\right) \\ (B_{11},\ B_{12},\ B_{22},\ B_{66},\ B_{16},\ B_{26}) &= \frac{H^2}{4} (0,\ 0,\ 0,\ 0,\ -U_3 \sin 4\phi,\ U_3 \sin 4\phi) \end{aligned} \tag{4.22}$$

4.2.2 When i is to be an odd number

In this case, $\frac{i}{2}$ is not a whole number, so the steps followed in the condition when i is even cannot be implemented directly. One additional step needs to be added after the first step i.e. anti-asymmetric condition and subsequent steps remain as it is. Two Adjacent Plies (AP) need to be preassigned 0° and 90° fiber angles in SL. Three positions of these AP are possible, as shown in Fig. 4.3. When these AP are placed at the mid-plane of laminate in SL, it refers as the inner-side. Similarly, the mid-side and outer-side refer to the position where AP is situated at the mid and most exterior of SL, respectively. The introduction of AP after applying the anti-symmetric condition reduces total unknown independent fiber angles to $2i - 2$. After this step, the second and third conditions that are used for i to be

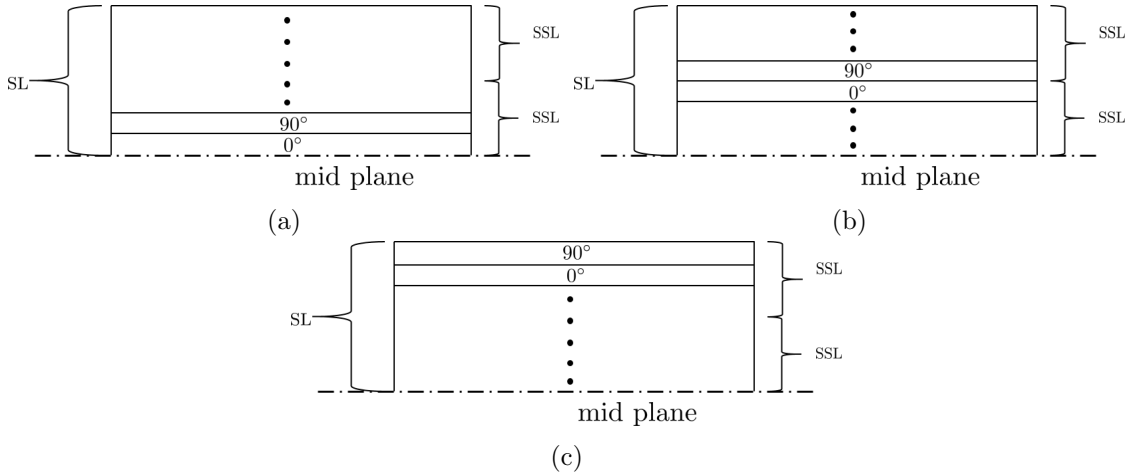

Figure 4.3: Position of 0° and 90° AP in SL (a) inner-side (b) mid-side (c) outer-side

even conditions can be implemented in this case also. For better understanding, let's take an example with $i = 5$. In this case, after applying the anti-symmetric condition ζ_3 and ζ_5 will vanish, and expression for ζ_1 and ζ_7 is given as

$$\begin{aligned}\zeta_1 &= \frac{1}{10}\big(\cos 2\theta_1 + \cos 2\theta_2 + \cos 2\theta_3 + \cos 2\theta_4 + \cos 2\theta_5 + \cos 2\theta_6 + \cos 2\theta_7 \\ &\quad + \cos 2\theta_8 + \cos 2\theta_9 + \cos 2\theta_{10}\big) \qquad (4.23)\\ \zeta_7 &= \frac{1}{200}\big(-19\sin 2\theta_1 - 17\sin 2\theta_2 - 15\sin 2\theta_3 - 13\sin 2\theta_4 - 11\sin 2\theta_5 \\ &\quad -9\sin 2\theta_6 - 7\sin 2\theta_7 - 5\sin 2\theta_8 - 3\sin 2\theta_9 - \sin 2\theta_{10}\big) \qquad (4.24)\end{aligned}$$

Implementation of the remaining condition depends on the position of the AP and will be discussed in each case separately. Here it should be noted that there are other combinations of 0° and 90° plies also possible that can serve the purpose. For example, any two plies situated at the symmetric position about the mid-plane of SL can be chosen to be preassigned the 0° and 90° fiber angle. This method is equally valid however, in this paper, only the AP method is studied and will be discussed in subsequent subsections.

AP at inner-side of SL

In this case, AP is selected in SL at the mid-plane of laminate to pre-assign 0° and 90° see figure (4.6a). Now other two remaining conditions can be implemented. In this case, for the symmetry condition, the plane of symmetry will be different from the mid-plane of SL. It will be mid-plane of the remaining $2i - 2$ plies. After applying the symmetry condition, there will be $i - 1$ independent fiber angles. Half of them $\left(\frac{i-1}{2}\right)$ will have to make ϕ_k $\left(k = 1, 2, 3...\frac{i-1}{2}\right)$ and remaining as $90° + \phi_k$. This will make ζ_1 and ζ_7 zero. Hence the hygrothermal condition is achieved.

Now, continue the example taken in the previous section (4.2.2) with $i = 5$. In the current case, plies with θ_9 and θ_{10} will be selected as AP and preassigned 0° and 90° fiber angles. After this assignment of fiber angle, the corresponding term in equations (4.23 and 4.24) will vanish. It can be seen from these equations that the assignment of 0° and

90° is arbitrary and will always vanish these terms. Next, the application of symmetry condition about the mid-plane of remaining plies i.e. plane between θ_4 and θ_5 plies will reduce these equations in the following form.

$$\zeta_1 = \frac{1}{5}\left(\cos 2\theta_1 + \cos 2\theta_2 + \cos 2\theta_3 + \cos 2\theta_4\right) \tag{4.25}$$

$$\zeta_7 = -\frac{3}{25}\left(\sin 2\theta_1 + \sin 2\theta_2 + \sin 2\theta_3 + \sin 2\theta_4\right) \tag{4.26}$$

In these equations (4.25 and 4.26) any two out of four fiber angles can be selected to take value ϕ_k and the remaining two as $90° + \phi_k$. This will vanish ζ_1 and ζ_7 also.
By following the steps given above for any permissible odd i, the elements of the ABD matrix can be calculated using equations (4.11-4.14). The generalized expression of the coefficients of $[A]$ and $[B]$ matrices are given as

$$(A_{11} = A_{22},\ A_{12},\ A_{66},\ A_{16},\ A_{26}) = \frac{H}{i}\Big(i\ U_1 + (1+2S_c)U_3,\ i\ U_4 - (1+2S_c)U_3,\ i\ U_5 - (1+2S_c)U_3,\ 0,\ 0\Big) \tag{4.27}$$

$$(B_{11},\ B_{12},\ B_{22},\ B_{66},\ B_{16},\ B_{26}) = \frac{(i+1)}{2i^2}H^2\Big(0,\ 0,\ 0,\ 0,\ -U_3S_s,\ U_3S_s\Big) \tag{4.28}$$

where,
$S_c = \sum_{k=1}^{\frac{i-1}{2}} \cos 4\phi_k \qquad S_s = \sum_{k=1}^{\frac{i-1}{2}} \sin 4\phi_k$

AP at mid-side of SL

In this case, all steps remain the same as discussed in the above section (4.2.2). The only position of AP and plane of symmetry will change. The position of the AP will be at the mid of SL, as shown in Fig.4.3b, and the plane of symmetry will coincide with the mid-plane of SL.
In this case, for the example under consideration, plies with θ_5 and θ_6 will be AP. So the terms corresponding to these fiber angles will vanish in Eqs. (4.23 and 4.24). After applying the symmetry conditions, these equations will be reduced to

$$\zeta_1 = \frac{1}{5}\left(\cos 2\theta_1 + \cos 2\theta_2 + \cos 2\theta_3 + \cos 2\theta_4\right) \tag{4.29}$$

$$\zeta_7 = -\frac{1}{10}\left(\sin 2\theta_1 + \sin 2\theta_2 + \sin 2\theta_3 + \sin 2\theta_4\right) \tag{4.30}$$

Above Eqs. (4.29 and 4.30) is similar to Eqs. (4.25 and 4.26) and can be made zero following the similar approach. In this case, the generalized expression of the coefficient of $[A]$ and $[B]$ matrices are given as

$$(A_{11} = A_{22},\ A_{12},\ ,\ A_{66},\ A_{16},\ A_{26}) = \frac{H}{i}\Big(i\ U_1 + (1+2S_c)U_3,\ i\ U_4 - (1+2S_c)U_3,$$

$$i\ U_5 - (1+2S_c)U_3,\ 0,\ 0\Big) \tag{4.31}$$

$$(B_{11},\ B_{12},\ B_{22},\ B_{66},\ B_{16},\ B_{26}) = \frac{1}{2i}H^2\Big(0,\ 0,\ 0,\ 0,\ -U_3S_s,\ U_3S_s\Big) \tag{4.32}$$

Where,
$S_c = \sum_{k=1}^{\frac{i-1}{2}} \cos 4\phi_k \qquad S_s = \sum_{k=1}^{\frac{i-1}{2}} \sin 4\phi_k$

AP at outer-side of SL

In this case, AP will be at the exteriormost position of the SL see Fig. 4.3c, and the plane of symmetry will be different from the mid-plane of SL. In the current numerical example, the AP will be the plies corresponding to θ_1 and θ_2, and the plane of symmetry will be the plane between θ_6 and θ_7. So after the application of symmetry conditions Eqs. (4.23 and 4.24) will reduce to

$$\zeta_1 = \frac{1}{5}\left(\cos 2\theta_3 + \cos 2\theta_4 + \cos 2\theta_5 + \cos 2\theta_6\right) \tag{4.33}$$

$$\zeta_7 = -\frac{2}{25}\left(\sin 2\theta_3 + \sin 2\theta_4 + \sin 2\theta_5 + \sin 2\theta_6\right) \tag{4.34}$$

Now following the procedure discussed in section (4.2.2) ζ_1 and ζ_7 will be made zero. and the resultant coefficients of the $[A]$ and $[B]$ matrices for any permissible odd i is given as

$$(A_{11} = A_{22},\ A_{12},\ ,\ A_{66},\ A_{16},\ A_{26}) = \frac{H}{i}\Big(i\ U_1 + (1+2S_c)U_3,\ i\ U_4 - (1+2S_c)U_3,$$
$$i\ U_5 - (1+2S_c)U_3,\ 0,\ 0\Big) \tag{4.35}$$

$$(B_{11},\ B_{12},\ B_{22},\ B_{66},\ B_{16},\ B_{26}) = \frac{(i-1)}{2i^2}H^2\Big(0,\ 0,\ 0,\ 0,\ -U_3S_s,\ U_3S_s\Big) \tag{4.36}$$

where,
$S_c = \sum_{k=1}^{\frac{i-1}{2}} \cos 4\phi_k \qquad S_s = \sum_{k=1}^{\frac{i-1}{2}} \sin 4\phi_k$

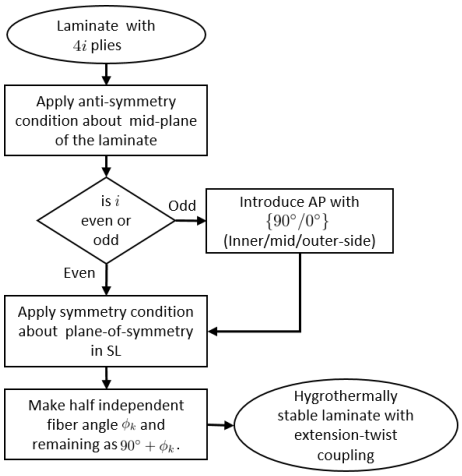

Figure 4.4: Steps to get hygrothermally stable laminate with extension-twist coupling

For all sub-cases of i to be odd cases, the expression of coefficients of the $[D]$ matrix is not given as its expression depends on the stacking sequence and varies accordingly. Besides this, similar to the even i condition, all the equations representing coefficients of $[A]$ and $[B]$ matrices can also be reduced for all ϕs are equal conditions for all sub-cases. It should also be noted that for i to be odd case, by following the above-given steps the resultant hygrothermal stable laminates can be obtained in factorial$(i-1)$ ways and each laminate will have $\frac{i-1}{2}$ independent fiber angles.
The whole procedure to obtain the hygrothermally stable laminate with extension-twist coupling is summarized in the following Fig. 4.4

4.2.3 Optimization

In this section, the proposed stacking sequence is optimized to get maximized extension-twist coupling for the given number of plies. This can be achieved by maximizing the compliance coefficient b_{16} provided in Eq. (4.37). This equation is the inverse of equation (Eq. 4.1). The compliance coefficient b_{16} is the objective function and hygrothermal stability conditions (Eqs. 4.17 and 4.18) serve as constraints of the current optimization problem. In the current work second set of hygrothermal stability conditions (Eq. 4.18) is being used as the first set (Eq. 4.17) nullify the entire coupling matrix $[B]$ which is not allowed in current work. As already discussed that the proposed stacking sequence inherently satisfies the required hygrothermal stability conditions for any set of fiber angles between $-90°$ and $90°$. Therefore the proposed stacking sequence reduces constrained optimization problems into unconstrained ones and can be solved analytically or numerically. For the calculation of the objective function, b_{16} materials properties are required. these material properties are given in table (4.1).

$$\begin{Bmatrix} \varepsilon_x^o \\ \varepsilon_y^o \\ \gamma_{xy}^o \\ \kappa_x \\ \kappa_y \\ \kappa_{xy} \end{Bmatrix} = \begin{bmatrix} a_{11} & a_{12} & a_{16} & b_{11} & b_{12} & b_{16} \\ a_{12} & a_{22} & a_{26} & b_{12} & b_{22} & b_{26} \\ a_{16} & a_{26} & a_{66} & b_{16} & b_{26} & b_{66} \\ b_{11} & b_{12} & b_{16} & d_{11} & d_{12} & d_{16} \\ b_{12} & b_{22} & b_{26} & d_{12} & d_{22} & d_{26} \\ b_{16} & b_{26} & b_{66} & d_{16} & d_{26} & d_{66} \end{bmatrix} \begin{Bmatrix} N_x + N_x^T \\ N_y + N_y^T \\ N_{xy} + N_{xy}^T \\ M_x + M_x^T \\ M_y + M_y^T \\ M_{xy} + M_{xy}^T \end{Bmatrix} \tag{4.37}$$

In the present work, the proposed stacking sequence is optimized analytically to get an optimized set of fiber angles using the 'Maximize' function of Wolfram Mathematica [111]. This function provides exact optimized parameters that maximize the given objective function. As already discussed that there are total $factorial(i)$ and $factorial(i-1)$ permutations are possible for i to be even and odd respectively. Each permutation has its own optimized ϕs and the optimized objective function value and corresponding stacking sequence do not necessarily represent globally optimized stacking sequence. Whenever the

Table 4.1: Material properties of graphite/epoxy T300/976 [2]

E_{11}	125 GPa
E_{22}	8.45 GPa
G_{12}	4.3 GPa
ν_{12}	0.328
t	0.152 mm

term 'globally optimized stacking sequence' is used in the context of analytic optimization, it shall refer to that permutation of the proposed stacking sequence that maximizes b_{16} upon optimization. Therefore the permutation carrying the maximum value of objective function b_{16} will be considered as the globally optimized permutation of the proposed stacking sequence. In this work, every permutation for $i = 2$ through $i = 7$ has been optimized to find the globally optimized stacking sequence for given i. There is more than one permutation that upon optimization provides the same value of the objective function for global as well as sub-optimal cases. Out of these same globally optimized stacking sequences, one is selected and given in the table (4.2). A similar optimization process has also been followed by taking each ϕs equal. In this case, each permutation provides the same optimized value of the objective function, and one of the optimized sequences with optimized objective function value is provided in the table (4.3). In both the tables, letters I, M, and O in the second column (Pos) represent the position of plies made 0° and 90° in SL as discussed in the preceding section and as shown in Fig. (4.3).

The analytically optimized results for both cases (all ϕs different and same) are not significantly different and can be observed from the tables (4.2 and 4.3). The calculated results show that for the case when all ϕs are the same, all permutations of the proposed stacking sequence produce same optimized value of objective function b_{16} which is insignificantly different from the globally optimized b_{16} obtained with different ϕs. This result creates an advantageous situation because it reduces all effort in finding globally optimized stacking sequences to just one calculation. On the other hand, the case when all ϕs are different provides different sub-optimal solution which is absent for the case when all ϕs same. The presence of sub-optimal solutions increases the application spectrum.

Numerical optimization is carried out using the 'fmincon' function of MATLAB [112] implemented with the SQP algorithm. It should be noted that for numerical optimization, most generic stacked laminate (i.e. laminate without specific conditions applied on stacking or having the number of independent fiber angles equal to the number of plies) has been used instead of the current proposed stacking sequence. Here objective function has been taken as $-b_{16}^2$ because 'fmincon' provides minimized results. $-90°$ and 90° form the lower and upper bounds of the problem. The following constraints are used.

$$\zeta_1 = \zeta_3 = \zeta_5 = \zeta_7 = 0 \tag{4.38}$$

These constraints are equivalent to the second set of hygrothermal stability conditions (Eq.

Table 4.2: Optimized fiber angles and stacking sequence for extension-twist coupling

i	Pos.	$\phi_1(^\circ)$	$\phi_2(^\circ)$	$\phi_3(^\circ)$	Stacking sequence ($^\circ$)	$b_{16}(N^{-1})$ in 10^{-5}
2	-	-67.5	-	-	$[-67.5/22.5/22.5/-67.5]_A$	7.56
3	I	14.66	-	-	$[14.66/-75.34/-75.34/14.66/0/90]_A$	2.23
	M	15.51	-	-	$[15.51/-74.49/0/90/-74.49/15.51]_A$	1.71
	O	20.89	-	-	$[0/90/20.89/-69.11/-69.11/20.89]_A$	1.71
4	-	-66.60	20.45	-	$[-69.55/20.45/-66.60/23.40/23.40/-66.60/20.45/-69.55]_A$	1.92
5	I	-72.88	15.39	-	$[-74.61/15.39/17.12/-72.88/-72.88/17.12/15.39/-74.61/0/90]_A$	0.96
	M	-74.90	18.17	-	$[-74.90/15.10/18.17/-71.83/0/90/-71.83/18.17/15.10/-74.90]_A$	0.792
	O	-71.35	21.53	-	$[0/90/-71.35/18.65/-68.47/21.53/21.53/-68.47/18.65/-71.35]_A$	0.816
6	-	23.57	19.63	22.25	$[-70.37/19.63/-67.75/22.25/-66.43/23.57/23.57/-66.43/22.25/-67.75/19.63/-70.37]_A$	0.854
7	I	17.51	15.69	18.48	$[15.69/-74.31/-72.49/17.51/-71.52/18.48/18.48/-71.52/17.51/-72.49/-74.31/15.69/0/90]_A$	0.527
	M	17.72	15.19	19.41	$[15.19/-74.81/17.72/-72.28/-70.59/19.41/0/90/19.41/-70.59/-72.28/17.72/-74.81/15.19]_A$	0.452
	O	21.80	20.42	17.80	$[0/90/-72.20/17.80/20.42/-69.58/21.80/-68.20/-68.20/21.80/-69.58/20.42/17.80/-72.20]_A$	0.466

I → inner-side, M → mid-side, O → outer-side

4.18). There are several local minima/optima present for the objective function. Therefore gradient-based 'fmincon' function often returns the sub-optimal solution, which depends on the initial guess. Hence to find and build confidence in the global optima, several iterations are required. As the number of plies increases, the number of these iterations increases drastically without guaranteeing the globally optimized value. However, in the present case at most, fifty thousand iterations with random initial guesses have been used for $i = 6$ and $i = 7$ cases. The obtained globally optimized values of b_{16} are given in table (4.3).

The results for $i = 2$ and $i = 3$ (or total plies 8 and 12) are in line with results available in earlier publication [103]. It should be noted here that although the total number of

Table 4.3: Optimized fiber angle and stacking sequence for extension-twist coupling with numerical optimization

i	Pos.	ϕ (°)	Stacking sequence (°)	$b_{16}(N^{-1})$ in 10^{-5} Ana. Opt.	Nu. Opt.
2	-	-67.5	$[-67.5/22.5/22.5/-67.5]_A$	7.56	8.98
3	I	14.66	$[14.66/-75.34/-75.34/14.66/0/90]_A$	2.23	4.95
	M	15.51	$[15.51/-74.49/0/90/-74.49/15.51]_A$	1.71	
	O	20.89	$[0/90/20.89/-69.11/-69.11/20.89]_A$	1.71	
4	-	-67.5	$[22.5/-67.5/22.5/-67.5/-67.5/22.5/-67.5/22.5]_A$	1.89	2.60
5	I	16.27	$[-73.73/16.27/16.27/-73.73/-73.73/16.27/16.27/-73.73/0/90]_A$	0.956	1.46
	M	16.69	$[-73.31/16.69/16.69/-73.31/0/90/-73.31/16.69/16.69/-73.31]_A$	0.782	
	O	-69.80	$[0/90/-69.80/-69.80/20.20/20.20/20.20/20.20/-69.80/-69.80]_A$	0.809	
6	-	-67.5	$[22.50/-67.50/-67.50/22.50/-67.50/22.50/22.50/-67.50/22.50/-67.50/-67.50/22.50]_A$	0.84	0.970
7	I	17.29	$[17.29/-72.71/17.29/-72.71/-72.71/17.29/17.29/-72.71/-72.71/17.29/-72.71/17.29/0/90]_A$	0.522	0.604
	M	17.57	$[17.57/-72.43/-72.43/17.57/-72.43/17.57/0/90/17.57/-72.43/17.57/-72.43/-72.43/17.57]_A$	0.445	
	O	20.21	$[0/90/20.21/20.21/-69.79/20.21/-69.79/-69.79/-69.79/-69.79/20.21/-69.79/20.21/20.21]_A$	0.46	

I → inner-side, M → mid-side, O → outer-side

plies is the same for both analytical and numerical optimization, the expression of the objective function b_{16} will be different. As discussed above for both cases the number of independent fiber angles is different (for analytical it is i and for numerical it is $4i$) therefore the globally optimized value of objective function b_{16} will be different. Hence both results cannot be compared directly. However, these two results prove helpful in choosing between these two approaches.

The proposed stacking sequence can also be optimized using 'fmincon'. As in this case, the independent fiber angles are lower (i instead of $4i$), and due to the unconstrained problem, fewer iterations are required to get the globally optimized solution. Which ultimately reduces the calculation time. The Fig. 4.5 shows plots of optimized b_{16} obtained analytically and numerically given in table (4.2 and 4.3). Analytical results are taken from the table (4.2) only as both analytical results are insignificantly different. Fig. (4.5) shows a significant deviation between two results for smaller values of i, but as i increases, the difference between these two results diminishes. It is because independent fiber angles are i for analytical results while $4i$ for numerical results, though total plies for both cases are the same ($4i$). This additional constraint on analytical results creates a difference between the two results. Additionally, b_{16} inversely depends on the square of the total thickness (H) of the laminate. For larger i, thickness starts to dominate and both the results approach each other asymptotically, as shown in Fig. (4.5). This observation together with the above discussion makes it clear that for large i the current proposed stacking sequence provides an efficient way to obtain optimized results without compromising much on coupling.

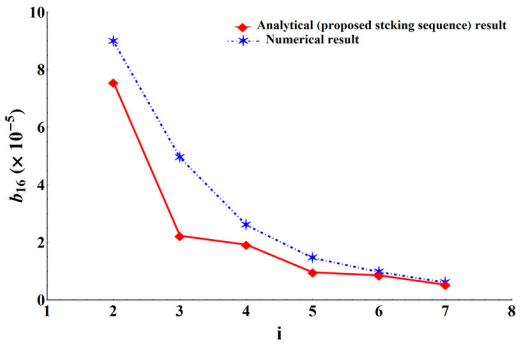

Figure 4.5: Plots of optimized b_{16} obtained analytically and numerically

4.2.4 Sensitivity Analysis

The exact implementation of the optimized stacking sequence is required during the manufacturing process of laminate to get better operational characteristics. However, in real life, it is nearly impossible to achieve the exact optimized stacking sequence in manufactured laminate due to the inevitable small errors. For the practical usefulness of the presented optimized stacking sequence, this small error in ply angles should not result in significant coupling loss. Therefore sensitivity analysis has been performed to investigate the loss of coupling due to small errors in ply angles. The loss of coupling is defined as the relative error between optimized and perturbed extension-twist coupling

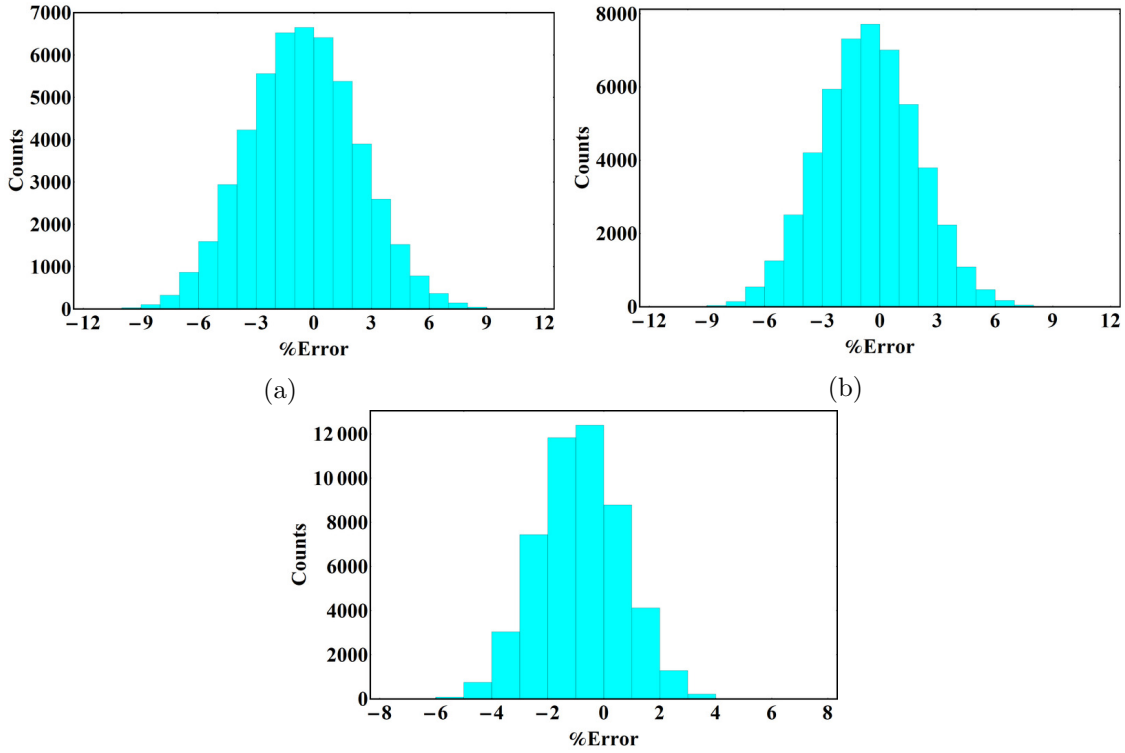

Figure 4.6: Histogram for i=4 due to (a) analytical optimization with different ϕs (b) analytical optimization with same ϕs (c) numerical optimization

coefficient and is given as

$$\%\text{Error} = \frac{|b_{16}^P| - |b_{16}^O|}{|b_{16}^O|} \times 100 \tag{4.39}$$

Here b_{16}^P is the coupling coefficient due to the perturbed stacking sequence, and b_{16}^O is the optimized coupling coefficient. Here, the sensitivity analysis results are given for the laminates with $i = 4$ and 5. For these laminates, both analytically (all ϕs are the same and different) and numerically optimized results are considered for perturbed stacking sequence. Total 5×10^5 sets of perturbed stacking sequence for each case are generated. It is assumed that each ply angle is uniformly distributed between $[\theta_k - 2°,\ \theta_k + 2°]$. Where θ_k is the optimized angle for k_{th} ply in the laminate.

All the results of this work are given in figure (4.6 and 4.7) in terms of histograms for $i = 4$ & $i = 5$ respectively. As discussed above direct correlation cannot be established between the sensitivity of analytically and numerically optimized results. It is also mentioned in earlier sections that there is more than one permutation of the proposed stacking sequence is possible which provides the same globally optimized value. Sensitivity analysis provides criteria for selection from these globally optimized stacking sequences. In figure (4.8) histograms corresponding to four different globally optimized permutations for $i = 4$ are given. By observing these results some important points can be made. These are the following

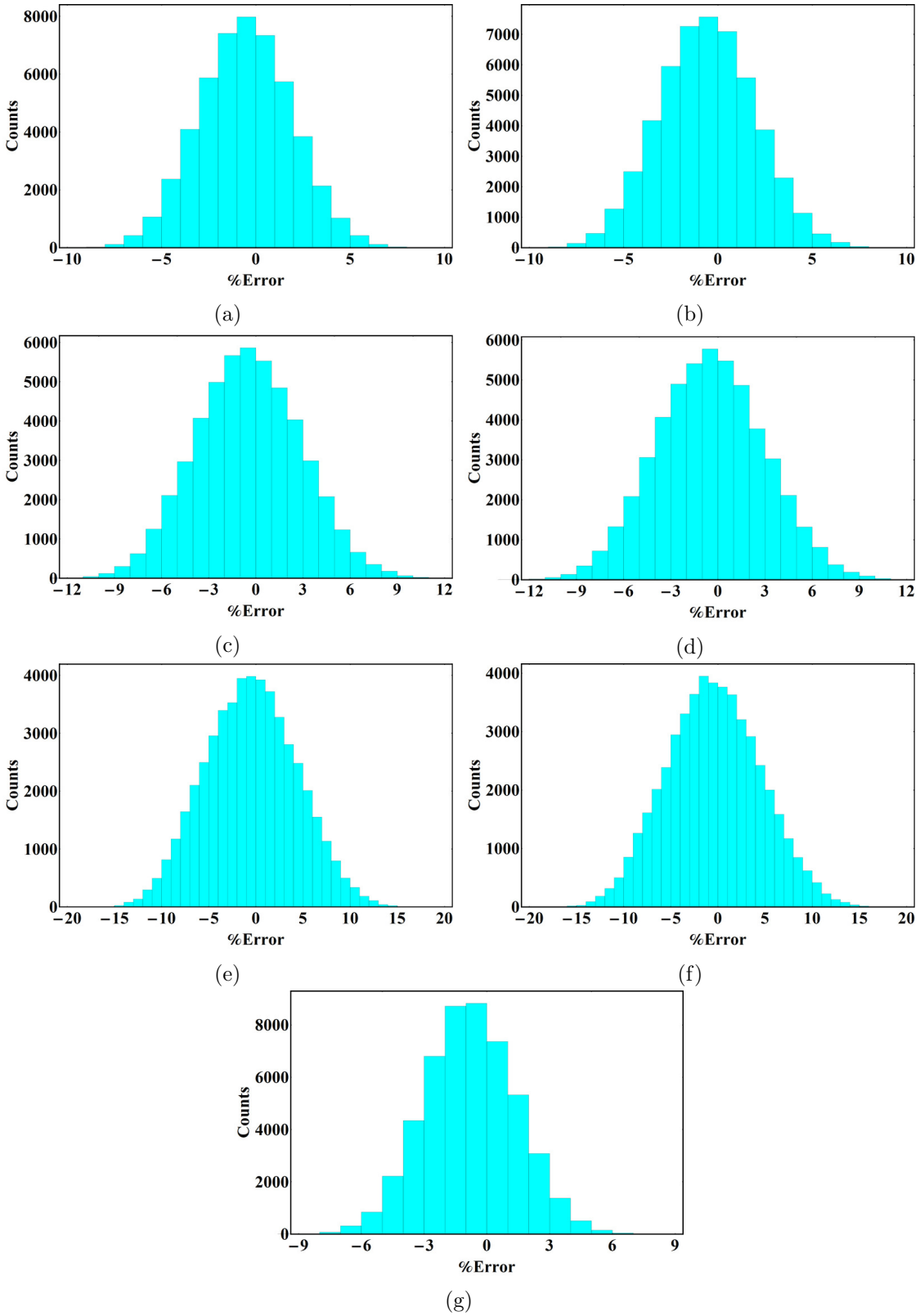

Figure 4.7: Histogram for i=5 due to (a,c,e) analytical optimization with different ϕs with 0° 90° pair at inner, mid and outer side of SL respectively (b,d,f) analytical optimization with same ϕs with 0° 90° pair at inner, mid and outer side of SL respectively (g) numerical optimization

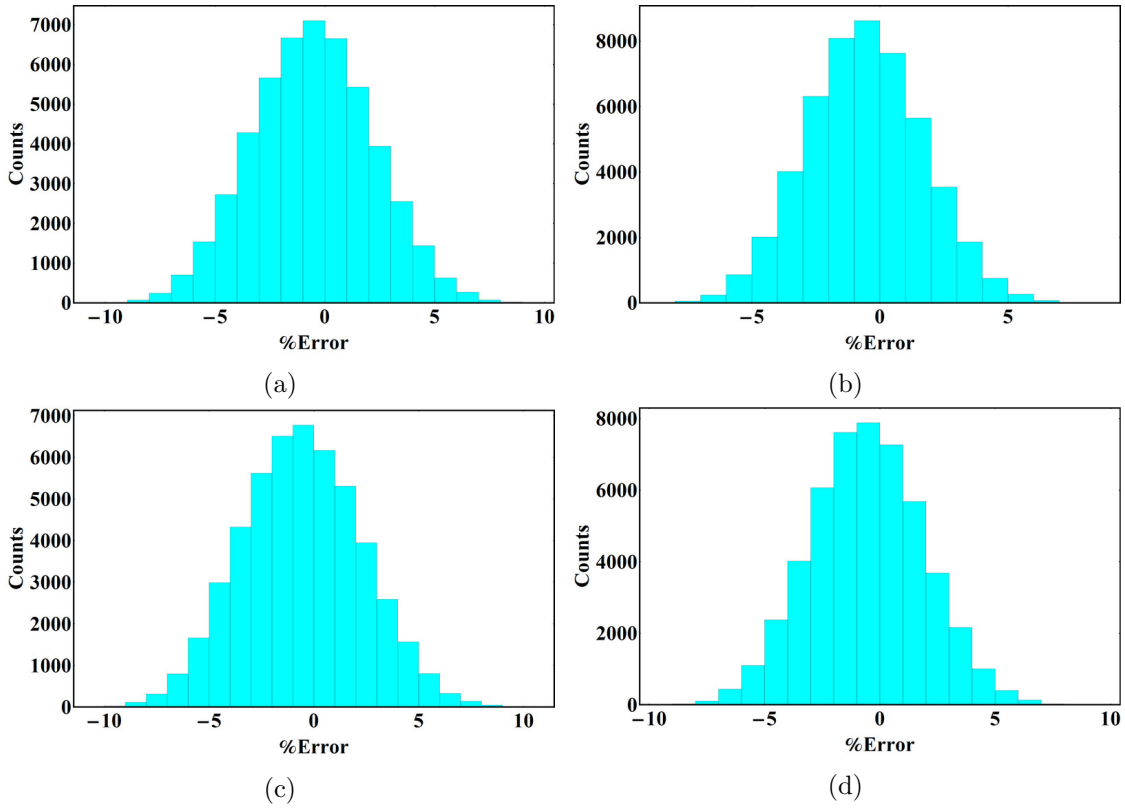

Figure 4.8: Histograms of four different globally optimized permutations for i=4

1. For both cases of analytical optimization (all ϕs are different and same), the resultant optimized stacking sequence is almost equally sensitive towards the perturbation. Hence selection between these two approaches will not be affected by sensitivity.

2. For i to be odd case, the optimized stacking sequence becomes more sensitive as AP shifts towards the outer side. This observation suggests that the laminate with AP at the inner-side is best suitable for this case.

3. Optimized stacking sequence obtained using the numerical approach is slightly more robust than the analytical approach. However, this difference may not influence much the selection of the approach to be followed.

4. from the figure (4.8) it can be observed that the distribution of the error is different and varies for each permutation. As the variation is not significant, thus for given i any globally optimized permutation can be selected randomly.

If the results of figures (4.7e,4.7f) are ignored, then for each remaining case the major portion of the error distribution comes between ±5% and the maximum error is within ±10%. Therefore these stacking sequences can be considered suitable for design purposes from the point of view of sensitivity.

4.3 Bend-Twist Coupling with Hygrothermal Stable Stacking

In laminated composites, to incorporate the bend-twist coupling, the stiffness coefficients D_{16} and D_{26} must be non-zero. For such composites to be completely hygrothermal stable, it is necessary to satisfy the second set of hygrothermal stability conditions (Eq. 4.18) as this condition prevents both in-plane and out-of-plane hygrothermal deformations. In the current work, two approaches have been provided to get hygrothermal stable laminates with bend-twist coupling. Each approach results in a special class of symmetric laminate having a total $4i$ ($i = 2, 3, 4...$ or $i = 1, 2, 3...$ depending on the approach) plies. Due to symmetry, these laminates are inherently hygrothermally curvature stable ($[B] = 0$ or $\zeta_5 = \zeta_6 = \zeta_7 = \zeta_8 = 0$). Besides this, these laminates also satisfy hygrothermal stability conditions (Eq. 4.18). Hence, these resulting laminates are completely hygrothermal stable. The two approaches mentioned above are as follows:

4.3.1 First approach

The first approach is further divided into two sub-cases depending on the value of i (i.e. even or odd). The division and sub-division of this case are similar to that of the extension-twist case and are as shown in Fig. 4.2b. For this approach, a minimum of 8 plies are required. Therefore i will take values starting from 2. The two cases are discussed in the following sub-sections.

When i is an even number

In this case, the hygrothermally stable laminate with bend-twist coupling is obtained by using the following steps:

(a) Make the laminate symmetric about the mid-plane of the overall laminate. This step introduces two Sub-Laminates (SL) in the laminate as depicted in Fig. 4.2a. Furthermore, the total number of independent fiber angles decreases from $4i$ to $2i$.

(b) Make one of the SL anti-symmetric about its own mid-plane. The corresponding angles in other SLs will change automatically because of the first step. This step introduces two Sub-Sub-Laminate (SSL) in each SL as depicted in Fig. 4.2a. After application of this step, the total number of independent fiber angles further decreases from $2i$ to i.

(c) In the last step, make half of the total independent fiber angles ($i/2$) as ϕ_k ($k = 1, 2, 3...i/2$) and the remaining $i/2$ fiber angles as $(90^\circ + \phi_k)$. This selection of fiber angles will be arbitrary. This final step will decrease the number of total independent fiber angles to $i/2$.

These steps provide hygrothermally stable laminate in $factorial(i)$ ways because of the last step. Here it should be noted that this resultant laminate will satisfy both the set of

hygrothermal stability conditions (4.17 and 4.18). As already discussed, because of the symmetry of the resultant laminate, it is inherently hygrothermal curvature stable. The in-plane hygrothermal stability condition ($\zeta_1 = \zeta_3 = 0$) is satisfied by the last step. This whole process can be understood by taking a numerical example with $i = 4$. In this case, the total plies in the laminate will be $n = 16$. After applying the symmetry condition, the resultant expression of ζ_1 and ζ_3 will be

$$(\zeta_1, \zeta_3) = \frac{1}{8} \sum_{k=1}^{8} (\cos 2\theta_k, \sin 2\theta_k) \tag{4.40}$$

Now, after applying the anti-symmetric condition, the ζ_3 term will vanish and the resultant ζ_1 will take the following form

$$\zeta_1 = \frac{1}{4} (\cos 2\theta_1 + \cos 2\theta_2 + \cos 2\theta_3 + \cos 2\theta_4) \tag{4.41}$$

Following the last step, any two fiber angles have to be taken as ϕ_1 and ϕ_2 and the remaining two have to be made $90^\circ + \phi_1$ and $90^\circ + \phi_2$. This choice of angles will vanish the ζ_1 term. Here it can be noted that any arbitrary selection of angles will always vanish the ζ_1 term. There are total $factorial(4)$ possible ways available for such selection.

When i is an odd number

All the steps given in section 4.3.1 for i to be even case are valid and will be followed for this case also. However, the direct implementation of these steps is not possible as, in this case, $i/2$ is not a whole number. For the implementation of these steps, one more step has to be added after step (a). This step is following

- Select two Adjacent Plies (APs) in SL, assign them fiber angles ϕ_c and $90^\circ + \phi_c$ arbitrarily. Three positions of these APs are identified, and according to their position, these are referred inner-side, mid-side and outer-side APs, as shown in Fig. 4.9.

after this step, the remaining two steps (b) and (c) can be applied. These four steps have to be followed in this sequence only and will be referred first, second, third and fourth steps respectively. By following these steps, the obtained resultant hygrothermally stable laminate will have total $(i+1)/2$ ($\phi_c \to 1$ and $\phi_k \to (i-1)/2$) independent fiber angles. Here it should be noted that the plane about which the anti-symmetric condition has to be applied will not necessarily be the mid-plane of SL. It will change according to the position of APs in SL. For a better understanding of these four steps, a numerical example with $i = 3$ has been explained below.
The first step (symmetry step) is common to all three sub-cases. After applying this first

step, the ζ_1 and ζ_3 terms take the following form

$$\begin{aligned}\zeta_1 &= \frac{1}{6}\left(\cos 2\theta_1 + \cos 2\theta_2 + \cos 2\theta_3 + \cos 2\theta_4 + \cos 2\theta_5 + \cos 2\theta_6\right)\\ \zeta_3 &= \frac{1}{6}\left(\sin 2\theta_1 + \sin 2\theta_2 + \sin 2\theta_3 + \sin 2\theta_4 + \sin 2\theta_5 + \sin 2\theta_6\right)\end{aligned} \tag{4.42}$$

Now, the second step (selection of APs) has to be applied. Depending on the position of APs, this step has been divided into following three sub-cases, given as follows:

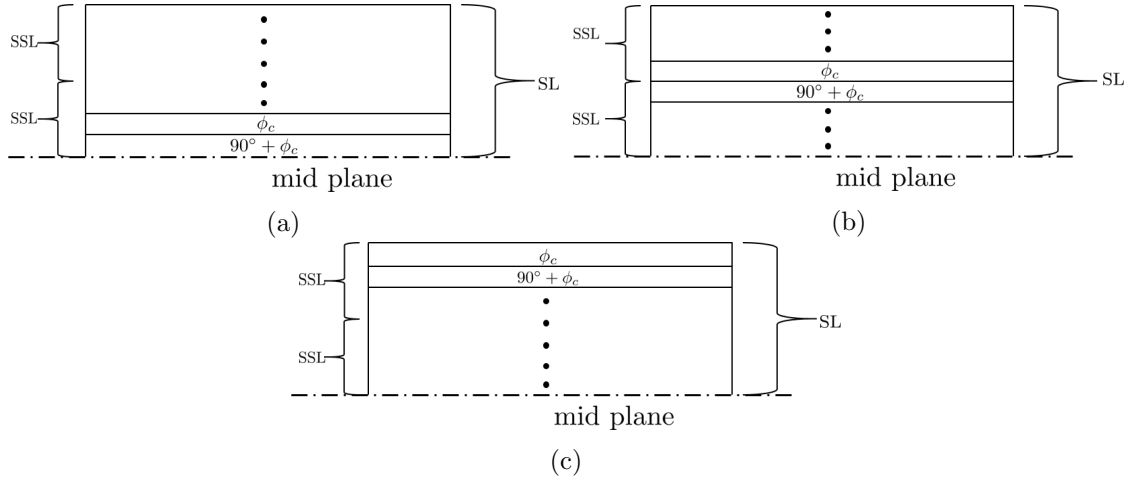

Figure 4.9: Position of APs in SL (a) inner-side (b) mid-side (c) outer-side

APs at inner-side

In this case, APs are situated at the mid-plane of the laminate, as shown in Fig. 4.9a. In the current example (4.42) these APs correspond to the plies with fiber angles θ_5 and θ_6. By taking these two fiber angles as ϕ_c and $90° + \phi_c$, the terms corresponding to these fiber angles will vanish from the expression of ζ_1 and ζ_3. The resultant expression for these terms will be,

$$\begin{aligned}\zeta_1 &= \frac{1}{6}\left(\cos 2\theta_1 + \cos 2\theta_2 + \cos 2\theta_3 + \cos 2\theta_4\right)\\ \zeta_3 &= \frac{1}{6}\left(\sin 2\theta_1 + \sin 2\theta_2 + \sin 2\theta_3 + \sin 2\theta_4\right)\end{aligned} \tag{4.43}$$

here it should be noted that the choice of ϕ_c and $90° + \phi_c$ is arbitrary. Now third step (anti-symmetric) will be applied about the plane between plies with fiber angles θ_2 and θ_3. After this step, ζ_3 will be vanished. The ζ_1 term will be nullified after applying the fourth step as demonstrated for the i to be even case in section 4.3.1 by using step (c).

APs at mid-side

In this case, the APs correspond to plies situated on either side of the mid-plane of SL, as shown in Fig. 4.9b. In the ongoing example (4.42), these APs are corresponds to θ_3 and

θ_4 plies. After application of the second step, the resultant expression of ζ_1 and ζ_3 will be,

$$\begin{aligned} \zeta_1 &= \frac{1}{6}\left(\cos 2\theta_1 + \cos 2\theta_2 + \cos 2\theta_5 + \cos 2\theta_6\right) \\ \zeta_3 &= \frac{1}{6}\left(\sin 2\theta_1 + \sin 2\theta_2 + \sin 2\theta_5 + \sin 2\theta_6\right) \end{aligned} \tag{4.44}$$

in this case, the plane about which the anti-symmetric condition has to be applied coincides with the mid-plane of SL. Like the previous case, after applying the third and fourth steps, ζ_1 and ζ_3 will become zero.

APs at outer-side

In this case, APs are situated at the outermost position in SL as depicted in Fig. 4.9c. In the current example(4.42), these APs correspond to fiber angles θ_1 and θ_2. The terms corresponding to these APs will be canceled out after the application of the second step and the resultant expression will be,

$$\begin{aligned} \zeta_1 &= \frac{1}{6}\left(\cos 2\theta_3 + \cos 2\theta_4 + \cos 2\theta_5 + \cos 2\theta_6\right) \\ \zeta_3 &= \frac{1}{6}\left(\sin 2\theta_3 + \sin 2\theta_4 + \sin 2\theta_5 + \sin 2\theta_6\right) \end{aligned} \tag{4.45}$$

in this case, the plane of anti-symmetry will be between θ_4 and θ_5 plies. Now again, the application of the third and fourth conditions will make ζ_1 and ζ_3 zero.
For any permissible odd i, for the 'APs at mid-side' case, the plane of anti-symmetry will be the mid-plane of SL. For the other two cases, it will be the mid-plane of plies excluding APs. By following these steps, for fixed order of APs' angles, the resulting hygrothermally stable laminate can be obtained in $factorial(i-1)$ ways. Fig. 4.10 summarizes the whole procedure to obtain hygrothermally stable laminate with bend-twist coupling.

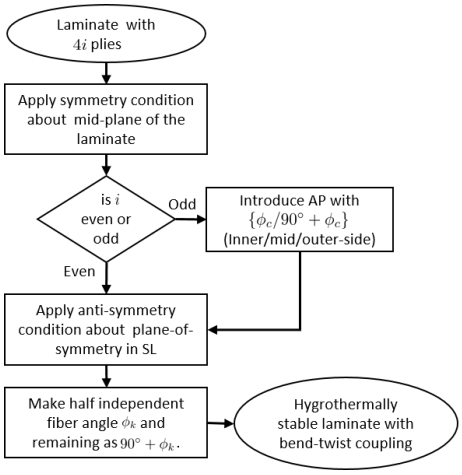

Figure 4.10: Steps to get hygrothermally stable laminate with bend-twist coupling

4.3.2 Second approach

The second approach, to get hygrothermally stable laminate with bend-twist coupling, is accomplished by following the steps (a) and (c) used for i to be even case of the first approach given in section 4.3.1. Unlike the first approach, in this second approach, i can be 1. By following this approach, the resulting hygrothermally stable laminate can be obtained in $factorial(2i)$ ways and the resulting laminate will have total i independent fiber angles.
An example with $i = 4$ is given here to explain the two-stepped procedure of this approach. For $i = 4$ there will be a total 16 plies in the laminate. After applying the first step (symmetric condition), the expression of ζ_1 and ζ_3 is given as,

$$\begin{aligned}\zeta_1 &= \frac{1}{8}\left(\cos 2\theta_1 + \cos 2\theta_2 + \cos 2\theta_3 + \cos 2\theta_4 + \cos 2\theta_5 + \cos 2\theta_6 + \cos 2\theta_7 + \cos 2\theta_8\right) \\ \zeta_3 &= \frac{1}{8}\left(\sin 2\theta_1 + \sin 2\theta_2 + \sin 2\theta_3 + \sin 2\theta_4 + \sin 2\theta_5 + \sin 2\theta_6 + \sin 2\theta_7 + \sin 2\theta_8\right) \quad (4.46)\end{aligned}$$

After this step, the total independent fiber angle will be reduced to half. In this example, it is 8. In the second and the final step of this approach, half of these independent fiber angles will be taken as ϕ_k $(k = 1, 2, 3, 4)$ and the remaining as $(90^\circ + \phi_k)$. This selection of fiber angles will vanish the ζ_1 and ζ_3 terms. Hence all conditions of hygrothermal stability have been satisfied. Here it should be noted that the assignment of fiber angles ϕ_k and $(90^\circ + \phi_k)$ is completely arbitrary and this assignment can be done in $factorial(8)$ ways or resulting hygrothermally stable laminate is obtained in $factorial(8)$ ways.

4.3.3 Optimization

The optimization of the proposed stacking sequence is carried out to get maximum bending-twisting coupling. For this purpose compliance coefficient d_{16} is taken as the objective function, given in Eq. (4.37). The hygrothermal stability conditions (4.17 and 4.18) are the constraints of this optimization problem. As discussed above, in this present work, the proposed stacking sequences inherently satisfy all the hygrothermal stability constraints for any fiber angles set between -90° and 90°. Therefore, these stacking sequences reduced the original constrained optimization problem into an unconstrained one. Hence, it can be solved by both analytical and numerical methods.
Similar to the extension-twist case, the proposed stacking sequences have been optimized using both analytical and conventional constrained optimization methods in this case also. The procedure of optimization will remain the same as provided in the optimization section 4.2.3 of the extension-twist case. For the convenience of further communication, this conventional constrained optimization will be referred 'numerical optimization' as it is completely based on numerical technique.
Each permutation of the proposed stacking sequence has its own optimized set of fiber angles that may not necessarily represent the globally optimized set of fiber angles for a given i within that class of laminate. Here, the set of optimized fiber angles corresponds

to the permutation, which provides maximum objective function value upon optimization among all possible permutations and has been referred as the globally optimized fiber angle set. The material properties used in the calculation of objective function d_{16} are given in Table 4.1.

The stacking sequence obtained by following the first approach is optimized using the 'Maximize' function. All the possible permutations for $i = 2$ through $i = 7$ have been optimized. The stacking sequence having maximum objective function value is selected as globally optimized stacking sequence. The global optimum value of unknown fiber angles

Table 4.4: Bend-twist optimized stacking sequence obtained with first approach (all ϕ_k different)

i	Pos.	$\phi_1(^\circ)$	$\phi_2(^\circ)$	$\phi_3(^\circ)$	$\phi_c(^\circ)$	Stacking sequence ($^\circ$)	d_{16} $(Nm)^{-1}$
2	-	68.14	-	-	-	[-21.86/68.14/-68.14/21.86]$_S$	0.21
3	I	-14.80	-	-	-22.87	[-14.80/75.20/-75.20/14.80 /-22.87/67.13]$_S$	0.033
	M	-22.17	-	-	-23.58	[67.83/-22.17/-23.58/66.42 /22.17/-67.83]$_S$	0.073
	O	-23.23	-	-	-22.69	[-22.69/67.31/-23.23/66.77 /-66.77/23.23]$_S$	0.084
4	-	-23.06	-20.70	-	-	[-23.06/-20.70/69.30/66.94 /-66.94/-69.30/20.70/23.06]$_S$	0.03
5	I	-18.88	-16.22	-	-23.45	[-18.88/-16.22/73.78/71.12/-71.12 /-73.78/16.22/18.88/-23.45/66.55]$_S$	0.0091
	M	-23.23	-21.99	-	-22.43	[-23.23/-21.99/68.01/66.77/-22.43 /67.57/-66.77/-68.01/21.99/23.23]$_S$	0.016
	O	67.53	65.82	-	-22.27	[-22.27/67.73/-24.18/-22.47/67.53 /65.82/-65.82/-67.53/22.47/24.18]$_S$	0.016
6	-	-23.42	-21.95	-20.27	-	[-23.42/-21.95/-20.27/69.73 /68.05/66.58/-66.58/-68.05 /-69.73/20.27/21.95/23.42]$_S$	0.0077
7	I	-20.58	-17.15	71.01	-23.92	[-20.58/-18.99/-17.15/72.85/71.01 /69.42/-69.42/-71.01/-72.85/17.15 /18.99/20.58/-23.92/66.08]$_S$	0.0037
	M	-22.59	-21.56	66.45	-21.98	[-23.55/-22.59/-21.56/68.44/67.41 /66.45/-21.98/68.02/-66.45/-67.41 /-68.44/21.56/22.59/23.55]$_S$	0.0056
	O	66.74	-21.96	65.54	-21.93	[-21.93/68.07/-24.46/-23.26/-21.96 /68.04/66.74/65.54/-65.54/-66.74 /-68.04/21.96/23.26/24.46]$_S$	0.0055

I → inner-side, M → mid-side, O → outer-side

(ϕ_k), unknown fiber angle (ϕ_c) of APs, stacking sequence and corresponding objective function value is provided in Table 4.4. A similar optimization process has also been done by taking all unknown fiber angles (ϕ_k) the same i.e. $\phi_k = \phi$. The corresponding optimized values are provided in the Table 4.5. In these two tables, the letters I, M, and O in the second column represent the position of APs in SL.

The stacking sequence obtained using the second approach has been optimized using the 'fmincon' function. In this case, random search has been used to obtain a globally optimized stacking sequence instead of optimizing all permutations. It is because, in this case, the total permutations are $factorial(2i)$, which becomes very large numbers as i increases. This randomization process is accomplished in two steps. In the first step, i fiber angles (ϕ_k) have been generated between $-90°$ and $90°$ randomly. By using these fiber angles, another i fiber angle ($90°+\phi_k$) has been generated by adding $90°$ to every previously generated ϕ_k. In the second step, these total $2i$ fiber angles are shuffled to randomize the sequence of these angles. Thereafter using this randomized stacking sequence, a symmetric stacking sequence with a total of $4i$ plies has been created. Hence a randomized second approach like stacking sequence has been generated. This randomized stacking sequence is used as the initial guess of the optimized fiber angles. To obtain global optimized results, several thousand iterations have been performed. The globally optimized fiber angles (ϕ_k), stacking sequence and objective function value have been given in Table 4.6. Similar to the first approach, in this second approach also, optimization has been performed by taking each fiber angle the same. The corresponding globally optimized values are provided in the Table 4.7.

In the case of numerical optimization, a randomized but symmetric stacking sequence is used as the initial guess of the optimized fiber angles. It is done by first generating $2i$ random fiber angles between $-90°$ and $90°$ then creating a symmetric stacking sequence ($4i$ fiber angles) using these $2i$ random fiber angles. This choice of initial guess of fiber angles enforces symmetric constraint in the laminate. $\zeta_1 = \zeta_3 = 0$ condition is used as the constraint of the problem. The lower and upper bounds of the problem are $-90°$ and $90°$ respectively. The optimized results of this case are provided in Table 4.7. The results correspond to $i = 1$ and $i = 2$ are in the same line as given by Aditya et al.[100].

On comparing the optimized results of the two cases (ϕ_k same and different) of the first approach given in Table 4.4 and Table 4.5, it is observed that these two results are almost identical. For both cases, when i is an odd number, APs at the inner-side condition provide poorer results than the mid and outer-side conditions. This type of clear indication is not observed when comparing mid-side and outer-side results. These observations suggest that for the first approach, the case when all ϕ_k are the same is computationally more efficient as in this case, only one unknown fiber angle has to be found, unlike other case. Similar observations are obtained for the second approach also and can be verified by comparing the optimized results given in Table 4.6 and Table 4.7. Moreover, the computational efficiency aspect becomes more important for the second approach because, in this case, the number of unknowns is twice as compared to the first approach.

Table 4.5: Bend-twist optimized stacking sequence obtained with first approach (all ϕs same)

i	Pos.	ϕ (°)	ϕ_c (°)	Stacking sequence (°)	d_{16} $(Nm)^{-1}$
2	-	68.14	-	$[-21.86/68.14/-68.14/21.86]_S$	0.21
3	I	-14.80	-22.87	$[-14.80/75.20/-75.20/14.80/-22.87/67.13]_S$	0.033
	M	67.83	-23.58	$[67.83/-22.17/-23.58/66.42/22.17/-67.83]_S$	0.073
	O	-23.23	-22.69	$[-22.69/67.31/-23.23/66.77/-66.77/23.23]_S$	0.084
4	-	68.14	-	$[-21.86/-21.86/68.14/68.14$ $/-68.14/-68.14/21.86/21.86]_S$	0.026
5	I	-17.82	-23.55	$[-17.82/-17.82/72.18/72.18/-72.18$ $/-72.18/17.82/17.82/-23.55/66.45]_S$	0.009
	M	67.89	-22.97	$[67.89/-22.11/-22.11/67.89/-22.97$ $/67.03/-67.89/22.11/22.11/-67.89]_S$	0.014
	O	-22.61	-22.43	$[-22.43/67.57/-22.61/67.39/-22.61$ $/67.39/-67.39/22.61/-67.39/22.61]_S$	0.015
6	-	-21.86	-	$[-21.86/-21.86/-21.86/68.14/68.14/68.14$ $/-68.14/-68.14/-68.14/21.86/21.86/21.86]_S$	0.0076
7	I	-19.19	-24.03	$[-19.19/-19.19/-19.19/70.81/70.81/70.81/-70.81$ $/-70.81/-70.81/19.19/19.19/19.19/-24.03/65.97]_S$	0.0037
	M	-22.55	-21.97	$[-22.55/-22.55/-22.55/67.45/67.45/67.45/-21.97$ $/68.03/-67.45/-67.45/-67.45/22.55/22.55/22.55]_S$	0.0055
	O	-22.10	-22.17	$[-22.17/67.83/67.90/-22.10/-22.10/-22.10/67.90$ $/67.90/-67.90/-67.90/22.10/22.10/22.10/-67.90]_S$	0.0051

I → inner-side, M → mid-side, O → outer-side

The optimized results of the second approach and numerical optimization can be compared from Table 4.7. It can be seen that these two results are almost identical. It should be noted that in Table 4.7, the second approach results are obtained from the unconstrained formulation with a single fiber angle. While numerical optimization results are obtained from the constrained formulation with $2i$ unknown fiber angles. Therefore second approach (with all ϕ_k same) becomes computationally very efficient. Likewise, in the second approach, with all ϕ_k different, the involved unknown fiber angles are i, which is half of the unknown involved in numerical optimization. Hence, this approach also provides better computational efficiency than the numerical approach.

The computational efficiency can be proved by comparing the time taken by different approaches (both cases of the second approach and numerical optimization) to obtain globally optimized results. In this regard, the time taken by the 'fmincon' function to converge to the globally optimized objective function value (up to 3 significant digits) for $i = 3$ has been recorded. For each case, to obtain the computational time distribution, a

Table 4.6: Bend-twist optimized stacking sequence obtained with second approach (all ϕs different)

i	ϕ_k (°)	Stacking sequence (°)	$d_{16}(Nm)^{-1}$
1	{-65.68}	$[24.32/\text{-}65.68]_S$	3.04
2	{22.99, -64.44}	$[25.56/22.99/\text{-}67.01/\text{-}64.44]_S$	0.39
3	{-24.80, -22.25, 64.19}	$[\text{-}25.81/\text{-}24.80/\text{-}22.25/67.75/65.20/64.19]_S$	0.114
4	{64.11, 68.17, -24.06, 64.62}	$[\text{-}25.89/\text{-}25.38/\text{-}24.06/\text{-}21.83$ $/68.17/65.94/64.62/64.11]_S$	0.048
5	{-25.67, -24.83, 66.54, -25.57, -21.61}	$[\text{-}25.57/\text{-}25.67/\text{-}24.83/\text{-}23.46/\text{-}21.61$ $/68.39/66.54/65.17/64.43/64.33]_S$	0.025
6	{-25.53, -24.23, -24.87, 65.51, -17.33, 67.95}	$[\text{-}24.49/\text{-}24.23/\text{-}24.87/\text{-}25.53/72.67/\text{-}22.05$ $/\text{-}17.33/67.95/65.51/65.77/64.47/65.13]_S$	0.014
7	{-64.79, 25.83,-70.89, -67.26,18.12,-67.04, 18.92}	$[25.21/25.83/22.96/\text{-}70.89/\text{-}71.08$ $/\text{-}71.88/\text{-}67.04/\text{-}67.26/19.11/18.92$ $/22.74/\text{-}64.17/18.12/\text{-}64.79]_S$	0.009

Table 4.7: Bend-twist optimized stacking sequence obtained with second approach (all ϕs same) and numerical optimization

i	ϕ (°)	Stacking sequence (°)	$d_{16}(Nm)^{-1}$	
			2nd Approach	Nu.Op.
1	-65.68	$[24.32/\text{-}65.68]_S$	3.04	3.04
2	-65.68	$[\{24.32\}_2/\{\text{-}65.68\}_2]_S$	0.38	0.38
3	-65.68	$[\{24.32\}_3/\{65.68\}_3]_S$	0.11	0.11
4	-66.00	$[\{24.00\}_4/\{\text{-}66.00\}_5]_S$	0.048	0.051
5	24.00	$[\{24.00\}_5/\{\text{-}66.00\}_5]_S$	0.024	0.027
6	66.00	$[\{\text{-}24.00\}_6/\{66.00\}_6]_S$	0.014	0.015
7	25.00	$[\{25.00\}_7/\{\text{-}65.00\}_7]_S$	0.009	0.009

Table 4.8: Computational time in seconds

Case	Mean	Mode	Median
Second approach (all ϕ_k same)	0.144	0.008	0.10
Second approach (all ϕ_k different)	0.848	0.020	0.59
Numerical optimization	2.09	0.141	1.45

sample size of 5×10^4 has been taken. The mean, mode and median of this computational time data are provided in Table 4.8. The computational time distribution for each case is provided in Fig. 4.11. From this figure, it can be observed that for the proposed second approach with all ϕ_k same, the computational time distribution is confined within

0.8 seconds. This computational time distribution is confined to 5 and 12 seconds for the case when all ϕ_k are different and numerical optimization cases, respectively. Mean, mode and median values of this computational time distribution also suggest that the proposed stacking sequence is computationally more efficient than numerical optimization. From these observations, all of these approaches can be arranged according to their computational efficiency in the following order

second approach (all ϕ_k same) > second approach (all ϕ_k same) > numerical optimization

In Fig. 4.12 optimized d_{16} is plotted against i obtained due to first approach and second

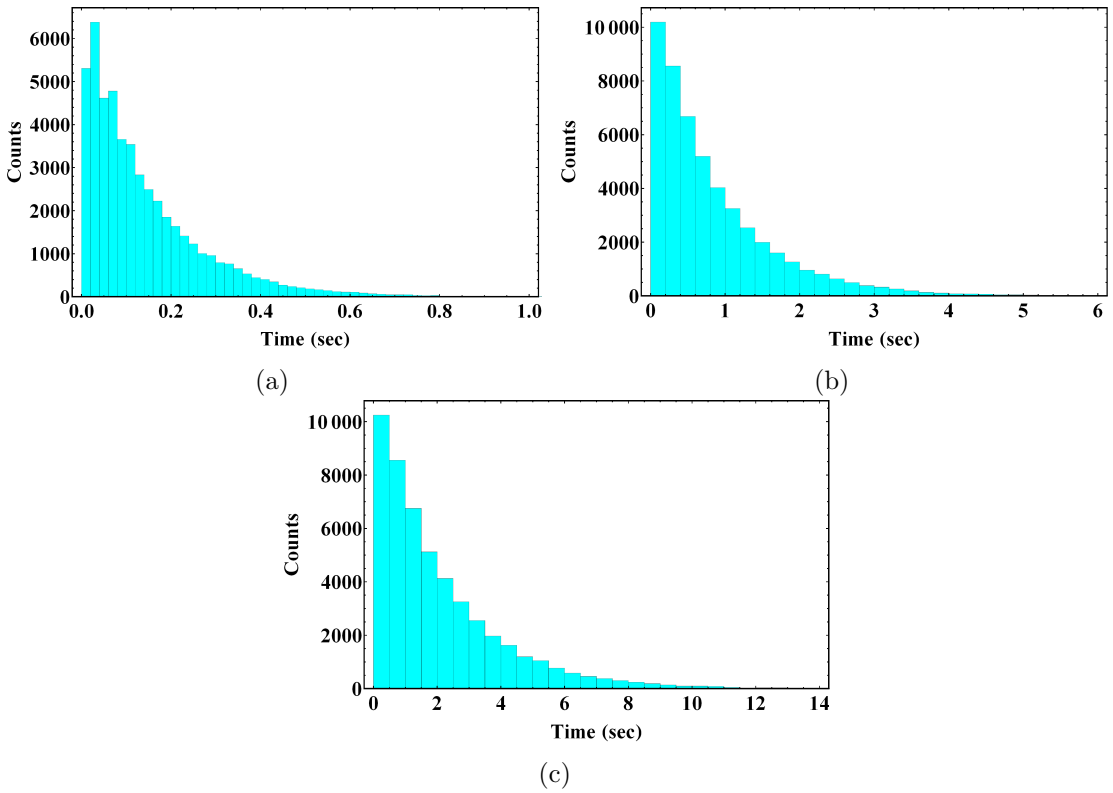

Figure 4.11: Computational time distribution (a) Second approach all ϕ_k same (b) second approach all ϕ_k different (c) numerical optimization

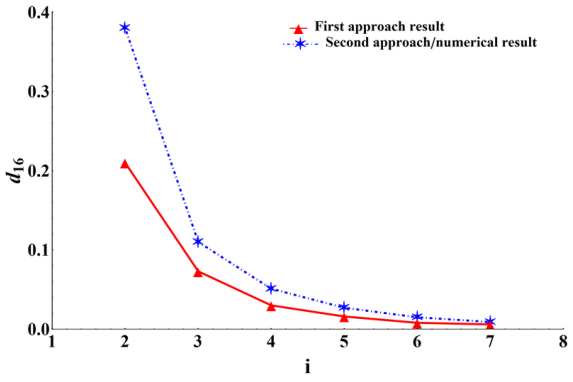

Figure 4.12: Plots of optimized d_{16} values

approach/numerical optimization. Here it should be noted that in the first approach, for i to be an odd case, the value of d_{16} is taken for APs at mid-side conditions. From this figure, it can be seen that as the i increases, the difference between the optimized results of the first approach and the second approach/numerical optimization reduces. Furthermore, as in the first approach, the independent fiber angles are only $i/2$ (or only one for all ϕ_k same) and the level of randomization ($factorial(i)$) is much less than the second approach ($factorial(2i)$). Hence, for higher i, the first approach with all ϕ_k is the best option to get hygrothermal stable laminate with bend-twist coupling as it will converge to its optimized value in the least time.

4.3.4 Sensitivity Analysis

The optimized stacking sequences have been investigated for their robustness to small perturbations in the optimized fiber angles using sensitivity analysis, as has been done for the extension–twist coupling case. Here, in this case, the coupling loss term is defined as the relative error between perturbed and optimized bend-twist coupling coefficient, and the mathematical expression is given as,

$$\%\text{Error} = \frac{|d_{16}^P| - |d_{16}^O|}{|d_{16}^O|} \times 100 \tag{4.47}$$

where d_{16}^O represents the optimized coupling coefficient and d_{16}^P represents the coupling coefficient due to perturbed stacking sequence. For the sensitivity analysis purpose, optimized results obtained with the first approach (both cases for $i = 3$), second approach (both cases for $i = 4, 5, 6$), and numerical optimization (for $i = 3, 4, 5, 6$) have been selected. For each case, total 5×10^5 perturbed stacking sequences have been generated. It is done by assuming that ply angles are uniformly distributed between $\theta_k - 2^\circ$ and $\theta_k + 2^\circ$ for each ply. Here θ_k represents the optimized fiber angle for k^{th} ply of laminate. In Fig. 4.13, the error histograms corresponding to both cases of the first approach are given. From this figure, two observations can be made. (i) The error distribution in bend-twist coupling due to perturbation in optimized stacking sequence is almost similar for both cases. (ii) Sensitivity-wise, the laminate with APs at the inner-side is the most sensitive among the three sub-cases. The error distribution for mid-side and outer-side cases is not much different but between these two sub-cases, mid-side laminate is the least sensitive.

The error histograms for both cases of the second approach have been provided in Fig. 4.14. It can be observed from this figure that for the case when all ϕ_k are equal, it is more robust than the case when all ϕ_k are different. The histogram of numerical optimization has been provided in Fig. 4.15. By comparing all the histograms (for first approach APs at mid-side case), it can be seen that for all given cases error distribution is within $\pm$ 6%.

4.4 Extension-Bend Coupling with Hygrothermal Stable Stacking

Laminates with extension-bend coupling and hygrothermal stability require asymmetric stacking sequence with nonzero B_{11}, B_{22} and B_{12}. Hence, the first set of hygrothermal stability conditions (Eq. 4.17), i.e., $[B] = 0$ or $\zeta_5 = \zeta_6 = \zeta_7 = \zeta_8 = 0$ cannot be implemented. From Eq. (4.12), it can be observed that B_{11} and B_{22} are function of ζ_5 and ζ_6, while B_{12} is function of ζ_6 only. Therefore, when the second set of hygrothermal stability conditions (Eq. 4.18), i.e., $\zeta_1 = \zeta_3 = \zeta_5 = \zeta_7 = 0$ has been applied, it leaves B_{11}, B_{22} and B_{12} nonzero. Hence, hygrothermally stable laminate with extension-bend

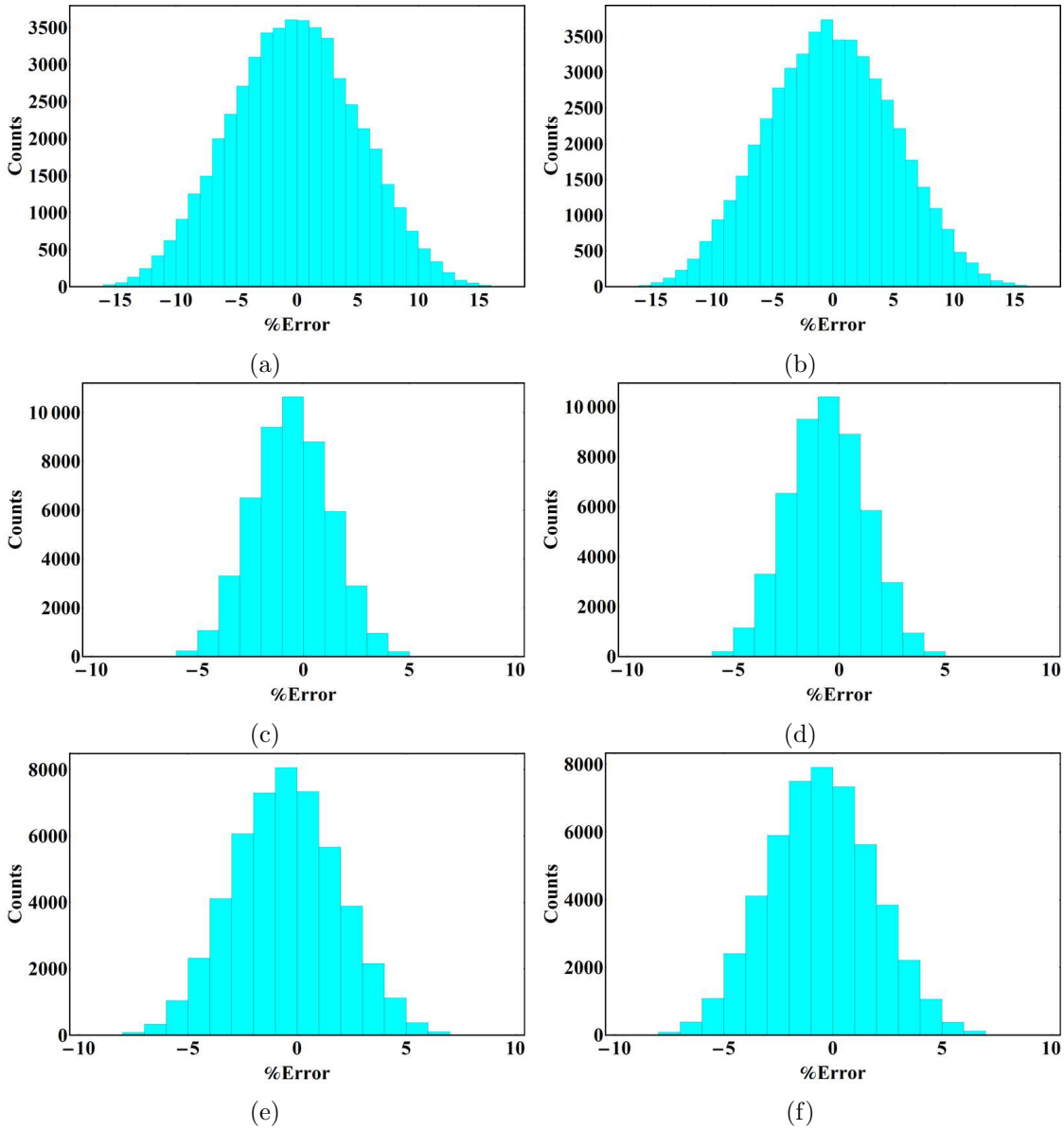

Figure 4.13: First approach for $i = 3$ (a,c,e) all ϕ_k different, for APs at inner-side, mid-side and outer-side respectively (b,d,f) all ϕ_k same, for APs at inner-side, mid-side and outer-side respectively

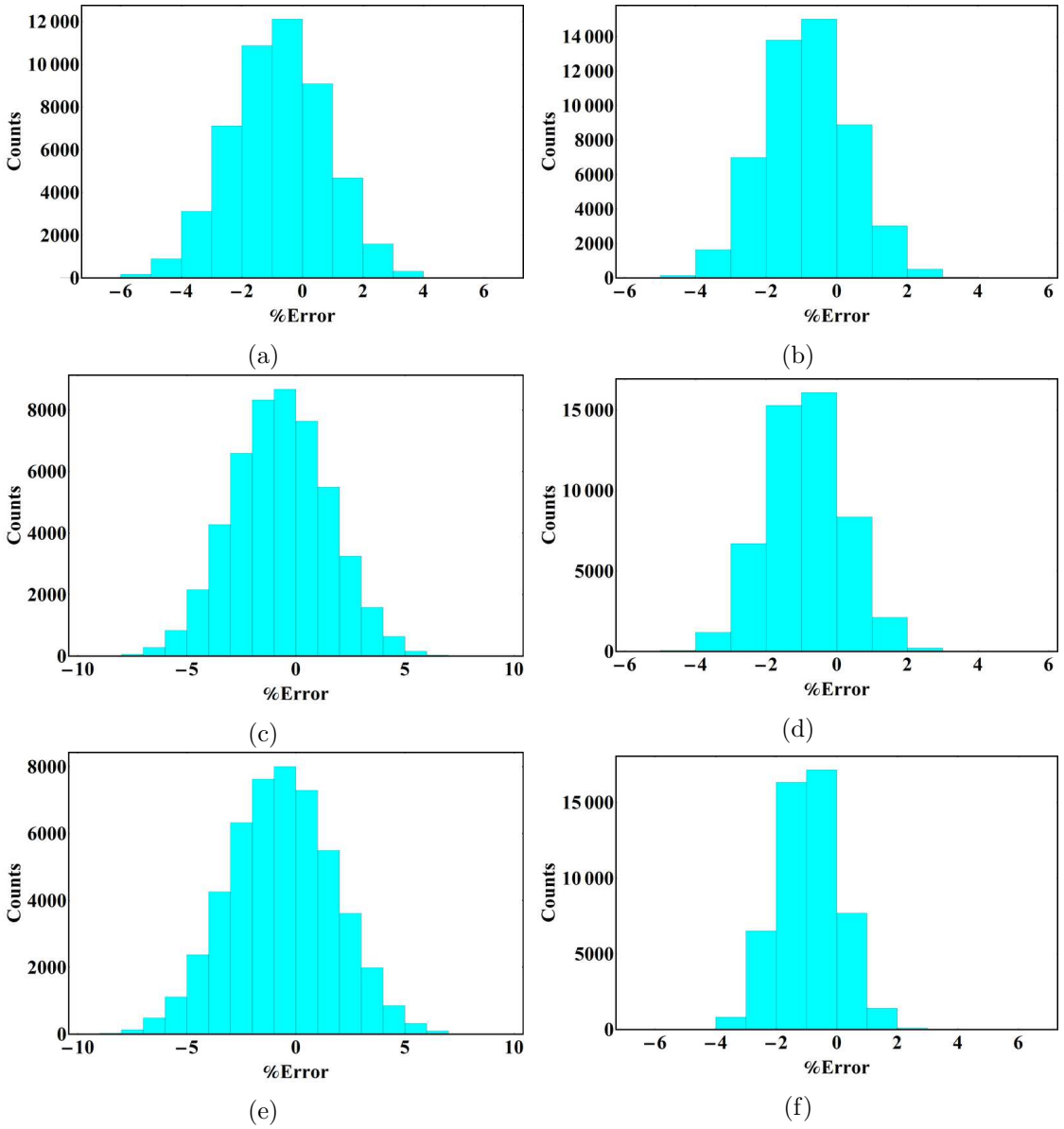

Figure 4.14: Second approach, (a,c,e) all ϕ_k different for $i = 4, 5$ and 6 respectively (b,d,f) all ϕ_k same for $i = 4, 5$ and 6 respectively

coupling can be obtained. Jones[109] suggests that anti-symmetric cross-laminate provides such coupling, but this laminate is not hygrothermally stable. The present study proposes an asymmetric stacking sequence for the laminate with a total $4i$ ($i = 2, 3, 4\ldots$) plies. Depending on the numerical value of i (whether it is even or odd), two cases arise and will be discussed in the following sub-sections.

4.4.1 When i is an even number

In this case, the hygrothermally stable laminate with extension-bend coupling is obtained using the following steps:

(a) The Sub-Laminates (SLs), on either side of the mid-plane of the overall laminate, have to be symmetric about their own mid-plane (division of laminate is given in

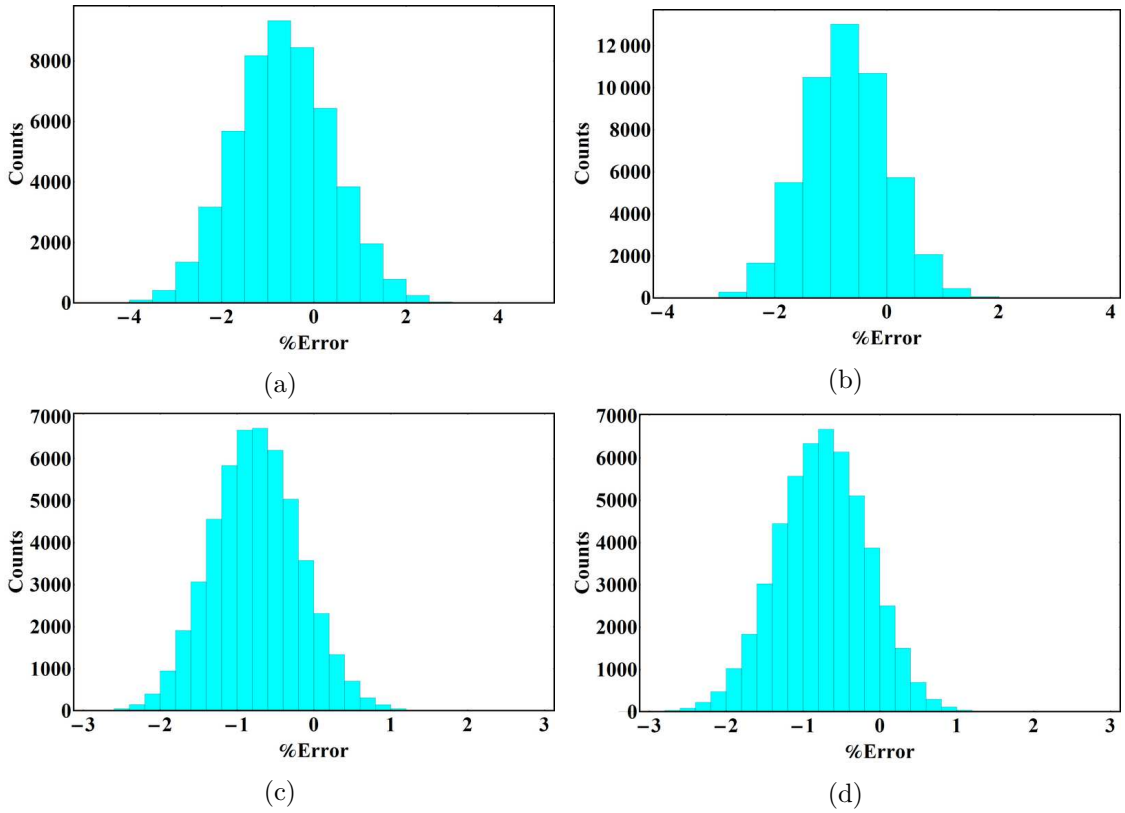

Figure 4.15: Numerical approach for $i = 3, 4, 5$ and 6 respectively

Fig. 4.2a). After this step, each SL leaves with i independent fiber angles. Hence, this step reduces total independent fiber angles to $2i$.

(b) In one SL, half $(i/2)$ independent fiber angles have to be made $45°$ and the remaining half as $-45°$. Similarly, in other SL, half-fiber angles have to be made $90°$ and the other half as $0°$. This assignment of values to independent fiber angles is completely arbitrary.

The above steps can be better understood by the following example of laminate having total plies 8 ($i = 2$). For the application of the first step ((a)), following replacement of fiber angles is required

$(\theta_4 \to \theta_1, \quad \theta_3 \to \theta_2, \quad \theta_8 \to \theta_5, \quad \theta_7 \to \theta_6)$

After the above replacement of fiber angles, for this laminate, the expression of $\zeta_1, \zeta_3, \zeta_5,$ and ζ_7 is given as

$$\zeta_1 = \frac{1}{4}\left(\cos 2\theta_1 + \cos 2\theta_2 + \cos 2\theta_5 + \cos 2\theta_6\right) \tag{4.48}$$

$$\zeta_3 = \frac{1}{4}\left(\sin 2\theta_1 + \sin 2\theta_2 + \sin 2\theta_5 + \sin 2\theta_6\right) \tag{4.49}$$

$$\zeta_4 = \frac{1}{8}\left(-\cos 2\theta_1 - \cos 2\theta_2 + \cos 2\theta_5 + \cos 2\theta_6\right) \tag{4.50}$$

$$\zeta_7 = \frac{1}{8}\left(-\sin 2\theta_1 - \sin 2\theta_2 + \sin 2\theta_5 + \sin 2\theta_6\right) \tag{4.51}$$

Fiber angles θ_1 and θ_2 corresponds to SL above the mid-plane, while fiber angles θ_5 and θ_6 corresponds to lower SL (as shown in Fig. 4.2a). Now, according to the second step

(b), one of the SLs can be chosen arbitrarily to assign fiber angles $45°/-45°$ or $90°/0°$. Let upper SL is chosen to be assigned with $45°/-45°$. Here it can be seen that the assignment of these fiber angles is completely arbitrary. Similar observations can be made for the lower SL with fiber angles $90°/0°$. After the application of this second step, Eqs. (4.48-4.51) will be vanished hence satisfying the hygrothermal stability condition.

4.4.2 When i is an odd number

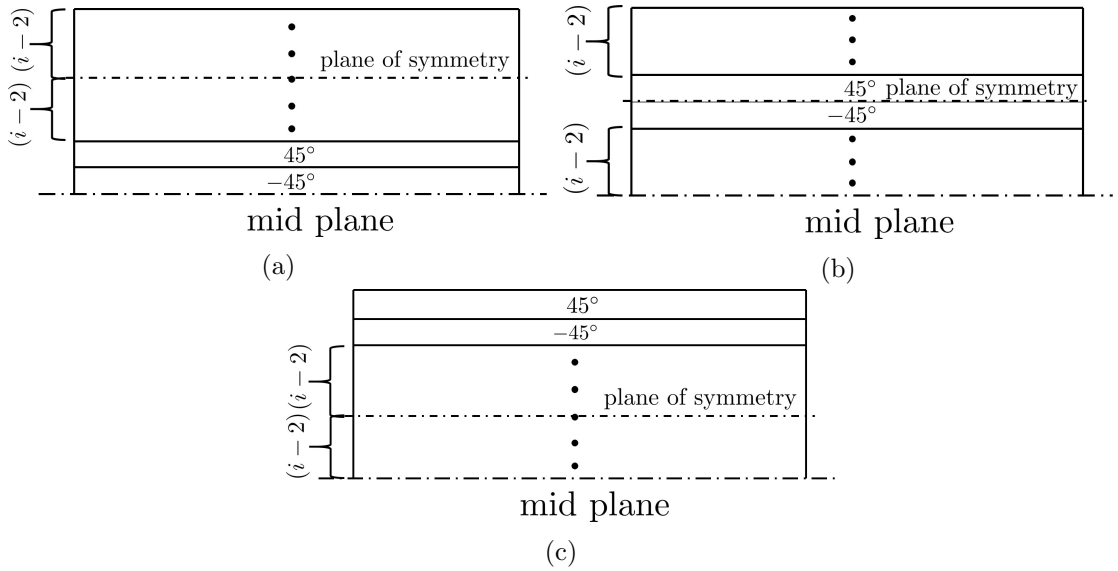

Figure 4.16: 3 position of adjacent plies (a) inner-side (b) mid-side (c) outer-side

In this case, $i/2$ is not a whole number; hence, the second step (b) of the previous section (4.4.1) cannot be implemented directly. In addition to the two steps provided in the previous section (4.4.1), one more step has been proposed. In this step, two Adjacent Plies (APs) have to be selected in both the SLs. APs of one SL will be in symmetry w.r.t APs of other SL. These APs have to be assigned with $45°$ and $-45°$ arbitrarily. In this work, three positions (inner-side, mid-side and outer-side) of APs in SL have been identified, as shown in Fig. 4.16. Hence, according to the position of APs, in this case, three different stacking sequences are possible. These three stacking sequences can be obtained by applying (i) the step of selection of APs, as discussed above, and (ii) the two steps (i.e.,(a) symmetry condition and (b) fiber angles assignment) provided in section (4.4.1).

Application of the first step leaves $2(i-1)$ independent fiber angles in each SL. Similarly, after applying the symmetry condition step, each SL leaves with $(i-1)$ independent fiber angles. Here, it should be noted that the application of the symmetry condition will depend on the position of APs in SL as it changes the plane of symmetry. Positions of the plane of symmetry correspond to the three positions of APs are shown in Fig.3. Now, as $(i-1)$ is an even number, the last step of the assignment of independent fiber angles with $45°/-45°$ and $90°/0°$ can be implemented as has been done in section (4.4.1). All of these steps for three subcases can be understood by taking an example with $i = 3$. The first two

steps and the resultant expression of $\zeta_1, \zeta_3, \zeta_5,$ and ζ_7 is given in table (4.9).The resultant expression of $\zeta_1, \zeta_3, \zeta_5,$ and ζ_7 given in this table, will be vanished after the application of the third step. Hence this stacking sequence meets the condition of hygrothermal stability. The whole procedure can be understood by the Fig. 4.17

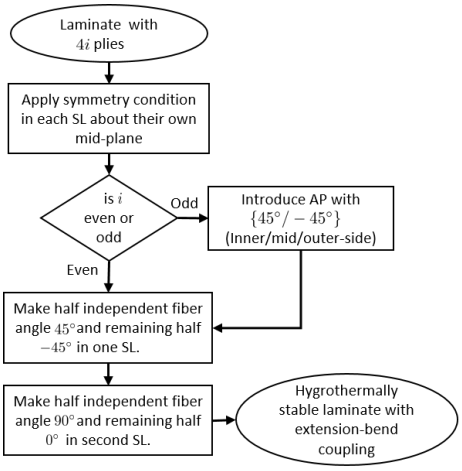

Figure 4.17: Steps to get hygrothermally stable laminate with extension-bend coupling

Table 4.9: steps to obtain hygrothermally stable laminate with extension-bend coupling for $i = 3$

Pos.	Fiber angles correspond to APs and corresponding replacement	Fiber angles replacement for symmetry condition	Resultant expression of $\zeta_1, \zeta_3, \zeta_5, \zeta_7$ after the first two steps
I	$\theta_8 \to \theta_5,$ $\theta_7 \to \theta_6$	$\theta_4 \to \theta_1,$ $\theta_3 \to \theta_2,$ $\theta_{12} \to \theta_9,$ $\theta_{11} \to \theta_{10}$	$\zeta_1 = 1/6\,(\cos 2\theta_1 + \cos 2\theta_2 + \cos 2\theta_9 + \cos 2\theta_{10})$ $\zeta_3 = 1/6\,(\sin 2\theta_1 + \sin 2\theta_2 + \sin 2\theta_9 + \sin 2\theta_{10})$ $\zeta_5 = 1/9\,(-\cos 2\theta_1 - \cos 2\theta_2 + \cos 2\theta_9 + \cos 2\theta_{10})$ $\zeta_7 = 1/9\,(-\sin 2\theta_1 - \sin 2\theta_2 + \sin 2\theta_9 + \sin 2\theta_{10})$
M	$\theta_{10} \to \theta_3,$ $\theta_9 \to \theta_4$	$\theta_6 \to \theta_1,$ $\theta_5 \to \theta_2,$ $\theta_{12} \to \theta_7,$ $\theta_{11} \to \theta_8$	$\zeta_1 = 1/6\,(\cos 2\theta_1 + \cos 2\theta_2 + \cos 2\theta_7 + \cos 2\theta_8)$ $\zeta_3 = 1/6\,(\sin 2\theta_1 + \sin 2\theta_2 + \sin 2\theta_7 + \sin 2\theta_8)$ $\zeta_5 = 1/12\,(-\cos 2\theta_1 - \cos 2\theta_2 + \cos 2\theta_7 + \cos 2\theta_8)$ $\zeta_7 = 1/12\,(-\sin 2\theta_1 - \sin 2\theta_2 + \sin 2\theta_7 + \sin 2\theta_8)$
O	$\theta_{12} \to \theta_1,$ $\theta_{11} \to \theta_2$	$\theta_6 \to \theta_3,$ $\theta_5 \to \theta_4,$ $\theta_{10} \to \theta_7,$ $\theta_9 \to \theta_8$	$\zeta_1 = 1/6\,(\cos 2\theta_3 + \cos 2\theta_4 + \cos 2\theta_7 + \cos 2\theta_8)$ $\zeta_3 = 1/6\,(\sin 2\theta_3 + \sin 2\theta_4 + \sin 2\theta_7 + \sin 2\theta_8)$ $\zeta_5 = 1/18\,(-\cos 2\theta_3 - \cos 2\theta_4 + \cos 2\theta_7 + \cos 2\theta_8)$ $\zeta_7 = 1/18\,(-\sin 2\theta_3 - \sin 2\theta_4 + \sin 2\theta_7 + \sin 2\theta_8)$

I $\to$ inner-side, M $\to$ mid-side, O $\to$ outer-side

4.4.3 Optimization

The optimization in the current work aims to maximize the extension-bend coupling. Hence, in this optimization process, the compliance coefficient b_{11} serves the purpose of the objective function. The hygrothermal stability conditions (Eq. 4.18) in terms of ζ, are the constraints of the optimization problem. The material properties used in the optimization process are provided in table (4.1).

As the proposed stacking sequence has already satisfied these constraints and the fiber

Table 4.10: optimized results obtained using the current approach

i	Pos.	Optimized Stacking sequence (°)	$b_{11}(N^{-1})$ (10^{-5})
2	-	$[(45/-45)_S/(90/0)_S]_T$	4.17
3	I	$[(45/-45)_S/(45/-45)_S/(90/0)_S]_T$	2.28
	M	$[(45/-45)/(45/-45)/(-45/45)/(90/0)/(-45/45)/(0/90)]_T$	1.65
	O	$[(45/-45)/(45/-45)_S/(90/0)_S/(-45/45)]_T$	1.67
4	-	$[(45_2/-45_2)_S/(90_2/0_2)_S]_T$	1.04
5	I	$[(45_2/-45_2)_S/(45/-45)_S/(90_2/0_2)_S]_T$	0.78
	M	$[(45_2/-45_2)/(45/-45)/(-45_2/45_2)/(90_2/0_2)/(-45/45)/(0_2/90_2)]_T$	0.624
	O	$[(45/-45)/(45_2/-45_2)_S/(90_2/0_2)_S/(-45/45)]_T$	0.649
6	-	$[(45_3/-45_3)_S/(90_3/0_3)_S]_T$	0.464
7	I	$[(45_3/-45_3)_S/(45/-45)_S/(90_3/0_3)_S]_T$	0.384
	M	$[(45_3/-45_3)/(45/-45)/(-45_3/45_3)/(90_3/0_3)/(-45/45)/(0_3/90_3)]_T$	0.325
	O	$[(45/-45)/(45_3/-45_3)_S/(90_3/0_3)_S/(-45/45)]_T$	0.336

I → inner-side, M → mid-side, O → outer-side

angles have already been assigned. Hence, the optimization of the proposed stacking sequence involves the rearrangement of the assigned fiber angles in both the SL and finding out the sequence of these assigned fiber angles, which provides maximized b_{11}. To obtain this optimized sequence, all possible sequences have been generated and the

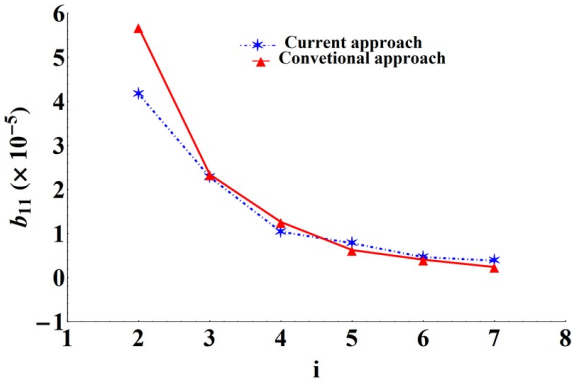

Figure 4.18: Plots of optimized b_{11} values

corresponding objecting function value has been obtained. The sequence that corresponds to the maximum objective function is selected as the globally optimized stacking sequence for the proposed stacking sequence. These optimized results are provided in table (4.10). This table contains the optimized results for laminates having $i = 2$ through 7. From table (4.10), it can be observed that for odd values of i, the better optimized objective function value is obtained when APs are at the inner-side.

The conventional optimization results of most generic stacked laminate are provided in the table (4.11). These optimized results are obtained using 'fmincon' function of MATLAB implemented with the SQP algorithm. The hygrothermal stability conditions serve as the equality constraints of the problem. To find and build confidence in globally optimized results, several thousand (even lakhs for larger i) iterations have been performed by taking different initial guesses.

The optimized results obtained from the two approaches are plotted against i and given

Table 4.11: optimized results obtained using the conventional approach

i	Optimized Stacking sequence ($^\circ$)	$b_{11}(N^{-1})$ (10^{-5})
2	$[-89.90/-44.88/3.27/31.53/35.30/-53.42/51.43/-52.85]_T$	5.68
3	$[-74.59/-89.86/-16.39/-12.18/26.14/41.28/38.04$ $/-42.48/58.08/-46.55/63.07/-41.49]_T$	2.34
4	$[53.50/49.11/-49.88/-46.90/43.38/-57.34/-39.75/38.89$ $/-32.87/50.45/-17.47/-8.21/9.92/-81.71/-82.98/55.99]_T$	1.26
5	$[38.70/-56.72/39.08/-55.30/-48.08/47.29/42.24/-52.39/44.48$ $/-47.18/-2.83/-26.77/-74.22/37.38/70.17/-17.51$ $/-12.18/-86.96/20.44/86.38]_T$	0.624
6	$[-78.11/-46.65/90.00/3.97/-69.18/36.47/35.77/7.62/-10.32$ $/-42.81/53.23/74.91/17.69/-40.61/-31.88/46.43/46.02$ $/-51.05/51.05/46.74/-42.77/55.84/-51.43/-46.16]_T$	0.406
7	$[79.27/90.00/2.96/90.00/69.81/-33.38/-16.72/28.24/25.62$ $/-37.45/0.69/-14.59/16.44/-30.52/80.85/-62.66/83.35$ $/-39.42/64.37/52.30/-48.26/-41.55/48.73/45.51/45.73/42.98$ $/-43.78/-42.93]_T$	0.239

in Fig. 4.18. Comparison of the two results using this figure reveals that for smaller i the conventional results are better than the current approach results. As i increases, the difference between the two results becomes insignificant and for larger i current approach provides better results than the conventional approach.

4.4.4 Sensitivity analysis

The sensitivity analysis for this case has also been done for the same reason as discussed in the previous two cases. The coupling loss in this case is also defined as the relative

% error between the perturbed result and optimized result but in this case coupling coefficient is b_{11} and mathematically it represents as

$$\%\text{Error} = \frac{|b_{11}^{P}| - |b_{11}^{o}|}{|b_{11}^{o}|} \times 100 \tag{4.52}$$

Similar to the previous cases, in this case also total of 5×10^4 perturbed results have

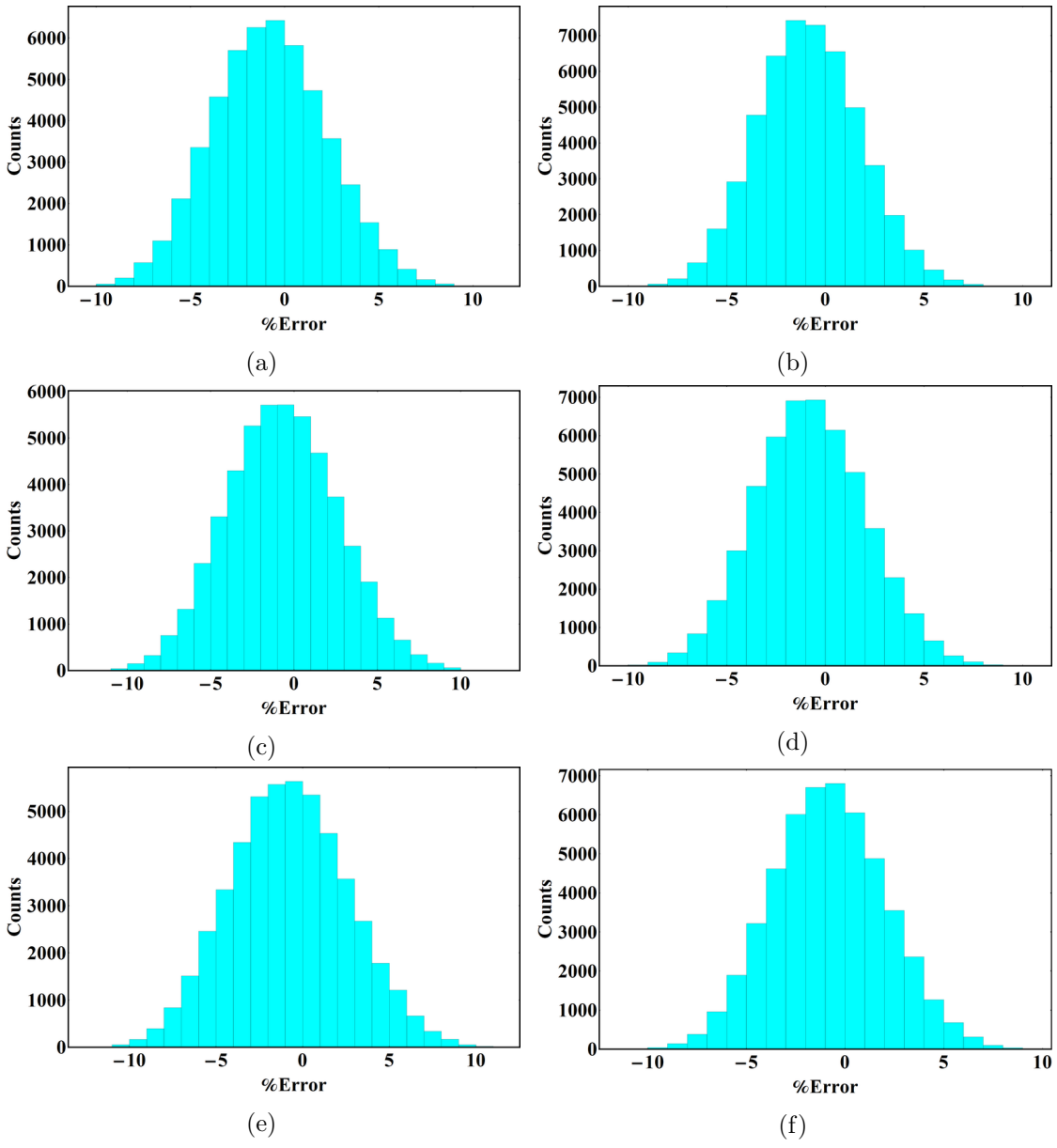

Figure 4.19: histograms for APs at inner-side, mid-side and outer-side (a,c,e) for $i = 5$ (b,d,f) for $i = 7$ respectively

been generated in the range $(\theta_k - 2°)$ and $(\theta_k + 2°)$ by assuming the perturbed results are uniformly distributed between these two limits. Here θ_k represents the optimized fiber angle of k^{th} ply. Optimized results obtained from the proposed approach and conventional numerical approach have been considered for this analysis. The results obtained from this analysis have been provided in the form of histogram in Fig. 4.19 and Fig. 4.20.

In Fig. 4.19, histograms obtained from the sensitivity analysis of optimized results of the current approach for three subcases of $i = 5$ and $i = 7$ have been provided. These histograms show the effect of the position of the APs on the robustness of the resultant laminate. From this figure, it can be observed that for three positions of APs, the difference in %error distribution is not significant. In other words, the position of APs does not affect the sensitivity significantly. However, a closer observation reveals that the % error distribution for the laminate with APs at the inner side has a marginally more central tendency than for the other two positions.
In Fig. 4.20 histogram corresponds to the sensitivity analysis of current optimized results and conventional optimized results have been provided. For both approaches, results are provided for $i = 2, 3, 4$. Here, the histogram for the current approach with $i = 3$ corresponds to laminate having APs at the inner side. This figure compares the robustness to perturbations in the optimized fiber angles of the resulting laminate obtained using both approaches. By comparing the results, it can be observed that for smaller i conventional approach provides a more robust stacking sequence; however, the difference between the two results is not significantly large. As i increases, the difference in error distribution becomes very small. Hence, for larger i, both approaches provide equally robust stacking sequences.

4.5 Analysis of Strip-like Beam

This section presents an analysis of the coupling behavior of an anisotropic-inhomogeneous beam, which is modeled as a strip-like composite beam. The elastic coupling in composite structures is well explored using CLPT. In this study, we used the VAM-based mathematical formulation developed by Hodges et al. [73] for the strip-like beam. We implemented the hygrothermally stable stacking sequences proposed in the previous section into this mathematical formulation to obtain the hygrothermally stable beam with the desired coupling. We have shown three types of coupling results here and compared them with the FEA results, which showed close agreement between the two. The FEA analysis verified the hygrothermal stability of these beams. For convenience, we have provided a brief introduction to this formulation before proceeding to the coupling results.

4.5.1 Mathematical Formulation

The Variational Asymptotic Method requires small parameters, as already discussed in chapter 2. For this class of beam, small parameters are width-to-length ratio $\delta_b = b/l$, thickness-to-width ratio $\delta_h = h/b$, and width times pre-twist angle per unit length $\delta_t = bk_1$. The beam geometry and associated coordinate system are shown in Fig. 4.21. In this analytical development, indices $i = 1, 2, 3$ while indices $\alpha = 1, 2$.

The position vector of any arbitrary material point in the undeformed configuration of

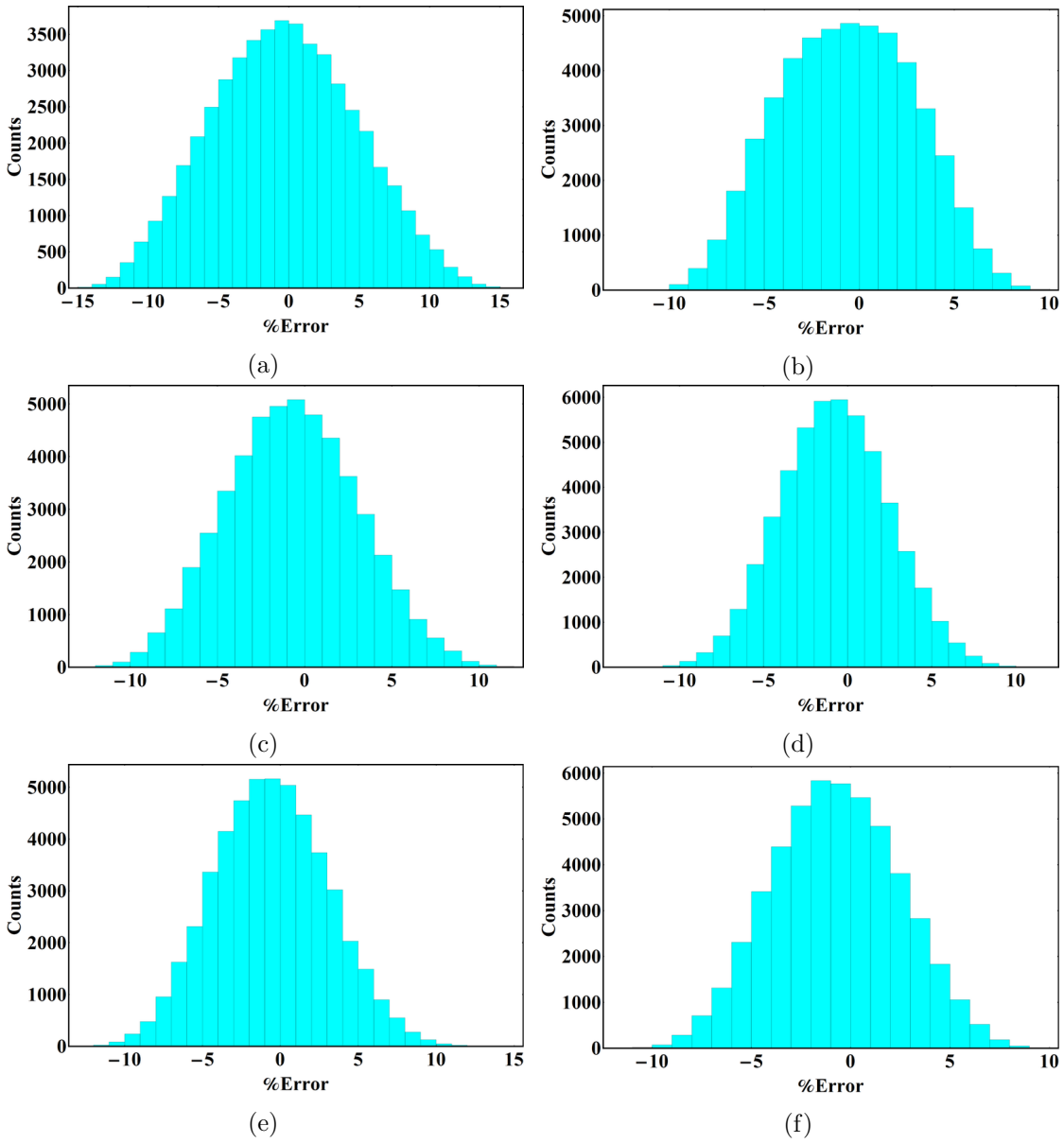

Figure 4.20: sensitivity histograms for $i = 2, 3$ and 3 (a, c, e) current approach and (b, d, f) conventional approach respectively

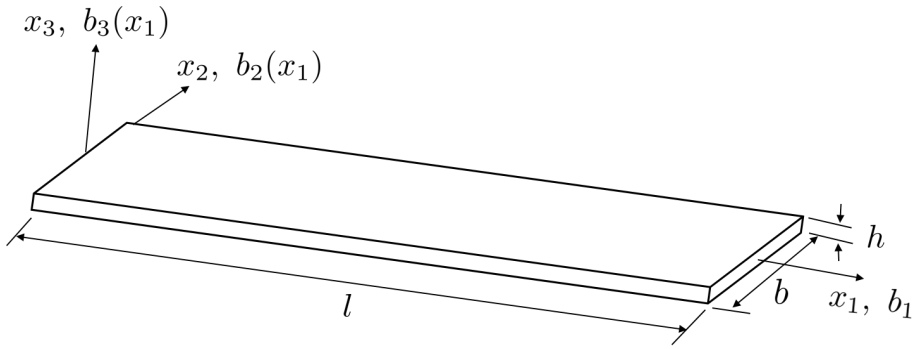

Figure 4.21: Schematic of the strip-like beam with associated coordinate system

this strip is given as

$$\hat{r} = x_1 b_1 + x_2 b_2(x_1) + x_3 b_3(x_1) \tag{4.53}$$

The respective covariant base vector in the undeformed state can be obtained by using the relation provided in Eq. (2.3) and given as

$$g_1 = b_1 + k_1(x_2 b_3 - x_3 b_2), \qquad g_2 = b_2, \qquad g_3 = b_3 \tag{4.54}$$

Using these covariant base vectors corresponding contravariant base vector can be calculated by using Eq. (2.4) and given as

$$g^1 = b_1, \qquad g^2 = b_2 + k_1 x_3 b_1, \qquad g^3 = b_3 - k_1 x_2 b_1 \tag{4.55}$$

Similar to the undeformed state, the position vector in the deformed state can be defined and given by

$$\hat{R} = x_1 b_1 + u_i(x_1) b_i + x_2 B_2(x_1) + x_3 B_3(x_1) + \overline{w}_i(x_1, x_2, x_3) B_i(x_1) \tag{4.56}$$

Here, in this expression, u_i represents the rigid body translation, B_i are orthogonal unit vectors of the deformed coordinate system obtained from rigid body rotation, and $\overline{w}_i$ represents the warping displacements of the beam cross-section.
The warping displacement component $\overline{w}_3$ can be divided into an average warping across the thickness and Poisson-like unknown variation as suggested by the reference [73] and is given as

$$\overline{w}_3(x_1, x_2, x_3) = w_3(x_1, x_2) + \Delta_3(x_1, x_2, x_3) \tag{4.57}$$

where

$$\int_{-\frac{h}{2}}^{\frac{h}{2}} \Delta_3 \left(x_1, x_2, x_3\right) dx_3 = 0 \tag{4.58}$$

Similarly, the above reference suggests that the warping components $\overline{w}_\alpha$ can be split into three parts (i) average warping, (ii) linear variation along the thickness and (iii) unknown variations; these are written as

$$\overline{w}_\alpha(x_1, x_2, x_3) = w_\alpha(x_1, x_2) + x_3 \phi_\alpha(x_1, x_2) + \Delta_\alpha(x_1, x_2, x_3) \tag{4.59}$$

where

$$\int_{-\frac{h}{2}}^{\frac{h}{2}} \Delta_\alpha \left(x_1, x_2, x_3\right) dx_3 = 0 \tag{4.60}$$

and

$$\int_{-\frac{h}{2}}^{\frac{h}{2}} \Delta_{\alpha,3} \left(x_1, x_2, x_3\right) dx_3 = 0 \tag{4.61}$$

By using these relations, Eq. (4.56) will be rewritten as

$$\hat{R} = x_1 b_1 + u_i b_i + w_i B_i + x_2 B_2 + x_3 \left(\phi_1 B_1 + \phi_2 B_2 + B_3\right) + \Delta_i B_i \tag{4.62}$$

Here, $B_i(x_1)$ and $u_i(x_1)$ are beam quantities, whereas $w_i(x_1, x_2)$ and $\phi_\alpha(x_1, x_2)$ shows the shell behavior. The $\phi_\alpha(x_1, x_2)$ represents local rotation and $w_i(x_1, x_2)$ are warping. These

variables are subjected to the following constraints

$$\langle w_i \rangle = 0, \quad \langle w_{3,2} \rangle = \langle \phi_2 \rangle \tag{4.63}$$

where

$$\langle \bullet \rangle = \int_{-\frac{b}{2}}^{\frac{b}{2}} (\bullet)\, dx_2 = 0 \tag{4.64}$$

Now the covariant base vector in the deformed state

$$G_i = \frac{\partial \hat{R}}{\partial x_i} \tag{4.65}$$

The above evaluation is completed by using the following identities.

$$\begin{aligned} B_1 =& \frac{[(x_1 + u_1)b_1 + u_2 b_2 + u_3 b_3]'}{s'}, \\ B_i' =& [(k_1 + \kappa_1)B_1 + \kappa_2 B_2 + \kappa_3 B_3] \times B_i \end{aligned} \tag{4.66}$$

where

$$\begin{aligned} b_i' =& k_1 b_1 \times b_i, \\ s' =& \sqrt{(1 + u_1')^2 + (u_2' - k_1 u_3)^2 + (u_3' + k_1 u_2)^2} = 1 + \gamma_{11} \end{aligned} \tag{4.67}$$

Here s denotes the running arc length along the reference line of the beam the deformation gradient tensor $A = G_i g^i$ can be calculated. The elements of this gradient tensor A in mixed bases system [113] is $A_{ij} = B_i.A.b_j$. For the small local rotation assumption, the 3D strain field is given as

$$E = \frac{A + A^T}{2} - I_3 \tag{4.68}$$

The 3D strain field for the moderate local rotation case [113] is defined as

$$\Gamma = E - \frac{\tilde{A}^2}{2} + \frac{E\tilde{A} - \tilde{A}E}{2} \tag{4.69}$$

Here, $\tilde{A}$ is the anti-symmetric part of A. The 3D strain components useful for further development are

$$\begin{aligned}
\Gamma_{11} =& \underbrace{\gamma_{11} - x_2\kappa_3 + x_3\kappa_2}_{O(\varepsilon)} + \overbrace{k_1 x_2^2 \kappa_1}^{O(\varepsilon\delta_t/\delta_h)} + \underbrace{\frac{x_2^2\kappa_1^2}{2} + w_3\kappa_2}_{O(\varepsilon^2/\delta_h^2)} + O\left(\varepsilon\delta_b, \varepsilon\delta_t, \frac{\varepsilon^2}{\delta_h}\right), \\
\Gamma_{22} =& \underbrace{w_{2,2} - x_3 w_{3,22}}_{O(\varepsilon)} + \overbrace{\frac{1}{2}w_{3,2}^2}^{O(\varepsilon^2/\delta_h^2)} + O(\varepsilon\delta_h) \\
2\Gamma_{12} =& \underbrace{w_{1,2} - 2x_3\kappa_1}_{O(\varepsilon)} + \overbrace{k_1(x_2 w_{3,2} - w_3)}^{O(\varepsilon\delta_t/\delta_h)} + \underbrace{k_1(x_2 w_{3,2} - w_3)}_{O(\varepsilon^2/\delta_h^2)} + O\left(\varepsilon\delta_b, \varepsilon\delta_h, \varepsilon\delta_t, \frac{\varepsilon^2}{\delta_h}\right).
\end{aligned} \tag{4.70}$$

The estimation of the order of the different quantities in the 3D strain field can be followed from the reference [73]. The 3D strain measures and 2D strain measures are related by $\Gamma_{\alpha\beta} = \varepsilon_{\alpha\beta} + x_3\rho_{\alpha\beta}$. Here, in this relation $\varepsilon_{\alpha\beta}$ represents the mid-plane stains while $\rho_{\alpha\beta}$ denotes mid-plane curvatures. Using this relation, membrane strain and curvature terms can be extracted from Eq. (4.70). The membrane strains are

$$\begin{aligned}
\varepsilon_{11} \approx& \gamma_{11} - x_2\kappa_3 + k_1 x_2^2\kappa_1 + \underline{\frac{x_2^2\kappa_1^2}{2}} + \underline{w_3\kappa_2}, \\
\varepsilon_{22} \approx& w_{2,2} + \underline{\frac{1}{2}w_{3,2}^2}, \\
2\varepsilon_{12} \approx& w_{1,2} + k_1(x_2 w_{3,2} - w_3) + \underline{\kappa_1(x_2 w_{3,2} - w_3)}
\end{aligned} \tag{4.71}$$

While membrane curvatures are

$$\begin{aligned}
\rho_{11} \approx& \kappa_2 \\
\rho_{22} \approx& -w_{3,22} \\
2\rho_{12} \approx& -2\kappa_1
\end{aligned} \tag{4.72}$$

In the above relations, non-underlined terms are of order $O(\varepsilon)$ and underlined terms are of order $O(\varepsilon\Delta)$; where $\Delta = \varepsilon/\delta_h^2$ is a new small parameter. The non-underlined terms are dominated terms and for zeroth order approximation, only these terms are required. The underlined terms are non-linear and are available due to moderate rotations. For first-order approximation, these terms have to be included. Further, it has been shown in the reference [73] that both CLST and CLPT contribute exactly the same in zeroth order and first order approximate energy.

4.5.2 Strain Energy of Strip-like Beam

In the current case, the beam is assumed to be a 2D elastic structure. The corresponding strain energy density (energy per unit mid-surface) is defined as

$$\mathcal{U}_{2D} = \frac{1}{2}\begin{Bmatrix} \varepsilon_{11} \\ \varepsilon_{22} \\ 2\varepsilon_{12} \\ \rho_{11} \\ \rho_{22} \\ 2\rho_{12} \end{Bmatrix}^T \begin{bmatrix} A & B \\ B & D \end{bmatrix} \begin{Bmatrix} \varepsilon_{11} \\ \varepsilon_{22} \\ 2\varepsilon_{12} \\ \rho_{11} \\ \rho_{22} \\ 2\rho_{12} \end{Bmatrix} \tag{4.73}$$

Here, $\varepsilon_{\alpha\beta}$ and $\rho_{\alpha\beta}$ are membrane strains and curvatures, respectively, given by Eqs. (4.71-4.72). A, B and D are extensional, coupling and bending stiffnesses, respectively. The unknown functions w_i can be obtained as the known function of x_2, κ_i and k_1 by minimizing strain energy functional $U = \int_0^l \langle U_{2D} \rangle dx_1$ along with the constraints (4.58), (4.60), (4.61) and (4.63). After that, the strain energy density (strain energy per unit length) $U_{1D} = \langle U_{2D} \rangle$ can be found.

4.5.3 Zeroth Order Approximation

The zeroth order approximation requires stain energy which is corrected up to order $E\varepsilon^2$. Hence, only the leading terms (non-underlined) of 2D membrane stains and curvatures in Eqs. (4.71) and (4.72) will be considered. As discussed above, the zeroth order approximate warping function w_i^0 can be obtained by minimizing zeroth-order energy. Ultimately 1D strain energy U_{1D} density and 1D constitutive relation can be found. The linear 1D constitutive relation is obtained in the following form.

$$\begin{Bmatrix} F_1 \\ M_1 \\ M_2 \\ M_3 \end{Bmatrix} = \begin{bmatrix} b\overline{\overline{A}}_{11} & -2b\overline{\overline{B}}_{16} + \frac{1}{12}b^3\overline{\overline{A}}_{11}k_1 & b\overline{\overline{B}}_{11} & 0 \\ -2b\overline{\overline{B}}_{16} + \frac{1}{12}b^3\overline{\overline{A}}_{11}k_1 & \frac{1}{80}b^5\overline{\overline{A}}_{11}k_1^2 - \frac{1}{3}b^3\overline{\overline{B}}_{16}k_1 + 4b\overline{\overline{D}}_{66} & \frac{1}{12}b^3\overline{\overline{B}}_{11}k_1 - 2b\overline{\overline{D}}_{16} & 0 \\ b\overline{\overline{B}}_{11} & \frac{1}{12}b^3\overline{\overline{B}}_{11}k_1 - 2b\overline{\overline{D}}_{16} & b\overline{\overline{D}}_{11} & 0 \\ 0 & 0 & 0 & \frac{1}{12}b^3\overline{\overline{A}}_{11} \end{bmatrix} \begin{Bmatrix} \gamma_{11} \\ \kappa_1 \\ \kappa_2 \\ \kappa_3 \end{Bmatrix} \tag{4.74}$$

The expressions of newly defined stiffness constants are provided in Appendix C.1. Here the expressions of warping functions w_i^0 are not provided as we are interested in the constitutive law only to observe the coupling behavior. However, expressions of these warping functions can be found in the reference [73]. For prismatic beam ($k_1 = 0$), the

Eq. (4.74) takes the form.

$$\begin{Bmatrix} F_1 \\ M_1 \\ M_2 \\ M_3 \end{Bmatrix} = \begin{bmatrix} b\overline{\overline{A}}_{11} & -2b\overline{\overline{B}}_{16} & b\overline{\overline{B}}_{11} & 0 \\ -2b\overline{\overline{B}}_{16} & 4b\overline{\overline{D}}_{66} & -2b\overline{\overline{D}}_{16} & 0 \\ b\overline{\overline{B}}_{11} & -2b\overline{\overline{D}}_{16} & b\overline{\overline{D}}_{11} & 0 \\ 0 & 0 & 0 & \frac{1}{12}b^3\overline{\overline{A}}_{11} \end{bmatrix} \begin{Bmatrix} \gamma_{11} \\ \kappa_1 \\ \kappa_2 \\ \kappa_3 \end{Bmatrix} \tag{4.75}$$

The first-order approximate solution can be obtained by perturbing the zeroth order solution and minimizing modified first-order strain energy as provided by Hodges et al. [73]. The resulting 1D strain energy corrected up to the first order is given as

$$U_{1D} = \frac{1}{2}\varepsilon_l^T[\mathcal{S}_l]\varepsilon_l + \varepsilon_l^T[\mathcal{S}_{ln}]\varepsilon_n + \frac{1}{2}\varepsilon_n^T[\mathcal{S}_n]\varepsilon_n \tag{4.76}$$

where,

$$\begin{aligned} \varepsilon_l &= \{\gamma_{11} \quad \kappa_1 \quad \kappa_2 \quad \kappa_3\}^T \\ \varepsilon_n &= \{\kappa_1^2 \quad \kappa_2^2 \quad \kappa_2\gamma_{11} \quad \kappa_2\kappa_3 \quad \kappa_2\kappa_1\}^T \end{aligned} \tag{4.77}$$

The Eq. (4.76) can be written as

$$2U_{1D} = \varepsilon^T[\mathcal{S}]\varepsilon \tag{4.78}$$

where

$$\begin{aligned} [\mathcal{S}] &= \begin{bmatrix} \mathcal{S}_l & \mathcal{S}_{ln} \\ \mathcal{S}_{ln}^T & \mathcal{S}_n \end{bmatrix}_{9\times 9} \\ \varepsilon &= \{\gamma_{11} \quad \kappa_1 \quad \kappa_2 \quad \kappa_3 \quad \kappa_1^2 \quad \kappa_2^2 \quad \kappa_2\gamma_{11} \quad \kappa_2\kappa_3 \quad \kappa_2\kappa_1\}^T \end{aligned} \tag{4.79}$$

The components of $[\mathcal{S}_l]$ already provided in Eq. (4.75), the remaining components of $[\mathcal{S}]$ are provided in Appendix C.2.

4.5.4 Coupling Analysis

The coupling behavior of these beams is examined by expressing the strain (γ_{11}) and curvatures (κ_i) in terms of the applied force (F_1) and moments (M_i). This is achieved by solving the equilibrium equations $\frac{\partial U_{1D}}{\partial \gamma_{11}}$ and $\frac{\partial U_{1D}}{\partial \kappa_i}$. We will then implement the stacking sequence scheme obtained previously to incorporate different elastic coupling modes, along with hygrothermal stability. The coupling result and the hygrothermal stability will be verified through FE simulation. The material properties used for the simulation are as

follows: $E_{11} = 132.2\ GPa$, $E_{22} = E_{33} = 10.75\ GPa$, $G_{12} = G_{13} = G_{23} = 5.65\ GPa$, $\nu_{12} = \nu_{13} = 0.239$ and $\nu_{23} = 0.4$. The dimensions of the strip model are length=279.4 mm, width=25.4 mm and thickness=1.168 mm. The simulation has been conducted using 3D solid element C3D8R.

In Fig. 4.22, the FEA simulation results depict a strip-like cantilever beam with an 8-ply general asymmetric stacking sequence. The simulation involves applying a temperature change of 80°C. The figure illustrates noticeable deformations in both bending and twisting as a consequence of the temperature fluctuations, highlighting the presence of hygrothermal instabilities.

In the following subsections, we will employ the proposed hygrothermally stable stacking sequences and assess their suitability for maintaining hygrothermal stability with the desired elastic coupling in the strip-like beam configuration. For the sake of convenience, this discussion is limited to linear results. However, nonlinear plots are also included, compared with the FEA results, to provide a comprehensive understanding.

Extension-Twist Coupling

The laminated composite beam incorporates the extension-twist coupling with hygrothermal stability by applying the stacking sequence scheme outlined in Section 4.2. This integration reduces the linear constitutive relation from Eq.(4.75) to Eq.(4.80). The newly defined coefficients are provided in appendix C.1. As demonstrated earlier, the proposed stacking sequence inherently satisfies the hygrothermal stability conditions for any arbitrary independent fiber angles. Consequently, one can freely choose arbitrary values for these independent fiber angles. However, in this specific instance, we have employed the optimized results obtained from this stacking sequence comprising 8 plies, with an independent fiber angle of $\phi_1 = -67.5°$, as implemented in Eq. (4.80) to derive the coupling results. It is important to note that the optimized results utilized in this context may not be representative of the optimal outcomes for this case. This is due to differences in coupling coefficients between the two cases.

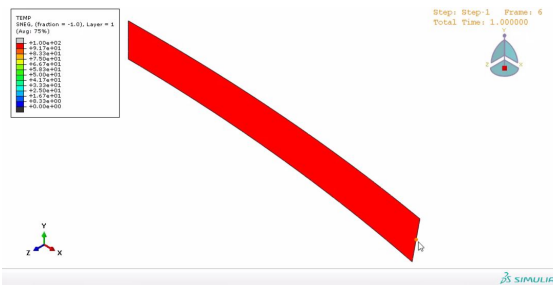

(a)

Figure 4.22: Thermal deformation due to temperature change in asymmetric laminate

$$\begin{Bmatrix} F_1 \\ M_1 \\ M_2 \\ M_3 \end{Bmatrix} = \begin{bmatrix} b\hat{A}_{11} & -2b\hat{B}_{16} & 0 & 0 \\ -2b\hat{B}_{16} & 4b\hat{D}_{66} & 0 & 0 \\ 0 & 0 & b\hat{D}_{11} & 0 \\ 0 & 0 & 0 & \frac{1}{12}\hat{A}_{11}b^3 \end{bmatrix} \begin{Bmatrix} \gamma_{11} \\ \kappa_1 \\ \kappa_2 \\ \kappa_3 \end{Bmatrix} \tag{4.80}$$

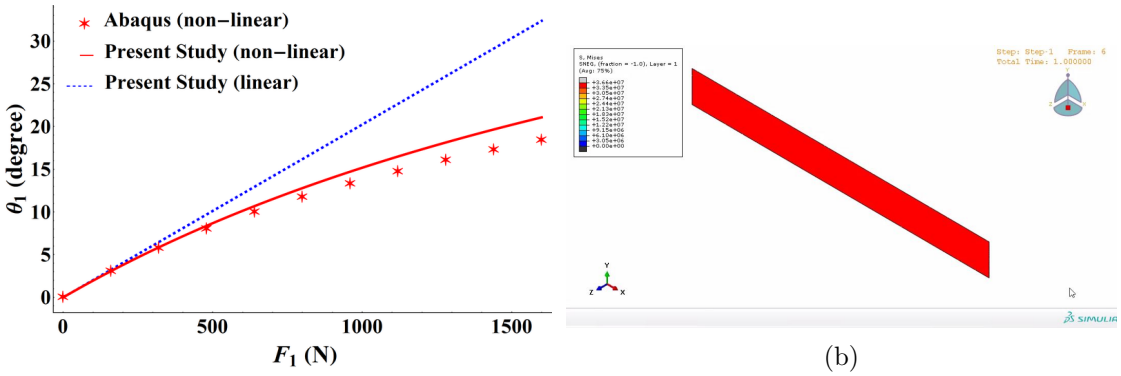

(a) (b)

Figure 4.23: (a) Extension-twist coupling plot (b)Thermal deformation due to temperature change

Considering Eq. (4.80), it is evident that the linear 1D constitutive law only captures extension-twist coupling with the proposed hygrothermally stable stacking sequences. In Fig. 4.23a, we plot the twist angle against the applied extension load, as dictated by the current linear constitutive law. The non-linear relation between twist angle and extension force is obtained by solving force and moment equilibrium equations stemming from virtual work application. Here, we have to employ the first-order strain energy (Eq. (4.78)). The twist angle derived from this non-linear relationship, along with the result from FEA analysis, is also showcased in Fig. 4.23a. This illustration suggests that the proposed stacking sequence effectively provides extension-twist coupling in the strip-like beam configuration.

The simulation results for the beam subjected to a temperature difference of 80°C are presented in Fig. 4.22. This result demonstrates that the proposed hygrothermally stable stacking sequence, incorporating extension-twist coupling, ensures hygrothermal stability even in strip-like beams.

Bend-Twist Coupling

In this case, we have implemented the stacking sequence scheme proposed in section 4.3 to incorporate bend-twist coupling with hygrothermal stability. This implementation results in the reduction of the linear constitutive law (Eq. (4.75)) to Eq. (4.81). The newly defined coefficients used in this relation are provided in appendix C.1. The 1D constitutive relation derived from this stacking sequence indicates that the proposed hygrothermally

stable stacking sequence imparts only bend-twist coupling to strip-like beams.

$$\begin{Bmatrix} F_1 \\ M_1 \\ M_2 \\ M_3 \end{Bmatrix} = \begin{bmatrix} b\hat{A}_{11} & 0 & 0 & 0 \\ 0 & 4b\hat{\bar{D}}_{66} & -2b\hat{D}_{16} & 0 \\ 0 & -2b\hat{D}_{16} & b\hat{\bar{D}}_{11} & 0 \\ 0 & 0 & 0 & \frac{1}{12}\hat{A}_{11}b^3 \end{bmatrix} \begin{Bmatrix} \gamma_{11} \\ \kappa_1 \\ \kappa_2 \\ \kappa_3 \end{Bmatrix} \tag{4.81}$$

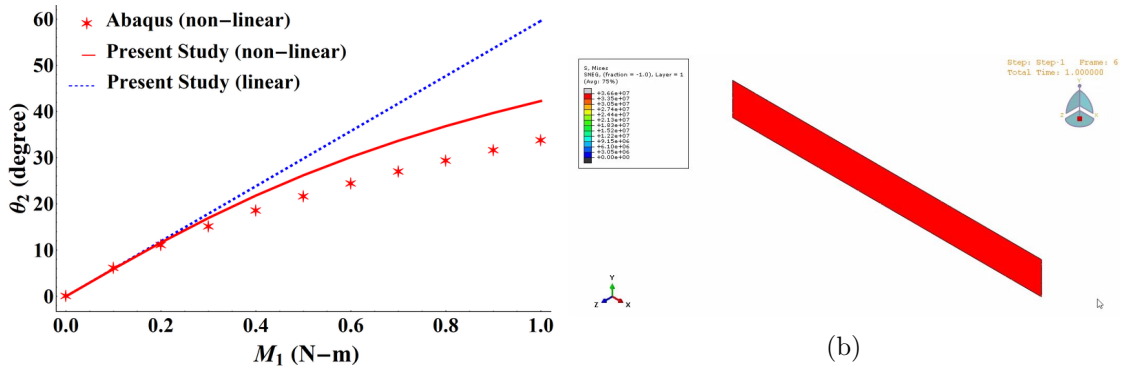

(a) (b)

Figure 4.24: (a) Bend-twist coupling plot (b)Thermal deformation due to temperature change

Recall that the hygrothermally stable stacking sequence proposed for bend-twist coupling always satisfies hygrothermal stability conditions for any arbitrary independent fiber angles. Hence, we have used previously obtained optimized independent fiber angle $\phi_1 = 68.14°$ for the calculation and simulation purpose for 8-ply laminate. The coupling results obtained from linear constitutive relation and FEA analyses have been plotted and provided in Fig. 4.25a. Here, we have plotted the bending angle θ_2 against the applied twisting moment. The non-linear relation between bending angle θ_2 and twisting moment is obtained by following the procedure as discussed in the previous case. The resulting non-linear relation is used to plot θ_2 against applied twisting moment M_1 and provided in Fig. 4.25a. These plots suggest that the proposed hygrothermally stable stacking sequences are applicable in strip-like beams also and impart bend-twist coupling to such beams.

Similar to the previous scenario, the Finite Element Analysis (FEA) results have confirmed the hygrothermal stability of the strip beam when employing the proposed stacking sequences, as illustrated in Fig. 4.24b. In this case, a temperature difference of 80°C was applied with the current stacking sequence, and no bending, twisting, or shear deformation was observed in response to this temperature change.

Extension-Bend Coupling

In this case, the constitutive relation for a hygrothermally stable strip-like beam can be derived by employing a stacking sequence designed to incorporate extension-bend coupling in the laminate. These stacking sequences are not presented in variable form; instead, they are pre-assigned with numerical values of ±45°, 0°, and 90°. However, it is still possible to express the constitutive law symbolically in this case. This can be accomplished by setting to zero those stiffness constants of the ABD matrix in Eq. (4.75) that become zero due to the implementation of the proposed stacking sequences. For the current scenario, $A_{16} = A_{26} = B_{16} = B_{26} = 0$, and the resulting constitutive relation is provided by Eq. (4.82). Appendix C.1 contains the newly defined constants utilized in this equation.

$$\begin{Bmatrix} F_1 \\ M_1 \\ M_2 \\ M_3 \end{Bmatrix} = \begin{bmatrix} b\hat{\bar{A}}_{11} & 2b\hat{\bar{B}}_{16} & b\hat{\bar{B}}_{11} & 0 \\ 2b\hat{\bar{B}}_{16} & 4b\hat{\overline{\bar{D}}}_{66} & -2b\hat{\bar{D}}_{16} & 0 \\ b\hat{\bar{B}}_{11} & -2b\hat{\bar{D}}_{16} & b\hat{\overline{\bar{D}}}_{11} & 0 \\ 0 & 0 & 0 & \frac{1}{12}b^3\hat{\bar{A}}_{11} \end{bmatrix} \begin{Bmatrix} \gamma_{11} \\ \kappa_1 \\ \kappa_2 \\ \kappa_3 \end{Bmatrix} \tag{4.82}$$

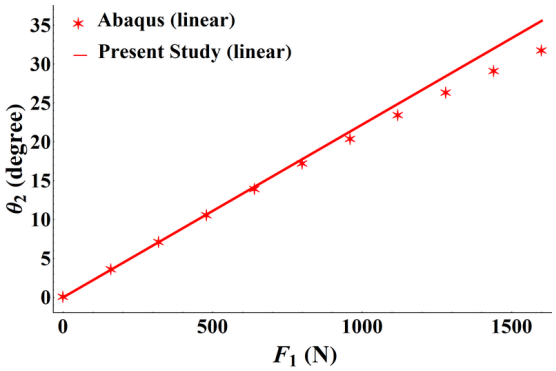

(a)

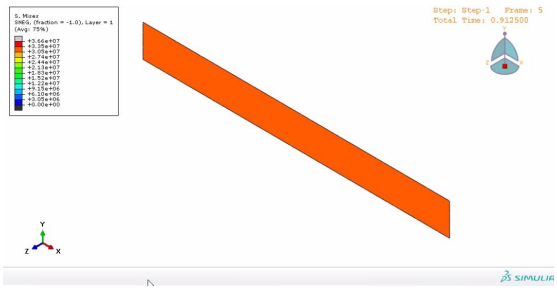

(b)

Figure 4.25: (a) Extension-Bend coupling plot (b)Thermal deformation due to temperature change

This equation is not completely decoupled from other deformation modes, as observed in the previous two cases. However, full decoupling can be achieved to exclusively provide extension-bend coupling and ensure hygrothermal stability. Examining Eq. (4.75), it is apparent that this decoupling can be attained by setting $\overline{\overline{B}}_{16}$ and $\overline{\overline{D}}_{16}$ to zero. Analyzing the unbarred expressions of these terms (provided in Appendix C.1), it becomes evident that these terms can be nullified by setting A_{16}, A_{26}, B_{16}, B_{26}, D_{16}, and D_{26} to zero. In the current case, we already have $A_{16} = A_{26} = B_{16} = B_{26} = 0$, so only two additional constants (D_{16} and D_{26}) need to be nullified. Considering the terms in terms of ζ (see Eqs. (4.11-4.11)), it is necessary to make ζ_3, ζ_4, ζ_7, ζ_8, ζ_{11}, and ζ_{12} zero. Additionally, two more zeta terms, ζ_1 and ζ_5, must be nullified to satisfy the hygrothermal stability conditions.

This condition can be achieved by devising a new systematic stacking sequence, similar to the current approach, or by employing constrained numerical optimization techniques, where the mentioned zero zeta terms serve as constraints. In the current case, we have $\zeta_1 = \zeta_3 = \zeta_4 = \zeta_5 = \zeta_7 = \zeta_8 = 0$, and thus, only two additional terms, ζ_{11} and ζ_{12}, need to be nullified.

In the current case, the stacking sequence utilized for calculations and FEA simulations is $[(45/-45)_S/(90/0)_S]_T$. When computing the compliance matrix (Cl) by taking the inverse of the stiffness matrix from Eq. (4.82), it is evident that the extension-twist compliance coefficient $Cl(2,1)$ is of the order of $O(10^{-5})$, while the extension-bend compliance coefficient $Cl(3,1)$ is of the order of $O(10^{-3})$. Consequently, the resulting relation effectively imparts extension-bend coupling exclusively. The bending angle θ_2 derived from this linear constitutive relation aligns closely with the FEA analysis, as depicted in Fig. 4.25a. The figure illustrates that the linear results obtained from the two different approaches are in close agreement. Non-linear results are not presented in this case due to observed discrepancies between analytical and FEA results, currently under investigation. Furthermore, such non-linear analysis is beyond the scope of this thesis, as the primary focus is to assess the applicability of the proposed hygrothermally stable stacking sequences with different elastic couplings in a strip-like beam configuration, for which the linear solution suffices.

The simulation results presented in Fig. 4.25b are obtained by applying a temperature change of 80°C, consistent with the approach adopted in previous cases. Notably, for the employed stacking sequence, the strip-like beam exhibits no thermal deformation in bending, twisting, or shearing. This observation serves to confirm the hygrothermal stability of the proposed stacking sequence in a beam-like structure as well.

Chapter 5

Conclusion and Future Scope

5.1 Conclusion

This thesis work presents a comprehensive analysis of elastic coupling in anisotropic homogeneous and inhomogeneous beams. This analysis has been carried out using VAM, which simplified the analysis of the 3D elasticity problem of the beam by splitting it into 2D linear cross-section analysis and 1D along-the-length analysis. To achieve the objectives of this thesis work, a prismatic beam with a solid elliptical cross-section has been considered for the analysis of anisotropic-homogeneous beams and a strip-like beam for the analysis of anisotropic-inhomogeneous beams.

The anisotropic-homogeneous beam analysis is divided into two parts based on the nature of the analysis and results. The first part of this analysis covers the orthotropic-homogeneous beam analysis (chapter 2) while the second part deals with the analysis of monoclinic and complete anisotropic homogeneous beam (chapter 3). There is a slight difference in the methodology used in the two parts; orthotropic beam analysis is completely analytical, whereas monoclinic and anisotropic beam analysis is semi-analytical. The solution procedure is the same for both cases. The beam under consideration has cross-sectional dimensions of the same order; hence, only a small parameter ($a/l \ll 1$) is available for this class of beams. This geometric small parameter, along with the smallness of strain ($\varepsilon \ll 1$), has been used to order the different terms involved in the 3D strain field. This ordering ultimately leads to the ordered stain energy functional. For the zeroth order approximate solution, the strain energy corrected up to $O(\mu\varepsilon^2)$ has been considered for the minimization using the variational principle. This minimization provides the Euler-Lagrange equations and associated boundary conditions. These Euler-Lagrange equations have been solved along with associated BCs to get zeroth order approximate solution. For the first-order approximate solution, the required strain energy should be corrected up to $O(\mu\varepsilon^4)$. The remaining procedure is the same as the zeroth order solution; however, the current and next higher order approximate solution is subjected to the constraints (see chapter 2). Similarly, other next higher-order approximate solutions have been obtained. The Timoshenko-like beam model has been extracted from the third-order approximate strain energy as suggested by [57]. The 1D constitutive law has been obtained from the 1D strain energy. The 1D strain measures, displacement and rotation, have been obtained from the 1D beam analysis. Determination of these 1D quantities allows the recovery of the 3D displacement, stress and strain field. The coupling behavior is governed by the cross-sectional stiffness constants provided in

the 1D constitutive law. The results obtained from this analysis are compared with the FEA results, where they show good agreement with FEA results.
In light of the observations made in the relevant chapters, the following key conclusions can be drawn about the deformations and coupling behavior of anisotropic-homogeneous beams:

- The zeroth order approximate solution represents the rigid body-like deformation of the beam-like structures. This zeroth order solution includes rigid body-like translation $\overline{u}_i(x_1)$ and rotation $\overline{\phi}_1(x_1)$ of the cross-section. As no elastic constants are involved in this solution, it represents the material-independent and most generic solution of beam deformation.

- The first-order approximate solution incorporates both rigid body-like rotation of cross-sections due to bending and elastic deformations. It provides the expression for out-of-plane warping due to torsion and in-plane deformation due to the Poisson effect.

- This analysis suggests that the beams of this class having material anisotropy level of orthotropy or less do not show any elastic coupling. It is observed for monoclinic and complete anisotropic materials. There is one exception if the monoclinic material case, the monoclinic material beam having cross-section plane ($x_2 - x_3$ plane) as the plane of elastic symmetry does not show any elastic coupling.

- It is observed that in monoclinic material beams having $x_1 - x_2$ plane as plane of elastic symmetry show coupling between $\overline{\kappa}_1$ and $\overline{\kappa}_2$. Similarly, for $x_1 - x_3$ plane as a plane of elastic symmetry, the coupling is observed between $\overline{\kappa}_1$ and $\overline{\kappa}_3$. Hence, monoclinic material beams show bend-twist coupling only.

- Even the complete anisotropic homogeneous beam does not show fully coupled behavior. The extensional strain term $\overline{\gamma}_{11}$ remains uncoupled from all curvature $\overline{\kappa}_i$ terms. In this case it is observed that $\overline{\kappa}_1$ is coupled to both $\overline{\kappa}_2$ and $\overline{\kappa}_3$. However, $\overline{\kappa}_2$ and $\overline{\kappa}_3$ remain uncoupled from each other. Hence, complete anisotropic-homogeneous beams also show bend-twist coupling only.

- The surface plots, showing the influence of direct (M_1) and coupling (M_2 and M_3) action on $\overline{\kappa}_1$ suggests that the coupling effect is not negligible; rather, it is almost 1/10 of direct action.

- This study suggests that the material beams, which show elastic coupling behavior, violate plane stress assumptions ($\sigma_{22} = \sigma_{33} = \sigma_{23} = 0$) which is the basis of many anisotropic-homogeneous beam analysis. This plane stress condition holds for all uncoupled cases theoretically.

The analysis of anisotropic-inhomogeneous beam has been carried out using a laminated composite strip-like beam. It is because laminated composite structures provide the

most feasible way to model anisotropic-inhomogeneous beams. This work also has two parts. In the first part, analysis of hygrothermal stability has been provided. The hygrothermal stability analysis becomes essential for composite beams as these structures are sensitive to changes in hygrothermal conditions. Generalized hygrothermally stable stacking sequences with different modes of elastic coupling have been proposed to eliminate these hygrothermal instabilities. This study provides a systematic and very simple way to obtain these proposed hygrothermally stable laminates. Optimization has also been carried out to maximize the desired coupling coefficient. The optimized results are compared with the conventional numerically optimized results. The optimized results are checked for robustness against the small perturbation in optimized results.
In the second part, a strip-like composite beam model has been modeled using VAM. This work extensively refers to the work by Hodges et al. [73]. It exploits the naturally available small parameter to dimensionally reduce the 3D elasticity problem into the strip-like beam problem. The smallness of the thickness allows to introduce the shell parameters. This nonlinear beam formulation facilitates expressing 2D shell parameters in terms of 1D beam parameters. Further, strain energy has been calculated using the CLPT energy equation. The zeroth order approximate solution has been obtained by minimizing stain energy corrected up to $O(E\varepsilon^2)$. The linear constitutive relation has been obtained using the zeroth order approximate solution. The first-order 1D strain energy has been used to obtain nonlinear elastic coupling relations. Previously obtained optimized stacking sequences have been implemented in this linear constitutive relation and nonlinear elastic coupling relations for different coupling modes. The same hygrothermally stable stacking sequence has been implemented in the FEA model to check the hygrothermal stability of the optimized stacking sequence. The linear and nonlinear results are compared with the FEA results for every optimized result.
The key observations of this analysis are the following:

- A generalized form of hygrothermally stable stacking sequences for a new class of laminated composites with extension-twist, bend-twist and extension-bend has been proposed. These proposed stacking sequences inherently satisfy the hygrothermal stability conditions. Hence optimization of these stacking sequences becomes an unconstrained problem that can be handled analytically and numerically.

- Comparison of optimized results of proposed stacking sequences with conventional numerically optimized results suggests that the current approach provides a better way to design the hygrothermally stable laminate with the abovementioned couplings for large i.

- As proposed stacking sequences reduces the number of independent fiber angles in laminate and reduces constrained optimization problems into unconstrained ones; Hence, it turns out to be more computationally efficient.

- The sensitivity analysis confirms the robustness of these stacking sequences against the perturbation in optimized results. The resultant error distribution has been

compared with those obtained from the conventional numerically optimized results. It has been found that for both approaches, error distribution is similar.

- These optimized results have been checked for hygrothermal stability in strip-like beam formulation using FEA simulation, which shows that these stacking sequences are also equally valid in strip-like beam formulation.
- Comparison analytical elastic coupling results with FEA results suggests that the nonlinear analytical coupling results are in close agreement with FEA results. This confirms the applicability of proposed stacking sequences in strip-like beam for the different types of coupling.

5.2 Future Scope

Some of the future work related to the anisotropic-homogeneous beam analysis in this thesis could focus on exploring the extensions and applications described below.

- The presented analysis used a prismatic beam with elliptical cross-section. This analysis can be extended for the initially curved and twisted beam.
- This analysis can also be extended to the hollow cross-section or any general cross-section.
- The monoclinic and complete anisotropic beam analysis used a semi-analytical approach. This solution can be completely analytic, providing deeper insight and understanding of the coupling and the elastic coefficient influencing it. A parametric study can be performed after getting the complete analytical results.
- In the present study, the analysis of monoclinic and complete anisotropic beams is limited to the Classical beam model. This study can be extended further to the Timoshenko-like beam, which would provide more accurate results.
- The present analysis uses the Cartesian coordinate system; this can be reformulated using curvilinear coordinate system.

The work related to the anisotropic-inhomogeneous beam analysis that can be used for future extension of this study is following:

- The hygrothermally stable stacking sequences provided in this study are derived for the flat surface. This work can be extended to the curved surfaces.
- In this study, optimization has been performed to maximize the coupling coefficient of the plate-like structure and used the same for the beam-like structure. This optimization can be performed for the beam coupling coefficient using the proposed stacking sequences, which need not to satisfy hygrothermal stability constraints. However, the most accurate optimized results required hygrothermal stability

constrained should be obtained for strip-like beam and proposed stacking sequences should be modified accordingly.

- Hygrothermal stability of the strip beam implemented with the proposed stacking sequence has been checked using FEA simulation. Though the FEA simulation suggests that the strip-like beam with the proposed stacking sequence is hygrothermally stable, hygrothermal stability conditions can be derived for the current strip-like beam to check analytically the applicability of the currently proposed stacking sequence in the strip-like beam. The degree of error can also be checked.

Chapter A

2D Functions

A.1 Orthotropic: 2D Functions

$$
\begin{aligned}
\mathcal{F}_1(x_2,x_3) &= \frac{1}{24G_{12}\left(3a^2G_{13}+b^2G_{12}\right)}\big[8a^2E_{11}G_{13}x_2^3+12a^2E_{11}G_{12}x_2x_3^2-24a^4E_{11}G_{13}x_2\\
&\quad -12a^2b^2E_{11}G_{12}x_2+4b^2E_{11}G_{12}x_2^3+\nu_{12}\big(9a^4G_{12}G_{13}x_2+3a^2b^2G_{12}^2x_2\\
&\quad -12a^2G_{12}G_{13}x_2^3-4b^2G_{12}^2x_2^3\big)+\nu_{13}\big(15a^2b^2G_{12}G_{13}x_2-36a^2G_{12}G_{13}x_2x_3^2\\
&\quad -3b^4G_{12}^2x_2-8b^2G_{12}G_{13}x_2^3+12b^2G_{12}^2x_2x_3^2\big)\big]\\
\mathcal{F}_2(x_2,x_3) &= \frac{1}{24G_{13}\left(a^2G_{13}+3b^2G_{12}\right)}\big[12b^2E_{11}G_{13}x_2^2x_3-24b^4E_{11}G_{12}x_3-12a^2b^2E_{11}G_{13}x_3\\
&\quad +8b^2E_{11}G_{12}x_3^3+4a^2E_{11}G_{13}x_3^3+\nu_{12}\big(-3a^4G_{13}^2x_3+15a^2b^2G_{12}G_{13}x_3\\
&\quad -8a^2G_{12}G_{13}x_3^3+12a^2G_{13}^2x_2^2x_3-36b^2G_{12}G_{13}x_2^2x_3\big)+\nu_{13}\big(3a^2b^2G_{13}^2x_3\\
&\quad -4a^2G_{13}^2x_3^3+9b^4G_{12}G_{13}x_3-12b^2G_{12}G_{13}x_3^3\big)\big]
\end{aligned}
$$

Chapter B

Stiffness & Flexibility Constants and 2D Functions

B.1 Complete Anisotropic

B.1.1 2D Functions

$$\psi_{aniso}(x_2,x_3) = \frac{3309107a^2x_3^2 - 2\left(9938248a^2 - 8764747b^2\right)x_3x_2 - 3309107b^2x_2^2}{2\left(9938248a^2 + 8764747b^2\right)}$$

$$\mathcal{F}_1^1(x_2,x_3) = \frac{210232453\ x_2 + 4753211\ x_3}{732963519}$$

$$\begin{aligned}\mathcal{F}_2^1(x_2,x_3) =& \frac{1}{5863708152\left(9938248a^2 + 8764747b^2\right)}\Big[-210232453a^2\big(9938248a^2\\ &+ 8764747b^2\big) + \left(8357369022249376a^2 + 7401994814522718b^2\right)x_2^2\\ &+ 377908717714624a^2x_2x_3 - 31457767585154a^2x_3^2\Big]\end{aligned}$$

$$\begin{aligned}\mathcal{F}_3^1(x_2,x_3) =& \frac{1}{5863708152(9938248a^2 + 8764747b^2)}\Big[-4753211\big(9938248a^2b^2\\ &+ 8764747b^4\big) + 2\left(790158861278127a^2 + 83321383705234b^2\right)x_3^2\\ &+ 14741074093875128b^2x_2x_3 - 1391363363698942b^2x_2^2\Big]\end{aligned}$$

$$\mathcal{F}_1^2(x_2,x_3) = -\frac{149537611\ x_2 + 39756813\ x_3}{732963519}$$

$$\begin{aligned}\mathcal{F}_2^2(x_2,x_3) =& \frac{1}{8\left(9938248a^2 + 8764747b^2\right)}\Big[4\left(5066337a^2 + 1415927b^2\right)x_3^2\\ &+ 3183704a^2x_2x_3 - 4053740b^2x_2^2 - 4052902a^2b^2 - 1415927b^4\Big]\end{aligned}$$

$$\begin{aligned}\mathcal{F}_3^2(x_2,x_3) =& \frac{1}{11727416304\left(9938248a^2 + 8764747b^2\right)}\Big[19925254111890 69b^4\\ &+ 4\big(2972283726891056a^2 + 26261357251886 19b^2\big)x_2^2\\ &- 15132816873544a^2x_2x_3 - 350383510930864a^2b^2\\ &- x_3^2\left(9103008857031020a^2 + 7970101644756276b^2\right)\\ &- 2972283726891056a^4\Big]\end{aligned}$$

$$\begin{aligned}\mathcal{F}_4^2(x_2,x_3) =& \frac{1}{11727416304(9938248a^2 + 8764747b^2)}\Big[-852227704024220b^2x_2^2\end{aligned}$$

$$
\begin{aligned}
&+ 4\left(2645560724369157a^2 + 1691507436364175b^2\right)x_3^2 \\
&- 2432503798363102a^2b^2 + 8\big(3055948464584295a^2 \\
&+ 2621318654798834b^2\big)x_2x_3 - 1691507436364175b^4\Big]
\end{aligned}
$$

$$
\mathcal{F}_1^3(x_2,x_3) = -\frac{39756813x_2 + 113283088x_3}{732963519}
$$

$$
\begin{aligned}
\mathcal{F}_2^3(x_2,x_3) =& \frac{1}{8\left(9938248a^2 + 8764747b^2\right)}\Big[6146956a^2x_3^2 - 11327416b^2x_2x_3 \\
&+ 2238911a^2b^2 + 397963a^4 - 4x_2^2\left(397963a^2 + 3775650b^2\right)\Big]
\end{aligned}
$$

$$
\begin{aligned}
\mathcal{F}_3^3(x_2,x_3) =& \frac{1}{11727416304(9938248a^2 + 8764747b^2)}\Big[29217778875716a^2x_3^2 \\
&+ 1582343871243689a^4 - 8\big(2251670845499648a^2 \\
&+ 1992525411189069b^2\big)x_2x_3 + 1404475646278465a^2b^2 \\
&- 4\left(1582343871243689a^2 + 1411780090997394b^2\right)x_2^2\Big]
\end{aligned}
$$

$$
\begin{aligned}
\mathcal{F}_4^3(x_2,x_3) =& \frac{1}{11727416304(9938248a^2 + 8764747b^2)}\Big[840339560877869a^2b^2 \\
&- 1985795211397472b^4 + 4\big(2574743255090415a^2 \\
&+ 1985795211397472b^2\big)x_3^2 - 2381390451831448b^2x_2x_3 \\
&- 4\left(3055948464584295a^2 + 3415082815968284b^2\right)x_2^2 \\
&+ 3055948464584295a^4\Big]
\end{aligned}
$$

$$
\begin{aligned}
\chi_1^1 =& 17\mathcal{F}_{2,33}^2 + 31\mathcal{F}_{2,23}^2 + 10\mathcal{F}_{2,22}^2 + 14\mathcal{F}_{2,33}^3 + 30\mathcal{F}_{2,23}^3 + 18\mathcal{F}_{2,22}^3 \\
&+ 50\psi_{aniso,33} + 28\psi_{aniso,23} + 45\psi_{aniso,22} \\
\chi_2^1 =& 50\mathcal{F}_{1,33}^1 + 28\mathcal{F}_{1,23}^1 + 45\mathcal{F}_{1,22}^1 + 17\mathcal{F}_{1,33}^2 + 31\mathcal{F}_{1,23}^2 + 10\mathcal{F}_{1,22}^2 \\
&+ 14\mathcal{F}_{1,33}^3 + 30\mathcal{F}_{1,23}^3 + 18\mathcal{F}_{1,22}^3 \\
\chi_3^1 =& 22\mathcal{F}_{1,3}^1 + 38\mathcal{F}_{1,2}^1 + 30\mathcal{F}_{1,3}^2 + 74\mathcal{F}_{1,2}^2 + 75\mathcal{F}_{1,3}^3 + 30\mathcal{F}_{1,2}^3 + 110 \\
\chi_4^1 =& 30\mathcal{F}_{2,3}^2 + 74\mathcal{F}_{2,2}^2 + 75\mathcal{F}_{2,3}^3 + 30\mathcal{F}_{2,2}^3 + 22\psi_{aniso,3} + 38\psi_{aniso,2} \\
&+ 11x_2 - 19x_3 \\
\chi_1^2 =& 5 - 55\mathcal{F}_{2,33}^2 - 30\mathcal{F}_{2,23}^2 - 100\mathcal{F}_{2,22}^2 - 11\mathcal{F}_{2,33}^3 - 81\mathcal{F}_{2,23}^3 - 15\mathcal{F}_{2,22}^3 \\
&- 17\psi_{aniso,33} - 31\psi_{aniso,23} - 10\psi_{aniso,22} \\
\chi_2^2 =& -17\mathcal{F}_{1,33}^1 - 31\mathcal{F}_{1,23}^1 - 10\mathcal{F}_{1,22}^1 - 55\mathcal{F}_{1,33}^2 - 30\mathcal{F}_{1,23}^2 - 100\mathcal{F}_{1,22}^2 \\
&- 11\mathcal{F}_{1,33}^3 - 81\mathcal{F}_{1,23}^3 - 15\mathcal{F}_{1,22}^3 \\
\chi_3^2 =& 19 + 30\mathcal{F}_{1,3}^1 + 74\mathcal{F}_{1,2}^1 + 36\mathcal{F}_{1,3}^2 + 20\mathcal{F}_{1,2}^2 + 30\mathcal{F}_{1,3}^3 + 31\mathcal{F}_{1,2}^3 \\
\chi_4^2 =& 45x_3 - 14x_2 - 36\mathcal{F}_{2,3}^2 - 20\mathcal{F}_{2,2}^2 - 30\mathcal{F}_{2,3}^3 - 31\mathcal{F}_{2,2}^3 \\
&- 30\psi_{aniso,3} - 74\psi_{anis0,2} \\
\chi_1^3 =& 4 + 11\mathcal{F}_{2,33}^2 + 81\mathcal{F}_{2,23}^2 + 15\mathcal{F}_{2,22}^2 + 95\mathcal{F}_{2,33}^3 + 22\mathcal{F}_{2,23}^3 + 55\mathcal{F}_{2,22}^3 \\
&+ 14\psi_{aniso,33} + 30\psi_{aniso,23} + 18\psi_{anisi,22}
\end{aligned}
$$

$$\chi_2^3 = 14\mathcal{F}_{1,33}^1 + 30\mathcal{F}_{1,23}^1 + 18\mathcal{F}_{1,22}^1 + 11\mathcal{F}_{1,33}^2 + 81\mathcal{F}_{1,23}^2 + 15\mathcal{F}_{1,22}^2 + 95\mathcal{F}_{1,33}^3 + 22\mathcal{F}_{1,23}^3 + 55\mathcal{F}_{1,22}^3$$

$$\chi_3^3 = 11 + 75\mathcal{F}_{1,3}^1 + 30\mathcal{F}_{1,2}^1 + 30\mathcal{F}_{1,3}^2 + 31\mathcal{F}_{1,2}^2 + 28\mathcal{F}_{1,3}^3 + 34\mathcal{F}_{1,2}^3$$

$$\chi_4^3 = 50x_2 - 14x_3 + 30\mathcal{F}_{2,3}^2 + 31\mathcal{F}_{2,2}^2 + 28\mathcal{F}_{2,3}^3 + 34\mathcal{F}_{2,2}^3 + 75\psi_{aniso,3} + 30\psi_{aniso,2}$$

$$\mathcal{B}_1^1 = 19 + 14\mathcal{F}_{1,3}^1 + 45\mathcal{F}_{1,2}^1 + 18\mathcal{F}_{1,3}^2 + 10\mathcal{F}_{1,2}^2 + 13\mathcal{F}_{1,3}^3 + 18\mathcal{F}_{1,2}^3$$

$$\mathcal{B}_2^1 = 14x_2 - 45x_3 + 18\mathcal{F}_{2,3}^2 + 10\mathcal{F}_{2,2}^2 + 13\mathcal{F}_{2,3}^3 + 18\mathcal{F}_{2,2}^3 + 14\psi_{aniso,3} + 45\psi_{aniso,2}$$

$$\mathcal{B}_3^1 = 19\mathcal{F}_1^1 + 45\mathcal{F}_1^2 + 14\mathcal{F}_1^3$$

$$\mathcal{B}_4^1 = 45\mathcal{F}_2^2 + 14\mathcal{F}_2^3 + 19\psi_{aniso}$$

$$\mathcal{B}_5^1 = 11 + 50\mathcal{F}_{1,3}^1 + 14\mathcal{F}_{1,2}^1 + 17\mathcal{F}_{1,3}^2 + 13\mathcal{F}_{1,2}^2 + 14\mathcal{F}_{1,3}^3 + 17\mathcal{F}_{1,2}^3$$

$$\mathcal{B}_6^1 = 50x_2 - 14x_3 + 17\mathcal{F}_{2,3}^2 + 13\mathcal{F}_{2,2}^2 + 14\mathcal{F}_{2,3}^3 + 17\mathcal{F}_{2,2}^3 + 50\psi_{aniso,3} + 14\psi_{aniso,2}$$

$$\mathcal{B}_7^1 = 11\mathcal{F}_1^1 + 14\mathcal{F}_1^2 + 50\mathcal{F}_1^3$$

$$\mathcal{B}_8^1 = 14\mathcal{F}_2^2 + 50\mathcal{F}_2^3 + 11\psi_{aniso}$$

$$\mathcal{B}_1^2 = 29 + 13\mathcal{F}_{1,3}^1 + 10\mathcal{F}_{1,2}^1 + 15\mathcal{F}_{1,3}^2 + 100\mathcal{F}_{1,2}^2 + 26\mathcal{F}_{1,3}^3 + 15\mathcal{F}_{1,2}^3$$

$$\mathcal{B}_2^2 = 13x_2 - 10x_3 + 15\mathcal{F}_{2,3}^2 + 100\mathcal{F}_{2,2}^2 + 26\mathcal{F}_{2,3}^3 + 15\mathcal{F}_{2,2}^3 + 13\psi_{aniso,3} + 10\psi_{aniso,2}$$

$$\mathcal{B}_3^2 = 29\mathcal{F}_1^1 + 10\mathcal{F}_1^2 + 13\mathcal{F}_1^3$$

$$\mathcal{B}_4^2 = 10\mathcal{F}_2^2 + 13\mathcal{F}_2^3 + 29\psi_{aniso}$$

$$\mathcal{B}_5^2 = 16 + 17\mathcal{F}_{1,3}^1 + 18\mathcal{F}_{1,2}^1 + 55\mathcal{F}_{1,3}^2 + 15\mathcal{F}_{1,2}^2 + 11\mathcal{F}_{1,3}^3 + 55\mathcal{F}_{1,2}^3$$

$$\mathcal{B}_6^2 = 17x_2 - 18x_3 + 55\mathcal{F}_{2,3}^2 + 15\mathcal{F}_{2,2}^2 + 11\mathcal{F}_{2,3}^3 + 55\mathcal{F}_{2,2}^3 + 17\psi_{aniso,3} + 18\psi_{aniso,2}$$

$$\mathcal{B}_7^2 = 16\mathcal{F}_1^1 + 18\mathcal{F}_1^2 + 17\mathcal{F}_1^3$$

$$\mathcal{B}_8^2 = 18\mathcal{F}_2^2 + 17\mathcal{F}_2^3 + 16\psi_{aniso}$$

$$\mathcal{B}_1^3 = 16 + 17\mathcal{F}_{1,3}^1 + 18\mathcal{F}_{1,2}^1 + 55\mathcal{F}_{1,3}^2 + 15\mathcal{F}_{1,2}^2 + 11\mathcal{F}_{1,3}^3 + 55\mathcal{F}_{1,2}^3$$

$$\mathcal{B}_2^3 = 17x_2 - 18x_3 + 55\mathcal{F}_{2,3}^2 + 15\mathcal{F}_{2,2}^2 + 11\mathcal{F}_{2,3}^3 + 55\mathcal{F}_{2,2}^3 + 17\psi_{aniso,3} + 18\psi_{aniso,2}$$

$$\mathcal{B}_3^3 = 16\mathcal{F}_1^1 + 18\mathcal{F}_1^2 + 17\mathcal{F}_1^3$$

$$\mathcal{B}_4^3 = 18\mathcal{F}_2^2 + 17\mathcal{F}_2^3 + 16\psi_{aniso}$$

$$\mathcal{B}_5^3 = 25 + 14\mathcal{F}_{1,3}^1 + 13\mathcal{F}_{1,2}^1 + 11\mathcal{F}_{1,3}^2 + 26\mathcal{F}_{1,2}^2 + 95\mathcal{F}_{1,3}^3 + 11\mathcal{F}_{1,2}^3$$

$$\mathcal{B}_6^3 = 14x_2 - 13x_3 + 11\mathcal{F}_{2,3}^2 + 26\mathcal{F}_{2,2}^2 + 95\mathcal{F}_{2,3}^3 + 11\mathcal{F}_{2,2}^3 + 14\psi_{aniso,3} + 13\psi_{aniso,2}$$

$$\mathcal{B}_7^3 = 25\mathcal{F}_1^1 + 13\mathcal{F}_1^2 + 14\mathcal{F}_1^3$$

$$\mathcal{B}_8^3 = 13\mathcal{F}_2^2 + 14\mathcal{F}_2^3 + 25\psi_{aniso}$$

B.1.2 Cross-sectional stiffness and flexibility constants

$$\mathcal{S}_{11} = \frac{136276798454\pi abP}{732963519} \quad \mathcal{S}_{22} = \frac{732963519\pi a^3b^3P}{9938248a^2 + 8764747b^2}$$
$$\mathcal{S}_{23} = -\frac{210232453\pi a^3b^3P}{9938248a^2 + 8764747b^2} \quad \mathcal{S}_{24} = -\frac{4753211\pi a^3b^3P}{9938248a^2 + 8764747b^2}$$
$$\mathcal{S}_{33} = \frac{\pi P\left(1398550303976265801a^3b^3 + 1194431660419301138ab^5\right)}{2931854076\left(9938248a^2 + 8764747b^2\right)}$$
$$\mathcal{S}_{34} = \frac{999279208156583\pi a^3b^3P}{1465927038\left(9938248a^2 + 8764747b^2\right)}$$
$$\mathcal{S}_{44} = \frac{\pi P\left(1354352619681868592a^5b + 1194454253434111659a^3b^3\right)}{2931854076\left(9938248a^2 + 8764747b^2\right)}$$
$$\overline{\Phi}_{11} = \frac{732963519}{136276798454\pi ab} \quad \overline{\Phi}_{22} = \frac{1908076279a^2 + 1629623061b^2}{136276798454\pi a^3b^3}$$
$$\overline{\Phi}_{33} = \frac{1465927038}{68138399227\pi ab^3} \quad \overline{\Phi}_{44} = \frac{1465927038}{68138399227\pi a^3b} \quad \overline{\Phi}_{23} = \frac{210232453}{68138399227\pi ab^3}$$
$$\overline{\Phi}_{24} = \frac{4753211}{68138399227\pi a^3b}$$

B.2 Monoclinic Beam with Plane $x_2 - x_3$ of Elastic Symmetry

B.2.1 Cross-sectional rigidity constant

$$\overline{\Phi}_{11} = \frac{460425}{88515418\pi ab} \quad \overline{\Phi}_{22} = \frac{5\left(10a^2 + 9b^2\right)}{4108\pi a^3b^3} \quad \overline{\Phi}_{33} = \frac{920850}{44257709\pi ab^3} \quad \overline{\Phi}_{44} = \frac{920850}{44257709\pi a^3b}$$

B.2.2 2D functions

$$\psi_{mx_1}(x_2, x_3) = \frac{14a^2x_3^2 + 5\left(9b^2 - 10a^2\right)x_3x_2 - 14b^2x_2^2}{50a^2 + 45b^2}$$
$$\mathcal{F}_1^2(x_2, x_3) = -\frac{785336\ x_2 + 361612\ x_3}{3683400}$$
$$\mathcal{F}_2^2(x_2, x_3) = \frac{83830(b^2 - x_3^2) - 98167(a^2 - 4x_2^2)}{3683400}$$
$$\mathcal{F}_3^2(x_2, x_3) = \frac{785336x_2x_3 - 90403\left(b^2 - 4x_3^2\right)}{3683400}$$
$$\mathcal{F}_1^3(x_2, x_3) = -\frac{361612\ x_2 + 670640\ x_3}{3683400}$$
$$\mathcal{F}_2^3(x_2, x_3) = \frac{670640x_2x_3 - 90403(a^2 - 4x_2^2)}{3683400}$$
$$\mathcal{F}_3^3(x_2, x_3) = \frac{98167(a^2 - 4x_2^2) - 83830(b^2 - 4x_3^2)}{3683400}$$

B.3 Monoclinic Beam with Plane $x_1 - x_3$ of Elastic Symmetry

B.3.1 Cross-sectional rigidity constant

$$\overline{\Phi}_{11} = \frac{59287}{11569970\pi ab} \quad \overline{\Phi}_{22} = \frac{445443845a^2 + 372529539b^2}{34841807658\pi a^3b^3} \quad \overline{\Phi}_{33} = \frac{118574}{5784985\pi ab^3}$$
$$\overline{\Phi}_{44} = \frac{118574}{5784985\pi a^3b} \quad \phi_{24} = \frac{1293}{1156997\pi a^3b}$$

B.3.2 2D functions

$$\psi_{mx_2}(x_2,x_3) = \frac{\left(18980424b^2 - 22825495a^2\right)x_2x_3}{22825495a^2 + 18980424b^2}$$
$$\mathcal{F}_1^1(x_2,x_3) = \frac{2489025\ a^2x_2x_3}{22825495a^2 + 18980424b^2}$$
$$\mathcal{F}_2^1(x_2,x_3) = -\frac{6465\left(b^2 - 4x_3^2\right)}{474296}$$
$$\mathcal{F}_3^1(x_2,x_3) = -\frac{6465\ x_3}{59287}$$
$$\mathcal{F}_1^2(x_2,x_3) = -\frac{13505\ x_2}{59287}$$
$$\mathcal{F}_2^2(x_2,x_3) = \frac{1}{8(22825495a^2 + 18980424b^2)}\Big[20\left(1039885a^2 + 905571b^2\right)x_2^2 - 5199425a^4 - 36\left(559055a^2 + 417294b^2\right)x_3^2 + 503640a^2b^2 + 3755646b^4\Big]$$
$$\mathcal{F}_3^2(x_2,x_3) = \frac{13505\ x_2x_3}{59287}$$
$$\mathcal{F}_4^2(x_2,x_3) = \frac{9\left[8\left(415009a^2 + 126909b^2\right)x_3^2 - 832676b^2x_2^2 - 621849a^2b^2 - 253818b^4\right]}{91301980a^2 + 75921696b^2}$$
$$\mathcal{F}_1^3(x_2,x_3) = -\frac{10953\ x_3}{59287}$$
$$\mathcal{F}_2^3(x_2,x_3) = \frac{9\left(468545a^2 + 417294b^2\right)\ x_2x_3}{22825495a^2 + 18980424b^2}$$
$$\mathcal{F}_3^3(x_2,x_3) = \frac{13505(a^2 - 4x_2^2) - 10953(b^2 - 4x_3^2)}{474296}$$
$$\mathcal{F}_4^3(x_2,x_3) = -\frac{4568724\ b^2x_2x_3}{22825495a^2 + 18980424b^2}$$

B.4 Monoclinic Beam with Plane $x_1 - x_2$ of Elastic Symmetry

B.4.1 Cross-sectional rigidity constant

$$\overline{\Phi}_{11} = \frac{94360}{17650107\pi ab} \quad \overline{\Phi}_{22} = \frac{5\left(426218129a^2 + 388302354b^2\right)}{173747653308\pi a^3b^3} \quad \overline{\Phi}_{33} = \frac{377440}{17650107\pi ab^3}$$
$$\overline{\Phi}_{44} = \frac{377440}{17650107\pi a^3b} \quad \overline{\Phi}_{23} = \frac{61954}{17650107\pi ab^3}$$

B.4.2 2D functions

$$\psi_{mx_3}(x_2,x_3) = \frac{\left(2594900b^2 - 2714483a^2\right) x_2x_3}{2714483a^2 + 2594900b^2}$$

$$\mathcal{F}_1^1(x_2,x_3) = -\frac{30977\left(a^2 - 4x_2^2\right)}{754880}$$

$$\mathcal{F}_2^1(x_2,x_3) = \frac{1703735\ b^2\ x_2x_3}{2\left(2714483a^2 + 2594900b^2\right)}$$

$$\mathcal{F}_3^1(x_2,x_3) = -\frac{30977\ x_2}{94360}$$

$$\mathcal{F}_1^2(x_2,x_3) = -\frac{40723\ x_2}{188720}$$

$$\mathcal{F}_2^2(x_2,x_3) = \frac{30040(b^2 - x_3^2) - 40723(a^2 - 4x_2^2)}{1509760}$$

$$\mathcal{F}_3^2(x_2,x_3) = \frac{5\left(1036081a^2 + 895906b^2\right) x_2x_3}{8\left(2714483a^2 + 2594900b^2\right)}$$

$$\mathcal{F}_4^2(x_2,x_3) = \frac{376533\ a^2x_2x_3}{2714483a^2 + 2594900b^2}$$

$$\mathcal{F}_1^3(x_2,x_3) = -\frac{751\ x_3}{4718}$$

$$\mathcal{F}_2^3(x_2,x_3) = \frac{751\ x_2x_3}{4718}$$

$$\mathcal{F}_3^3(x_2,x_3) = \frac{1}{64\left(2714483a^2 + 2594900b^2\right)}\Big[8\left(2148453a^2 + 1652200b^2\right) x_3^2 - 4\left(5180405a^2 + 6585966b^2\right) x_2^2 + 5\left(1036081a^4 + 457812a^2b^2 - 660880b^4\right)\Big]$$

$$\mathcal{F}_4^3(x_2,x_3) = \frac{2559440a^2x_3^2 - 68x_2^2\left(22149a^2 + 94360b^2\right) + 376533a^4 + 964260a^2b^2}{8\left(2714483a^2 + 2594900b^2\right)}$$

Chapter C

Stiffness Constants

C.1 Stiffness Variables

$$
\begin{aligned}
\overline{A}_{11} =& A_{11} + \frac{A_{66}A_{12}^2 - 2A_{16}A_{26}A_{12} + A_{16}^2A_{22}}{A_{26}^2 - A_{22}A_{66}} \\
\overline{B}_{11} =& B_{11} + \frac{\left(A_{16}A_{22} - A_{12}A_{26}\right)B_{16} + \left(A_{12}A_{66} - A_{16}A_{26}\right)B_{12}}{A_{26}^2 - A_{22}A_{66}} \\
\overline{B}_{12} =& B_{12} + \frac{\left(A_{16}A_{22} - A_{12}A_{26}\right)B_{26} + \left(A_{12}A_{66} - A_{16}A_{26}\right)B_{22}}{A_{26}^2 - A_{22}A_{66}} \\
\overline{B}_{16} =& B_{16} + \frac{\left(A_{16}A_{22} - A_{12}A_{26}\right)B_{66} + \left(A_{12}A_{66} - A_{16}A_{26}\right)B_{26}}{A_{26}^2 - A_{22}A_{66}} \\
\overline{D}_{11} =& D_{11} + \frac{A_{66}B_{12}^2 - 2A_{26}B_{16}B_{12} + A_{22}B_{16}^2}{A_{26}^2 - A_{22}A_{66}} \\
\overline{D}_{12} =& D_{12} + \frac{B_{16}\left(A_{22}B_{26} - A_{26}B_{22}\right) + B_{12}\left(A_{66}B_{22} - A_{26}B_{26}\right)}{A_{26}^2 - A_{22}A_{66}} \\
\overline{D}_{22} =& D_{22} + \frac{A_{66}B_{22}^2 - 2A_{26}B_{26}B_{22} + A_{22}B_{26}^2}{A_{26}^2 - A_{22}A_{66}} \\
\overline{D}_{16} =& D_{16} + \frac{B_{16}\left(A_{22}B_{66} - A_{26}B_{26}\right) + B_{12}\left(A_{66}B_{26} - A_{26}B_{66}\right)}{A_{26}^2 - A_{22}A_{66}} \\
\overline{D}_{26} =& D_{26} + \frac{-A_{26}B_{26}^2 + B_{26}\left(A_{22}B_{66} + A_{66}B_{22}\right) - A_{26}B_{22}B_{66}}{A_{26}^2 - A_{22}A_{66}} \\
\overline{D}_{66} =& D_{66} + \frac{A_{66}B_{26}^2 - 2A_{26}B_{66}B_{26} + A_{22}B_{66}^2}{A_{26}^2 - A_{22}A_{66}} \\
\overline{\overline{A}}_{11} =& \overline{A}_{11} - \frac{\overline{B}_{12}^2}{\overline{D}_{22}}, \\
\overline{\overline{B}}_{11} =& \overline{B}_{11} - \frac{\overline{B}_{12}\overline{D}_{12}}{\overline{D}_{22}}, \\
\overline{\overline{B}}_{16} =& \overline{B}_{16} - \frac{\overline{B}_{12}\overline{D}_{26}}{\overline{D}_{22}} \\
\overline{\overline{D}}_{11} =& \overline{D}_{11} - \frac{\overline{D}_{12}^2}{\overline{D}_{22}}, \\
\overline{\overline{D}}_{16} =& \overline{D}_{16} - \frac{\overline{D}_{12}\overline{D}_{26}}{\overline{D}_{22}}, \\
\overline{\overline{D}}_{66} =& \overline{D}_{66} - \frac{\overline{D}_{26}^2}{\overline{D}_{22}}
\end{aligned}
$$

$$
\begin{aligned}
\hat{D}_{11} =& D_{11} + \frac{B_{16}^2 D_{22} - 2B_{26}B_{16}D_{12} + A_{66}D_{12}^2}{B_{26}^2 - A_{66}D_{22}} \\
\hat{A}_{11} =& A_{11} - \frac{A_{12}^2}{A_{22}} \\
\hat{B}_{16} =& B_{16} - \frac{A_{12}B_{26}}{A_{22}} \\
\hat{D}_{66} =& D_{66} - \frac{B_{26}^2}{A_{22}} \\
\hat{\bar{D}}_{66} =& D_{66} - \frac{D_{26}^2}{D_{22}} \\
\hat{D}_{16} =& D_{16} - \frac{D_{12}D_{26}}{D_{22}} \\
\hat{\bar{D}}_{11} =& D_{11} - \frac{D_{12}^2}{D_{22}} \\
\hat{\bar{A}}_{11} =& A_{11} + \frac{A_{22}B_{12}^2 - 2A_{12}B_{22}B_{12} + A_{12}^2 D_{22}}{B_{22}^2 - A_{22}D_{22}} \\
\hat{\bar{B}}_{11} =& B_{11} + \frac{B_{12}\left(A_{12}D_{22} + A_{22}D_{12}\right) - A_{12}B_{22}D_{12} - B_{12}^2 B_{22}}{B_{22}^2 - A_{22}D_{22}} \\
\hat{\bar{\bar{D}}}_{66} =& D_{66} + \frac{A_{22}B_{66}^2 D_{22} - B_{22}^2 B_{66}^2 + A_{22}A_{66}D_{26}^2}{A_{66}\left(B_{22}^2 - A_{22}D_{22}\right)} \\
\hat{\bar{D}}_{16} =& D_{16} + \frac{A_{22}D_{12}D_{26} - B_{12}B_{22}D_{26}}{B_{22}^2 - A_{22}D_{22}} \\
\hat{\bar{\bar{D}}}_{11} =& D_{11} + \frac{B_{12}^2 D_{22} - 2B_{22}B_{12}D_{12} + A_{22}D_{12}^2}{B_{22}^2 - A_{22}D_{22}} \\
\hat{\bar{B}}_{16} =& \frac{D_{26}\left(A_{12}B_{22} - A_{22}B_{12}\right)}{B_{22}^2 - A_{22}D_{22}}
\end{aligned}
$$

C.2 Coefficient of stiffness matrix $[S]$

$$
\begin{aligned}
&\mathcal{S}_{16} = \mathcal{S}_{17} = \mathcal{S}_{18} = \mathcal{S}_{19} = \mathcal{S}_{28} = \mathcal{S}_{29} = \mathcal{S}_{36} = \mathcal{S}_{37} = \mathcal{S}_{38} = \mathcal{S}_{39} = \mathcal{S}_{45} = \\
&\mathcal{S}_{46} = \mathcal{S}_{47} = \mathcal{S}_{49} = \mathcal{S}_{56} = \mathcal{S}_{58} = \mathcal{S}_{68} = \mathcal{S}_{78} = \mathcal{S}_{89} = 0 \\
&\mathcal{S}_{15} = \frac{1}{24} b^3 \overline{\overline{A}}_{11} \\
&\mathcal{S}_{25} = \frac{1}{160} b^5 \overline{\overline{A}}_{11} k_1 - \frac{1}{12} b^3 \overline{\overline{B}}_{16} \\
&\mathcal{S}_{26} = \frac{b^5 \overline{\overline{A}}_{11} \overline{D}_{12} k_1}{360 \overline{D}_{22}} \\
&\mathcal{S}_{27} = \frac{b^5 \overline{\overline{A}}_{11} \overline{B}_{12} k_1}{360 \overline{D}_{22}} \\
&\mathcal{S}_{35} = \frac{b^7 \overline{\overline{A}}_{11} \overline{B}_{12} {k_1}^2}{10080 \overline{D}_{22}} - \frac{b^5 \overline{\overline{A}}_{11} \overline{D}_{26} k_1}{180 \overline{D}_{22}} + \frac{1}{24} b^3 \overline{\overline{B}}_{11} \\
&\mathcal{S}_{48} = -\frac{b^5 \overline{\overline{A}}_{11} \overline{B}_{12}}{720 \overline{D}_{22}}
\end{aligned}
$$

$$\mathcal{S}_{55} = \frac{1}{320} b^5 \overline{\overline{A}}_{11}$$

$$\mathcal{S}_{57} = \frac{b^5 \overline{\overline{A}}_{11} \overline{B}_{12}}{720 \overline{D}_{22}}$$

$$\mathcal{S}_{59} = \frac{b^7 \overline{\overline{A}}_{11} \overline{B}_{12} k_1}{10080 \overline{D}_{22}} - \frac{b^5 \overline{\overline{A}}_{11} \overline{D}_{26}}{360 \overline{D}_{22}}$$

$$\mathcal{S}_{66} = \frac{b^5 \overline{\overline{A}}_{11} \overline{D}_{12}^2}{720 \overline{D}_{22}^2}$$

$$\mathcal{S}_{67} = \frac{b^5 \overline{\overline{A}}_{11} \overline{B}_{12} \overline{D}_{12}}{720 \overline{D}_{22}^2}$$

$$\mathcal{S}_{69} = -\frac{b^7 \overline{\overline{A}}_{11} \overline{B}_{12} \overline{D}_{12} k_1}{60480 \overline{D}_{22}^2} - \frac{b^5 \overline{\overline{A}}_{11} \overline{D}_{12} \overline{D}_{26}}{360 \overline{D}_{22}^2}$$

$$\mathcal{S}_{77} = \frac{b^5 \overline{\overline{A}}_{11} \overline{B}_{12}^2}{720 \overline{D}_{22}^2}$$

$$\mathcal{S}_{79} = -\frac{b^7 \overline{\overline{A}}_{11} \overline{B}_{12}^2 k_1}{60480 \overline{D}_{22}^2} - \frac{b^5 \overline{\overline{A}}_{11} \overline{B}_{12} \overline{D}_{26}}{360 \overline{D}_{22}^2}$$

$$\mathcal{S}_{88} = \frac{b^7 \overline{\overline{A}}_{11} \overline{B}_{12}^2}{10080 \overline{D}_{22}^2} - \frac{b^7 \overline{\overline{A}}_{11}^2}{30240 \overline{D}_{22}}$$

$$\mathcal{S}_{99} = -{k_1}^2 \left(\frac{b^9 \overline{\overline{A}}_{11} \overline{B}_{12}^2}{403200 \overline{D}_{22}^2} + \frac{b^9 \overline{\overline{A}}_{11}^2}{90720 \overline{D}_{22}} \right) + \frac{b^7 \overline{\overline{A}}_{11} \overline{B}_{12} \overline{D}_{26} k_1}{15120 \overline{D}_{22}^2} + \frac{b^5 \overline{\overline{A}}_{11} \overline{D}_{26}^2}{180 \overline{D}_{22}^2} + \frac{b^5 \overline{\overline{A}}_{11} \overline{D}_{12}}{360 \overline{D}_{22}}$$

References

[1] Nishant Shakya and Srikant Sekhar Padhee. Asymptotic Analysis of Elastic Coupling in Anisotropic-Homogeneous Beam. *Journal of Applied Mechanics*, pages 1–5, 12 2022. ISSN 0021-8936. doi: 10.1115/1.4056458.

[2] Robert A. Haynes and Erian A. Armanios. The challenge of achieving hygrothermal stability in composite laminates with optimal couplings. *International Journal of Engineering Science*, 59:74–82, 2012. ISSN 00207225. doi: 10.1016/j.ijengsci.2012.03.013.

[3] Stephen Timoshenko. *History of strength of materials: with a brief account of the history of theory of elasticity and theory of structures*. Courier Corporation, 1983.

[4] James M Gere and Barry J Goodno. *Mechanics of materials*. Cengage learning, 2012.

[5] Oliver A Bauchau and James I Craig. Euler-bernoulli beam theory. In *Structural analysis*, pages 173–221. Springer, 2009.

[6] Dewey H. Hodges, Robert A. Ormiston, and David A. Peters. on the Nonlinear Deformation Geometry of Euler-Bernoulli Beams. Technical Report 1566, 1980. URL https://ntrs.nasa.gov/api/citations/19800012135/downloads/19800012135.pdf.

[7] Clive L Dym, Irving Herman Shames, et al. *Solid mechanics*. Springer, 1973.

[8] Nikolaĭ Ivanovich Muskhelishvili et al. *Some basic problems of the mathematical theory of elasticity*, volume 15. Noordhoff Groningen, 1953.

[9] S Timoshenko and JN Goodier. Theory of elasticity" mcgraw-hill book company. *Inc. New York*, 1951.

[10] GT Mase and GE Mase. Continuum mechanics for engineers, crc press, boca raton-london-new york-washington. 1999.

[11] Martin H Sadd. *Elasticity: theory, applications, and numerics*. Academic Press, 2009.

[12] Stephen P Timoshenko. Lxvi. on the correction for shear of the differential equation for transverse vibrations of prismatic bars. *The London, Edinburgh, and Dublin Philosophical Magazine and Journal of Science*, 41(245):744–746, 1921.

[13] Allan F Bower. *Applied mechanics of solids*. CRC press, 2009.

[14] Zvi Hashin. Plane Anisotropic Beams. *Journal of Applied Mechanics*, 34(2):257–262, 06 1967. ISSN 0021-8936. doi: 10.1115/1.3607676. URL https://doi.org/10.1115/1.3607676.

[15] Hidenori Murakami and Junya Yamakawa. On approximate solutions for the deformation of plane anisotropic beams. *Composites Part B: Engineering*, 27(5): 493–504, 1996.

[16] HJ Ding, DJ Huang, and WQ2304402 Chen. Elasticity solutions for plane anisotropic functionally graded beams. *International Journal of Solids and Structures*, 44(1): 176–196, 2007.

[17] JL Sullivan and H Van Oene. An elasticity analysis for the generally and specially orthotropic beams subjected to concentrated loads. *Composites science and technology*, 27(2):133–155, 1986.

[18] Jürgen Schöftner and Johannes Gahleitner. Refined orthotropic beam models based on castigliano's theorem and an approximate solution of the compatibility equation. *International Journal of Solids and Structures*, 230:111167, 2021.

[19] Anssi T Karttunen and Raimo Von Hertzen. On the foundations of anisotropic interior beam theories. *Composites Part B: Engineering*, 87:299–310, 2016.

[20] EH Mansfield and AJ Sobey. The fibre composite helicopter blade: part i: stiffness properties: part ii: prospects for aeroelastic tailoring. *Aeronautical Quarterly*, 30 (2):413–449, 1979.

[21] Lawrence W Rehfield, Ali R Atilgan, and Dewey H Hodges. Nonclassical behavior of thin-walled composite beams with closed cross sections. *Journal of the American Helicopter Society*, 35(2):42–50, 1990.

[22] JB Kosmatka and PP Friedmann. Vibration analysis of composite turbopropellers using a nonlinear beam-type finite-element approach. *AIAA journal*, 27(11): 1606–1614, 1989.

[23] R Worndle. CALCULATION OF THE CROSS SECTION PROPERTIES AND THE SHEAR STRESSES OF COMPOSITE ROTOR BLADES CALCULATION OF THE CROSS SECTION PROPERTIES AND THE SHEAR STRESSES OF COi' lPOS ITE ROTOR BLADES. Technical Report 65, 1981.

[24] Vittorio Giavotto, Marco Borri, Paolo Mantegazza, Gianluca Ghiringhelli, V Carmaschi, GC Maffioli, and F Mussi. Anisotropic beam theory and applications. *Computers & Structures*, 16(1-4):403–413, 1983.

[25] JB Kosmatka and SB Dong. Saint-venant solutions for prismatic anisotropic beams. *International Journal of Solids and Structures*, 28(7):917–938, 1991.

[26] Erasmo Carrera et al. A class of two-dimensional theories for anisotropic multilayered plates analysis. *Atti della accademia delle scienze di Torino. Classe di scienze fisiche matematiche e naturali*, 19:1–39, 1995.

[27] Erasmo Carrera and Gaetano Giunta. Refined beam theories based on a unified formulation. *International Journal of Applied Mechanics*, 2(01):117–143, 2010.

[28] Erasmo Carrera, Gaetano Giunta, Pietro Nali, and Marco Petrolo. Refined beam elements with arbitrary cross-section geometries. *Computers & structures*, 88(5-6): 283–293, 2010.

[29] Erasmo Carrera, Federico Miglioretti, and Marco Petrolo. Computations and evaluations of higher-order theories for free vibration analysis of beams. *Journal of Sound and Vibration*, 331(19):4269–4284, 2012.

[30] Erasmo Carrera, Matteo Filippi, and Enrico Zappino. Laminated beam analysis by polynomial, trigonometric, exponential and zig-zag theories. *European Journal of Mechanics-A/Solids*, 41:58–69, 2013.

[31] Erasmo Carrera, Marco Petrolo, and Enrico Zappino. Performance of cuf approach to analyze the structural behavior of slender bodies. *Journal of Structural Engineering*, 138(2):285–297, 2012.

[32] Erasmo Carrera and Alberto Varello. Dynamic response of thin-walled structures by variable kinematic one-dimensional models. *Journal of Sound and Vibration*, 331 (24):5268–5282, 2012.

[33] Erasmo Carrera. Theories and finite elements for multilayered plates and shells: a unified compact formulation with numerical assessment and benchmarking. *Archives of Computational Methods in Engineering*, 10:215–296, 2003.

[34] Luciano Demasi. ∞^3 hierarchy plate theories for thick and thin composite plates: the generalized unified formulation. *Composite Structures*, 84(3):256–270, 2008.

[35] Luciano Demasi. ∞^6 mixed plate theories based on the generalized unified formulation. part iv: Zig-zag theories. *Composite Structures*, 87(3):195–205, 2009.

[36] Dewey H. Hodges. *Nonlinear Composite Beam Theory*. Progress in Astronautics and Aeronautics, Volume 213. American Institute of Aeronautics and Astronautics, 2006. ISBN 978-1-61583-075-6,978-1-56347-697-5.

[37] V. L. Berdichevskii. Variational-asymptotic method of constructing a theory of shells. PMM vol. 43, no.4, 1979, pp. 664-687. *Journal of Applied Mathematics and Mechanics*, 43(4):711–736, jan 1979. ISSN 00218928. doi: 10.1016/0021-8928(79) 90157-6.

[38] VL Berdichevskii. On the energy of an elastic rod. *Journal of Applied Mathematics and Mechanics*, 45(4):518–529, 1981.

[39] V. L. Berdichevskii and L. A. Starosel'skii. On the theory of curvilinear timoshenko-type rods. *Journal of Applied Mathematics and Mechanics*, 47(6): 809–817, 1983. ISSN 00218928. doi: 10.1016/0021-8928(83)90121-1.

[40] V. L. Berdichevskii and Le Khan' Chau. High-frequency long-wave shell vibration. *Journal of Applied Mathematics and Mechanics*, 44(4):520–525, 1980. ISSN 00218928. doi: 10.1016/0021-8928(80)90044-1.

[41] Victor Berdichevsky, Erian Armanios, and Ashraf Badir. Theory of anisotropic thin-walled closed-cross-section beams. *Composites Engineering*, 2(5-7):411–432, jan 1992. ISSN 09619526. doi: 10.1016/0961-9526(92)90035-5.

[42] VL Berdichevskii and LA Starosel'skii. On the theory of curvilinear timoshenko-type rods. *Journal of Applied Mathematics and Mechanics*, 47(6):809–817, 1983.

[43] D. A. Danielson and D. H. Hodges. Nonlinear Beam Kinematics by Decomposition of the Rotation Tensor. *Journal of Applied Mechanics*, 54(2):258–262, 06 1987. ISSN 0021-8936. doi: 10.1115/1.3173004. URL https://doi.org/10.1115/1.3173004.

[44] Ali R Atilgan and Dewey H Hodges. Unified nonlinear analysis for nonhomogeneous anisotropic beams withclosed cross sections. *AIAA journal*, 29(11):1990–1999, 1991.

[45] Mark V Fulton and Dewey H Hodges. Aeroelastic stability of composite hingeless rotor blades in hover—part i: theory. *Mathematical and computer modelling*, 18 (3-4):1–17, 1993.

[46] MV Fulton and DH Hodges. Aeroelastic stability of composite hingeless rotor blades in hover—part ii: Results. *Mathematical and computer modelling*, 18(3-4):19–35, 1993.

[47] Dewey H Hodges, Ali R Atilgan, Carlos ES Cesnik, and Mark V Fulton. On a simplified strain energy function for geometrically nonlinear behaviour of anisotropic beams. *Composites Engineering*, 2(5-7):513–526, 1992.

[48] Carlos ES Cesnik and Dewey H Hodges. Stiffness constants for initially twisted and curved composite beams. *ASME AEROSP DIV PUBL AD, ASME, NEW YORK, NY(USA), 1992,*, 30:1–8, 1992.

[49] Carlos E. S. Cesnik and Dewey H. Hodges. Variational-Asymptotical Analysis of Initially Curved and Twisted Composite Beams. *Applied Mechanics Reviews*, 46 (11S):S211–S220, 11 1993. ISSN 0003-6900. doi: 10.1115/1.3122638. URL https://doi.org/10.1115/1.3122638.

[50] Carlos E. S. Cesnik and Dewey H. Hodges. Stiffness Constants for Composite Beams Including Large Initial Twist and Curvature Effects. *Applied Mechanics Reviews*, 48(11S):S61–S67, 11 1995. ISSN 0003-6900. doi: 10.1115/1.3005084. URL https://doi.org/10.1115/1.3005084.

[51] Carlos ES Cesnik, Dewey H Hodges, and Vladislav G Sutyrin. Cross-sectional analysis of composite beams including large initial twist and curvature effects. *AIAA journal*, 34(9):1913–1920, 1996.

[52] Carlos ES Cesnik and Dewey H Hodges. Vabs: a new concept for composite rotor blade cross-sectional modeling. *Journal of the American helicopter society*, 42(1): 27–38, 1997.

[53] Dewey H Hodges, Xiaoyang Shang, and Carlos ES Cesnik. Finite element solution of nonlinear intrinsic equations for curved composite beams. *Journal of the American helicopter society*, 41(4):313–321, 1996.

[54] Wenbin Yu, Dewey H Hodges, Vitali Volovoi, and Carlos ES Cesnik. On timoshenko-like modeling of initially curved and twisted composite beams. *International Journal of Solids and Structures*, 39(19):5101–5121, 2002.

[55] Bogdan Popescu and Dewey H Hodges. On asymptotically correct timoshenko-like anisotropic beam theory. *International Journal of Solids and Structures*, 37(3): 535–558, 2000.

[56] Bogdan Popescu, Dewey H Hodges, and Carlos ES Cesnik. Obliqueness effects in asymptotic cross-sectional analysis of composite beams. *Computers & Structures*, 76(4):533–543, 2000.

[57] Wenbin Yu and Dewey H. Hodges. Elasticity solutions versus asymptotic sectional analysis of homogeneous, isotropic, prismatic beams. *J. Appl. Mech*, 71(1):15–23, January 2004. ISSN 0021-8936. doi: 10.1115/1.1640367.

[58] Anurag Rajagopal. Variational asymptotic based shear correction factor for isotropic circular tubes. *AIAA journal*, 57(10):4125–4131, 2019.

[59] J.D. Renton. Generalized beam theory applied to shear stiffness. *International Journal of Solids and Structures*, 27(15):1955–1967, 1991. ISSN 0020-7683. doi: https://doi.org/10.1016/0020-7683(91)90188-L.

[60] Stanley B Dong, Can Alpdogan, and Ertugrul Taciroglu. Much ado about shear correction factors in timoshenko beam theory. *International Journal of Solids and Structures*, 47(13):1651–1665, 2010.

[61] P.Frank Pai and Mark J. Schulz. Shear correction factors and an energy-consistent beam theory. *International Journal of Solids and Structures*, 36(10):1523–1540, 1999. ISSN 0020-7683. doi: https://doi.org/10.1016/S0020-7683(98)00050-X.

[62] Jimmy C. Ho. Shear stiffness of homogeneous, orthotropic, prismatic beams. *AIAA Journal*, 55(12):4357–4363, dec 2017. doi: 10.2514/1.j056110.

[63] Göran Tolf. Saint-Venant bending of an orthotropic beam. *Composite Structures*, 4 (1):1–14, jan 1985. ISSN 02638223. doi: 10.1016/0263-8223(85)90017-0.

[64] V.V. Volovoi. On end effects in prismatic beams, (ph.d. thesis), georgia institute of technology, atlanta, georgia, U.S.A. 1997.

[65] Dineshkumar Harursampath and Dewey H Hodges. Asymptotic analysis of the non-linear behavior of long anisotropic tubes. *International journal of non-linear mechanics*, 34(6):1003–1018, 1999.

[66] JC Buckley. Lxxxiv. the bifilar property of twisted strips. *The London, Edinburgh, and Dublin Philosophical Magazine and Journal of Science*, 28(168):778–787, 1914.

[67] Herbert Wagner. Torsion and buckling of open sections. Technical report, 1936.

[68] Maurice Anthony Biot. Increase of torsional stiffness of a prismatical bar due to axial tension. *Journal of Applied Physics*, 10(12):860–864, 1939.

[69] D. H. Hodges. Torsion of Pretwisted Beams Due to Axial Loading. *Journal of Applied Mechanics*, 47(2):393–397, 06 1980. ISSN 0021-8936. doi: 10.1115/1.3153675. URL https://doi.org/10.1115/1.3153675.

[70] Marco Borri and Teodoro Merlini. A large displacement formulation for anisotropic beam analysis. *Meccanica*, 21:30–37, 1986.

[71] Erian A Armanios, Andrew Makeev, and David Hooke. Finite-displacement analysis of laminated composite strips with extension-twist coupling. *Journal of Aerospace Engineering*, 9(3):80–91, 1996.

[72] B. Popescu. Asymptotically correct refinements in numerical cross-sectional analysis of composite beams, (ph.d. thesis), georgia institute of technology, atlanta, georgia, U.S.A. 1998.

[73] Dewey H Hodges, Dineshkumar Harursampath, Vitali V Volovoi, and Carlos ES Cesnik. Non-classical effects in non-linear analysis of pretwisted anisotropic strips. *International Journal of Non-Linear Mechanics*, 34(2):259–277, 1999.

[74] Bogdan Popescu and Dewey H Hodges. Asymptotic treatment of the trapeze effect in finite element cross-sectional analysis of composite beams. *International Journal of Non-Linear Mechanics*, 34(4):709–721, 1999.

[75] Chang-Ho Hong and Inderjit Chopra. Aeroelastic stability analysis of a composite rotor blade. *Journal of the American Helicopter Society*, 30(2):57–67, April 1985. doi: 10.4050/JAHS.30.57.

[76] Chang-Ho Hong and Inderjit Chopra. Aeroelastic stability analysis of a composite bearingless rotor blade. *Journal of the American Helicopter Society*, 31(4):29–35, October 1986. doi: 10.4050/JAHS.31.4.29.

[77] E. H. Mansfield and A. J. Sobey. The fibre composite helicopter blade: Part i: Stiffness properties: Part ii: Prospects for aeroelastic tailoring.

Aeronautical Quarterly, 30(2):413–449, May 1979. ISSN 0001-9259. doi: 10.1017/S0001925900008623. Publisher: Cambridge University Press.

[78] Ramesh Chandra and Inderjit Chopra. Experimental and theoretical analysis of composite i-beams with elastic couplings. *AIAA journal*, 29(12):2197–2206, 1991.

[79] Ashraf M Badir, Victor L Berdichevsky, and Erian A Armanios. Theory of composite thin-walled opened-cross-section beams. In *AIAA/ASME/ASCE/AHS/ASC 34th Structures, Structural Dynamics, and Materials Conference*, pages 2761–2770, 1993.

[80] Vitali V Volovoi, Dewey H Hodges, Victor L Berdichevsky, and Vladislav G Sutyrin. Asymptotic theory for static behavior of elastic anisotropic i-beams. *International Journal of Solids and Structures*, 36(7):1017–1043, 1999.

[81] Wenbin Yu, Vitali V. Volovoi, Dewey H. Hodges, and Xianyu Hong. Validation of the variational asymptotic beam sectional analysis. *AIAA Journal*, 40(10):2105–2112, 2002. ISSN 0001-1452. doi: 10.2514/2.1545.

[82] Tohid. Bagherpour, X.M. Li, D.I. Manolas, and V.A. Riziotis. Modeling of material bend-twist coupling on wind turbine blades. *Composite Structures*, 193:237–246, 2018. ISSN 0263-8223.

[83] W.C. de Goeij, M.J.L. van Tooren, and A. Beukers. Implementation of bending-torsion coupling in the design of a wind-turbine rotor-blade. *Applied Energy*, 63(3):191–207, 1999. ISSN 0306-2619. doi: https://doi.org/10.1016/S0306-2619(99)00016-1.

[84] Sh. Shams, M. H. Sadr, and D. Badiei. Nonlinear aeroelasticity of high-aspect-ratio wings with laminated composite spar. *Journal of the Brazilian Society of Mechanical Sciences and Engineering*, 43(7), jun 2021. doi: 10.1007/s40430-021-02993-8.

[85] Khazar Hayat and Sung Kyu Ha. Load mitigation of wind turbine blade by aeroelastic tailoring via unbalanced laminates composites. *Composite Structures*, 128:122–133, 2015. ISSN 0263-8223. doi: https://doi.org/10.1016/j.compstruct.2015.03.042.

[86] CA Ie and JB Kosmatka. Saint-venant elasticity solutions of a tip-loaded anisotropic cantilevered beam with an elliptical section. *Composites Engineering*, 3(12):1149–1164, 1993.

[87] Jimmy C Ho. Stiffness constants of homogeneous, anisotropic, prismatic beams. *AIAA Journal*, 53(2):473–478, 2015.

[88] You Zhen Yang, Han Lin Ma, and Hu Wang. Analytical solution for solving bending problem of orthotropic beams. *Advanced Materials Research*, 1065-1069:2044–2048, dec 2014. doi: 10.4028/www.scientific.net/amr.1065-1069.2044.

[89] J.L. Sullivan and H. Van Oene. An elasticity analysis for the generally and specially orthotropic beams subjected to concentrated loads. *Composites Science and Technology*, 27(2):133–155, jan 1986. doi: 10.1016/0266-3538(86)90068-0.

[90] J. Schoeftner and J. Gahleitner. Refined orthotropic beam models based on castigliano's theorem and an approximate solution of the compatibility equation. *International Journal of Solids and Structures*, 230-231:111167, nov 2021. doi: 10.1016/j.ijsolstr.2021.111167.

[91] Jang-Keun LIM and Seog-Young HAN. A higher order deformation theory of orthotropic beams. *JSME International Journal Series A*, 44(3):370–373, 2001. doi: 10.1299/jsmea.44.370.

[92] Roberta Santoro. The line element-less method analysis of orthotropic beam for the De Saint Venant torsion problem. *International Journal of Mechanical Sciences*, 52 (1):43–55, 2010. ISSN 00207403. doi: 10.1016/j.ijmecsci.2009.10.002.

[93] D. Gaspari and M. Aristodemo. Torsion and flexure analysis of orthotropic beams by a boundary element model. *Engineering Analysis with Boundary Elements*, 29 (9):850–858, sep 2005. doi: 10.1016/j.enganabound.2005.05.002.

[94] Vladimir Rovenski Omri Rand. *Analytical methods in anisotropic elasticity: with symbolic computational tools.* Birkhäuser, 1 edition, 2005. ISBN 0817642722,9780817642723.

[95] Richard J. Cross, Robert A. Haynes, and Erian A. Armanios. Families of hygrothermally stable asymmetric laminated composites. *Journal of Composite Materials*, 42(7):697–716, 2008. ISSN 00219983. doi: 10.1177/0021998308088597.

[96] H. P. Chen. Study of hygrothermal isotropic layup and hygrothermal curvature-stable coupling composite laminates. In *Collection of Technical Papers - AIAA/ASME/ASCE/AHS/ASC Structures, Structural Dynamics and Materials Conference*, volume 2, pages 958–967, Reston, Virigina, apr 2003. American Institute of Aeronautics and Astronautics. ISBN 978-1-62410-100-7. doi: 10.2514/6.2003-1506.

[97] R. J. Cross, R. A. Haynes, and E. A. Armanios. Design of hygrothermally stable laminated composites for extension-twist coupling. In *American Society for Composites - 22nd Technical Conference of the American Society for Composites 2007 - Composites: Enabling a New Era in Civil Aviation*, volume 1, pages 533–542, 2007. ISBN 9781604239669.

[98] Robert Haynes, Ryan Carey, and Erian Armanios. A New Class of Hygrothermally Stable Laminates with Extension-twist Coupling. In *Annual Forum Proceedings - AHS International*, volume 3, pages 2250–2255, 2009.

[99] New Families of Hygrothermally Stable Composite Laminates with Optimal Extension-Twist Coupling. *AIAA Journal*, 48(12):2954–2961, dec 2010. ISSN 0001-1452. doi: 10.2514/1.J050596.

[100] Aditya Apte, Robert Haynes, Bo Wang, and Erian Armanio. Design of Optimal Hygrothermally Stable Laminates with Bending-Twist Coupling by Ant Colony Optimization. In *13th AIAA/ISSMO Multidisciplinary Analysis Optimization Conference*, pages 1–11, Reston, Virigina, sep 2010. American Institute of Aeronautics and Astronautics. doi: 10.2514/6.2010-9180.

[101] Daokui Li, Da Cui, and Shiming Zhou. Families of hybrid multi-coupled laminates with extension-twisting coupling. *Composite Structures*, 276(August):114543, 2021. ISSN 02638223. doi: 10.1016/j.compstruct.2021.114543.

[102] Robert A Haynes and Erian A. Armanios. Hygrothermally stable extension-twist coupled laminates with bending-twist coupling. In *ASME International Mechanical Engineering Congress and Exposition, Proceedings (IMECE)*, volume 9, pages 285–290, 2010. ISBN 9780791844465. doi: 10.1115/IMECE2010-40014.

[103] Jin Li and Daokui Li. Multi-objective optimization of hygro-thermally curvature-stable antisymmetric laminates with extension-twist coupling. *Journal of Mechanical Science and Technology*, 28(4):1373–1380, apr 2014. ISSN 1738-494X. doi: 10.1007/s12206-013-1171-y.

[104] Steven J. Winckler. Technical Notes: Hygrothermally Curvature Stable Laminates with Tension-Torsion Coupling. *Journal of the American Helicopter Society*, 30(3): 56–58, jul 1985. ISSN 2161-6027. doi: 10.4050/JAHS.30.56.

[105] R. W. Ogden. *Non-linear elastic deformations*. E. Horwood ; Halsted Press, Chichester; New York, 1984. ISBN 0-85312-273-3 978-0-85312-273-9 0-470-27508-1 978-0-470-27508-5.

[106] Robert M. Jones. *Mechanics of Composite Materials, Second Edition (Materials Science & Engineering Series)*. Taylor & Francis, 2 sub edition, 1998. ISBN 156032712X,9781560327127.

[107] Martin H Sadd. *Elasticity : theory, applications, and numerics*. Elsevier Butterworth Heinemann, 2005. ISBN 1417549629.

[108] S.P. Timoshenko. LXVI. on the correction for shear of the differential equation for transverse vibrations of prismatic bars. *The London, Edinburgh, and Dublin Philosophical Magazine and Journal of Science*, 41(245):744–746, may 1921. doi: 10.1080/14786442108636264.

[109] Robert M. Jones. *Mechanics of Composite Materials*. CRC Press, oct 2018. ISBN 9781315272986. doi: 10.1201/9781498711067.

[110] S W Tsai and N. J. Pagano. Invariant properties of composite materials. *Composite Materials Workshop*, pages 233–253, 1968.

[111] Wolfram Research, Inc. Mathematica, Version 11.0, 2016. Champaign, IL.

[112] *MATLAB version 9.10.0.1602886 (R2021a).* The Mathworks, Inc., Natick, Massachusetts, 2021.

[113] D. A. Danielson and D. H. Hodges. Nonlinear Beam Kinematics by Decomposition of the Rotation Tensor. *Journal of Applied Mechanics*, 54(2):258–262, 06 1987. ISSN 0021-8936. doi: 10.1115/1.3173004. URL https://doi.org/10.1115/1.3173004.